



UNIVERSIDADE D
COIMBRA

Luís Miguel Sousa Santos

**FATIGUE BEHAVIOUR OF MARAGING STEEL
COMPONENTS BUILT BY SELECTIVE LASER
MELTING**

**PhD Thesis in Mechanical Engineering, Structural Integrity, supervised by
Professor José António Martins Ferreira and Professor Carlos Alexandre Bento
Capela, submitted to the Department of Mechanical Engineering, Faculty of
Sciences and Technology of the University of Coimbra**

October, 2023

Faculty of Sciences and Technology
of the University of Coimbra

FATIGUE BEHAVIOUR OF MARAGING STEEL COMPONENTS BUILT BY SELECTIVE LASER MELTING

Luís Miguel Sousa Santos

PhD Thesis in Mechanical Engineering, Structural Integrity, supervised by Professor José António Martins Ferreira and Professor Carlos Alexandre Bento Capela, submitted to the Department of Mechanical Engineering, Faculty of Sciences and Technology of the University of Coimbra.

October, 2023



UNIVERSIDADE D
COIMBRA

I would like to acknowledge the FCT (Fundação para a Ciência e a Tecnologia) for sponsoring and support the current research work, under the project number 016713 (PTDC/EMS-PRO/1356/2014) financed by Project 3599, Promover a Produção Científica e Desenvolvimento Tecnológico e a Constituição de Redes Temáticas (3599-PPCDT) and FEDER funds.



Fundação
para a Ciência
e a Tecnologia



UNIÃO EUROPEIA

Fundo Europeu
de Desenvolvimento Regional



“I think, therefore I *print*”
adapted from René Descartes, 17th century

to Elisabete and the Little Ones,
for all their love!

Acknowledgements

The current thesis was only possible to develop due to the efforts of my friends and a multidisciplinary team and due to their expertise in many areas of knowledge, some more scientific, others more technological and empiric. Thus, I would like to especially acknowledge and express my gratitude to everyone that made all the difference...

To my wife Elisabete, for all her love, patience and time “given away”, which I will never be able to give back, and to my Son and Daughter, whom I love so much, who made it even more challenging, but much more rewarding too, and that with the grace of God we are continuing to enjoy our journey.

To my mother, father and brother, who with their presence made it so much easier when it was hard, much appreciated even when I was frustrated and impatient.

To Professor José António Martins Ferreira for all the knowledge he transmitted, for is immense patience and for his sincere opinions as well as his encouragement that made me grow in terms of knowledge and as a person too.

To Professor Carlos Alexandre Bento Capela for all his help, for his dedicated time during the day and the night, and for his friendly and venting talks, not always at the best time, and especially for his availability, even when life seems unfair, but always present and showing me the right path.

To Professor José Domingos, Professor Joel de Jesus, Professor Fernando Ventura, Professor Ricardo Branco, Professor Amílcar Ramalho and Professor Luís Borrego, for all the valuable knowledge shared and all the help during the trials and tests, always pursuing the best practices and helping with their expertise, even in the smallest of details, which made all the difference.

To CEMMPRE (Centre for Mechanical Engineering, Materials and Processes) for the opportunity to work side by side with a great research team that was always ready to assist and contribute, and for the availability of the laboratories and instruments needed to do the research.

To the UC (University of Coimbra), more specifically to the FCTUC (Faculdade de Ciências e Tecnologia da Universidade de Coimbra) for having the necessary conditions and infrastructures to develop knowledge and enable the students to do their work.

To EROFIO, Engineering and Mold Manufacturing, under the leadership of its founder and administrator, Mr. Manuel Novo, for all the support, availability and the opportunity to work and learn from you, side by side.

To Mr. João Frade and Mr. Miguel Marcelino, for all the help during this period and to make all the resources available when needed.

To the rest of the EROFIO team, that helped in countless different ways, and especially to the ones that have been sharing their lunch time and their good mood with me, making it possible to do research work even after a working day.

To the fellow students, colleagues and friends, for the shared knowledge, time and talks, making the long road shorter, little by little.

To the FCT (Fundação para a Ciência e a Tecnologia) for sponsoring and support the current research work, under the project number 016713 (PTDC/EMS-PRO/1356/2014) financed by Project 3599, Promover a Produção Científica e Desenvolvimento Tecnológico e a Constituição de Redes Temáticas (3599-PPCDT) and FEDER funds.

Abstract

Selective Laser Melting (SLM) is a 3D Printing technology, being one of the most known and preferred by the industry to build complex geometric parts, using 100% metal powder, and being a process virtually free from contaminations. As a relatively recent way of processing metals, it has been used to produce parts for the medical field (namely prosthesis), for the aeronautical industry (turbine blades), and conformal cooling inserts in the tooling industry, among others. It has even been used to build critical parts, to repair damaged or worn-down components, even if they are made in different metal alloys, obtaining a “hybrid part”. In this case, the metal alloy used in the SLM process is the AISI 18Ni300. Due to its mechanical properties, it is commonly applied in mechanical and structural components, as well as in tooling applications. It was one of the first steel alloys used by the SLM technology, not only, but also due to its low carbon content in its composition, reducing the risk of a crack arising during the processing of the material in a “cold process”. Due to these facts, the thesis research was focused in the assessment of the mechanical fatigue behaviour of different SLMed specimens’ formulations, and under different testing conditions, indicated below.

The tensile behaviour was studied to assess the laser scan speed (200, 400 and 600 mm/s) influence on the achieved porosity and the mechanical properties. The best results were achieved for the scan speed of 200 mm/s.

Fatigue endurance was assessed using the common $S - N$ curves and cylindrical “bone-shaped” specimens for components obtained by SLM and hybrids (printed or SLMed on top of a substrate with a different metal alloy), tested under constant amplitude load and strain control, and under variable amplitude load by blocks.

Fatigue crack growth endurance was analysed using CT specimens obtained by SLM and hybrids, under different stress ratios ($R = 0.05, 0.3$ and 0.6). The Paris law constants (C and m) were determined, and the “crack closure” phenomenon under constant amplitude loads and for single or by blocks overloads was also studied.

The influence of the heat treatment was analysed, including its impact on the microstructure and the fatigue crack growth rates, and also on the effect of the overloads. The fracture mechanisms were studied, using scanning electron microscopy to analyse the fracture surfaces.

KEYWORDS: Additive manufacturing; fatigue; fatigue crack growth; hybrid materials; selective laser melting.

Resumo

A Fusão Seletiva por Laser (SLM) é uma tecnologia de impressão 3D, sendo uma das mais conhecidas e preferenciais pela indústria para construir peças com geometria complexa, utilizando pós 100% metálicos, e sendo um processo virtualmente livre de contaminações. Como forma relativamente recente de processar metais, tem sido utilizada para produzir peças no campo médico (nomeadamente próteses), na indústria aeronáutica (pás de turbina), postigos com refrigeração conformada na indústria das ferramentas, entre muitas outras. Tem sido utilizada até para construir peças críticas, para reparar componentes danificados/desgastados, mesmo se feitos em ligas metálicas diferentes, obtendo-se uma “peça híbrida”. Neste caso, a liga metálica utilizada no processo de SLM é a AISI 18Ni300. Devido às suas propriedades mecânicas, é usualmente aplicada em componentes mecânicos e estruturais, bem como em ferramentas. Foi uma das primeiras ligas de aço a ser utilizada pela tecnologia de SLM, não só, mas também devido ao seu baixo teor de carbono na sua composição, reduzindo o risco de surgir uma fenda durante o processamento do material num “processo a frio”. Devido a estes factos, o trabalho de investigação foi focado na avaliação do comportamento mecânico à fadiga de diferentes formulações de provetes obtidos por SLM, e para diferentes condições de teste, abaixo indicadas.

Foi estudado o comportamento à tração para avaliar a influência da velocidade de varrimento do laser (200, 400 e 600 mm/s) na porosidade obtida e nas propriedades mecânicas. Os melhores resultados foram obtidos para a velocidade de varrimento de 200 mm/s.

A resistência à fadiga foi estudada recorrendo às tradicionais curvas $S - N$ e a provetes cilíndricos em forma de “osso” para componentes obtidos por SLM e híbridos (imprimido/SLMed no topo de um substrato de liga metálica diferente), ensaiados com controlo de carga e deformação a amplitude constantes, e com carregamentos a amplitude variável por blocos.

A resistência à propagação de fendas de fadiga foi analisada usando provetes CT obtidos por SLM e híbridos, sob diferentes razão de tensão ($R = 0,05, 0,3$ e $0,6$). Foram determinadas as constantes da lei de Paris (C e m) e estudado o fenómeno de “fecho de fenda” para solicitações de amplitude constante e também para sobrecargas únicas ou na forma de blocos.

A influência do tratamento térmico foi analisada, incluindo o seu impacto na microestrutura e nas velocidades de propagação de fenda, e também no efeito das sobrecargas. Os mecanismos de rotura foram estudados, analisando por microscopia eletrónica de varrimento as superfícies de fratura.

PALAVRAS-CHAVE: Fabricação aditiva; fadiga; propagação de fendas de fadiga; materiais híbridos; fusão seletiva a laser.

Table of Contents

Acknowledgements	i
Abstract	iii
Resumo	iv
Table of Contents	vii
List of Figures	ix
List of Tables.....	xiv
List of Acronyms.....	xv
List of Symbols	xvii
1. Introduction and Objectives.....	1
1.1. Objectives.....	4
2. Literature Review	5
2.1. Main Additive Manufacturing Processes	5
2.1.1. Binder Jetting.....	5
2.1.2. Material Jetting.....	6
2.1.3. Material Extrusion	7
2.1.4. Vat Photopolymerisation	7
2.1.5. Laminated Object Manufacturing.....	8
2.1.6. Direct Energy Deposition	9
2.1.7. Cold Spray Additive Manufacturing – CSAM	11
2.1.8. Friction Stir Additive Manufacturing – FSAM	13
2.1.9. Powder Bed Fusion Systems	15
2.1.9.1. Selective Laser Sintering – SLS	15
2.1.9.2. Electron Beam Melting – EBM	18
2.1.9.3. Selective Laser Melting – SLM.....	21
2.2. 3D Printing Overview: Facts and Trends	26
2.3. Considerations About Fatigue Behaviour of Materials	32
2.3.1. The Microstructure and the Materials Fatigue Behaviour	38
2.3.2. Loading Effect on the Materials Fatigue Behaviour.....	39
2.3.3. Influence of Surface Finishing and Treatments on Materials Fatigue Behaviour ..	39
2.3.4. Residual Stress on the Materials Fatigue Behaviour	40
2.3.5. Low Cycle Fatigue	40

2.3.6.	Fracture Modes	44
2.3.7.	Stress Intensity Factor – K	44
2.3.8.	Stress ratio and crack propagation speed	47
2.4.	Fatigue Notes in Metal 3D Printed Materials	49
3.	Main Results and Discussion of Fatigue Life Assessment of Maraging Steel Components and Hybrid Formulations Built by Selective Laser Melting	57
3.1.	Experimental Overview and Materials	57
3.2.	Microstructure and Porosity.....	61
3.3.	Monotonic Mechanical Properties	63
3.4.	Fatigue Assessment.....	65
3.5.	Low Cycle Fatigue Assessment	67
3.6.	Fatigue Fracture Analysis	74
	Appendix I	76
	Appendix II	83
	Appendix III.....	95
4.	Main Results and Discussion of Fatigue Crack Growth in 18Ni300 Maraging Steel Alloy and Hybrid Formulations Built by Selective Laser Melting	111
4.1.	Experimental Overview and Materials	111
4.2.	Microstructure Analysis of Hybrid Specimens and the Effect of the Age Hardening Heat Treatment of SLMed 18Ni300 Steel Alloy	113
4.3.	Assessment of the FCG on a 18Ni300 Alloy in as Printed Condition and in Heat-Treated Condition	115
4.4.	FCG Numerical Analysis Based on Plastic CTOD (δ_p) for 18Ni300 Material in as Printed Condition.....	120
4.5.	Fracture Surface Analysis	125
	Appendix IV.....	127
	Appendix V	140
	Appendix VI.....	146
5.	Conclusion and Future Works.....	157
6.	References	161

List of Figures

Figure 2.1: Casted metal part on the left and some of the corresponding sand mold components used and built by binder jetting, on the right [Ziaee <i>et al</i> , 2019].	6
Figure 2.2: XJet material jetting machine (a) used to build a zirconia component (b) [Oh <i>et al</i> , 2019].	6
Figure 2.3: Mark2 extruder composite 3D printer machine on the left, and on the right, a built part where it is possible to see the Kevlar fibre in yellow, next to the outer border, reinforcing the black polymer and strengthening the final part [Markforged (1); Markforged (2)].	7
Figure 2.4: Hearing aids (a) [Thompson <i>et al</i> , 2016] built by vat photopolymerisation and an example of a scaffold for tissue engineering built by micro-photopolymerisation (b) [Chartrain <i>et al</i> , 2018].	8
Figure 2.5: Examples of built parts by LOM. A “sandwich” metallic matrix composite (a) of aluminium and tantalum used for electronic insulation, intended for satellite application [Fabrisonic], and a dog built in high resolution printed paper (b) [Mcor].	9
Figure 2.6: Description of the DED process using a laser as a heat source and a wire as feed-stock material [Froend <i>et al</i> , 2019].	10
Figure 2.7: Examples of multi-material parts built by powder DED in hybrid (DED + CNC milling) DMG Mori machines. In a) is a multi-material heat exchanger made of stainless steel and bronze [DMG Mori (1)] and in b) is a multi-material turbine casing built in Inconel 718 and bronze for the aerospace industry [DMG Mori (2)].	10
Figure 2.8: Schematic presentation of a CSAM system [Li (2) <i>et al</i> , 2019].	11
Figure 2.9: Metal composite flange built by the CSAM process after mechanical finishing [Li (1) <i>et al</i> , 2019].	12
Figure 2.10: Damaged tee box housing from an aircraft flap transmission that was repaired by CSAM and machined in to the “as new” state [Yin <i>et al</i> , 2018].	12
Figure 2.11: Examples of FSAM_1 deposition process. In a) rotary friction welding was used to build a few piles of layers and in b) the surface friction deposition was used to create 3 “surface” layers [Padhy <i>et al</i> , 2018].	14
Figure 2.12: Schematic view of the FSAM_2 process where overlapped metal sheets are used, following the Friction Stir Lap Welding (FSLW) of the last sheet with the previous one or the substrate, and optional milling of the last welded sheet to prepare for the overlap by another sheet. The process is repeated until the desired height is reached [Srivastava <i>et al</i> , 2019].	14
Figure 2.13: Defects of the Friction Stir process. In a) the hooking bonding defect, and in b) the black region corresponds to a cavity defect [Zhao <i>et al</i> , 2019; Padhy <i>et al</i> , 2018].	15

Figure 2.14: Representation of an SLS system process [Chen <i>et al</i> , 2018].	16
Figure 2.15: Samples built by an SLS system. Single layer of polymeric composite made of Polyamide matrix and wood powder filler (5 and 10 % wt) [Velu <i>et al</i> , 2016].	17
Figure 2.16: Shoes midsole produced by the SLS process from the trade mark “Under Armour” [Wu <i>et al</i> , 2020].	18
Figure 2.17: Scheme of the inside of an ARCAM EBM machine system [Fayazfar <i>et al</i> , 2018].	19
Figure 2.18: Detail of the inside of an ARCAM’s machine building chamber, processing a nickel 718 alloy. The electron beam is defining the contour in a), following the bulk melting region in b) [ARCAM (1)].	20
Figure 2.19: Components that are typically built in Titanium alloys, built by ARCAM EBM process. Low pressure blade commonly used in aeronautical turbines and an acetabular cup implant with details of its 3D trabecular like texture to optimize osseointegration [ARCAM (1); ARCAM (2)].	20
Figure 2.20: Schematic view of a Concept Laser machine [Concept Laser].	21
Figure 2.21: Schematic workflow of a 3D printing job [Adapted from EOS].	22
Figure 2.22: Dissimilar materials achieved by “LPBF” systems. In (a) a detail of a part built from a metal alloy and a ceramic (316L/soda-lime glass), and in (b) a part made by different metal alloys (316L/CuCrZr) produced by Aerosint SA [Wang <i>et al</i> , 2022].	24
Figure 2.23: Relative comparison of the 3D printing popularity throughout its history [Adapted from Hubs].	26
Figure 2.24: Comparison between the local, national and international cycle of polymeric material [Garmulewicz <i>et al</i> , 2018].	27
Figure 2.25: Relation between the number of printed open-source designs and the cost savings for Prosumers using low-cost printers at home [Pearce <i>et al</i> , 2022].	28
Figure 2.26: Overview of the 3D Printing market economy and its growing forecasts up to 2026 [Adapted from Hubs].	30
Figure 2.27: Number of printed parts per batch of the surveyed entities [Hubs].	30
Figure 2.28: Door latch printed as a metamaterial, monolithic part. In a) the latch structure is relaxed and in b) the structure is under a torque creating function/movement, as indicated by the arrow [Adapted from Ion <i>et al</i> , 2016].	31
Figure 2.29: Schematic view of a 6D printed part process [Adapted from Nida <i>et al</i> , 2022].	31
Figure 2.30: Example of a sinusoidal curve.	33
Figure 2.31: Example of a stress curve at variable amplitude by blocks.	33
Figure 2.32: Fatigue crack mechanism in the slip bands [Based on Meyers <i>et al</i> , 2009].	35
Figure 2.33: Generic S-N curve for a material.	37
Figure 2.34: Example of cyclic stress-strain diagram and its hysteresis cyclic loop.	41
Figure 2.35: Hysteresis cyclic loop curve and respective cyclic stress-strain curve.	42

Figure 2.36: Total strain amplitude curve, and elastic and plastic strain amplitude curves versus number of reversals to failure.....	43
Figure 2.37: Fracture modes, Mode I, II and III (the arrow indicates the loading direction).....	44
Figure 2.38: Depiction of a crack length growth curve with an applied fatigue loading and the respective number of cycles.	45
Figure 2.39: Identification of Regime I, II and III limits, depicted on $dadN-\Delta K$ curve, representative of a metal.....	47
Figure 2.40: Depiction of the influence of the stress ratio on the $dadN-\Delta K$ curves.....	48
Figure 2.41: Relation between the stress range and the stress intensity factor according to the Elber's theory. [Suresh <i>et al</i> , 2004].....	49
Figure 3.1: Geometry and dimensions of cylindrical fully built specimens and hybrid formulations. In the hybrid formulations, and as indicated in Table 3.2, one half of it corresponds to the substrate made from HS or SS bulk material (darker region).	58
Figure 3.2: Concept Laser M3 Linear machine (a) during the building of the specimens and selectively laser melting the 18Ni300 powder (b). Courtesy of Erofió S.A.....	58
Figure 3.3: Specimens after the SLM process built at a scan speed of 200 mm/s. In a) the specimens are in <i>as printed</i> condition and on the build plate, and after the wired electrical discharging cutting of them from the build plate in b). In c) it is possible to observe the hybrid specimens after the SLM process, being formed by an AISI 420 substrate (darker region) with the intrinsic melted top (rougher region). In d) is possible to see the specimens after all the finishing iterations of lathe, grinding and polishing.....	59
Figure 3.4: Tensile test apparatus in the Instron EletroPuls E10000 (a) with a detail of the assembled specimen (b).....	59
Figure 3.5: CT's specimen dimensions and, if hybrid, with the spotted region made from a different substrate material, as indicated on Table 3.2. Where $a_0 = 7$ and $e = 6$ mm.	60
Figure 3.6: Servohydraulic Instron test machine and its apparatus during a fatigue crack growth rate test (a), and detail of the CT specimen and travelling measuring microscope (b).	61
Figure 3.7: Low-cycle fatigue specimen's dimensions.	61
Figure 3.8: Microstructure and porosity of specimens built with scan speeds of 200 mm/s (a) and 400 mm/s (b), and how it was detected by the image "J" software (c).	62
Figure 3.9: Microstructure of the SLMed 18Ni300 material with a red boundary around acicular structure (a); interface of H13 material with the SLMed material (b); interface of 420 material with the SLMed.	63
Figure 3.10: Monotonic tensile load-strain curves of the different specimen formulations.....	64
Figure 3.11: Comparison between <i>S-N</i> curves under Load and Displacement control for the fully SLMed 18Ni300 specimen.	65
Figure 3.12: Plot of <i>S-N</i> curves under load control (a) and displacement control (b) for fully SLMed and hybrid specimen formulations.	66
Figure 3.13: Scheme of the stress pattern loop load during the variable amplitude fatigue tests... 66	66

Figure 3.14: Comparison between experimental and predicted lives using Miner’s law for fully SLMed specimens (a), and hybrid formulations with substrate materials in AISI H13 (b), and in AISI 420 (c).	67
Figure 3.15: Peak, mean and valley stress variation throughout its normalized life.....	68
Figure 3.16: Plastic strain energy density per cycle throughout its normalized life, during low-cycle fatigue test at different strain rates.	69
Figure 3.17: Total strain energy density per cycle throughout its normalized life, during low-cycle fatigue test at different strain rates.....	69
Figure 3.18: Stable mid-life circuits at different strain amplitudes with joined lower tips (a) and with merged upper branches (b).....	70
Figure 3.19: Relation between the cyclic stress amplitude and the plastic and elastic strain amplitude, using the unloading modulus resulting from the tests and depicted by the dashed line, the Young’s Modulus (E) resulted from the monotonic tensile tests, depicted by the dashed-dot line.	71
Figure 3.20: Comparison between the monotonic tensile stress-strain curve and the cyclic stress-strain curve, enlightening the softening of the AISI 18Ni300 SLMed material.	72
Figure 3.21: Plastic, elastic and total strain amplitude against number of reversals to failure.	72
Figure 3.22: Plastic strain energy (Equation 26) and total strain energy (Equation 27) versus number of reversals to failure in the mid-life hysteresis loop.....	73
Figure 3.23: Fracture surfaces resulting from fatigue tests; in a) the fracture surface is revealing the cross-hatch texture done by the laser scanning strategy and in b) it is possible to observe the brittle crack propagation facets.	74
Figure 3.24: Fracture surfaces resulting from the low-cycle fatigue tests; a) multi-nucleation cracks; b) crack nucleation on lack of penetration defect; c) crack propagation by mixed mode, starting with brittle fracture and passing to ductile fracture when growing in the direction of the specimen’s center; d) unmolten particles defect.	75
Figure 4.1: Low-cycle fatigue specimen’s dimensions for the SLMed material.	112
Figure 4.2: Example of CT specimens used in the different tests. In a) it is possible to observe one layer finished during the SLM process, it being possible to observe the CT specimens with a thickness of 3 and 6 mm, and in b) the respective build job after the SLM process, powder removal and still “welded” to the build plate, contrasting with the hybrid ones in c), that were produced individually “attached” to the substrate material. Finally, in d), it is a manufactured specimen ready to test, after grinding, after wired electro discharging process and polishing....	112
Figure 4.3: Instron EletroPuls E10000 testing machine (a) with an assembled traveling measuring device used for crack tip measurement and details of specimen assembling holes (b) for the micro gauge (c) used to measure the crack tip opening.	113
Figure 4.4: SLMed 18Ni300 microstructure in as printed (a) and heat-treated condition (b).	114
Figure 4.5: Comparison of residual tensile stress in as printed condition and after heat treatment for the SLMed 18Ni300.	114

Figure 4.6: Experimental results comparison of SLMed 18Ni300 material da/dN-ΔK curves with different materials (a) and under different conditions (b) at R=0.05.....	115
Figure 4.7: Mean stress influence in the da/dN-ΔK curves of the hybrid specimen built on top of an AISI 420 stainless steel substrate.	117
Figure 4.8: Opening load determination using the maximization of the correlation coefficient technique.	118
Figure 4.9: Transient regime after single overload with and without heat treatment (a) and the influence of block overloads in heat-treated specimens (b).	119
Figure 4.10: Transient regime after single and block overloads for specimens with an AISI 420 substrate (a) and the influence of the substrate when applying blocks of 100 overloads (b).	119
Figure 4.11: Crack path and bifurcation resulting from a single overload for heat-treated SLMed material (a) and for the hybrid formulation with a CK45E substrate.	120
Figure 4.12: Experimental curve resulting from cyclic tests to acquire stress-strain relationship (a) and the superimposed numerical fitted curve (b).	121
Figure 4.13: Representation of the FE model used to determine CTOD with loading conditions (a), boundary conditions for plane stress state (b) and detail of the refined finite element mesh (c).	122
Figure 4.14: Representation of CTOD evolution under a remote single load at stress plane and with an initial crack length of $a_0 = 24$ mm.	123
Figure 4.15: Plastic CTOD range (δp) evolution with the effective load range ($R = 0.01$).	123
Figure 4.16: Comparison of FCGR behaviour with the plastic CTOD range, δp , for different materials.	124
Figure 4.17: Numerical determination of $\Delta K_{th} = 11.2$ MPam, for 2 different cases, based on numerical prediction of plastic CTOD versus load plots, and comparison with the experimental value of 5.2 MPam.	125
Figure 4.18: Microscopy of fracture crack path of 18Ni300 SLMed material in as printed condition (a) and after precipitation hardening heat treatment (b).	126
Figure 4.19: SEM of fracture surfaces in the transient regime, resulted from an applied single overload in the 18Ni300 SLMed material in as printed condition (a) and after precipitation hardening heat treatment (b).	126

List of Tables

Table 3.1: Chemical composition of the different materials used in the specimens, presented in weight % and according to supplier.....	57
Table 3.2: Hybrid specimens' design.....	58
Table 3.3: Materials' monotonic tensile properties; a – experimental values from tensile tests of SLMed specimens; b – values according to materials' supplier datasheet.	60
Table 3.4: Mechanical properties of the SLMed 18Ni300 material, assessed under different scan speeds.....	62
Table 4.1: Chemical composition of the new substrate material in weight %, according to the supplier.....	111
Table 4.2: Materials' monotonic tensile properties according to supplier.....	111

List of Acronyms

3D – Three Dimensions
4D – Four Dimensions
AM – Additive Manufacturing
BSE – Backscattered Electron (microscopy)
CAD – Computer Aided Design
CNC – Computer Numerical Control
CS – Cold Spray
CSAM – Cold Spray Additive Manufacturing
CT – Compact Tension (specimens)
CTOD, CTOD_p – Crack Tip Opening Displacement; Plastic CTOD
DED – Direct Energy Deposition
DLF – Directed Light Fabrication
DMD – Direct Metal Deposition
DMLS – Direct Metal Laser Sintering
EBAM – Electron Beam Additive Manufacturing
EBM – Electron Beam Melting
EBSD – Electron Backscatter Diffraction
EDM – Electrical Discharge Machining
EDS – Energy Dispersive X-Ray Spectroscopy
FCG – Fatigue Crack Growth
FCGR – Fatigue Crack Growth Rate
FDM – Fused Deposition Modelling
FEG – Field Emission Gun
FSAM – Friction Stir Additive Manufacturing
HCF – High Cycle Fatigue
HIP – Hot Isostatic Pressing
HT – Heat Treatment
L-PBF, LPBF – Laser Powder Bed Fusion
LEFM – Linear Elastic Fracture Mechanics
LENS – Laser Engineered Net Shaping
LoF – Lack of Fusion
LOM – Laminated Object Manufacturing
LSF – Laser Solid Forming

MEX – Material Extrusion
MS – Maraging Steel
OLR – Overload Ratio
PBF – Powder Bed Fusion
PBLM – Powder Bed Laser Melting
SEM – Scanning Electron Microscope
SLA – Stereolithography
SLM – Selective Laser Melting (metals)
SLS – Selective Laser Sintering (polymers and polymeric composites)
UV – Ultra Violet (radiation)
VED – Volumetric Energy Density
VHCF – Very High Cycle Fatigue
WAAM – Wire Arc Additive Manufacturing

List of Symbols

- a | a_0 | a_c – crack length, initial crack length and critical crack length, respectively
- b – fatigue strength exponent
- c – fatigue ductility exponent
- B – constant of material
- E | E'' – Young's modulus and unloading modulus (hysteresis loop), respectively
- ε_f' – fatigue ductility coefficient
- ε – strain
- P – laser power
- v – scanning velocity
- h – hatch distance
- t – layer thickness
- σ_a – stress amplitude or alternating stress
- σ_{f0} – fatigue limit or endurance
- σ_f' – fatigue strength coefficient
- σ_m – mean stress
- σ_{max} – maximum stress level (fatigue stress cycle)
- σ_{min} – minimum stress level (fatigue stress cycle)
- σ_{ar} – equivalent stress amplitude
- σ_u – ultimate tensile strength
- r – correlation coefficient
- R – stress ratio
- R_{cr} – critical stress ratio
- R_{op} – stress ratio when the crack is fully open
- k – number/quantity of blocks
- n' – cyclic hardening exponent
- n_i – number/quantity of cycles for the respective block
- N_i – fatigue duration for the corresponding stress σ_i
- N_f – number of cycles to failure
- N_r – number of rupture cycles
- N_p – number of cycles predicted
- $2N_T$ – number of reversals to failure in a transient regime
- P_{op} – opening load

S – nominal stress, degree of softening (cyclic behaviour)
 K – stress intensity factor
 k' – cyclic hardening coefficient
 K_c | K_{1c} – critical fracture toughness stress intensity factor and critical fracture toughness stress intensity factor in fracture mode I, respectively
 K_{cl} – stress closure intensity factor
 K_{max} and K_{min} – maximum and minimum stress intensity factor on a fatigue stress cycle, respectively
 K_{op} – stress intensity factor when the crack is fully open
 δ_p – plastic crack tip opening displacement
 $\Delta\sigma$ – stress range
 $\Delta\varepsilon$ – strain range
 $\Delta\varepsilon_e$ – elastic strain range
 $\Delta\varepsilon_p$ – plastic strain range
 ΔK – stress intensity factor range
 ΔK_0 – threshold stress intensity factor range in mode I
 ΔK_{BL} – baseline stress intensity factor range
 ΔK_{OL} – maximum peak stress intensity factor
 ΔK_{op} – stress intensity factor range when the crack is fully open
 ΔK_{th} – fatigue crack growth threshold range
 Y – geometric factor related to the specimen geometry

1. Introduction and Objectives

Additive Manufacturing or simply AM, is with every passing day becoming an unavoidable reality of the world. It has been a long-held dream since the existence of rapid prototyping that is becoming a reality through advances in the technological means needed to achieve it.

At the beginning, the so-called prototyping machines, nowadays simply designated as *3D Printers*, were only used for prototyping ends, evaluation, and as an important conceptual tool even for the purposes of aesthetics. It was not meant to produce parts for real applications because their tolerances and mechanical properties were unable to match the industry specifications and the end-user's applications. The most common materials used were polymers such as waxes, thermoplastics and resins.

With the technological evolution, the materials have evolved from polymers to reinforced polymers, metals and ceramics (e.g.: glass and alumina), and the use of engineering polymers (PEEK), silicones, metals, from the light-weight alloys, like aluminium and titanium, to high strength steels, nickel-based super-alloys, encompassing precious metals, like gold and platinum, refractory metals like tungsten molybdenum, and amorphous metal alloys [Chen *et al*, 2018; Wu *et al*, 2020; Greiner *et al*, 2017; Zeng *et al*, 2019; Velu *et al*, 2016; Wang *et al*, 2022; Concept Laser; EOS]. Today, it is theoretically possible to use any metal available to build “any part” using AM processes.

At the present, the so-called 3D Printers are being used to produce almost everything needed, from metal components, through food, medicaments (pills), organs and houses too [Sheng, 2022]. The applications field is growing at the same time as the technology becomes available [Sheng, 2022; Hubs].

Nowadays, there is still a lot of research in the field of AM because everyone wants to be able to do what they need and when they need it, with the required specifications and as quickly as possible. Other concepts are emerging like the “4D, 5D and 6D Printers/Materials”, creating new possibilities and providing the solutions for today's issues [Ion *et al*, 2016].

This is definitely the present and it will be the future, until humanity reaches the “nD Atomic” Printers and Materials.

In this way, the current thesis is meant to provide a deeper insight in the assessment of the mechanical fatigue behaviour of a 18Ni300 steel powder alloy processed by the SLM technology,

for fully SLMed specimens and for hybrid or discrete bimetallic specimens. In this research a hybrid specimen is achieved by adding the SLMed material on top of an existing preform, called substrate, achieved by conventional means and from different steel alloys.

The results were published in specialty journals in the form of the following research papers:

- “Fatigue behaviour of selective laser melting steel components”, Santos L.M.S., Ferreira J.A.M., Jesus J.S., Costa J.M., Capela C., *Theoretical and Applied Fracture Mechanics*, Volume 85, Part A, 2016, Pages 9-15, ISSN 0167-8442. <https://doi.org/10.1016/j.tafmec.2016.08.011>. (Appendix I)
- “Fatigue Behaviour of Hybrid Components Containing Maraging Steel Parts Produced by Laser Powder Bed Fusion”, Santos L., de Jesus J., Borrego L., Ferreira J.A.M., Fernandes R.F., da Costa J.D.M., Capela C., *Metals*. 2021; 11(5):835. <https://doi.org/10.3390/met11050835>. (Appendix II)
- “Low-Cycle Fatigue Behaviour of AISI 18Ni300 Maraging Steel Produced by Selective Laser Melting”, Branco R., Costa J.D.M., Berto F., Razavi S.M.J., Ferreira J.A.M., Capela C., Santos L., Antunes F., *Metals*, 2018; 8(1):32. <https://doi.org/10.3390/met8010032>. (Appendix III)
- “Fatigue Crack Growth in Maraging Steel Obtained by Selective Laser Melting”, Antunes F., Santos L., Capela C., Ferreira J., Costa J., Jesus J., Prates P., *Applied Sciences*, 2019; 9(20):4412. <https://doi.org/10.3390/app9204412>. (Appendix IV)
- “Effect of heat treatment on the fatigue crack growth behaviour in additive manufactured AISI 18Ni300 steel”, Santos L.M.S., Borrego L.P., Ferreira J.A.M., de Jesus J., Costa J.D., Capela C., *Theoretical and Applied Fracture Mechanics*, Volume 102, 2019, Pages 10-15, ISSN 0167-8442. <https://doi.org/10.1016/j.tafmec.2019.04.005>. (Appendix V)
- “Fatigue crack propagation along interfaces of selective laser melting steel hybrid parts”, Santos L.M.S., Ferreira J.A.M., Borrego L.P., Costa J.D., Capela C., de Jesus J., *Fatigue Fract Eng Mater Struct*. 2019; 42: 2431–2440. <https://doi.org/10.1111/ffe.13072>. (Appendix VI)

The research was also present in the following conferences and events:

- XV Portuguese Conference on Fracture (PCF 2016), Paço de Arcos, Portugal, 2016.

- XVIII International Colloquium on Mechanical Fatigue of Metals (ICMFM XVIII), Gijón, España; 2016.
- XXXIV Encuentro del Grupo Español de Fractura, Santander, Spain; 2017.
- XVI Portuguese Conference on Fracture (PCF 2018), Universidade da Beira Interior, Covilhã, Portugal, 2018.
- 18th International Conference on New Trends in Fatigue and Fracture (NT2F18), Lisbon, Portugal, 2018.
- XXXV Encuentro del Grupo Español de Fractura, Santander, Málaga; 2018.
- First International Symposium on Risk and Safety of Complex Structures and Components (IRAS 2019) Porto, Portugal, 2019.
- 1st Virtual Iberian Conference on Structural Integrity, Coimbra, Portugal, 2020.

The author was responsible for the production of the specimens, including the Additive Manufacturing/SLM process and all the postprocessing required to finish them, like milling, turning, grinding, heat-treatment, wired electrical discharging, drilling and polishing. The manufacture of the specimens was done at EROFIO S.A., under the supervision of the supervisors. The author, with the supervisors' guidance and the help of the research team from CEMMPRE, contributed to the writing of published papers, participation in conferences and in the experimental tests carried out in the Department of Mechanical Engineering of the University of Coimbra.

The following thesis has five more chapters, developed around the research work and the published papers:

- Chapter 2: Literature Review – where the main 3D printing technologies and their main differences, trends from the global market and 3D printing industry are enumerated. There is a summary explaining fatigue principles, mainly applied to metal alloys traditionally obtained by casting, and research about fatigue applied to materials achieved by 3D printing technologies.
- Chapter 3: Main Results and Discussion of Fatigue Life Assessment of Maraging Steel Components and Hybrid Formulations Built by Selective Laser Melting – summary of

results from fatigue tests from hybrid and totally built specimens achieved by the SLM technology, mainly regarding $S-N$ curves and low-cycle fatigue behaviour under different load conditions. Closing the Chapter with the Appendixes of the published research.

- Chapter 4: Main Results and Discussion of Fatigue Crack Growth in 18Ni300 Maraging Steel Alloy and Hybrid Formulations Built by Selective Laser Melting – the fatigue crack propagation assessment of the SLM specimens, including hybrid ones, and the influence of the post-heat-treatment. The overload and the crack retardation effect were also studied. The Chapter is closed with the published research works in the form of Appendixes.
- Chapter 5: Conclusion and Future Works – summary with the main conclusions drawn from all the research work and some suggestions of future research topics.
- Chapter 6: References – Last Chapter indicating all the literature and websites that have supported the thesis development.

1.1. Objectives

The main goal of the present thesis and research work involved is to evaluate and assess the mechanical properties and fatigue behaviour of the AISI 18Ni300 maraging steel alloy, and “hybrid” or bimetallic discrete formulations too, produced by the Selective Laser Melting process, more specifically by the LaserCUSING® process. This has been done for the material in “as printed” and heat-treated conditions and for different load conditions.

It is important to mention that the fatigue results and achieved curves are not meant for project engineering but to provide in-depth knowledge about the material properties and to identify trends and limits that could validate the application of the AISI 18Ni300 material in the Selective Laser Melting process to build different mechanical components for aviation, motorsports, tooling and other industries that need mechanical components with complex geometries. Some of these industries require certified components due to the risk of failure and catastrophic fatigue rupture, which can lead to disasters and injuries. In many critical components, it is not enough to only assess the fatigue curves according to the scientific standards, through the tests of specimens or coupons, but to demand a statistical approach towards of the specific component integrity and their intrinsic fatigue properties, often creating metrics that attempt to create a correlation between “good mechanical properties”, at the material level, and the parts built by SLM.

2. Literature Review

2.1. Main Additive Manufacturing Processes

The following technologies and developments are briefly described and were identified by generic names accordingly to the different literature, and not according to any established standard, like the “ISO/ASTM – 52900:21(en): Additive Manufacturing – General principles – Fundamentals and vocabulary” [ISO, 2023].

2.1.1. Binder Jetting

The binder jetting technique is a layer-by-layer process which uses powders that is distributed evenly on each layer in the building platform with subsequent agglomeration. The agglomeration occurs from the interaction between the powder and the liquid binder that acts like “glue”. The binder is deposited through an inkjetting/jetting system, drop by drop, on the areas corresponding to the built object. There are some materials available like polymers, ceramics, gypsum, sand and metals. [Shahrubudin *et al*, 2019]

This technology is currently used to produce casting sand molds (Figure 2.1) for the industry, in the medical field for denture framework, surgical implants, bone scaffolds, and there are still investigation studies being conducted in pharmaceuticals, for controlled drug release and in the electronic industry for capacitors and piezoelectric applications. [Ziaee *et al*, 2019]

Binder Jetting is main advantage is that it can use virtually any powdered material to create a *green part* at high-speed rates, 200 cm³/min. A *green part* is the result of the binder jetting process, where its mechanical properties are mainly the result of interaction between the binder and the powder material, typically with densities around 50-60%. The parts are post-processed. Firstly, the debinding occurs and later the sintering (powder from the green part) or the infiltration (with a lower melting point material) to achieve higher densities and mechanical properties. In metals, it is theoretically possible to achieve densities higher than 99%. [Ziaee *et al*, 2019]

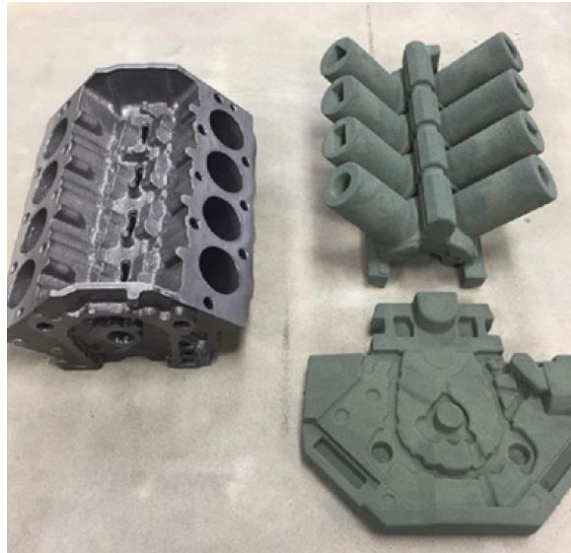


Figure 2.1: Casted metal part on the left and some of the corresponding sand mold components used and built by binder jetting, on the right [Ziaee *et al*, 2019].

2.1.2. Material Jetting

Material Jetting consists of a layer-by-layer process and uses fine solid particles dispersed (they could be nanoparticles) in a liquid matrix and is very similar to the Binder Jetting. This is often called an inkjet process that uses a printhead to selectively deposit the material on the building platform [Shahrubudin *et al*, 2019]. The most used liquids are photosensitive materials that solidify under ultraviolet radiation/light, or they can use waxes [Shen *et al*, 2019]. The parts built by Material Jetting have a high dimensional accuracy and a smooth surface finishing. It is possible to print polymers, ceramics (Figure 2.2.b), metals, biologicals and multi-material [Bandyopadhyay *et al*, 2018; Tofail *et al*, 2018]. The typical post-processing includes the debinding and/or support removal, and final sintering of the green part in an oven.

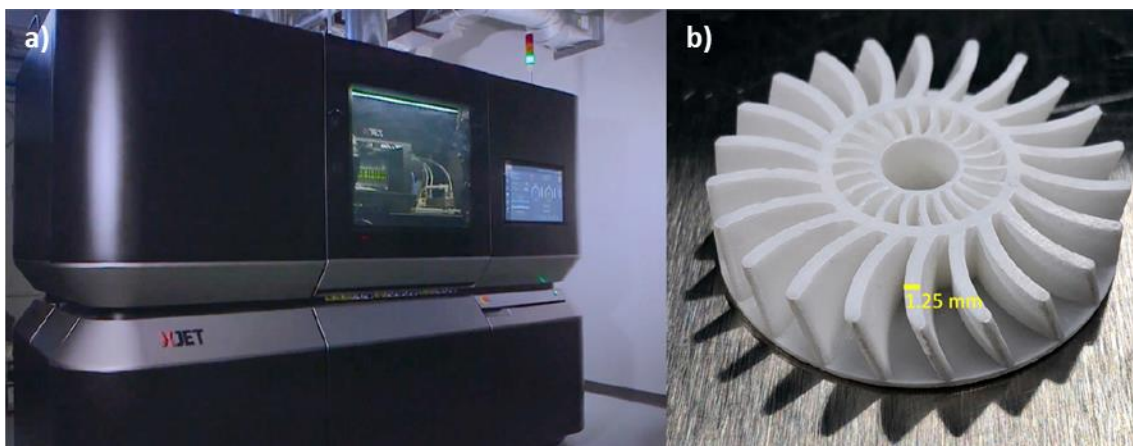


Figure 2.2: XJet material jetting machine (a) used to build a zirconia component (b) [Oh *et al*, 2019].

2.1.3. Material Extrusion

The extruder systems for 3D printing, commonly called MEX (Material Extrusion), or by FDM (Fused Deposition Modelling), are quite simple and easy to operate at a low cost. They mainly use thermoplastics as extruded material and it is possible to extrude a multi-material and multi-colour part [Shahrubudin *et al*, 2019]. The thermoplastic is heated up to a semi-liquid state and then is extruded through a nozzle creating a filament that will be laid down on top of the building platform or the previous layer and will be freezing at room temperature. Some of the main disadvantages are the weak mechanical properties, the poor surface quality due to the step effect and the limited availability of materials [Ngo *et al*, 2018].

There still exist some systems that are able to process thermoplastic fibre reinforced materials, the so-called composite materials, see Figure 2.3. These materials have better mechanical properties but have some issues related to the orientation of the fibres, fibre bonding with the thermoplastic matrix, and the formation of voids. [Ngo *et al*, 2018]

The 3D printing extrude technology is currently being used to print plastic prototypes and functional parts, and to extrude food and living cells [Shahrubudin *et al*, 2019].



Figure 2.3: Mark2 extruder composite 3D printer machine on the left, and on the right, a built part where it is possible to see the Kevlar fibre in yellow, next to the outer border, reinforcing the black polymer and strengthening the final part [Markforged (1); Markforged (2)].

2.1.4. Vat Photopolymerisation

The Vat Photopolymerisation, also known as stereolithography (SLA), is a technique that uses photo-reactive polymers in a liquid state like acrylic or epoxy resins [Shahrubudin *et al*, 2019; Ngo *et al*, 2018]. The resins have a photo initiator that will be irradiated by a laser or an UV light, which will trigger, under certain conditions, the polymerization chemical reaction [Shahrubudin *et*

al, 2019]. The polymerization process consists of the solidification of the resin of the corresponding layer of the part and occurs inside the vat. The process can use resins with some dispersed ceramics, dyes and pigments. It is a process that can create parts with high precision and micro details [Chartrain *et al*, 2018] with a smooth surface. However, it still needs support structures [Mitchell *et al*, 2018] and is limited to photopolymers resins, which limits the mechanical properties, even after full curing in an oven [Ngo *et al*, 2018]. It has been used to produce several parts for the industry and for small custom parts, such as removable teeth aligners and hearing aids [Thompson *et al*, 2016] as well as to build scaffolds (Figure 2.4.b) for tissue engineering [Chartrain *et al*, 2018].

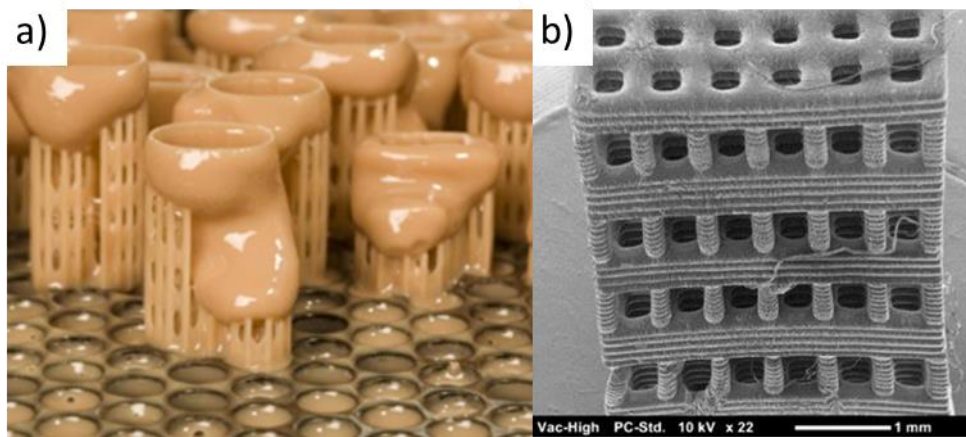


Figure 2.4: Hearing aids (a) [Thompson *et al*, 2016] built by vat photopolymerisation and an example of a scaffold for tissue engineering built by micro-photopolymerisation (b) [Chartrain *et al*, 2018].

2.1.5. Laminated Object Manufacturing

The Laminated Object Manufacturing (LOM), also called sheet lamination, is a technology that uses sheets of a material to build the part layer by layer or sheet by sheet. Typically a sheet is applied and it has a system that limits the layer/part boundary that will be cut. [Ngo *et al*, 2018] The cutting system can be a laser beam, a mechanical system with a blade, or a milling tool in the case of the ultrasonic additive manufacturing. [Ngo *et al*, 2018] In this last case, it uses metal sheets that are joined through ultrasonic welding by metallic diffusion. Beyond the ultrasonic approach, there are adhesives to bind or join the successive sheets or foils for the different materials, like polymer composites, polymers, metals, ceramics [Tofail *et al*, 2018] and organics, like paper, cork and wood [Thompson *et al*, 2016]. In Figure 2.5, it is possible to find two examples of LOM built parts in different materials.

The LOM technique has been applied by the paper, foundry, electronics [Ngo *et al*, 2018] and aerospace industries [Fabrisonic].

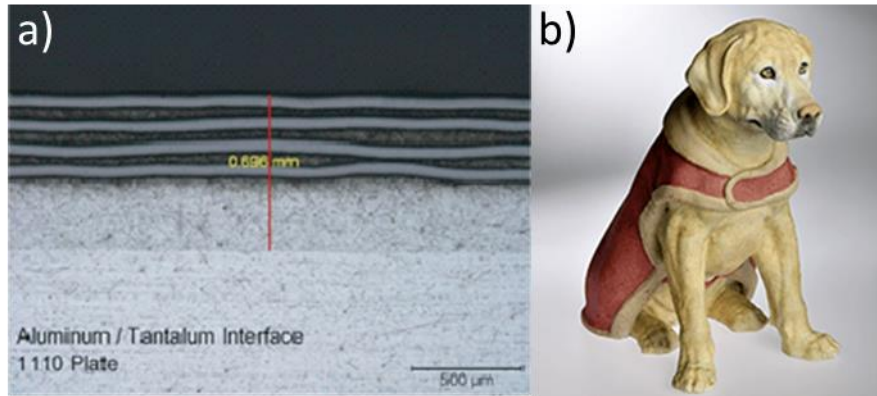


Figure 2.5: Examples of built parts by LOM. A “sandwich” metallic matrix composite (a) of aluminium and tantalum used for electronic insulation, intended for satellite application [Fabrisonic], and a dog built in high resolution printed paper (b) [Mcor].

2.1.6. Direct Energy Deposition

The Direct Energy Deposition (DED) technique, also referred in the literature as “cladding” [Childerhouse *et al*, 2019], uses metals as feed-stock and can achieve greater deposition/building rates of material when compared with the Powder Bed Fusion (PBF); according to Gisario *et al*, 2019, it is possible to achieve 10 to 40 times higher rates for a titanium alloy.

This technology is suitable for building big parts and there are some variants of the process. The process can use wire or powder as feed-stock materials. The wired version is mainly used to produce parts that do not have much geometrical complexity, and the powder feed-stock, mainly to achieve complex geometric parts. The build happens under a vacuum atmosphere or under an inert shielding gas like argon or helium and a laser beam or an electron beam can be used to melt the feed-stock material. Another difference from the other metal AM technologies is that the feed-stock is being melted at the same time as it is deposited/projected. Depending on the systems configurations, they have different designations, like, Directed Light Fabrication (DLF), Direct Metal Deposition (DMD), Electron Beam Additive Manufacturing (EBAM), Laser Engineered Net Shaping (LENS), Laser Solid Forming (LSF) and Wire Arc Additive Manufacturing (WAAM). [Fayazfar *et al*, 2018; Ngo *et al*, 2018]

Typically, during the deposition, the powder feed-stock is injected from the sides of the nozzle, to the middle where it will be hit by the beam (laser/electron) which will melt and create the melt pool on top of the previous layer or in a given substrate. When using a wire feed-stock, the concept is the same, see Figure 2.6. During the process, the nozzle’s movement can be performed by a robot or a CNC machine and moves in a specific trajectory, according to the layer of the part and geometry from the 3D file.

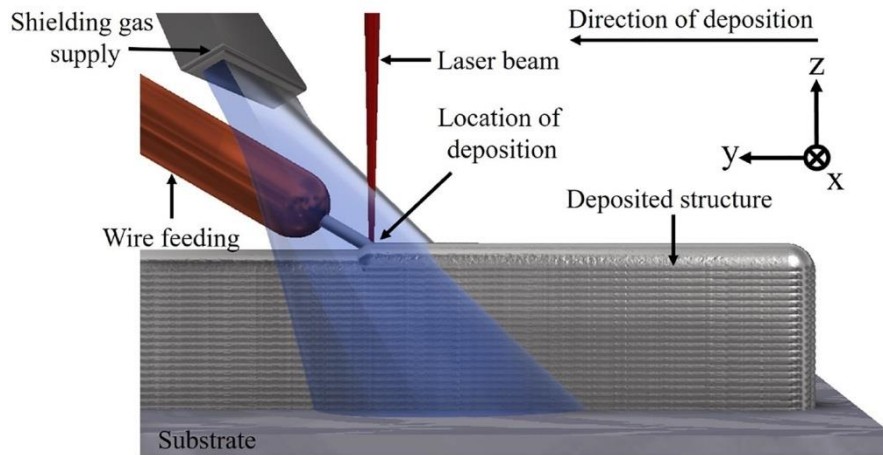


Figure 2.6: Description of the DED process using a laser as a heat source and a wire as feed-stock material [Froend et al, 2019].

There is hybrid equipment with a DED and CNC milling machine in one system, building and milling to produce the final part, see Figure 2.7 [Childerhouse *et al*, 2019; Fayazfar *et al*, 2018].

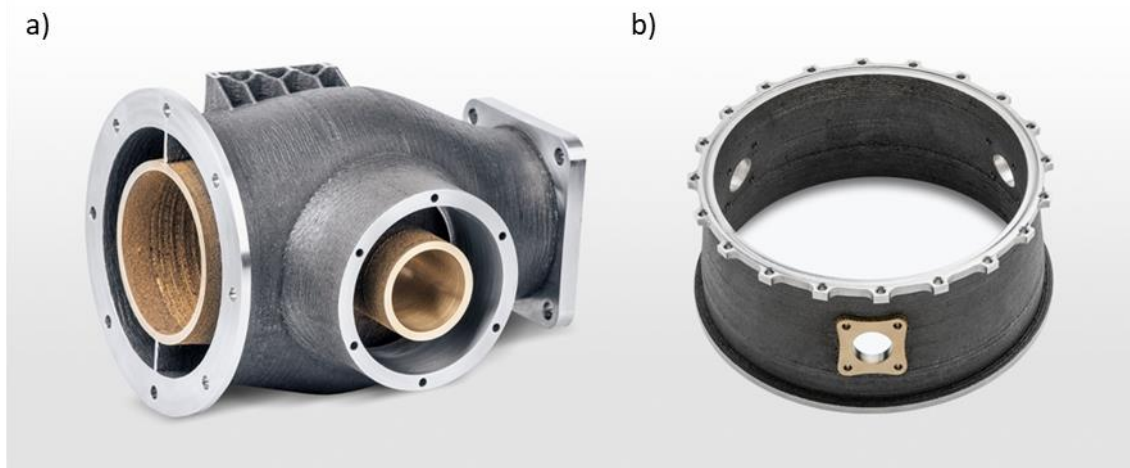


Figure 2.7: Examples of multi-material parts built by powder DED in hybrid (DED + CNC milling) DMG Mori machines. In a) is a multi-material heat exchanger made of stainless steel and bronze [DMG Mori (1)] and in b) is a multi-material turbine casing built in Inconel 718 and bronze for the aerospace industry [DMG Mori (2)].

The aerospace industry is the main prosecutor regarding the development of this technology and is using it to build parts in high performance super alloys, like Titanium and Nickel and it is even possible to build parts in multigradient metal materials [Akinlabi *et al*, 2019; Ngo *et al*, 2018].

The DED is under scrutiny from the tooling, automotive, oil and gas and aeronautic sectors. This technology is suited for repairing worn-out components, for example, for the automotive industry and for repairing turbine engines for the aeronautic industry [Akinlabi *et al*, 2019; Childerhouse *et al*, 2019; Gisario *et al*, 2019; Ngo *et al*, 2018; Shahrubudin *et al*, 2019].

2.1.7. Cold Spray Additive Manufacturing – CSAM

The CSAM technology is a development of the Cold Spray (CS) technology and both technologies consists of a solid-state material deposition, where the main difference is the goal. It is possible to find different names in literature for processes similar to the CS process, like “Micro-Forging” or “Solid-State Cold Spraying”. The CS process consists of the powder feed-stock deposition through the use of a supersonic gas flow, typically air or nitrogen, achieved by the injection of the pressurized gas in a convergent-divergent nozzle, accelerating the powder particles to velocities between 300 and 1000 m/s, depending on materials. Depending on the requirements, sometimes the gas is heated to compensate the later temperature drop that happens at the divergent region of the nozzle. It is called “Cold” Spray, because, during the process, the powder feed-stock material never reaches temperatures higher than the metal melting point. The adhesion between the metallic particles is achieved by the high kinetic energy of the process that creates local metallurgical bonding and mechanical interlocking, happening between the deposited particles and between the substrate and the deposited particles interfaces. For the CS, the main goal is to create thin surface coatings to increase the resistance to chemicals, corrosion, erosion, high temperatures and oxidation, and, for the CSAM, the goal is to add layers on top of each other in order to create a 3D structure, component. To do this, the system must have a way to create relative movement between the nozzle and the substrate to create several tracks/layers of deposited material, see Figure 2.8. [Garmeh *et al*, 2020; Li (1) *et al*, 2019; Yin *et al*, 2018]

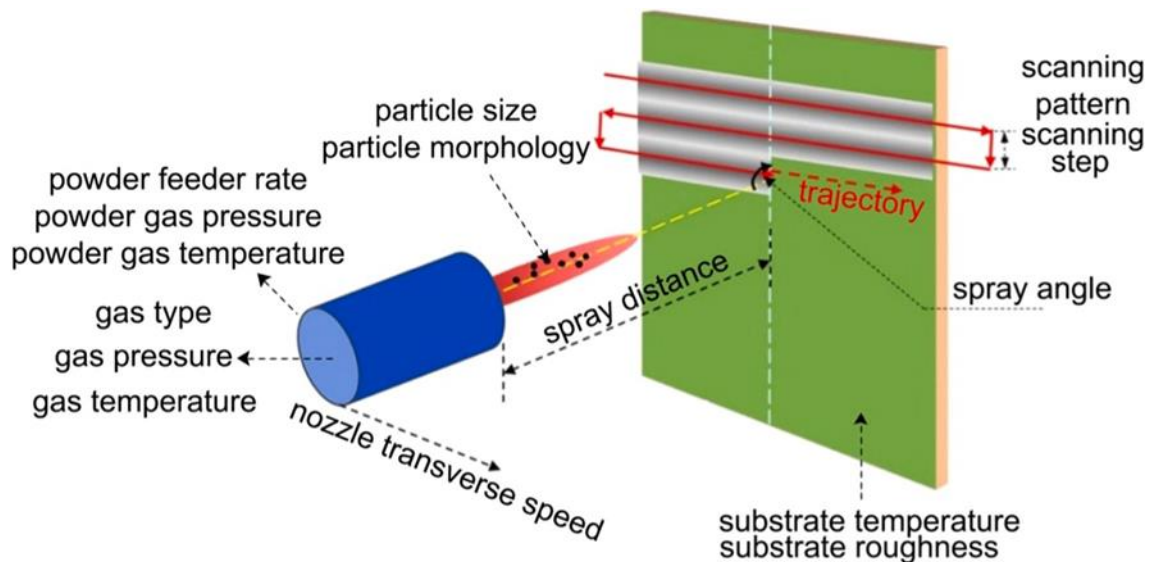


Figure 2.8: Schematic presentation of a CSAM system [Li (2) *et al*, 2019].

Hermle (CNC machine producer) have created a CSAM like system coupled to a CNC milling machine that is able to build components and to finish them by milling and with the possibility to create internal features, like hollows and conformal cooling channels for injection mold application [MPReport, 2015].

CSAM technology has been mainly used to deposit metal powder alloys like titanium, steel, nickel, aluminium, copper and brass, with particle sizes at the range of 10 to 100 μm . It is a good process to build metallic composites components like the one in Figure 2.9 [Yin *et al*, 2018].

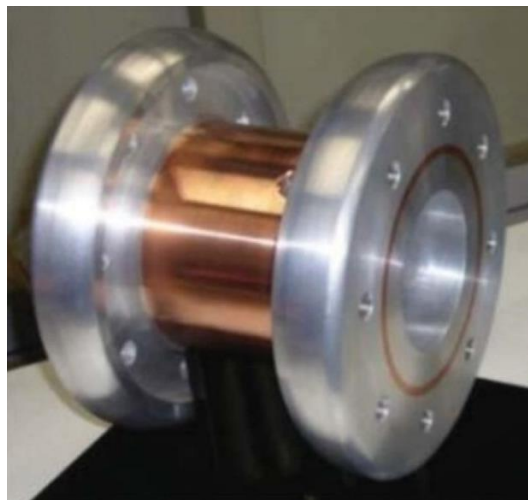


Figure 2.9: Metal composite flange built by the CSAM process after mechanical finishing [Li (1) *et al*, 2019].

The CS has been used mainly by the aerospace, automotive (research into a possible manufacture of electric permanent magnetic engines by Lamarre *et al*, 2019), energy, medical and marine industries. The CSAM is a relatively new process and it has been mainly used to repair damaged components in the automotive (damaged cast components, worn out oil housings) and aerospace industries (worn out propeller blades, helicopter gearbox sump, and oil tube bores, and rotor transmission housing), see Figure 2.10 [Yin *et al*, 2018].



Figure 2.10: Damaged tee box housing from an aircraft flap transmission that was repaired by CSAM and machined in to the “as new” state [Yin *et al*, 2018].

2.1.8. Friction Stir Additive Manufacturing – FSAM

The Friction Stir processes have been used to repair worn out surfaces and to seal cracks at the surface. Nowadays it has been more used to create coats with fine grained microstructures to increase wear and corrosion resistance. It is a solid-state process where the material never reaches the melting point, reducing the components residual stress, leading to the possibility of depositing dissimilar alloys with hard phases, like tool steels and Cobalt alloys that may be difficult to deposit through the conventional melting processes. [Padhy *et al*, 2018; Griffiths *et al*, 2019]

The FSAM processes are relatively recent and they are under research to validate their suitability for building components. Several metal alloys have been successfully processed by Friction Stir techniques, like tool steels, stainless steels, mild steels, copper, nickel, titanium, aluminium and magnesium under similar and dissimilar substrates, creating composites like carbon steel and Chromium-Nickel alloys. [Padhy *et al*, 2018; Zhang *et al*, 2019]

Several techniques based on Solid State Friction have been researched with the intention of building parts additively layer by layer. Just two methods will be mentioned, which are a combination of “AM concept + Friction Surfacing” or “Rotary Friction Welding + Friction Deposition” technique for FSAM_1, while FSAM_2 is a combination between the “AM concept + Friction Stir Welding” technique. [Padhy *et al*, 2018; Srivastava *et al*, 2019]

In the FSAM_1 a “rotary consumable friction deposition welding” happens between the consumable rotary rod and the substrate plate, where, by rubbing the material from the consumable rod at the substrate plate surface, solid state material will be transferred or deposited at the substrate rubbing surface/interface. The material transference occurs due to an application of a defined load at the consumable rod with rotational movement, creating a torsional shear between the plasticized material and the rotating rod, leading to a material transference from the rod to the substrate, defining a layer; see Figure 2.11.a). If the consumable rotating rod has linear movement, it will create a single track of continuous deposited material. This FSAM process is based on the friction surfacing technique. If there are several tracks side by side, it will lead to a larger deposited layer, see Figure 2.11.b). In this process, the first layer could work as a substrate for the next layer and so on, until the desired thickness is achieved. [Padhy *et al*, 2018]

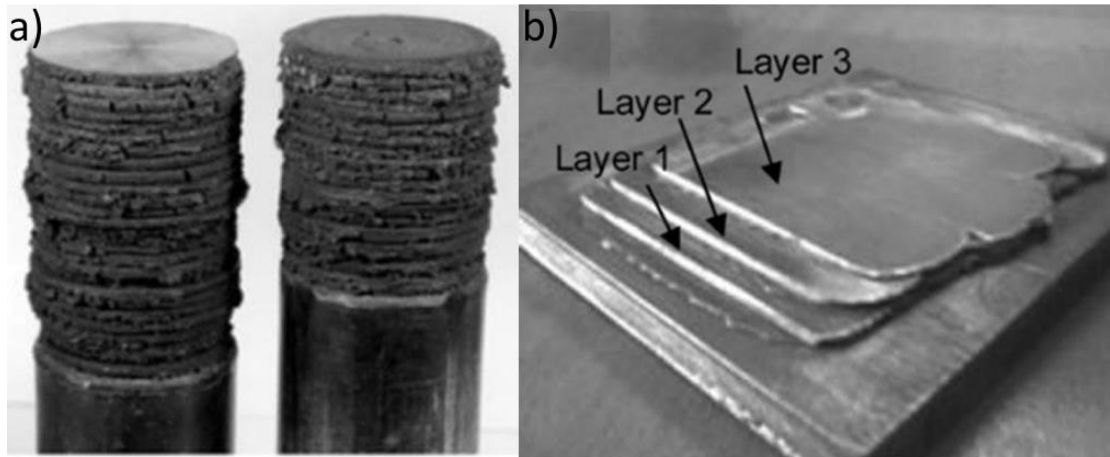


Figure 2.11: Examples of FSAM_1 deposition process. In a) rotary friction welding was used to build a few piles of layers and in b) the surface friction deposition was used to create 3 “surface” layers [Padhy *et al*, 2018].

For the FSAM_2, the process consists of the Friction Stir Welding process of sheet plates. The Friction Stir Welding occurs between the first sheet plate and the second one, corresponding to the first and second layer, respectively. After the welding, a new sheet/layer can be placed and followed by the Friction Stir Welding to join the different plates. The process can be repeated until the desired thickness is achieved, see Figure 2.12. [Padhy *et al*, 2018]

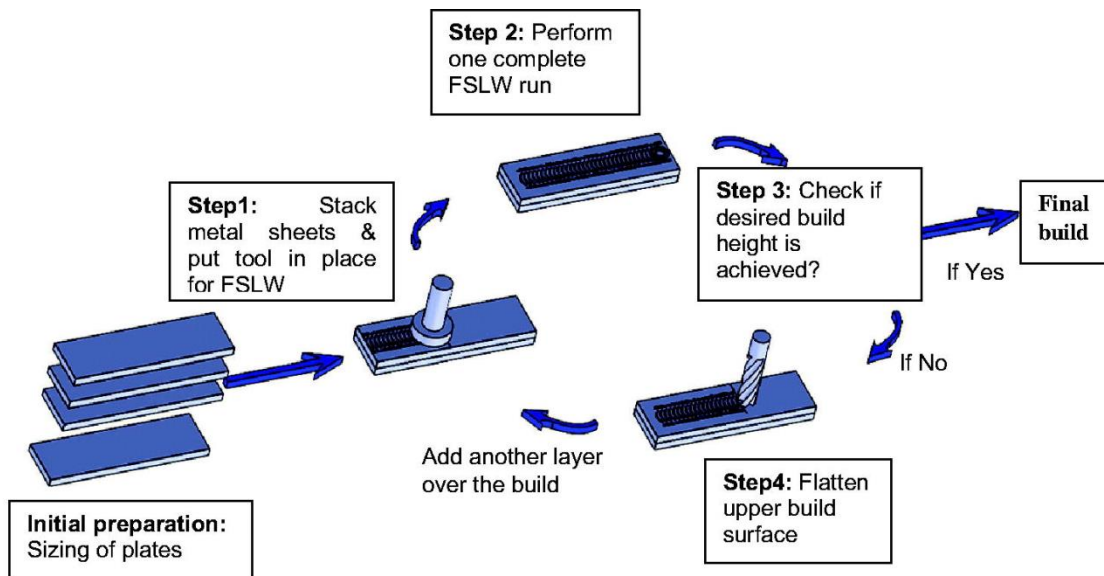


Figure 2.12: Schematic view of the FSAM_2 process where overlapped metal sheets are used, following the Friction Stir Lap Welding (FSLW) of the last sheet with the previous one or the substrate, and optional milling of the last welded sheet to prepare for the overlap by another sheet. The process is repeated until the desired height is reached [Srivastava *et al*, 2019].

The Friction Stir technique has been applied as a complement to components built by other AM processes like, DED, Cold Spray, SLS, and others. The components will be subjected to the Friction Stir process to improve the microstructure (refinement and reduction of porosity) and the mechanical properties of the components, leading many times to mechanical properties which are better than the ones from the deposited material. [Padhy *et al*, 2018; Srivastava *et al*, 2019]

One of the main limitations of the FSAM is the control of the process, the suitability of materials, tools and substrates, and mainly the understanding of what happens with the microstructure of different successive layers, because the microstructure from the first layer could be different from the next one and the previous layer could be affected when processing the next layer by FSAM. Another difficulty is related to the use of wrong parameters that could form defects such as channels, cracks, hooks, and pores or cavities, see Figure 2.13. [Padhy *et al*, 2018; Srivastava *et al*, 2019]

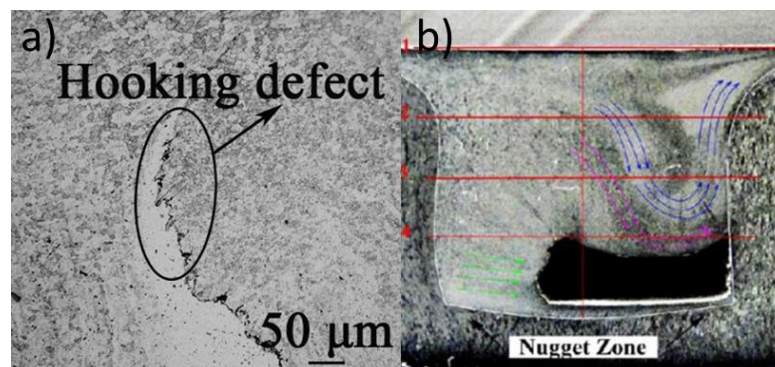


Figure 2.13: Defects of the Friction Stir process. In a) the hooking bonding defect, and in b) the black region corresponds to a cavity defect [Zhao *et al*, 2019; Padhy *et al*, 2018].

2.1.9. Powder Bed Fusion Systems

2.1.9.1. Selective Laser Sintering – SLS

The SLS process is the precursor of the SLM process that will be described later on in this thesis. It is important that, in the present work, SLS is related to the laser sintering of polymers, composites of polymeric matrix and indirect sintering, which will be described during this topic. On the other hand, in this thesis, the SLM process is considered as the process that laser sinter/melt/fuse the metal powder completely.

The SLS arose in the 1980s, and, as happens in the present days, the system uses a 3D CAD file of the part to build, that will be sliced and reproduced layer by layer. This is a PBF process where

the polymer powder is layered down and coated to form a uniform layer, typically with a roller. Later on, the laser will sinter the powder selectively in order to build the respective layer and will place a new coat/layer of powder (Figure 2.14). During the process the powder bed is preheated to reduce the thermal stress intrinsic to the process, to avoid crack formation during the build. [Chen *et al*, 2018]

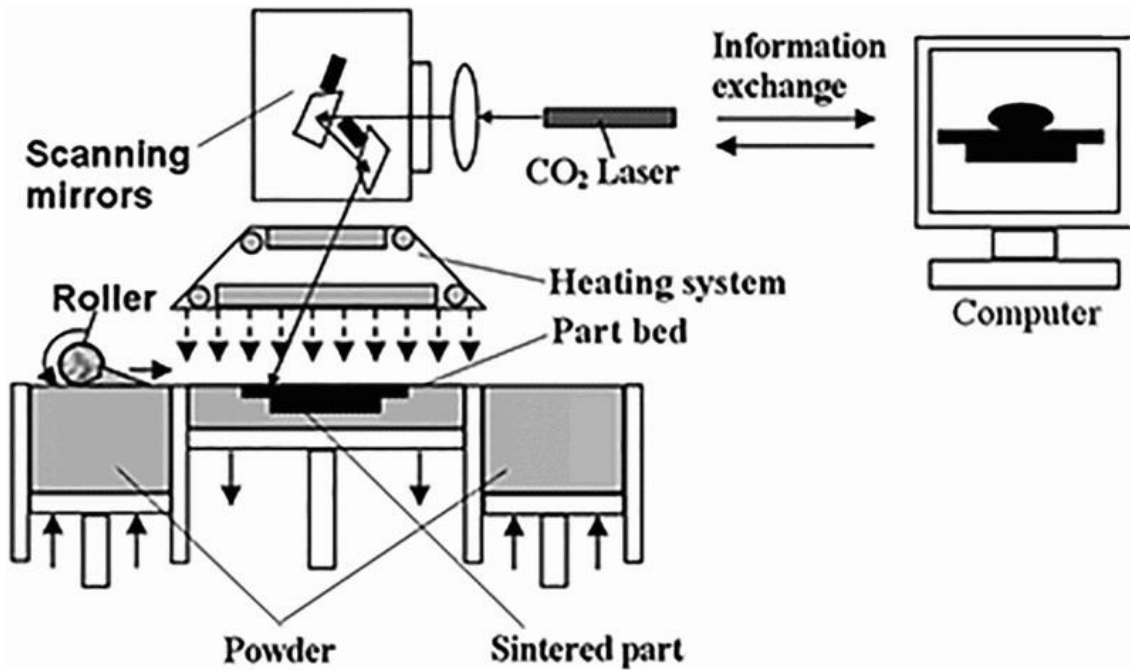


Figure 2.14: Representation of an SLS system process [Chen *et al*, 2018].

The most common material powders are in the range around 75 μm to 200 μm of particle size. [Chen *et al*, 2018; Wu *et al*, 2020] Regarding the processed polymers, 90% of the consumption are from the Polyamide (Pa) family, followed by the rest like the Polyetherketone (PEK) family (PEKK – Polyetherketoneketone; PEEK – Polyetheretherketone), and some studies with Polybutylene Terephthalate (PBT), Polystyrene (Ps), and composites filled with inorganic fillers like, glass spheres, silicon carbide, aluminium, and even organic fillers like rice husks and wood (Figure 2.15) [Chen *et al*, 2018; Wu *et al*, 2020; Greiner *et al*, 2017; Zeng *et al*, 2019; Velu *et al*, 2016].



Figure 2.15: Samples built by an SLS system. Single layer of polymeric composite made of Polyamide matrix and wood powder filler (5 and 10 % wt) [Velu *et al*, 2016].

For the indirect sintering, ceramics, metals, and other materials which are difficult to process by direct laser powder bed systems are used, which are coated with a binder that will be sintered by SLS, building a green part that requires further debinding in an oven or chemical debinding and later sintering in an oven, as was previously stated in the Material Jetting processes. [Chen *et al*, 2018; Shirazi *et al*, 2015; Wu *et al*, 2020]

Some of the advantages of the process are the creation of complex geometric parts, the powder can be reused i.e., recycled (most of the time it is mixed in proportion with fresh new powder), and during the build the powder itself acts as a support, eliminating the support needs in overhang zones [Wu *et al*, 2020].

Depending on the powder composition it is possible to have non-uniform shrinkage, leading to warpage during the sintering that could lead to cracks and dimensional inaccuracy, poor surface quality and the removal of the loose powder from small structures or pipes from the built part can be very difficult [Greiner *et al*, 2017; Shirazi *et al*, 2105; Wu *et al*, 2020]. Other issues are related with the final applications, since most of the time they need some kind of post-processing. The most common ones are the blasting, polishing, coating, painting and heat-treatment [Wu *et al*, 2020].

The SLS process has been applied in many different industries and for a variety of purposes. Some of the main industries are the aerospace, motorsports, automotive, electronics, consumer products, packaging, industrial applications and sportswear ones as well as in medicine, such as implants, and for biomedical (tissue) engineering, to produce scaffolds. [Wu *et al*, 2020; Shirazi *et al*, 2105]

In Figure 2.16, it is a product made with the SLS process that is within everyone's reach.



Figure 2.16: Shoes midsole produced by the SLS process from the trade mark “Under Armour” [Wu et al, 2020].

2.1.9.2. Electron Beam Melting – EBM

The Electron Beam Melting technology, proprietary technology of ARCAM (Figure 2.17), differs from the other powder bed systems mainly due to the origin of its heat source. This uses a tungsten filament as a cathode to generate an electron beam. This beam will selectively melt the existing powder at the powder bed layer by layer and it can reach a maximum beam power of 3000 W, from the commercially available systems from ARCAM. [ARCAM (1); Wang (1) *et al*, 2018]

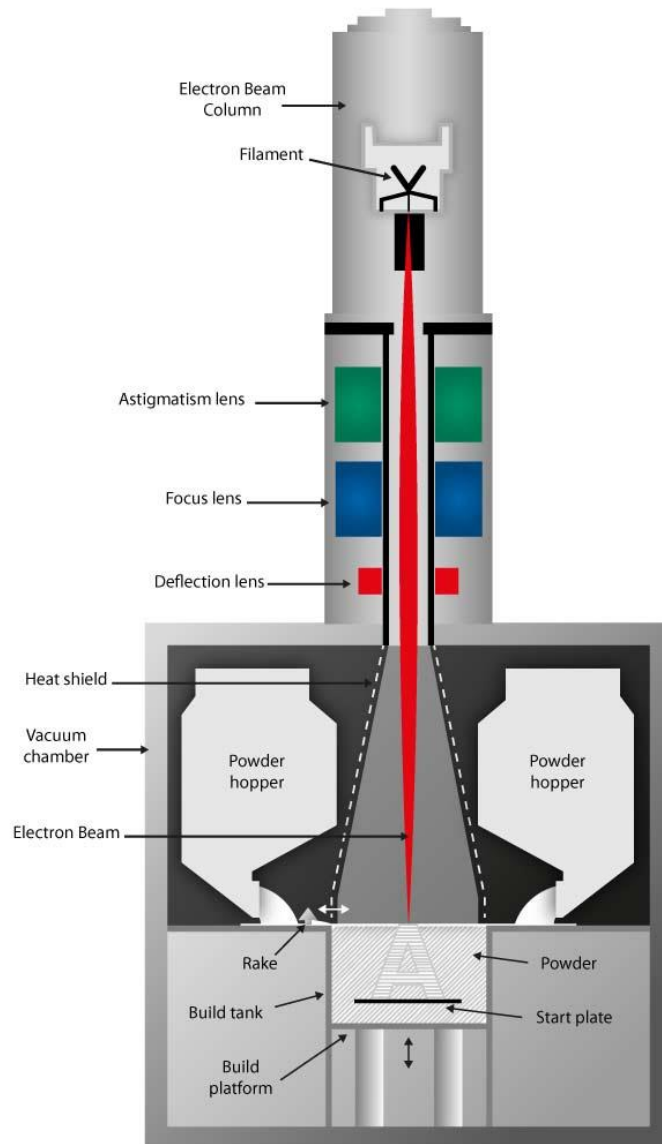


Figure 2.17: Scheme of the inside of an ARCAM EBM machine system [Fayazfar *et al*, 2018].

Another characteristic of the system is the use of a high vacuum building chamber and the use of helium as an inert gas atmosphere and the heating of powder prior to the melting process. The vacuum can reduce the influence of contaminants, like the oxygen, but it can strip out other chemical elements that have a lower enough boiling point. During the process the electron beam can heat/pre-heat the powder layer up to 1100 °C, before the melting step starts (Figure 2.18), depending on the material specifications, reducing or eliminating the residual stress and the martensitic structures from the parts. This systems concept offers a good potential for microstructure control. Some of the process limitations are related to the electrostatic charge that can disrupt the powder “smoothness” distribution on the powder bed [Cordero *et al*, 2017], and for that reason the use of powder smaller than 40µm is not recommended; the high surface

roughness inherent to the process and the few approved materials such as some titanium, cobalt-chrome and nickel alloys. There are a few studies that have tested some “non-approved” steel alloys. [ARCAM (1); Fayazfar *et al*, 2018; Wang (2) *et al*, 2018]

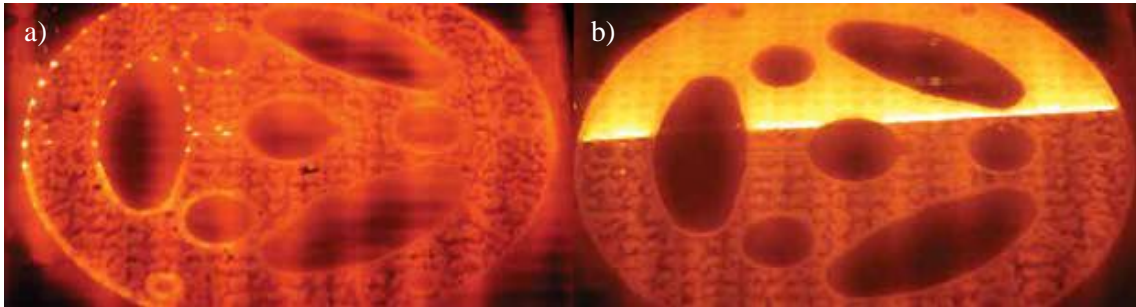


Figure 2.18: Detail of the inside of an ARCAM’s machine building chamber, processing a nickel 718 alloy. The electron beam is defining the contour in a), following the bulk melting region in b) [ARCAM (1)].

The shortage of materials approved for these systems could be related to the fact that the ARCAM is still the only company that has commercial EBM systems available due to its patent until 2022 [Fayazfar *et al*, 2018].

The ARCAM EBM technology is most known for the use of Titanium alloys, and, as a consequence it is being more explored by the aerospace (Figure 2.19.a), biomedical (Figure 2.19.b) and military industries [Wang *et al*, 2018].

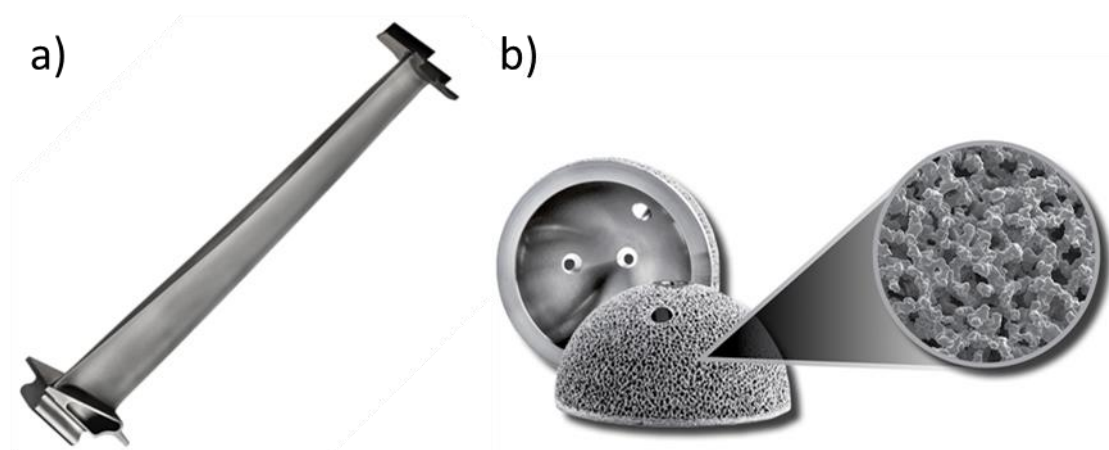


Figure 2.19: Components that are typically built in Titanium alloys, built by ARCAM EBM process. Low pressure blade commonly used in aeronautical turbines and an acetabular cup implant with details of its 3D trabecular like texture to optimize osseointegration [ARCAM (1); ARCAM (2)].

2.1.9.3. Selective Laser Melting – SLM

The process of Powder Bed Laser Melting, most of the time known as Selective Laser Melting – SLM, or Direct Metal Laser Sintering – DMLS, or Laser CUSING, are all processes that are very alike and are consequences of the technological development of the SLS process used to process polymers, as was previously stated in this thesis (Chapter 2.10.1.). These processes all use fine metal powder particles, ideally spherical and typically bigger than 10 μm and smaller than 63 μm , laid in a tray or chamber that moves vertically, where it will have the interaction of a laser beam that will be moving on a planar bed and melting/fusing/sintering selectively the powder. The process typically runs in a closed envelope under inert gas. The most common gases used are nitrogen and argon, depending on the materials and the quality requirements. The laser and all the process is controlled by a computational system. For the process to run, it needs a 3D CAD model that will be sliced. Usually, the slice or layer thickness is between 20 and 100 μm , and it has a coating system that will make the application of a new powder layer which will be melted by the laser system. To make a real component, the building platform will be lowered by the layer thickness amount, and it will repeat the process steps until finished. Later on, the part is removed from the building envelope and the unmelted powder is commonly recovered and “recycled”, and reused once again. The simplest way of recycling, it is to resort to a sieving system to remove the agglomerated and oversized powder that was affected by the heat generated by the laser during the powder processing.

In Figure 2.20, it is a schematic concept with the main components of a machine, in this case, a Concept Laser machine.

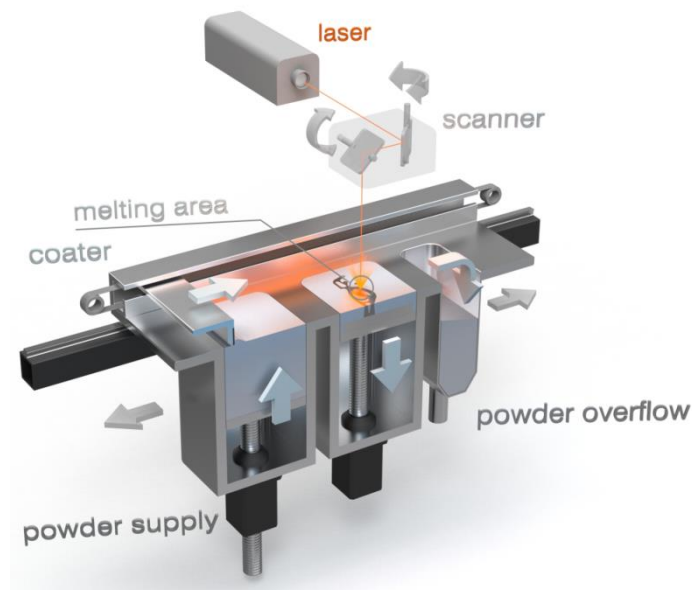


Figure 2.20: Schematic view of a Concept Laser machine [Concept Laser].

Figure 2.21 is a description of the process workflow, from the 3D CAD until the finished part completion.

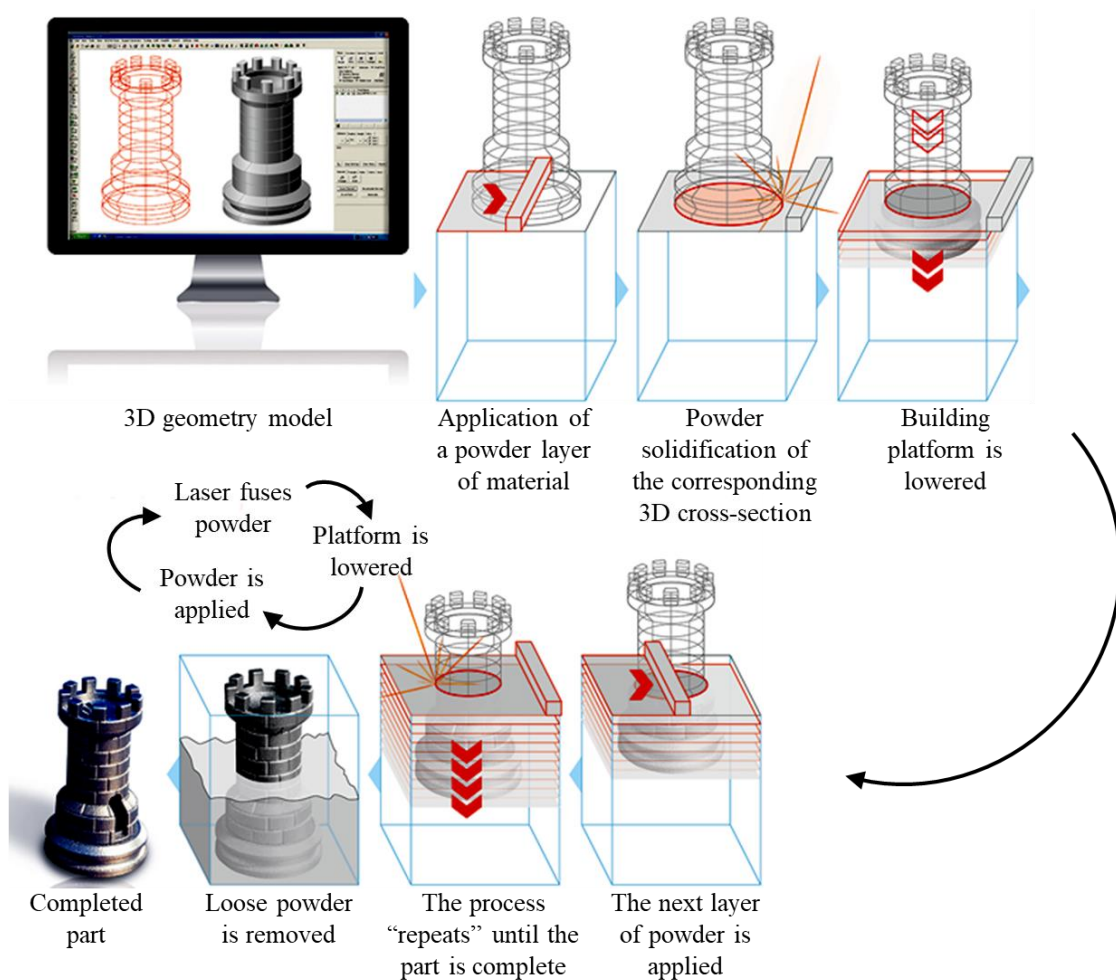


Figure 2.21: Schematic workflow of a 3D printing job [Adapted from EOS].

Nowadays there are plenty of commercial solutions that have all kind of machines, from small sizes around $100 \times 100 \times 100 \text{ mm}^3$ up to machines that are being developed to reach around the $1000 \times 1000 \times 1000 \text{ mm}^3$, with 1 up to 12 lasers, from 200W to 1kW laser power, with cold and preheated build plates up to $500 \text{ }^\circ\text{C}$, enabling the possibility to melt materials with high content of carbon with a low risk of cracks and decreasing the internal stresses typically associated with these technologies. There is a vast list of commercial materials available, namely, iron-based alloys, stainless steels, maraging steels, tool steels, chromium-cobalt alloys, nickel alloys, aluminum, pure copper and its alloys, titanium alloys and precious alloys like gold. These materials could be non-reactive or reactive, and they fit almost all the demands for all kind of applications and industries. The most common industries that use this kind of technology are the Aerospace, Automotive, Medical, Jewellery, Mould and Dental ones [Concept Laser; EOS].

There are several commercial trademarks for SLM systems that are slightly different from each other. Mainly they work on the same way, but with small technological implementations that might make the difference to the others.

For example, Matsuura and Sodick have hybrid systems that build parts by the SLM based process, with a CNC milling machine incorporated, that will build the part layer by layer and intercalating with milling (defined by user) to completely finish the parts with small geometric tolerances [Matsuura; Sodick].

For example, VELO 3D highlights the support free of overhang zones, “down to zero degrees”, thin and tall parts with high aspect ratios, and big internal diameter features up to 100 mm with high quality, with their “Sapphire” system, which, due to a tight control of the process, enables the possibility to build the “impossible” [Velo3D].

Aurora Labs has a multi-layer concurrent system that can place powder on several layers, processing them at the same time, building parts in 20 minutes that with other systems will need at least 2 days [3DPrinting, TCT].

Addcreative has a big system (AddCreator) with the possibility to create parts with a volume of $1000 \times 1000 \times 500 \text{ mm}^3$, which can have up to 6 lasers on a head that is moving from “tile to tile”, scanning at the same time they melt, patented as Tiled Laser Melting [Addcreative].

SLM Solutions presented a system that can build parts up to $600 \times 600 \times 600 \text{ mm}^3$, withstanding 12 lasers operating simultaneously, significantly improving the build rate and the possibility to reach new markets [SLMSolutions].

Another interesting variant is the Micro-SLM process from 3D MicroPrint with systems up to $60 \times 60 \times 30 \text{ mm}^3$ but with the possibility to work with layer thicknesses from 1 to $5 \mu\text{m}$ ensuring the best dimensional accuracy and precision [3DMicroPrint].

Other alternative noncommercial systems are being developed, bearing in mind the possibility to create parts built even with dissimilar materials (Figure 2.22), like metal alloys, ceramics and polymers. Research teams are mainly assessing a few things, like the processability, interface of different materials, interlocking systems, recyclability of powders, different strategies to improve the process reducing defects, like delamination, unmolten powder, cracks and evaporation of materials, among others. The technology concepts could be very different from each other, they may have the possibility to create parts with discrete and/or gradual transitions between different materials, but what they have in common is the goal of taking out multi-material 3D or 4D parts directly from the printing. Some of the most relevant applications are intended for biomedical, electronic and aerospace applications. [Wang *et al*, 2022]

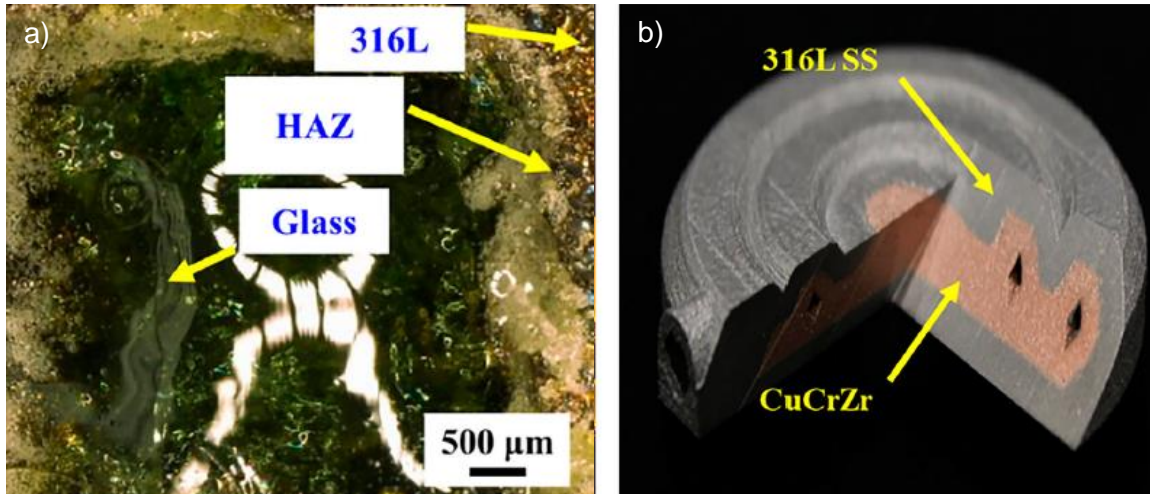


Figure 2.22: Dissimilar materials achieved by “LPBF” systems. In (a) a detail of a part built from a metal alloy and a ceramic (316L/soda-lime glass), and in (b) a part made by different metal alloys (316L/CuCrZr) produced by Aerosint SA [Wang *et al*, 2022].

Selective Laser Melting Main Process Parameters

The SLM process typically has four laser system related variables as its main process parameters which are most of the time ruled by the Volumetric Energy Density [Mugwagwa *et al*, 2019; Souza *et al*, 2019] that can be calculated accordingly to the Equation 1:

$$VED = \frac{P}{v \cdot h \cdot t} \quad (1)$$

where,

- VED – volumetric energy density [J/mm^3]
- P – laser power [W]
- v – scanning speed or velocity [mm/s]
- h – hatch distance [mm]
- t – layer thickness [mm]

Typically, with the increase of VED, it decreases the forming porosity during the build and as a consequence of the final built part, at least up to a certain threshold. So, from Equation 1, one can say that with the increase of the Laser Power there will be less porosity if the rest remain constant. On the other hand, if the Scanning Velocity or Hatching Distance or Layer Thickness are decreased and the Laser Power remains constant, the VED value will be increased. The decrease of the porosity is directly related with the improvement of the mechanical performance. [Ning *et al*, 2004; Simchi, 2006; Souza *et al*, 2019]

On the other hand, high values of VED will create over-heating and consequently evaporation of the metal, leading to an increase in porosity and a decrease in the mechanical properties [Ning *et al*, 2004; Simchi, 2006].

Despite the simplicity of the VED equation, it has been reported that this value itself is not enough to compare the process parameters or the mechanical properties of the built part [Xiang *et al*, 2018].

Another major parameter/variable that was not taken into consideration is related to the exposure or hatching strategy that has an important role in the final part's mechanical properties, mainly related with the exposure vectors length and residual stress of built parts [Simchi, 2006; Mugwagwa *et al*, 2019]. Another variable that influences the final mechanical properties is related with the part build orientation, as observed by Souza *et al*, 2019, that achieved different mechanical properties for different build orientations for the same porosity (horizontal/0°, tilted at 45°, vertical/90° = built under the same direction of the load application).

Depending on the laser hardware and configuration of the systems, there will be plenty more laser related parameters that could be adjusted and will influence the process performance. Typically, they are related with laser “timers”, related to the on and off of the laser exposure delays, in other words compensation and optimizations on a very fine scale. [Simchi, 2006]

Other variables that are not most of the time taken into consideration, because they can be material or system dependent or mandatory or very difficult to evaluate and compare with other studies or machines, are related to powder (particle size and distribution, shape – the most suitable are spherical due to the flowability, porosity, oxygen content, humidity/contaminants) [Simchi, 2006], with the inert gas atmosphere that prevents oxygen from having a major influence in the process (typically nitrogen or argon, lesser used are the helium and forming gases (hydrogen + inert gas) [Zhang *et al*, 2013], initial building platform temperature (cold/room temperature, pre-heated platform), coating speed and blades (hard, soft blades, brushes) and welding gases exhaustion and flow during the process.

It is very important to say that this is a process that is characterized by steep temperature gradients, because the powder's changes of phase are in the range of a fraction of a second. As Simchi (2006) stated, this is a process of high-power density with a short interaction time.

For the present thesis it was not possible to have access to or to measure all the parameters and variables, but there are some that will be present in the following work and papers. Once again, the main focus is to understand if it is possible and viable to use the SLM process to produce hybrid parts under the current conditions and parameters, and not to set a fine optimization of the process.

2.2. 3D Printing Overview: Facts and Trends

The AM, a term more used by the industry for the production of high-end products, or more broadly known as 3D Printing, has been developed and come to the light of the world due to the strength of its strong marketing, and, since 2012, it has had a stage of its own [Hubs], due to the proliferation of the different advances of the technologies, and mainly due to the availability of these technologies to the masses, like the MEX or FDM. In the last 6 years some trends regarding 3D Printing technologies have been shared, materials and their usability in terms of industrialization have also been shared, forecasting growing markets regarding the complete value chain of AM, starting with the research, including the manufacturers, the users, the applications, logistics, raw materials, and so on. With time, the so-called 3D Printing technology has been found to be present in a very large number of industries and in research that is trying to empower its unique possibilities to solve pressing issues, like the electrical mobility (powertrain, batteries), green energies, carbon neutral, and so on. There are already a large number of industries that are exploiting that opportunity, such as: aerospace; aeronautic; automotive; chemical; construction; dental; drone; education; fashion; food; footwear; healthcare; hearing; maritime; mechanical; movies; tooling and die, and toys. [Sheng, 2022]

In Figure 2.23, it is possible to observe the historic influence of the new developments (technology and fusion of companies) that taken place in the world (industry and population), and its recognition or perception.

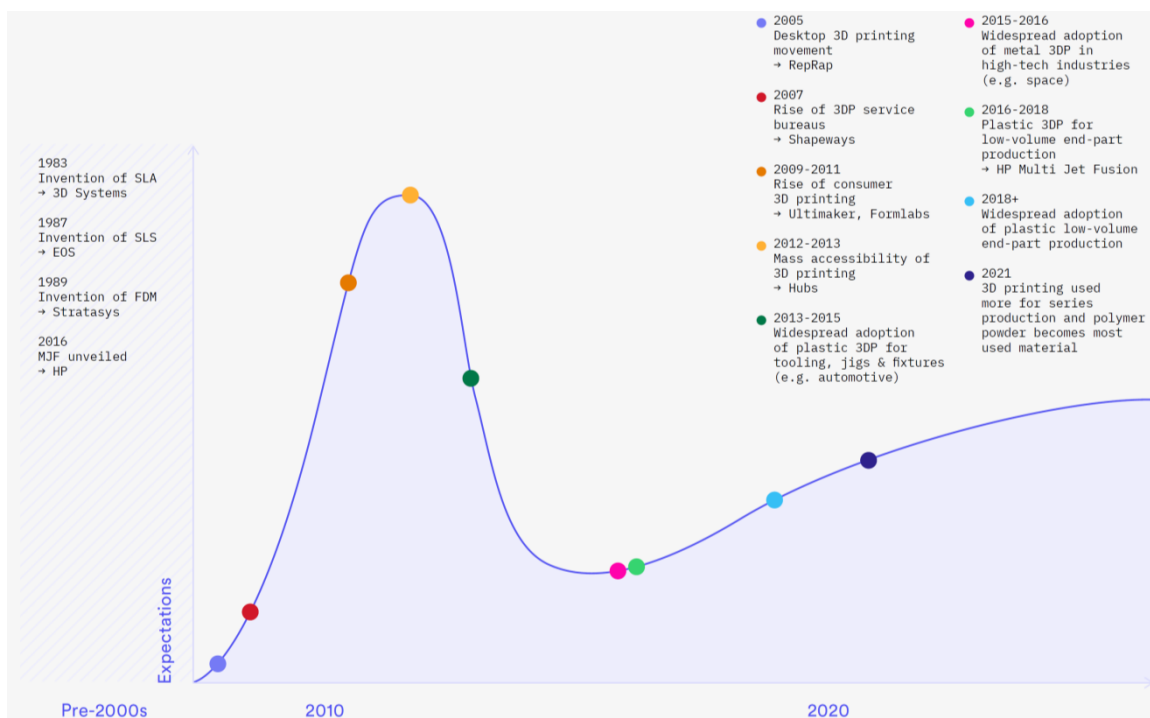


Figure 2.23: Relative comparison of the 3D printing popularity throughout its history [Adapted from Hubs].

The European Commission has requested a few reports related with the 3D Printing, and Van de Velde (1) *et al*, 2021, has stated that is a “disruptive technology”, meaning that there are key technologies that could create great changes in the way that things are currently done, with a huge potential for innovation. In this specific report, he talked mainly about “hybrid components” made from metal and carbon fiber reinforced polymers and the impact that they could have in the fields of robotics, rotor blade, motorcycle parts, aircraft structures, aeronautics interior parts, satellite parts, manufacturing equipment and prosthetics. Another mentioned fact is the possibility for 3D Printing to change the current supply chains, as happened during the COVID-19 pandemic situation, enabling missing parts to be produced locally. [Van de Velde (1) *et al*, 2021]

A different approach was the perspective from Garmulewicz *et al*, 2018, of trying to understand if the 3D Printing as a disruptive technology could enable a local circular economy. This would be characterized as an economy that would be working in a close loop between the printing of new parts, and when the part life ends, how they would integrate the waste into the value chain, and print new parts from the recycled polymeric feedstock once again, see Figure 2.24.

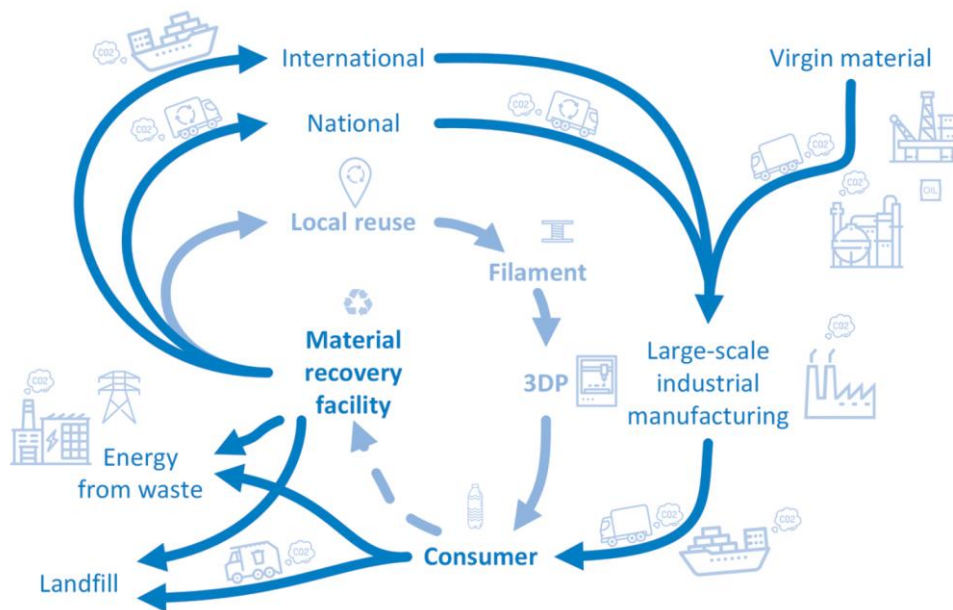


Figure 2.24: Comparison between the local, national and international cycle of polymeric material [Garmulewicz *et al*, 2018].

Today’s trends to pursue sustainability and a green economy were possibly influenced by a report requested by the European Union. This report says that twin green and digital transition are key for the decarbonization of the industry and for the circular economy. Like this, the report points out that 3D Printing technology, among others, has the potential to produce parts in a more

efficient way through the mass/material reduction, thereby reducing carbon emissions. This comes from the technology potential to create highly complex geometric parts, being of the most importance to digital transformation and as part of the fourth industrial revolution – Industry 4.0. [Van de Velde (2) *et al*, 2021]

One interesting study is showing the economic influence of low-cost 3D Printing parts or consumer products at home with commercial filament (polymeric), and the cost savings. It is the case of Prosumers, which are producing (producer) a part and using it for their own purposes (consumer). In Figure 2.25, it is possible to observe that more printed designs from open-source databases correspond to more costs savings. [Pearce *et al*, 2022]

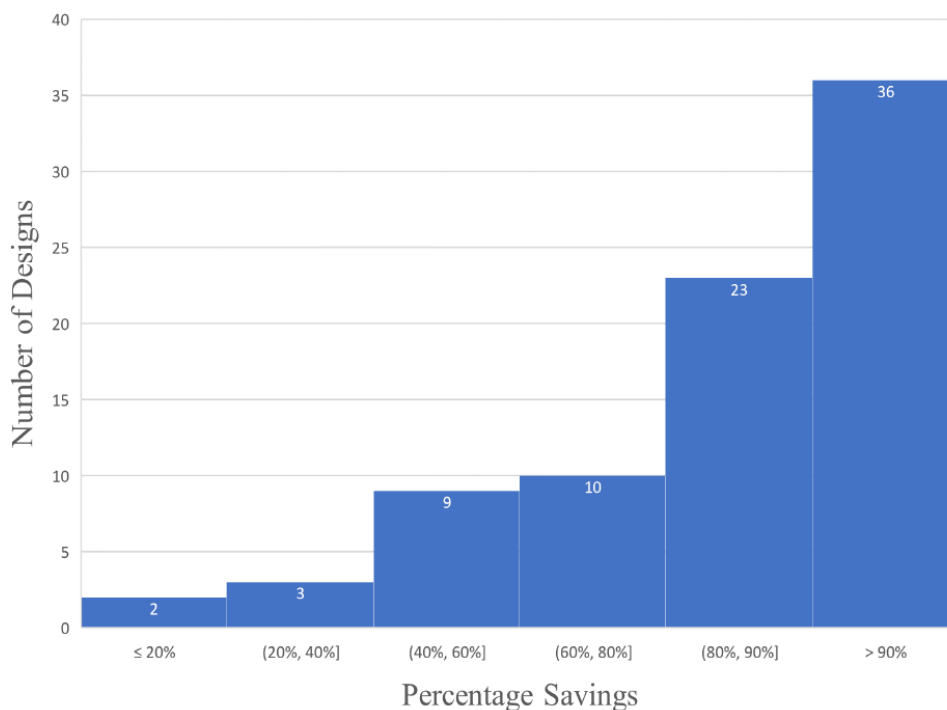


Figure 2.25: Relation between the number of printed open-source designs and the cost savings for Prosumers using low-cost printers at home [Pearce *et al*, 2022].

A different study is focused on the worldwide economic trading of 3D Printing technology (broad term) and its value chain around the globe, trying to quantify its influence throughout the years and pointing out the future trends. Some of the difficulties encountered by the authors were to identify from the traditional and different categories (transaction, products, materials and digital) which ones were dealing with or influenced by the 3D Printing value chain. Even though, they were able to find evidence since the beginnings of 3D Printing, between the worldwide trade of the increasing number of 3D Printing adoption and the 3D Printing goods, such as materials

(polymers, metals, and so on) and even at an intellectual level by the means of design service. Authors suggest that the 3D Printing economy should continue to grow and have a positive effect on the worldwide economy. [Andrenelli *et al*, 2021]

Jiang *et al*, 2017, made a study trying to forecast the influence of the 3D Printing (all kinds of technologies) in 2030 on the economy and on society based on surveys and interviews with experts, most of whom were influenced by the European reality. Some of their projections, for 2030 based on those with the greatest probability of happening, say that the 3D Printing will be more used due to its agile capacity to produce under demand under a sustainable production, including spare parts, but with mass products and materials continuing to be global. New business models around design and conceptual development of parts will grow due to the proliferation of printing machines. This way, different or new ways of intellectual property will be needed, in order to make the process more agile, like having to pay for a CAD file, even when printing it for low-end-user applications, and for the governments to create regulations for the sharing of Design files to help to protect the intellectual property and to foment the spare parts market, reducing or eliminating the needs for stock. [Jiang *et al*, 2017]

A different perspective is given by Jiménez *et al*, 2019, who made a fair comparison between 3D Printing technologies, main advantages and limitations, some with a critical point of view. But the authors would like to enlighten two main points regarding the future, according to the study. One of them is that it will be a key technology to generate high end parts with higher added value in a more sustainable way, when compared with the traditional technologies, and that it will be a complementary technology to the existing ones. The last point is that the 3D Printer technology is mainly chosen by the application, and based on the lasers systems capacity to produce finished products or semi-finished products, being expected that the laser based systems and applications continues to growth. [Jiménez *et al*, 2019]

According to the Hubs' 2022 February survey, it seems that the trend of the 3D printing industry is to continue to grow at least up to 2026 (Figure 2.26), and this year is to be expected to have a growth and a full recovery of the industry prior to COVID 19 pandemic situation. It is stating another interesting fact, that in 2021, and for the first time, the most used material was polymer powder. [Hubs]

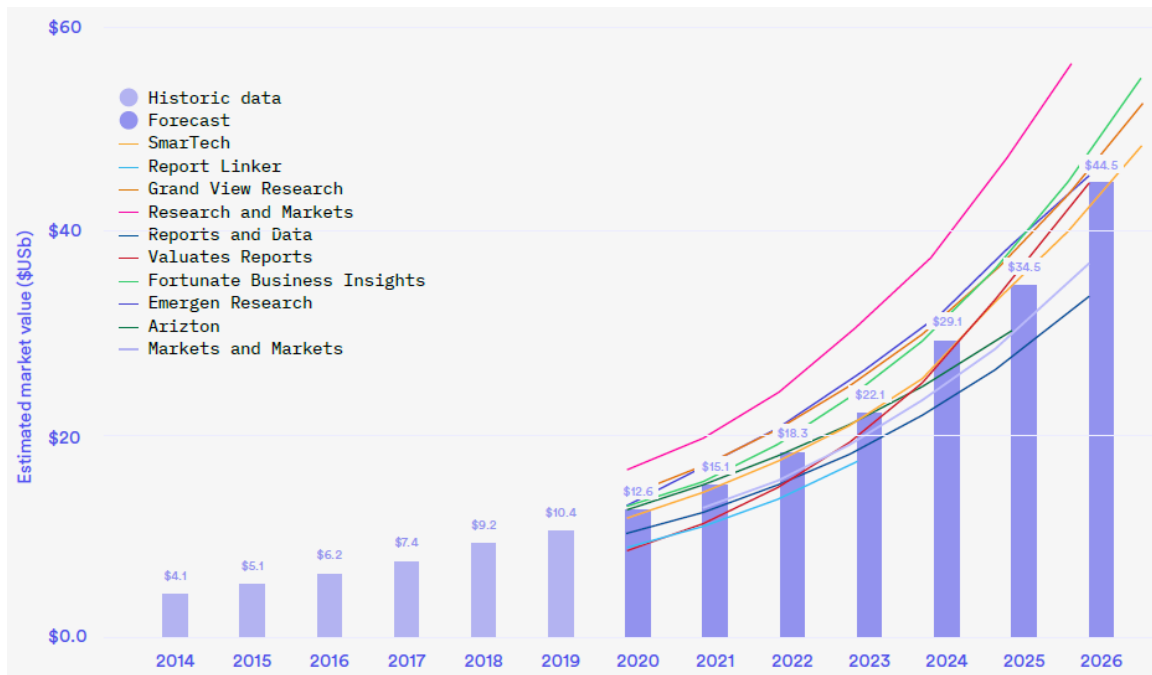


Figure 2.26: Overview of the 3D Printing market economy and its growing forecasts up to 2026 [Adapted from Hubs].

Even though the powder polymer was the most used material in 2021, the metal segment at Q3 of 2021 showed a growing rate of 18%, against the 12% from polymer, suggesting a growing trend. Other signals that are showing the growing of the industry are the increase of end-use parts from 21% in 2020, against 29% in 2021 and the quantity of low-volume printed parts per batch (more than 10 parts per tray/build plate) that increased from 36% in 2021 to 49% in 2022 (see Figure 2.27). From the survey, 62% of the built parts were meant for prototyping applications and the rest for end-user and industrial applications. [Hubs]

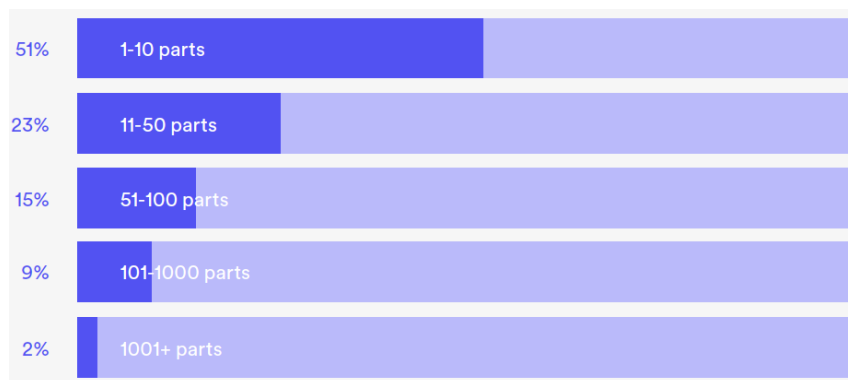


Figure 2.27: Number of printed parts per batch of the surveyed entities [Hubs].

A very interesting concept is 4D printing. It is important to say that the 4D printing could be achieved using the 3D printing technologies and adding a “new” dimension to the printed part. This “new” dimension could be called “functionality”, or rather, a “new or extra” function that is attributed to the new 4D part. These “functions” could be attributed to the part by the use of “shape memory materials”, “metamaterials” (see Figure 2.28), which could be “activated” by the means of an external “condition/stimulus” (mechanical, electrical, optical and thermal), or by “programmed” materials/structures. In this list, concepts such as “self-healing materials”, “self-deploying structures”, and functional mechanical components without any external motor or hinges, creating a “preprogrammed” motion could be included. [Ion *et al*, 2016; Ryan *et al*, 2021]

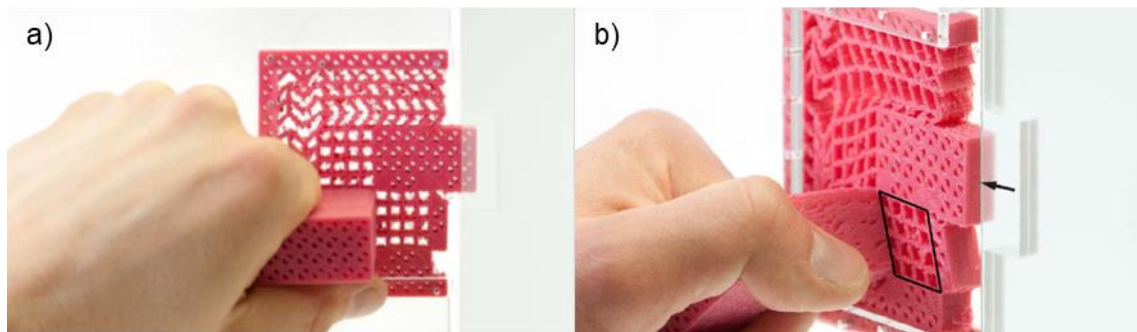


Figure 2.28: Door latch printed as a metamaterial, monolithic part. In a) the latch structure is relaxed and in b) the structure is under a torque creating function/movement, as indicated by the arrow [Adapted from Ion *et al*, 2016].

Other concepts are emerging like the 5D printing, which could be used in the healthcare industry, for drug delivery systems and in the food industry. The 5D printing concept is a natural evolution of the 3D printing like it was for the milling machines, which evolved from the 3 axes to 5 the axes, and in a similar way, the idea is to create curved and complex shapes like semi-spheres [Nida *et al*, 2022; Anas *et al*, 2022]. If we add to the 5D Printing concept the 4D Printing concept we will have the 6D Printing concept, creating new possibilities for more complex parts and systems [Nida *et al*, 2022].

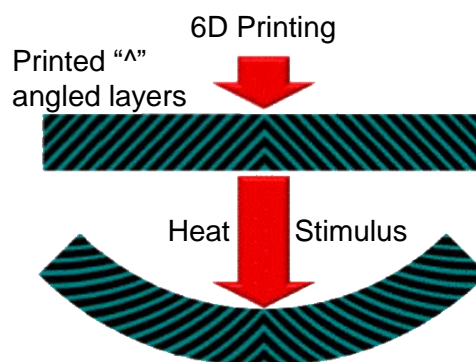


Figure 2.29: Schematic view of a 6D printed part process [Adapted from Nida *et al*, 2022].

2.3. Considerations About Fatigue Behaviour of Materials

The Fatigue of Materials is a process resulting from cumulative damage to a body or component, and it occurs when a dynamic load is applied cyclically to it during a certain period of time, originating cyclic dynamic stresses or strains that change with time. The fatigue process starts with a single or more cracks that will propagate until they reach a critical limit, leading to the rupture of the component, due to the dynamic stresses applied to it. This evolutionary process is characterized by 3 steps: crack nucleation or crack initiation (including the microscopy crack growth), crack propagation (macroscopy crack growth) and final rupture. The mechanical fatigue failure is the most common phenomenon responsible for the failures of mechanical components. [Stephens *et al*, 2001]

A stress cycle is defined by the following stress parameters and respective equations, from Equation 2 to 5 [Dowling *et al*, 2013]:

- Stress range: $\Delta\sigma = \sigma_{max} - \sigma_{min}$ (2)

- Mean stress: $\sigma_m = \frac{\sigma_{max} + \sigma_{min}}{2}$ (3)

- Stress amplitude or alternating stress: $\sigma_a = \frac{\sigma_{max} - \sigma_{min}}{2}$ (4)

- Stress ratio: $R = \frac{\sigma_{min}}{\sigma_{max}}$ (5)

where, σ_{max} and σ_{min} are the maximum and minimum stress level, respectively.

The applied cyclic loads to the mechanical components can be divided into constant amplitude loading and variable amplitude loading. For cycles with a loading at constant amplitude, the stress amplitude keeps constant with time, so the component is under stress with the same amplitude in each cycle. The typical examples for these loadings are the cycles at pulsating stress ($R = 0$) and at alternating stress ($R = -1$). For a cycle with pulsating stress, the mean stress is different from zero and the minimum stress is zero or $R = 0$. On the other hand, in an alternated stress cycle, where $R = -1$, the mean stress is zero. It is common to find these kinds of stress cycles in mechanical applications that work at constant speed like: shafts, crankshafts, cams, camshafts, rods, connecting rods, eccentrics, bolts, bearing, gears, screws, welded structures and others. [Suresh *et al*, 2004]

The function that defines the stress cycle, called a stress wave, can take different shapes, like sinusoidal, triangular, trapezoidal, square, parabolic, and others. Typically, the function is

represented with the stress on the ordinate axis and the time on the abscissas axis, and the most common wave that is used in everyday applications is the sinusoidal wave type. Figure 2.30 is an example of a sinusoidal loading cyclic curve. [Suresh et al, 2004; Meyers *et al*, 2009]

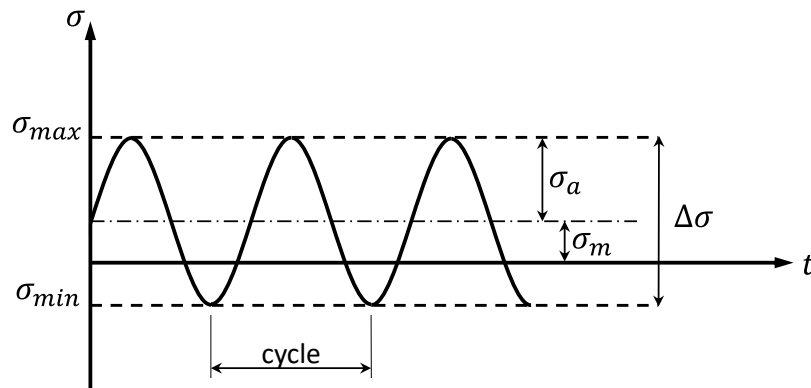


Figure 2.30: Example of a sinusoidal curve.

In load patterns with variable amplitude, the stress amplitude changes with time. The stress cycle could be formed by blocks and by a succession of blocks with constant stress amplitude, where each block corresponds to a defined number of cycles (n_i). In Figure 2.31 could be seen an example of a stress wave at variable amplitude by blocks. [Suresh *et al*, 2004]

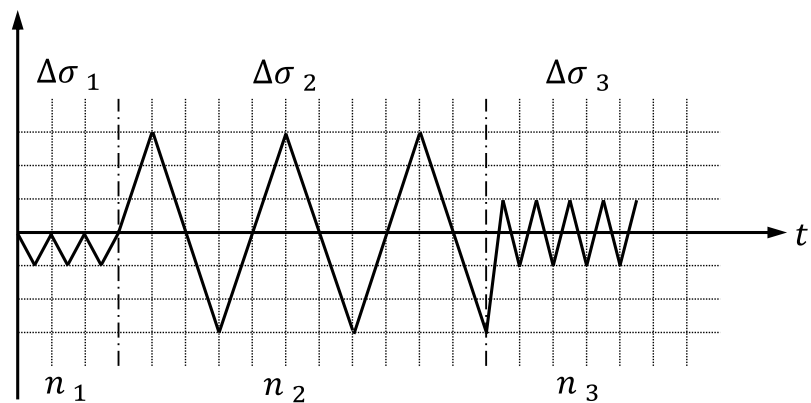


Figure 2.31: Example of a stress curve at variable amplitude by blocks.

Lastly, there are the stress cycles in which the wave is random, known by irregular or random stress cycles. Loadings with variable stress amplitude are the most frequent in welded structures and in the aeronautic industry, being the most difficult to analyse. For these types of random cycles, the curves are usually acquired experimentally and are generally simplified as stress cycles at constant amplitude, in which the amplitude value has a safety factor. The simplification

of these problems is possible through the approach presented by Miner at 1945, where he established the Equation 6, also known as Miner's Law, in which the damage from each block is linearly cumulative until the component rupture. [Suresh *et al*, 2004]

- Miner's Law:

$$\sum_{i=1}^k \frac{n_i}{N_i} = 1 \quad (6)$$

where, k is the sequence number of blocks; N_i is the fatigue duration for the corresponding stress σ_i from the material S - N curves, and n_i is the number of cycles for the respective block. Since then, several models have been suggested to represent the fatigue damage accumulation, but, due to its simplicity of usage, Miner's law has been one of the most used [Fatemi *et al*, 1998].

As previously stated, the materials fatigue happens in three steps: crack initiation, crack propagation and final rupture. Typically, the crack initiation happens at the components surface, because this zone has less restriction to the material deformation than inside of the component material, favoring the plastic's deformation occurrence. Other contributions that facilitate the crack initiation is related with the components surface, where they typically have geometric defects like, micro defects (surface roughness, microporous, inclusions, scratches or grooves from the mechanical/technological processes, and so on), or macro defects like (welding seams, geometric variations, section variations, holes, threads, etc.), originating stress concentration regions. There are other contributions which generate the same effects, such as the corrosion of the materials, due to the weather or the ambient conditions, or simply due to the wear of the components interaction in a mechanical system. On the other hand, if the surface conditions are favourable, the biggest portion of the component's life is spent at the initiation stage and the crack growth is influenced by the component thickness. [Suresh *et al*, 2004; Dowling *et al*, 2013; Stephens *et al*, 2001]

The initiation period is marked by occurrences at the level of the material's microstructure. The cyclic loading leads to a localized deformation caused by the irreversible dislocations of the crystal lattice. These dislocations happen in well-defined planes of the crystal lattice, forming a pattern of parallel slip planes that are suffering cumulative dislocations. These slip planes, commonly in ductile deformation, for a cyclic loading, have a much finer morphology than for a monotonic loading. [Meyers *et al*, 2009]

The crack initiation process happens, most of the times, at the component's surface due to the stress concentration effect. The fatigue propagation happens in three different steps. Step I, is defined by a crack growth under a direction of 45° angle with the loading direction, resulting in a growth in planes under high stress shear values. At Step II, the crack is mainly propagating normally to the loading direction and the intrinsic propagation speed is in function of the stress intensity factor amplitude. [Branco *et al*, 2006]

For long fatigue lives, the maximum stress originating from the cyclic loadings, which will eventually lead to the component's failure, could be below the material's tensile strength and without much plastic deformation. However, on a free surface, the plastic deformation could cumulate as a result of the movement dislocations. The dislocations are a defect or irregularity in the crystal lattice that could move and multiply with shear stress, causing a permanent deformation (plastic deformation). So, the dislocation is the amount of deformation or slip and is higher on a component free ("external") surface than those inside crystalline materials, due to the lack of the grain boundaries restrictions. In metals with polycrystalline structures, the grains are random and individually orientated. Despite their distribution, each grain has an ordered atomic structure, granting directional mechanical properties. The deformation happens in easy slipping crystallographic planes where it will be easier for the dislocations to move than in the other planes. The slippage is mainly controlled by the shear stress, and the shear stress will be higher in crystallographic planes which form 45° angles with the tensile stress direction, where the slippage will be higher too. Roughness and slip bands emerge on the plastic deformed surface as a result of the slippage between atomic planes. During each additional cycle, the slip band intensifies on the surface and grows to the inside of the grain, forming the so-called persistent slip bands (PSBs). The name, persistent, had its origin in the beginning of the fatigue studies, due to the observation of the reappearance of the slip band; the slip band was always persisting/present in the same place, even after the removal of a thin layer of material (electropolishing). The flux created by the cumulative plastic deformation originates superficial spikes/teeth and dimples, called extrusions and intrusions, see Figure 2.32. [Meyers *et al*, 2009]

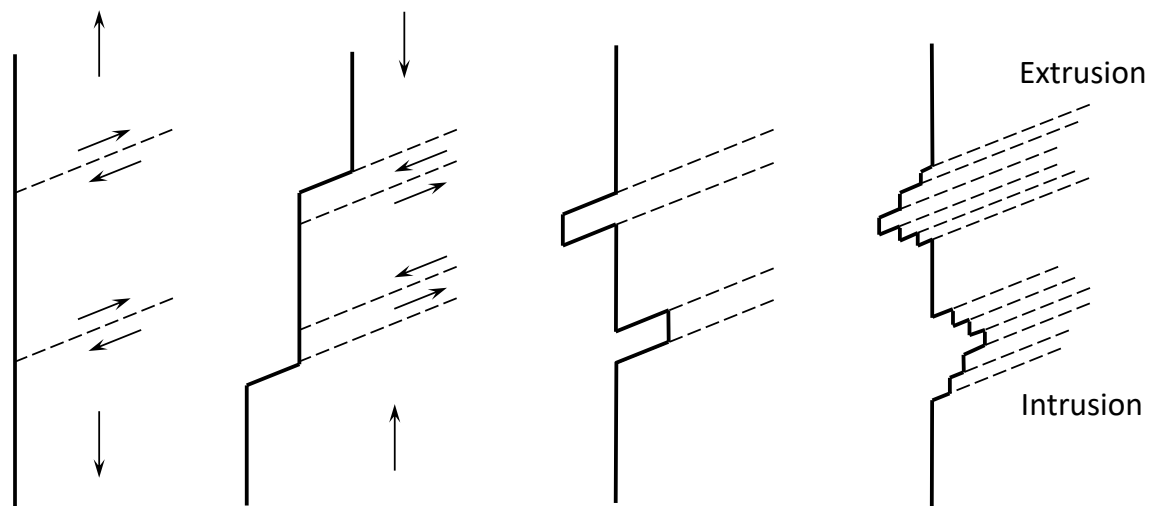


Figure 2.32: Fatigue crack mechanism in the slip bands [Based on Meyers *et al*, 2009].

During the process small cracks will eventually appear in the intrusions. These microcracks grow along the slip planes and are induced by the shear stress. The crack growth in the shear mode, designated as crack growth stage I, grows until it reaches a crack length between three to four times the size of the grain. The size of the cyclic plastic deformation region, created at the crack tip, is influenced by the stress amplitude. On the other hand, the slip mechanisms, that control the crack growth at stage I, are helped when the size of the cyclic plastic region is smaller than the grain size. When continuing to apply the cyclic loading, one or more dominant cracks will have their origin in the coalescence of the micro cracks in different grains. The cyclic stress range and deformations, associated with the crack tip or tips, leads to the crack growth under the action of an applied stress. This Stage II is called Crack Propagation. At stage II, the crack path mainly grows normal to the loading direction. The crack growths are influenced by the crystallographic orientation of the grains on the slip and on the cleavage planes, grain by grain, and it changes direction when it reaches the grain boundaries, creating a zig-zag path. Most of the time, the fatigue crack grows through the grains in a transgranular mode. Under certain conditions, like higher temperatures or under corrosive environments, the grain boundaries' forces will be weaker than the grain matrix, leading to a crack growth under the intergranular mode. At stage III, the fracture surface resulting from the crack growth, for ductile metals, is defined by the resulting grooves that can have a bigger density or wither accordingly to the applied stress level. Later on, during the fatigue process, when the crack reaches a certain critical length, it will cause the component's rupture/failure. [Meyers *et al*, 2009]

Most of the times, the life of a part is indicated as the cycle number until rupture and it could be estimated by the sum of cycles from the crack nucleation to the crack propagation, until final rupture. The crack initiation is established by the number of cycles from the low-cycle fatigue tests, done under the deformation control, resulting in high stress, typically higher than the material tensile strength and subsequent low life expectancy for the part or component. From the tests, it is possible to determine empirically the law that rules the fatigue crack initiation behaviour, depicted as the material deformation-life curves. On the other hand, the number of cycles belonging to the crack growth until rupture could be estimated through the Paris-Erdogan law, empirically obtained from the propagation tests. These concepts will be detailed further ahead in this work. Typically, the fatigue data for a material whose life is defined by a crack initiation, followed by crack growth are depicted on $S-N$ curves (Figure 3.4), where the applied stress S is presented as a function of the number of cycles until failure, N_f . These curves are commonly used in mechanical engineering projects because they are easy to use when doing structural project, and it needs to take fatigue into account, in a safe way. [Meyers *et al*, 2009]

The most used methods for the fatigue strength prediction are based on the nominal stress or on the local (true) stress. Typically, the nominal stress is more used for welded structures and the local stress for mechanical components.

The method that uses the nominal stress is depicted as $S-N$ curves (Figure 2.33), where the stress is purely nominal and calculated for the critical transversal section considering the external loading and discarding the stress concentration and is ruled by the Equations 7 and 8:

$$\log \sigma_a = \log B - c \log N_r \quad (7)$$

where,

$$\sigma_a N_r^c = B \quad (8)$$

and c and B are material constants. [Suresh *et al*, 2004]

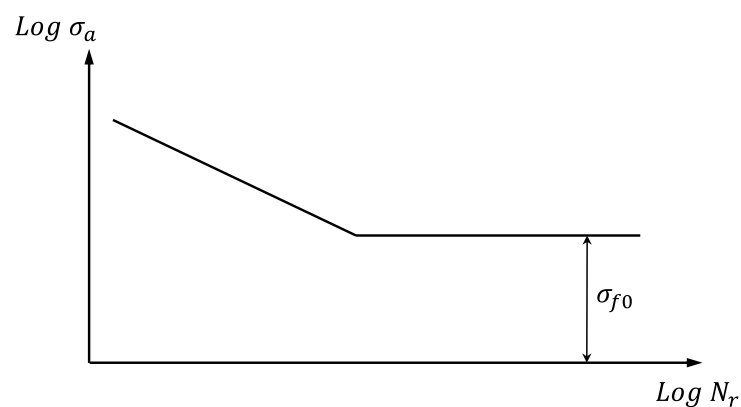


Figure 2.33: Generic S-N curve for a material.

For example, on a generic case at constant or linear stress distribution, the critical loading or the critical nominal stress values that are related to global phenomena are used like the global plasticization or the total fracture of the sample [Suresh *et al*, 2004].

At the ordinate axis is the stress range or the stress amplitude and at the abscissas axis is the corresponding number of rupture cycles. Ideally, the specimens are tested under the same conditions (high gloss surface finishing, geometry, heat treatment, environment, temperature, and so on) and stress ratio, but at different stress amplitudes. Most of the times the tests are performed for $R = 0$ or $R = -1$. When the curve tendency is horizontal, it means that it is reaching the fatigue limit stress (σ_{f0} or σ_e) of the material and it will have “infinite life”. [Suresh *et al*, 2004]

The local stress method enables the critical stress level region to be determined considering parameters as the stress concentration, the residual stress and the plasticization resulting from the cyclic loading [Suresh *et al*, 2004].

2.3.1. The Microstructure and the Materials Fatigue Behaviour

There are different factors that influence the fatigue strength positively or negatively. The ones that are intrinsic to the material are the grain size, microstructure orientation and the existence of precipitates in the microstructure. Kurita et al., 1996 and Anderson, 1991, concluded in their research that for high fatigue strength values are typically associated with materials that have small grain size, delaying the crack initiation. In this way, for a smaller grain size, most of the fatigue cycles will be spent at the fatigue crack initiation. On the other hand, for bigger grain sizes most of the fatigue cycles will be spent at the fatigue crack propagation. Due to this, for a small grain size, the crack initiation life should be longer than the propagation life, on the contrary of what happens for bigger grain sizes. [Suresh *et al*, 2004]

The presence of precipitates will affect the materials' fatigue life too. Sheared precipitates and unsheared precipitates may originate local deformation, leading to a fatigue crack initiation. Depending on the size, distance, shape, nature and coherence grade of the precipitates during the plastic deformations, the dislocations will shear or turn around the precipitates. When the dislocation shears the coherent particles, the material strength is decreased. This is continuously happening with any additional movement of the dislocations, destroying the agents/elements responsible for the material mechanical strength. At small deformation amplitudes, the material with unsheared precipitates will harden much more when comparing with a sheared precipitated material which will soften. As a result, for a deformation-controlled test, the flaw happens much earlier for unsheared precipitated materials, which will be acting as stress concentration points, and like this, preferential zones where the dislocations could pile up, resulting in damage accumulation, originating PSBs, crack nucleation or initiation, and crack growth until final material rupture. [Suresh *et al*, 2004]

The microstructure grain orientation also influences the fatigue life. A grain that has its boundary normal to the crack propagation plane will create restriction to the crack propagation, increasing the propagation time but helping the crack initiation process. On the other hand, when the microstructure is formed by grains that have their boundary parallel to the propagation direction, the propagation will be easier and faster. [Suresh *et al*, 2004]

2.3.2. Loading Effect on the Materials Fatigue Behaviour

The stress ratio influence and the mean stress effect are of paramount importance for the fatigue life and are interdependent. When the stress ratio (R) increases so the mean stress increases (σ_m), both decreasing the fatigue strength for a given stress range. There are different ways to assess the mean stress effect of a fatigue cycle with a given stress amplitude (σ_a). [Dowling *et al*, 2013]

In 1919, Goodman presented the following Equation (9):

$$\sigma_{ar} = \frac{\sigma_a}{1 - \frac{\sigma_m}{\sigma_u}} \quad (9)$$

where, σ_{ar} is the equivalent stress amplitude for a stress cycle with a null mean stress ($R = -1$) and σ_u is the ultimate tensile strength. Later, Smith, Watson and Topper (SWT) in 1970 proposed another method, according to the following Equation 10. [Dowling *et al*, 2013]

$$\sigma_{ar} = \sqrt{\sigma_{max} + \sigma_a} \quad (10)$$

This SWT method has the advantage of being independent from the material constants [Dowling *et al*, 2013].

2.3.3. Influence of Surface Finishing and Treatments on Materials Fatigue Behaviour

The surface finishing is an important factor that influences the fatigue crack initiation. For example, for a very good superficial finish, like high gloss finishing, the better will be the fatigue behaviour, but for a higher superficial roughness a worse fatigue behaviour is expected. On a micro scale, the roughness of a surface, peaks and valleys, will act as a stress concentration points, increasing the effective stress and the chance for a crack initiation to occur. [Suresh *et al*, 2004]

The heat and chemical treatments, like the nitriding, carburizing, hardening, annealing, age-hardening, and so on, will modify the superficial and/or the bulk microstructure of the material, which will increase or decrease the material hardness and/or stress levels, influencing the material's fatigue strength behaviour. This could increase or decrease the fatigue life according to the treatment and the material. [Suresh *et al*, 2004]

There are other superficial treatments, like the mechanical ones, that will influence the fatigue life through the induction of near surface residual stress. The most useful are the ones that create

compressive residual stress, leading to an increase in mechanical strength (strain hardening) and the change of the superficial roughness through the superficial plastic deformation (hammer peening, laser shot peening, shot peening, and so on). [Suresh *et al*, 2004; Murakami, 2002]

Lastly, there are the heat treatments for relaxing the tensile residual stress, typically mechanically superimposed (sawing, milling, drilling, and so on), improving the fatigue life of a component [Suresh *et al*, 2004].

2.3.4. Residual Stress on the Materials Fatigue Behaviour

An existing stress in a component without having any applied external forces is called “residual stress”. The residual stress is elastic and must be added to the resulting stress from the applied loading. They could be beneficial or prejudicial to the structures, equipment and systems, according to their magnitude, type or sign, and distribution. The residual stress in a system it is in equilibrium. Any new input or modification to a component like milling, welding, applied mechanical or thermal loading, will change the equilibrium state, causing a redistribution of the residual stress, achieving a new equilibrium state of the residual stress. [Dowling *et al*, 2013]

The residual stress interacts with the applied loading, changing the applied loading cycle. The residual stress acts similarly to the mean stress (σ_m), so it will affect the mean stress. As stated before, the residual stress could be beneficial or prejudicial to the fatigue behaviour, depending on how they are distributed throughout the component, magnitude and their sign (tensile: “+”; compressive: “-”). Their magnitude will interact, more or less, with the applied stress cycle, bearing in mind that the sign is of the most importance. For example, with a pulse loading ($R = 0$ or $R > 0$) and at a compressive residual stress, it will decrease the mean stress, leading to an increase of the fatigue life. On the other hand, for tensile residual stress, it will increase the mean stress, leading to a decrease in the fatigue life. These are the main reason behind the usage of heat treatments or mechanical treatments, inducing residual stress, increasing the fatigue strength in regions with geometric defects and regions with higher stress intensity values. [Dowling *et al*, 2013]

2.3.5. Low Cycle Fatigue

For stress or strain levels above the elastic regime, the rupture could happen at a relatively small number of cycles, commonly below 10^4 . This phenomenon is called Low Cycle Fatigue. Some real applications that are subject to this specific fatigue are reservoirs under pressure, steam turbines and frequently, other components under thermal dilatations. [Meyers *et al*, 2009]

The way the cyclic strain at materials is assessed is important because it enables life at the crack initiation of the notched components to be assessed. From this, can be concluded that there is a hypothesis to originate a crack that starts on the notch in a component. The same number of cycles as in a polished specimen will be needed, assuming that both the crack initiation regions are subjected to the same stress-strain curve history. [Stephens *et al*, 2001]

The material behaviour in a low cycle fatigue can be assessed by tests at constant cyclic stress amplitude or at constant cyclic strain amplitude. In both cases, plastic strain for each fatigue cycle, will happen creating the hysteresis loops in the stress-strain diagram (Figure 2.34). [Stephens *et al*, 2001]

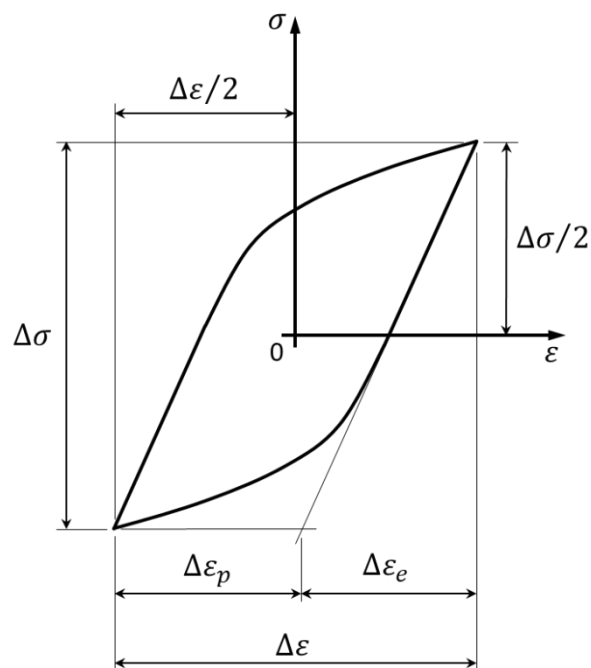


Figure 2.34: Example of cyclic stress-strain diagram and its hysteresis cyclic loop.

During the low cycle fatigue tests the mechanical properties could increase, decrease or remain approximately constant, depending on material, initial metallurgic state, applied stress or strain amplitude and temperature. A progressive increase of the mechanical properties is called cyclic hardening; on the other hand, when the mechanical properties are decreasing, it is called cyclic softening. [Stephens *et al*, 2001]

Later on, during the low cycle fatigue test, the hysteresis loops will stabilize and the material will be in a state of equilibrium for the applied stress or strain. This equilibrium state will be disturbed with the continuation of the test by the crack initiation, followed by crack propagation, which could lead to a final rupture. Connecting the “corner/vertices” dots resulting from the hysteresis

loop curves, it is possible to draw the so called “cyclic stress-strain curve” (Figure 2.35). This stabilized cyclic stress-strain curve could be very different from the monotonic curve for the same material. The stabilized cyclic stress-strain curve gives important information about the cyclic behaviour of the material. [Stephens *et al*, 2001]

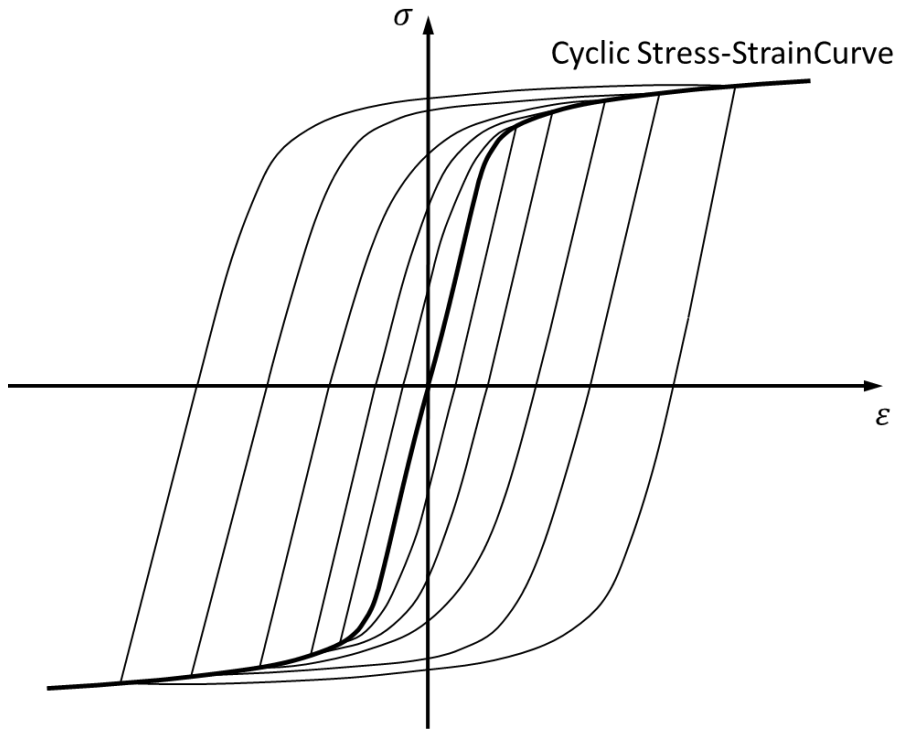


Figure 2.35: Hysteresis cyclic loop curve and respective cyclic stress-strain curve.

Morrow has defined the cyclic stress-strain curve through the following Equation 11:

$$\frac{\Delta\sigma}{2} = k' \left(\frac{\Delta\varepsilon_p}{2} \right)^{n'} \quad (11)$$

with k' , being the cyclic hardening coefficient and n' the cyclic hardening exponent. [Morrow, 1965]

The cyclic stress-strain curve, as suggested by Ramberg-Osgood, could be depicted by the relation between the total cyclic strain amplitude ($\Delta\varepsilon/2$) and the cyclic stress amplitude ($\Delta\sigma/2$) through the following Equation 12:

$$\frac{\Delta\varepsilon}{2} = \frac{\Delta\sigma}{2E} + \left(\frac{\Delta\sigma}{2k'} \right)^{\frac{1}{n'}} \quad (12)$$

where, E is the Young's Modulus. [Stephens *et al*, 2001]

The total cyclic strain amplitude ($\Delta\varepsilon/2$) consists of two parts, one relative to the elastic strain amplitude ($\Delta\varepsilon_e/2$) and the other related with the plastic strain amplitude ($\Delta\varepsilon_p/2$) [Stephens *et al*, 2001].

Experimentally, it is possible to characterize the low cycle fatigue strength of a material conducting tests under a range of different strain values [Stephens *et al*, 2001].

The relation between the plastic strain amplitude component ($\Delta\varepsilon_p/2$) and the number of reversals to failure ($2N_f$) was presented by Coffin and Manson through Equation 13:

$$\frac{\Delta\varepsilon_p}{2} = \varepsilon_f' (2N_f)^c \quad (13)$$

where, ε_f' is the fatigue ductility coefficient and c is the fatigue ductility exponent [Stephens *et al*, 2001].

The elastic strain component ($\Delta\varepsilon_e/2$) is shown, since Basquin, most of the time, as a function of the number of reversals to failure ($2N_f$) through Equation 14:

$$\frac{\Delta\varepsilon_e}{2} = \frac{\Delta\sigma}{2E} = \frac{\sigma_f'}{E} (2N_f)^b \quad (14)$$

where, E is the Young's Modulus of the material, σ_f' is the fatigue strength coefficient and b is the fatigue strength exponent [Stephens *et al*, 2001].

The low cycle fatigue regime changes to the high cycle fatigue regime at the corresponding "transition fatigue life", identified as $2N_T$, where the total cyclic strain is formed by equal parts of elastic and plastic strain amplitudes, see Figure 2.36 [Stephens *et al*, 2001].

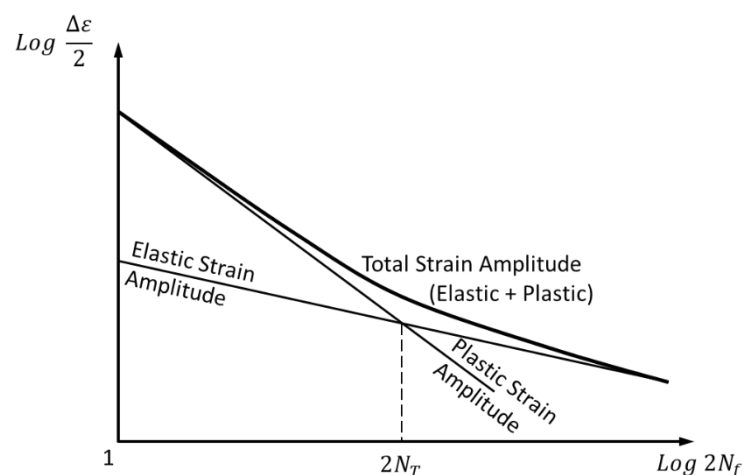


Figure 2.36: Total strain amplitude curve, and elastic and plastic strain amplitude curves versus number of reversals to failure.

The fatigue strength for the total strain amplitude curve is defined for the low cycle, transient and high cycle fatigue regimes, and it could be related by the Basquin and Coffin-Manson equations, see Equation 15 [Stephens *et al*, 2001].

$$\frac{\Delta\varepsilon}{2} = \frac{\sigma_f'}{E}(2N_f)^b + \varepsilon_f'(2N_f)^c \quad (15)$$

2.3.6. Fracture Modes

There are three basic modes of fracturing a body with an existing crack that is subjected to a loading. The three fracture modes are called Mode I, Mode II and Mode III. At Mode I, the body is subjected to tensile forces, at Mode II, to shearing forces and at Mode III, to shearing forces, as depicted in Figure 2.37. [Stephens *et al*, 2001]

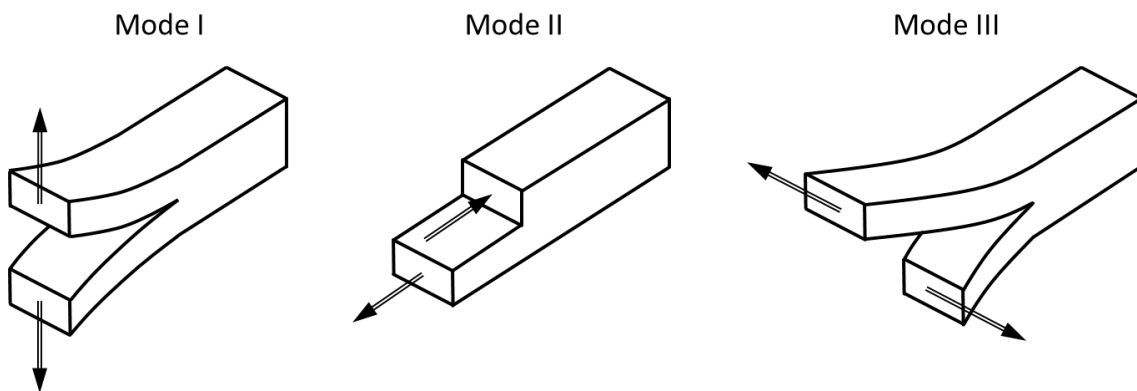


Figure 2.37: Fracture modes, Mode I, II and III (the arrow indicates the loading direction).

2.3.7. Stress Intensity Factor – K

The stress intensity factor has an important role in the fatigue strength life of a component. This factor defines the stress field near the crack tip. The K factor controls the crack growth at a component under a dynamic loading (fatigue) if the applied stress is lower than the Yield stress and if the plastic region in the crack tip has a small dimension when compared with the crack length and with overall dimensions of the component (simplification: crack in an infinite body). [Stephens *et al*, 2001]

The assessment of the stress intensity factor on the fatigue life is most of the time achieved by the $S - N$ curves obtained from the tests with smooth/polished/unnotched specimens ($K_t = 1$) and with notched specimens ($K_t > 1$), where K_t is the static or elastic stress concentration factor. At the $S - N$ fatigue curves, the fatigue strength limit for the notched specimens is lower than for the smooth/polished/unnotched ones. [Stephens *et al*, 2001]

After the fatigue crack nucleation, the crack can grow under a controlled stable regime, if K is smaller than the critical value of the fracture toughness (K_{1c} or K_c). Otherwise, the fracture would be unstable. [Stephens *et al*, 2001]

The crack growth rate curve (Figure 2.38) depicts the relation between the crack growth length (a) and the number of cycles (N) needed to reach it under a stable crack growth regime. The unstable crack growth limit is defined by the critical crack length (a_c) accordingly to the Equation 16. [Stephens *et al*, 2001]

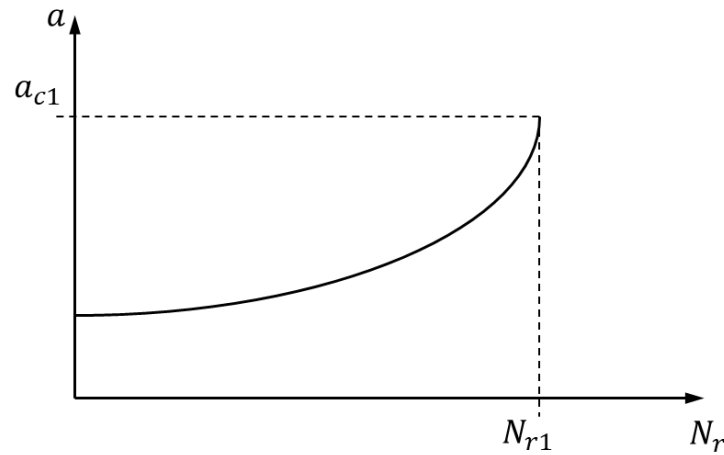


Figure 2.38: Depiction of a crack length growth curve with an applied fatigue loading and the respective number of cycles.

$$a_c = \frac{K_c^2}{Y^2 \sigma^2 \pi} \quad (16)$$

where, K_c is the critical stress intensity factor and Y is a geometric factor related to the specimen geometry [Stephens *et al*, 2001].

It is usual to use $da/dN-\Delta K$ curves to assess the crack growth, which relates the fatigue crack growth speed (da/dN) and the stress intensity factor range (ΔK) of the corresponding loading cycle. Through these curves, it is possible to compare the crack growth between two different cracks. For example, for two different cracks, the crack growth would happen at the same speed if they have the same ΔK value, and is independent of the geometry. The ΔK can be calculated according to the following Equation 17. [Stephens *et al*, 2001]

$$\Delta K = K_{max} - K_{min} \quad (17)$$

where, K_{max} and K_{min} are the maximum and minimum values assumed by K at the corresponding fatigue stress cycle. It is possible to rewrite Equation (17) according to Equation 18 and 19 [Stephens *et al*, 2001].

$$K_{max} = Y\sigma_{max}\sqrt{\pi a} \quad (18)$$

$$K_{min} = Y\sigma_{min}\sqrt{\pi a} \quad (19)$$

where, σ_{max} and σ_{min} are the maximum and the minimum stress for the same fatigue stress cycle and Y is the geometric factor related to the specimen geometry and a is the crack length [Stephens *et al*, 2001].

The da/dN - ΔK curve is usually depicted in a bilogarithmic scale for a range of da/dN values between 10^{-8} and 10^{-2} mm/cycle.

In Regime I, the material's microstructure has an important role in the crack propagation, like the stress ratio R and the environment. The crack propagation is very slow, on average, smaller than the lattice spacing, and the minimum ΔK value is called threshold stress intensity factor (ΔK_{th}) for which there is no crack propagation or it could have, but at a very slow rate, smaller than 10^{-7} mm/cycle, in an unstable way. [Meyers *et al*, 2009; Stephens *et al*, 2001]

Regime II has a continuous nature and the propagation speed is linearly related to ΔK and is the main growth's influencer. The microstructure, the R and the environment has a secondary role in the crack growth. Due to its characteristics, it is possible to apply the Paris Law, Equation 20. [Meyers *et al*, 2009; Stephens *et al*, 2001]

$$\frac{da}{dN} = C(\Delta K)^m \quad (20)$$

where, C corresponds to the value of the intersection of the straight line on the abscissa axis when $\Delta K = 1 \text{ Mpa}\sqrt{\text{m}}$ and m is the corresponding slope [Stephens *et al*, 2001].

Regime III has a very high propagation speed, which increases when the cycle maximum stress intensity factor (K_{max}) approaches the fracture toughness (K_{1c}). The propagation speed can change drastically with small changes of ΔK . The crack growth is mainly influenced by the microstructure and the R , but the environment has a small contribution. [Meyers *et al*, 2009; Stephens *et al*, 2001]

In Figure 2.39, a da/dN - ΔK curve that has defined 3 regions as a result of the different behaviour of the ΔK values is depicted and it is possible to correspond each of its region to Regime I, II and III.

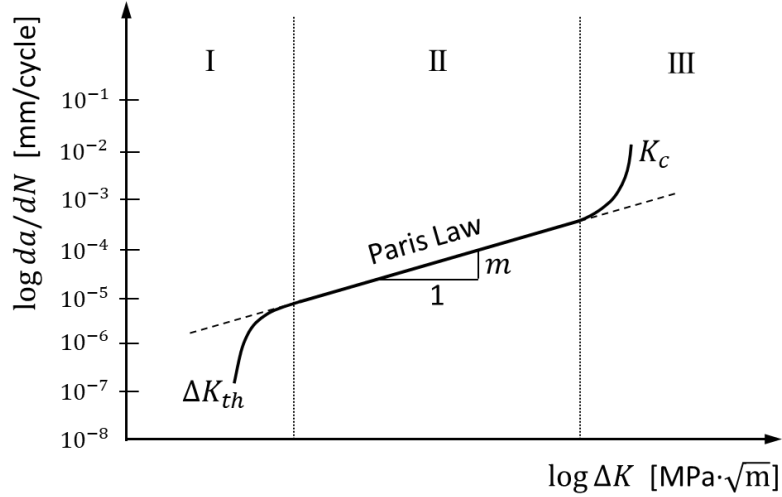


Figure 2.39: Identification of Regime I, II and III limits, depicted on da/dN - ΔK curve, representative of a metal.

The fatigue crack propagation curves are influenced by the material microstructure, mean stress, environment, frequency, temperature, thickness, load history, among others [Stephens *et al*, 2001].

It is possible to calculate the general fatigue life through the integration of the Paris Law from Equation 20, obtaining Equation 21 [Zhang *et al*, 2020]:

$$N_f = \int_0^{N_f} dN = \frac{1}{C(\Delta\sigma)^m (\pi)^{m/2}} \int_{a_0}^{a_c} \frac{da}{Y^m a^{m/2}} \quad (21)$$

2.3.8. Stress ratio and crack propagation speed

The stress ratio (R) may influence the da/dN - ΔK curves depending on the material and the environment that the test is performed in. The influence of the mean stress at the da/dN - ΔK steels is depicted in Figure 2.40 for approximately inert environments. In Regime I and III, there is a great influence of R , increasing the crack propagation speed when R increases. The threshold stress intensity factor decreases when the mean stress increases. In Regime II, the mean stress influence is very small and in Regime III, the curve position is dependent on the ΔK value for which the $K_{max} = K_c$.

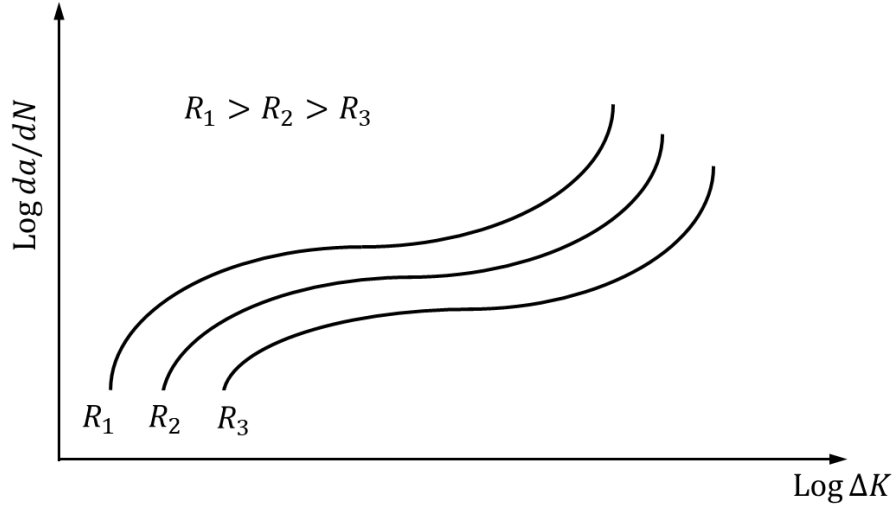


Figure 2.40: Depiction of the influence of the stress ratio on the da/dN - ΔK curves.

The most used relation, that correlates the ΔK_{th} with R , is Elber's. Elber introduced the Crack Closure concept and stated that one crack can only propagate when it is opened. The crack closure can happen due to the plastic zone at the front of the crack tip. This is called plasticity-induced crack closure. When the crack goes through the highly deformed plastic region located on the crack front, the deformed material when relaxing originates a wedge that has a tendency to close the crack during the unloading of the applied force, especially for higher loadings than the expected ones during the ideal conditions. Due to this, the crack could induce compression stress between the two sides of the crack when closed and the corresponding part of the cycle not being effective. The main 3 causes for the induction of crack closure are the plasticity-induced, the roughness and the oxidation ones. [Suresh *et al*, 2004]

In Figure 2.41, the two curves that relate the ΔK_0 with R and are ruled by the Equations 22 and 23 are depicted, but also considering Equation 24 [Suresh *et al*, 2004].

$$\Delta K_{th} = \Delta K_0 = K_{max}(1 - R) \text{ when } R \leq R_{op} \quad (22)$$

$$\Delta K_0 = \Delta K_{op} \text{ when } R > R_{op} \quad (23)$$

where,

$$R = \frac{K_{min}}{K_{max}} \quad (24)$$

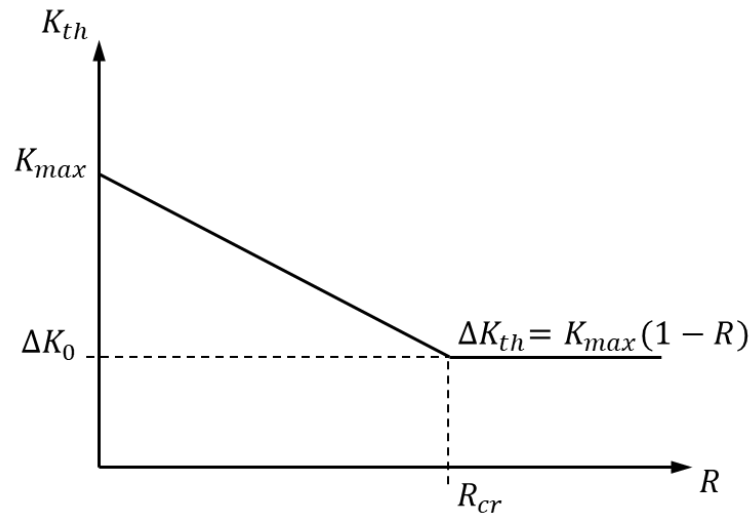


Figure 2.41: Relation between the stress range and the stress intensity factor according to the Elber's theory. [Suresh *et al*, 2004]

2.4. Fatigue Notes in Metal 3D Printed Materials

The influence of the microstructure on the fatigue properties of a Ti-13Nb-13Zr alloy obtained through the SLM process was researched by Zhou *et al*, 2019. They found that, the steep cooling rate inherent to the SLM process resulted in high residual stress and an enhancement of the microstructure, porosity and fatigue behaviour. They also processed the alloy at different scanning speeds, 1200, 1100, 1000 and 900 mm/s at a stable laser power of 325 W with a hatching distance of 0.13 mm and a layer thickness of 0.03 mm, corresponding to different energy densities of 69.44, 75.76, 83.33 and 92.59 J/mm³, respectively. At the highest energy density (92.59 J/mm³), microcracks and the balling effect were observed due to the excessively high thermal stress and long liquid duration; and at lower energy densities (69.44, 75.76 J/mm³) they found high porosities due to the lack of a proper melt pool. At an energy density of 83.33 J/mm³ they achieved the best mechanical performance of the SLM material. It was possible to achieve the best relative density ($97.8 \pm 0.5\%$), a nanohardness of 519.448 HV and a tensile strength of 1106.07 MPa, superior properties when compared with the traditional thermomechanical processing technique with a hardness of 280 ± 15 HV and a tensile strength of 732 MPa. Even the fatigue properties were enhanced with the microstructure change from BCC to HCP ([111] $\beta \rightarrow$ [1-21-3] α') with the increase of the energy density from 69.44 J/mm³ to 83.33 J/mm³, originating finer grains and precipitates, acting like crack retardation, leading to a fatigue life around 150000 cycles at around 340 MPa, close to the life of the Ti-6Al-4V alloy that have a fatigue limit around 360 MPa. The fatigue tests were performed under a stress ratio $R=0.1$ and at a frequency of 20 Hz.

Balachandramurthi *et al*, 2018, have compared the influence of defects and the as built surface condition in the fatigue life between specimens built by two different powder bed fusion technologies, SLM and EBM, and with different post-treatment methods for the metallic alloy 718. The specimens were produced with adequate parameters and powder properties for each building technology. At the SLM they were built without preheating, with a layer thickness of 40 μm , an average powder size of 40 μm and smaller than 65 μm , under an argon inert gas atmosphere, and regarding the EBM process they were built with a high heating bed temperature, with a layer thickness of 75 μm , powder size between 40 to 105 μm and under a vacuum atmosphere. Half of the specimens were subjected to HIP treatment and all of them were subjected to a solution and a two-step ageing heat treatment. From these, some of them are machined and polished to be able to evaluate the influence of the as-built surface in the fatigue life. Metallographic techniques identified three major defects: lack of fusion – LoF, spherical porosity (pores), and shrinkage porosity. The best density, i.e., fewer defects/porosity, was achieved for the HIP+HT condition and is quite similar for both PBF technologies, around 0.05%, and that the worst density was found in the EBM-HT specimens. The LoF defects could have partially melted or unmelted powder and were present on the layer plane. Through SEM-EDS analysis, it was seen that the LoF and the pores could be empty or filled with oxides composed of aluminum and particles of titanium nitride, but the empty LoF could only be observed in the EBM+HT specimens, and the shrinkage porosity could not be observed in the EBM+HIP+HT specimens. Another interesting fact that is related with the contour scanning strategy used for the EBM specimens, is that they are the only ones that have wide ($> 10 \mu\text{m}$) LoF defects around 2 mm from the as build surface. They measured the as built surface roughness using a technique based on the focus variation microscopy with the help of an Alicona Infinite Focus SL microscope and within the evaluated area of $2.5 \times 2.5 \text{ mm}^2$. They found, as expected, a maximum total roughness deviation of almost 3 times higher for the EBM surfaces (around 360 μm) than for the SLM process (around 125 μm). The 4-point fatigue tests were carried out at constant amplitude and load controlled at room temperature with a stress ratio $R = 0.1$ at a frequency of 20 Hz, with three different stress ranges (600, 725, 875 MPa) for the EBM and with 2 different stress ranges (725, 875 MPa) for the SLM specimens. The fatigue performance was better for the SLM+HT specimens than for the EBM+HT specimens, machined (at 725 MPa with more 260000 cycles for SLM and more than 18000 cycles for the EBM specimens) against the as built (at 725 MPa with 90000 more cycles for SLM and around 12500 cycles for the EBM specimens); mainly due to the higher presence of defects near the surface related to the EBM processing of specimens, especially for the as built specimens that have higher roughness due to higher layer thickness and powder size. The fatigue life increased for the HIP+HT specimens for the machined and as built conditions, due to the healed or partially healed defects, leading to a reduced presence of defects, for example, HIP+HT+Machined at 725 MPa they achieved more than 700000 cycles and the EBM around 35000 cycles. One interesting analysis that they made is that the machined specimens have a larger scatter of values in the fatigue life results, most likely

due to the much higher number of crack initiation sites for the as built specimens which leads to a reduced randomness in the fatigue life and lower scatter. These partially healed LoF defects are unable to heal during the HIP due to the presence of oxides. The fracture surfaces were observed and the crack propagation is more ductile for the HT specimens than for the HIP+HT ones that resembles more of a cleavage, possibly due to the influence of HIP in the recrystallization and coarsening of the grain.

The team growth and the research continued, and later on, Balachandramurthi *et al*, 2019, published a new research paper using the previous one as a support, where they studied in more detail the influence of the microstructure on the fatigue crack growth of the metallic alloy 718 achieved with the same methods and conditions previously stated. They measured the grain width and the biggest ones were found in the EBM+HIP+HT, almost 100 μm , with a respective hardness around 475 HV₁, and the smallest grain width was found for the SLM+HT condition specimens with a width grain size around 20 μm and with the highest hardness achieved around the 485 HV₁. It is important to refer to the fact that the HIP treatment homogenized the microstructure and with that, the grain width sizes are quite similar between the SLM and the EBM specimens and even the hardness. The microstructure was evaluated with the help of a light optical microscope, a SEM-BSE-EDS and a FEG-SEM-EDS-EBSD microscope. The EBM-HT specimens present different grains distribution in each of the contours. The outer contour, which makes boundary with the powder bed, had many small equiaxed grains, and on the inside and adjacent contours, the grains were elongated and converging to the centre of the track and orientated with the building direction. Regarding the hatching region inside the contours, the grains were columnar, with a few millimetres in length and growing towards the building direction and through a few layers. Regarding the EBM-HIP-HT specimens, in the contour region they maintained the proportion and direction but they grew and were bigger. In both conditions NbC and TiN were detected, but the δ -phase was not possible to observe in the HIP-HT specimens. The grain width is very similar for all the conditions of the EBM specimens. [Balachandramurthi *et al*, 2019]

Regarding the SLM-HT specimens, the hatching and the contour regions had a similar microstructure with elongated grains randomly orientated and growing mostly towards the building direction. The exception applies to the partially melted powder in the contour region that makes a boundary with the powder bed, which had fine equiaxed grains. The presence of NbC was detected in the grain and at its boundaries and δ phase along the grain boundaries. The SLM-HIP-HT had a very similar microstructure to the HT condition. The biggest microstructure difference is in terms of the grain size and width that have grown, the absence of δ phase, the presence of plenty of annealing twins and the size homogeneity through the sample, resembling a forged material. However, the grains are still smaller than for the EBM specimens. As expected, due to the intrinsic characteristics of the SLM process, the steep cooling rate and thermal gradients originated fine grain structures and sub-grain structures, in opposition with the EBM

process, which due to the process characteristics has coarsened grains. [Balachandramurthi *et al*, 2019]

Regarding the fatigue results, they were already indicated previously (Balachandramurthi *et al*, 2018). Regarding the crack growth, it is transgranular and was unaffected by the precipitates' phases (NbC, TiN and δ phase), the grain size being the only difference between specimens' conditions and responsible for the faceted appearance of the fracture surface for the SLM-HIP-HT and EBM-HIP-HT. Due to this, the crack propagates in single shear mode and normal to the applied force, because the grain seems to be big enough to have the crack tip plasticity region inside it. For the EBM-HIP-HT, this was true for the contour, but regarding the hatch region, the grains are smaller and they observed striations suggesting that the crack grows by duplex slip mechanism. [Balachandramurthi *et al*, 2019]

Alafaghani *et al*, 2018, studied the influence of the building direction and temperature of SLM manufactured specimens, on the microstructure and the respective mechanical properties of two different precipitate hardenable metal alloys, 15-5PH stainless steel and an Inconel 718. They built 3 specimens for each different condition and combination of material, building direction (under X, Y and Z axis), and for each tensile test temperature (room temperature, 200 °C and 300 °C). The authors do not state anything clearly about the postprocess of the specimens, so they should have been tested as built and without any heat treatment. The tensile tests were performed on an Instron 3369 with an environmental chamber accordingly to the ASTM E8/E8M and ASTM E21 standards at a speed of 0.16 mm/min. The best overall mechanical performance for both materials and all conditions were achieved at room temperature for all the directions but, even though, the ones built under the Z axis have the lowest Young's Modulus and Tensile Strength. The authors say that the differences are related to the microstructure that was evaluated through SEM. The authors state that the microstructure maintains unchanged for all the different testing temperatures, but the microstructure between the specimens built under the Z axis is quite different from the ones built under the X and Y directions that have a similar microstructure. Like this, the authors say that the anisotropy between the specimens built on the X and Y are not related with the microstructure and needs further investigation.

Hu *et al*, 2020, investigated the effects of the building direction and of the stress ratio on the fatigue crack growth behaviour of CT specimens built by the SLM technology in an Inconel 625 metal powder alloy with size from 5 to 40 μm . They were built with layers of 40 μm and at two different directions (vertical specimens but with the notch with the same direction as the building direction and normal to it) in a single bar that was cut down and finished to the final dimensions, and subjected to solution annealing heat treatment at 1100 °C/h under argon atmosphere in order to reduce or eliminate the residual stress and to reduce the anisotropy of the microstructure. They did not find any cracks, voids or inclusions, but the microstructure was anisotropic in all the analysed directions. They used an Instron 8872 servo hydraulic to run the Fatigue Crack Growth

(FCG) tests at room temperature at different stress ratios ($R = 0.1, 0.5$ and 0.7) and with the control of K to acquire the data for the threshold region at 20 Hz and for the Paris region at 10 Hz. In the Paris region, the horizontal notched specimens had a slightly higher FCG rate than the vertical ones, but near the threshold limit the FCG rate was much higher for the horizontal notched specimens than for the vertical ones for the tests running at $R = 0.1$. Regarding the ones tested at $R = 0.5$, they have a higher FCG rate with the increase of the R , but even in the two different orientations they have similar behaviour. They have also compared the results with the results from different researchers for the same alloy, and for a similar Inconel 718 alloy, achieved through a similar process and wrought state (just for the Inconel 625). The interesting part, is that the results for FCG rate in the Paris region ($20 \text{ MPa}\cdot\sqrt{m} < \Delta K < 40 \text{ MPa}\cdot\sqrt{m}$) are quite similar for all the building directions and different AM process and wrought, suggesting that the FCG resistance is quite similar and independent from the AM process, and similar to the wrought conventional material and controlled mainly by the load. They have also made SEM on the fracture surfaces and discovered that the micro voids had a neglected effect on the FCG rate at the threshold region, when compared with the anisotropy of the microstructure due to the build orientation of the specimen. They have also developed a model, through the correlation of different theorems (Elber's, Griffith's) and formulations, called "FCG driving force" to analyze the FCG behaviour of these family of materials.

Sarkar *et al*, 2017, have studied the influence of inducing different levels of mean stress (zero, $R = -1$; compressive, $R = -2$; tensile, $R = 0$) and its relation with the failure modes and the fatigue life under cyclic loading. The specimens were produced by an EOSINT M270 with 200 W laser power, using an EOS stainless steel powder PH1 (PH15-5) and the standard parameters for this material from the supplier to process. They were postprocessed according to the ASTM E466 and assessed in an Instron 1344 under cyclic load controlled mode with a frequency of 7 Hz. As expected, the compressive mean stress improved the fatigue life and the presence of the tensile mean stress was detrimental for the fatigue life, when compared with the zero mean stress. The fracture surface analysis was performed through SEM and they found all the crack growth regions for the tensile and the compressive mean stress, starting with crack initiation, stable crack growth, unstable crack growth and fracture region. On the other hand, at zero mean stress, they did not observe any unstable crack growth region, and the stable crack region was characterized by having dark and bright strips, corresponding to ductile-brittle mixed failure mode. Like this, they associated the presence of the unstable crack growth region to the presence of mean stress different from zero. For the compressive mean stress, the main failure mode is brittle, and regarding the tensile mean stress the fracture surfaces have quasi-cleavage and dimples, corresponding to brittle and mixed-rupture modes.

Qian *et al*, 2020, have studied the influence of the mean stress and the building direction of specimens, under High Cycle Fatigue (HCF) and Very High Cycle Fatigue (VHCF). The

specimens were built using an aluminium powder alloy of AlSi10Mg through the technique of SLM under two different directions/angles, at 0° (horizontal built) and at 90° (vertical built), with “bone” shaped specimens for the monotonic tensile tests, and whereas the hourglass shape was used for the fatigue tests. The tensile tests were performed according to the Chinese standard of GB/T228-2002, under 2 mm/min of loading rate. The best mechanical performance was achieved for the horizontal built specimens with 0°, with Yield Strength = 170 MPa (90° = 235 MPa), Ultimate Tensile Strength = 465 MPa (90° = 440 MPa) and the Elongation at Break = 12.7% (90° = 4.3%). Interesting is that the specimens at 0° have a fracture surface angle of approximately 45° mainly due to the shear stress and the ones built at 90° have a fracture surface normal to the applied loading, the tensile stress being holdup the main responsibility for it. The microstructure of the specimens is similar for both directions, presenting grains like a “fish scale” pattern under the building direction, and elongated grains under the powder bed plane. They plotted S-N curves and checked that the increase of the tensile mean stress has a great influence on the HCF and the VHCF, decreasing their life. The fatigue life for the 0° specimen is higher than for the ones at 90°, possible due to the action of different stresses for each direction and due to the increased defects in the built specimens under 90°. They have performed SEM on the fracture surfaces and detected four root causes for the crack initiation process, lack-of-fusion or inclusion, internal pore, with no detected defect, and by tearing. The most common crack initiation process is due to lack-of-fusion and it happens on the surface, next to the surface and on the inside. They only detected crack initiation by pore on the specimens tested under VHCF. The torn ones seem to happen due to the stress concentration region originated by the HAZ of the melt pool. They have also calculated the fatigue crack threshold for this material, about 1.5 MPa \sqrt{m} , and presented a model inspired on the Murakami’s one, Equation 25, of the crack initiation effect on the fatigue life.

$$\sigma = \frac{C_m}{\sqrt{area}^{\beta_1}} \left(\frac{1-R}{2} \right)^{\beta_2} \exp \left(\beta_3 \sqrt{1 - \frac{distance}{r}} \right) \quad (25)$$

where,

- $C_m, \beta_1, \beta_2, \beta_3$ are constants that are determined using the least square method.
- area – encircled area of the defect;
- distance – from the center of the defect area to the specimen’s surface;
- r – fracture surface radius;

Kouraytem *et al*, 2020, aims to evaluate the specimens’ position inside the build volume and the influence of the loading direction. The specimens were subjected to a direct-age hardening heat treatment and produced in an Inconel 718 alloy through a L-PBF system, with recommended parameters, and tested under different mechanical responses/conditions, quasi-static and dynamic

loading. They have used a Concept Laser M2 machine, layers of 50 μm thickness, and virgin powder to build the bulk block of $80 \times 80 \times 100 \text{ mm}^3$ from which they cut the specimens cylinders under the 3 main directions using wired EDM and cut them again to be similar to coins with a thickness of 3.5 mm.

3. Main Results and Discussion of Fatigue Life Assessment of Maraging Steel Components and Hybrid Formulations Built by Selective Laser Melting

3.1. Experimental Overview and Materials

Different process scanning speeds were tried, in order to assess process performance and the resulting material through the build of different specimens, including hybrid formulations, according to ASTM standards which will be indicated along the research. In this case, a hybrid specimen is the one that was achieved by building on top of an existing steel preform. This preform, corresponding to half of the specimen, was manufactured by conventional technologies from raw casting materials.

Defects and limitations from process *versus* material and specimen formulations were found, like porous, voids, tensile residual stress and lack of laser penetration. The microstructure and several specimens' geometries were required to assess the different behaviour of material/specimens under different test conditions. Tensile tests were performed to achieve the monotonic properties, fatigue behaviour through fatigue tests and low-cycle fatigue tests, assessing a fatigue mechanism controlled by strain-range. Resulting fracture surfaces were analysed and brittle and ductile fracture mechanisms were identified.

In Table 3.1, the different chemical compositions of used steels to manufacture the different specimens' formulations can be seen. The AISI 18Ni300, or simply, the only used SLMed steel powder material in this research work, is common to all specimens, even for the hybrid formulations.

Table 3.1: Chemical composition of the different materials used in the specimens, presented in weight % and according to supplier.

Alloy [AISI]	C	Ni	Co	V	Mo	Ti	Al	Cr	P	Si	Mn	Fe
18Ni300	0.01	18.2	9.0	-	5.0	0.6	0.05	0.3	0.01	0.1	0.04	Balance
H13	0.40	-	-	0.94	1.30	-	-	5.29	0.017	1.05	0.36	Balance
420	0.37	-	-	0.17	-	-	-	14.22	0.021	0.64	0.37	Balance

The configuration and sample code hybrid specimens used in the research work of Chapter 3, are as follows in Table 3.2.

Table 3.2: Hybrid specimens' design.

Sample Code	SLMed or LPBF Powder	Substrate or Preform Material
LPBF/HS	AISI 18Ni300	AISI H13 – Hot work tool Steel (DIN 1.2344)
LPBF/SS	AISI 18Ni300	AISI 420 – Stainless tool Steel (DIN 1.2083)

In Figure 3.1, the specimens' dimensions are indicated, and in Figure 3.2, the machine used to additively build them. These specimens (Figure 3.3) were tested in a 10 kN capacity Instron EletroPuls E10000 machine (Figure 3.4) for monotonic and fatigue tests to achieve mechanical properties and S-N curves respectively.

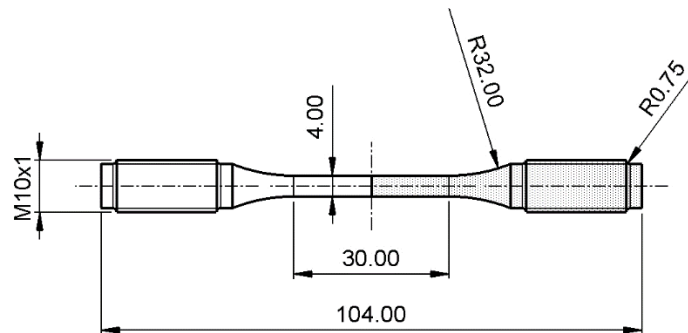


Figure 3.1: Geometry and dimensions of cylindrical fully built specimens and hybrid formulations. In the hybrid formulations, and as indicated in Table 3.2, one half of it corresponds to the substrate made from HS or SS bulk material (darker region).

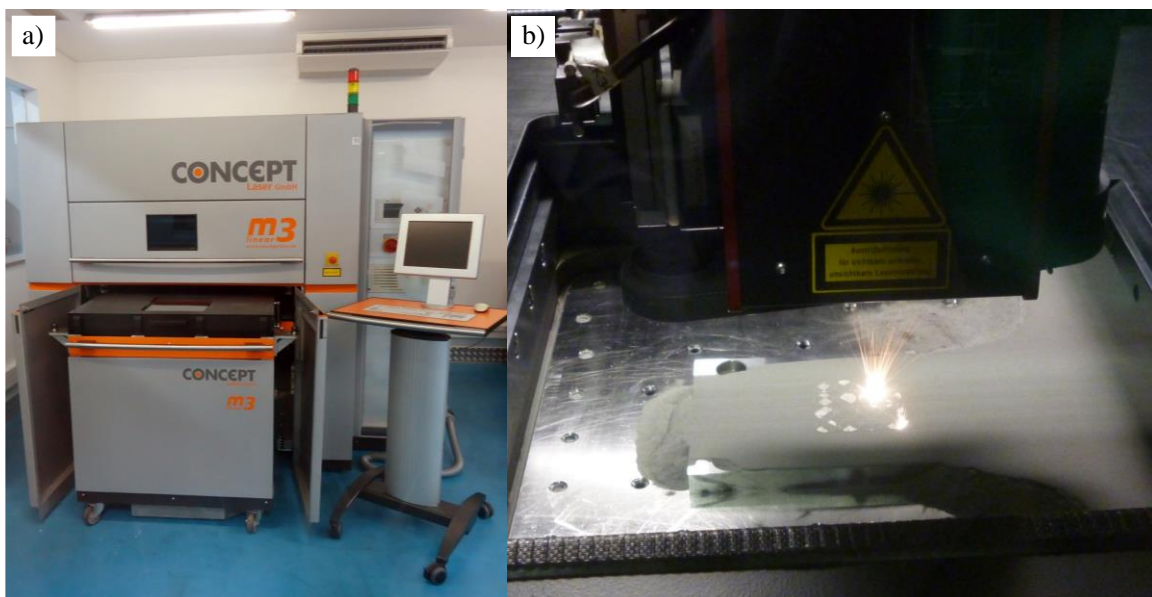


Figure 3.2: Concept Laser M3 Linear machine (a) during the building of the specimens and selectively laser melting the 18Ni300 powder (b). Courtesy of Erofio S.A..

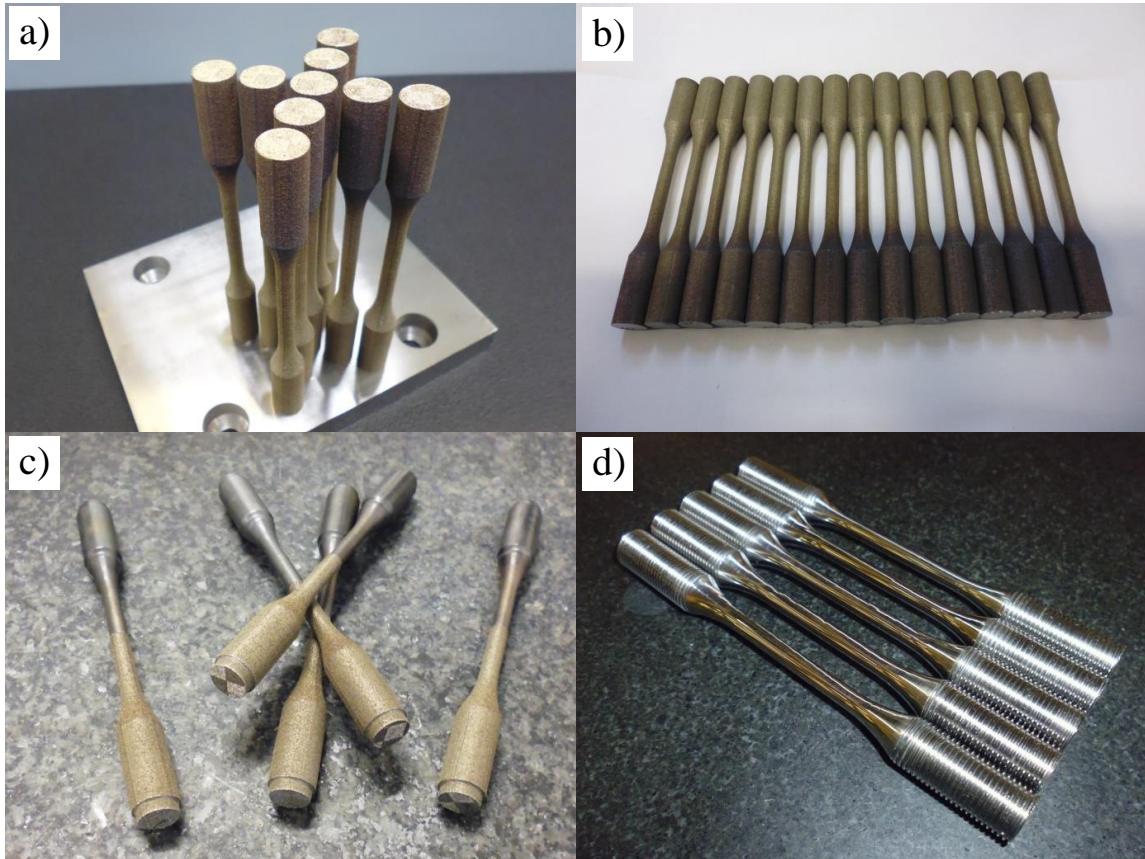


Figure 3.3: Specimens after the SLM process built at a scan speed of 200 mm/s. In a) the specimens are in *as printed* condition and on the build plate, and after the wired electrical discharging cutting of them from the build plate in b). In c) it is possible to observe the hybrid specimens after the SLM process, being formed by an AISI 420 substrate (darker region) with the intrinsic melted top (rougher region). In d) it is possible to see the specimens after all the finishing iterations of lathe, grinding and polishing.

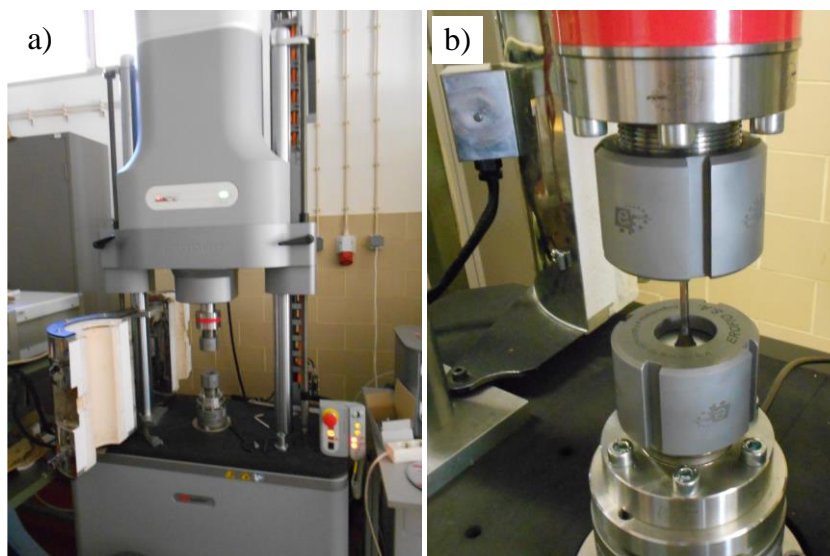


Figure 3.4: Tensile test apparatus in the Instron EletroPuls E10000 (a) with a detail of the assembled specimen (b).

The monotonic tensile properties of the different used materials are listed in Table 3.3.

Table 3.3: Materials' monotonic tensile properties; a – experimental values from tensile tests of SLMed specimens; b – values according to materials' supplier datasheet.

Material [AISI]	Yield Stress [MPa]	UTS [MPa]	Strain at Failure [%]
18Ni300 ^(a)	1000	1147	6
H13 ^(b)	1280	1520	12
420 ^(b)	1360	1600	12

In Figure 3.5 is the design of the CT specimen used to assess the fatigue crack growth rate curves, according to the ASTM E647.

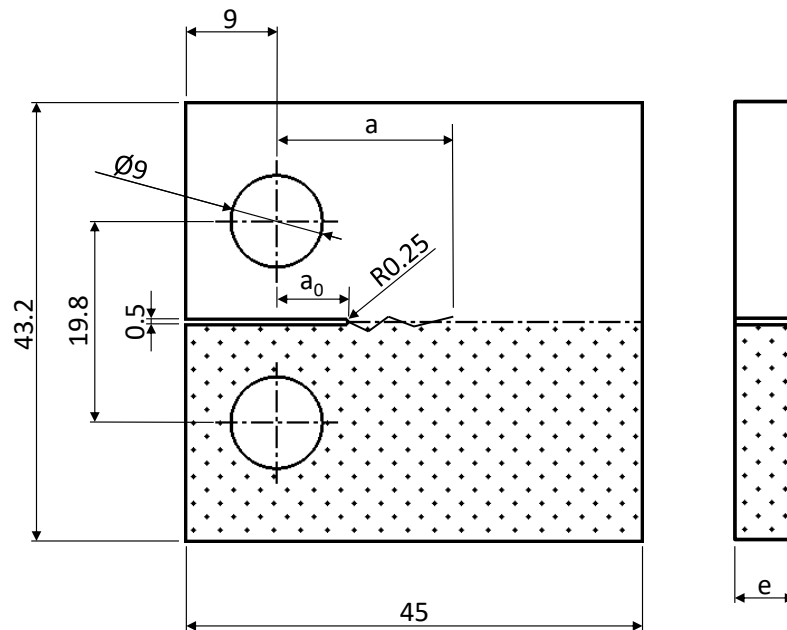


Figure 3.5: CT's specimen dimensions and, if hybrid, with the spotted region made from a different substrate material, as indicated on Table 3.2. Where $a_0 = 7$ and $e = 6$ mm.

The fatigue crack growth rate and the low-cycle fatigue tests were performed in a servohydraulic Instron test machine with 100 kN capacity, Figure 3.6. The low-cycle fatigue specimens' dimensions are depicted in Figure 3.7.

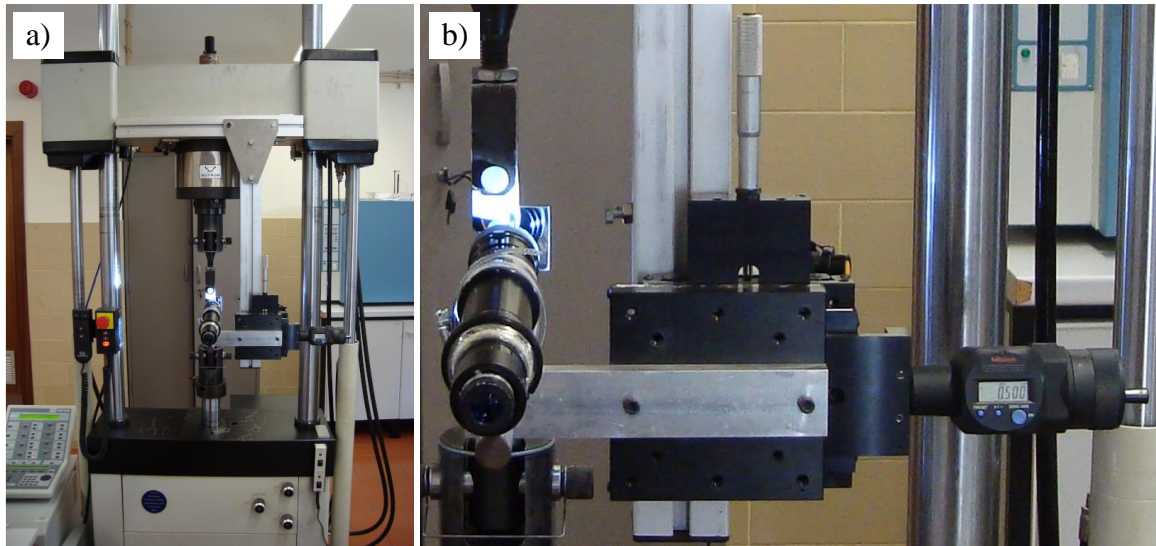


Figure 3.6: Servohydraulic Instron test machine and its apparatus during a fatigue crack growth rate test (a), and detail of the CT specimen and travelling measuring microscope (b).

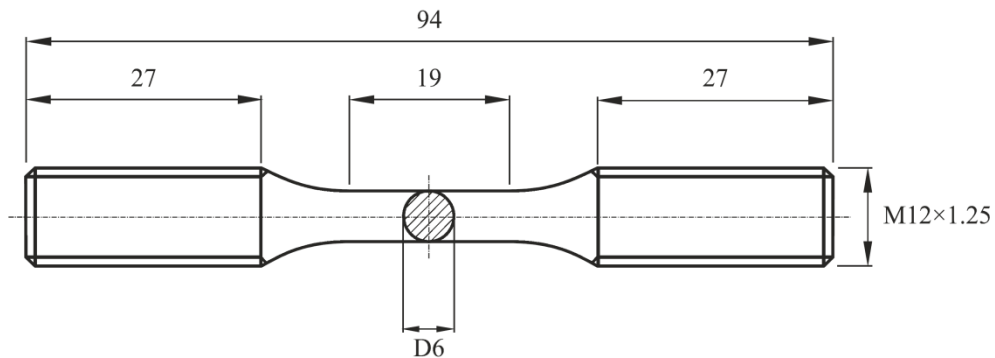


Figure 3.7: Low-cycle fatigue specimen's dimensions.

3.2. Microstructure and Porosity

Samples were prepared accordingly to the metallographic ASTM E407-99 standard from cross and long sections of the specimens in order to be observed with the optical microscope and so that the porosity and the microstructure could be assessed. From the SLMed samples built at different scan speeds, 200, 400 and 600 mm/s, some differences in the porosity level were found but not a noticeable difference at the microstructure level, even regarding grain size and shape. The biggest consequence of the scan speed increase was to affect the melting process, mainly the *VED*, with consequences in the percentage of porosity, that is around 10 and 14 times bigger for the scan speed of 400 and 600 mm/s respectively, when compared with the porosity reference value of $0.74 \pm 0.09\%$ achieved for a scan speed of 200 mm/s. The measured porosity was calculated with the help of the “Image J” software that by contrast image automatically calculates the total porosity of that image (Figure 3.8).

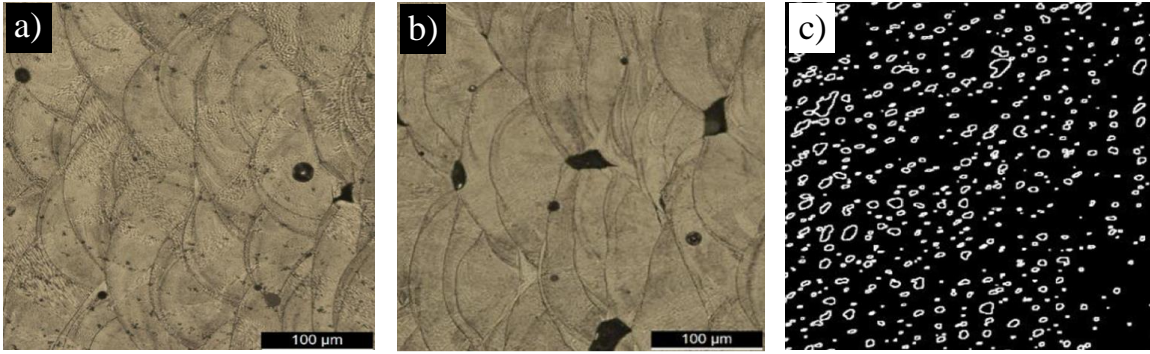


Figure 3.8: Microstructure and porosity of specimens built with scan speeds of 200 mm/s (a) and 400 mm/s (b), and how it was detected by the image “J” software (c).

Another approach was to evaluate volumetric (3D) porosity through the Archimedes principle, and as expected, achieving the highest density of 7.42 g/cm³ for a scan speed of 200 mm/s (see Table 3.4). This method achieved lower porosity, because the 2D measurement takes into account the porous shape in the plane directions and the presence of impurities resulting from the etching process. The porous shapes roughly suggest that they are changing from circular, to elliptical and to deformed/undefined, at the same time as the porous area increases. For specimens with the lowest porosity, the microstructure is quite coherent along the deposited layers. It is mainly formed by elongated grains with approximately 150 μm in length and 30 to 35 μm in width, being directly related with the nominal layer thickness of 30 μm used during the SLM process, see Figure 3.9. The formation of acicular cellular structures was observed, indicating the presence of a martensitic structure [Yao *et al*, 2018], associated with the increases in the mechanical properties.

The hardness was evaluated according to the ASTM E384-11e1 standard at 0.5 kgf load. A slight decrease in the microhardness and dispersion’s increase was found due to the scan speed/porosity increase, see Table 3.4.

Table 3.4: Mechanical properties of the SLMed 18Ni300 material, assessed under different scan speeds.

Scan speed [mm/s]	Porosity [%]	Density [g/cm ³]	Hardness [HV1]	Young’s modulus [GPa]	Tensile strength [MPa]	Strain at failure [%]
200	0.74 ± 0.09	7.42	354 ± 5	168 ± 29	1147 ± 13	5.12 ± 0.001
400	7.37 ± 0.99	7.29	348 ± 6	155 ± 30	1032 ± 27	1.45 ± 0.01
600	10.38 ± 2.88	7.14	341 ± 8	104 ± 38	612 ± 22	0.71 ± 0.002

The integrity and adhesion of the interface between the steel base and the SLMed material for the hybrid specimens' formulations were observed on the SLM/H13's interface. A new white region was detected in H13's microstructure, indicating a decarburization, followed by a corrugated darker region, indicating an increase in the carbon content. It is a consequence of the diffusion of the carbon from the "white" to the darker "region", enabled by the remelt of the H13 steel by the laser scanning during the first layer, see Figure 3.9 b). The corrugated profile is related to the hatching distance between two consecutive laser trajectories. The matter should be looked at carefully and more research done about it, because, a similar corrugated effect on the AISI 420 material was expected to be found, especially because they have a similar carbon content, AISI H13 – 0.39% C / AISI 420 – 0.38% C. This could be related with the different orientation of the laser scan paths, being parallel to the observed section. It is important to refer to the fact that despite having porosity in the SLMed material, no porosity was detected in the interface and right next to it.

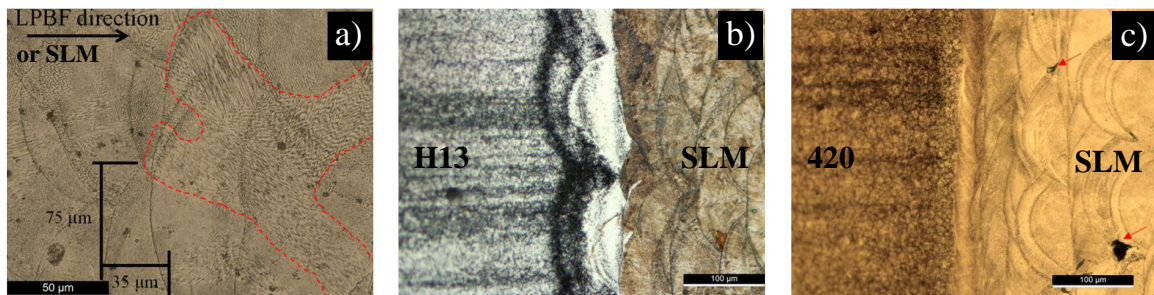


Figure 3.9: Microstructure of the SLMed 18Ni300 material with a red boundary around acicular structure (a); interface of H13 material with the SLMed material (b); interface of 420 material with the SLMed.

Similar microstructures were found for the different specimen formulations of the SLMed material, if built under the same conditions (parameters/scan speed), even for the hybrid formulations.

3.3. Monotonic Mechanical Properties

The assessment of mechanical properties of all specimens was done by monotonic tensile tests in an Instron Electropuls E10000 machine running at a speed of 2 mm/s and at room temperature, with round "bone" like shaped specimens, see Figure 2, Appendix I and Figure 1, Appendix II.

The load-strain curves resulting from the tests were plotted and can be seen, for the fully SLMed specimens and for the hybrid ones, in Figure 3.10. The behaviour of the material curves is similar to the ones from the metal alloys, starting with an initial linear region, followed by a non-linear

one. In the fully SLMed specimens, it is possible to observe a decrease in the mechanical properties due to the increased porosity, consequence of the scanning speed increase from 200 to 400 and to 600 mm/s. This porosity is affecting the specimens' cross-section area, leading to a drop in the ultimate tensile stress from 1147 ± 13 MPa (200 mm/s) to 612 ± 22 MPa (600 mm/s), and a drop of the Young's modulus from 168 ± 29 GPa (200 mm/s) to 104 ± 38 GPa (600 mm/s), see Table 3.4. Another big contribution to the degradation of the mechanical properties comes from the irregular (3D) porous shape in association with the porous growing effect from the increasing scanning speed, which leads to an increase of the stress concentration.

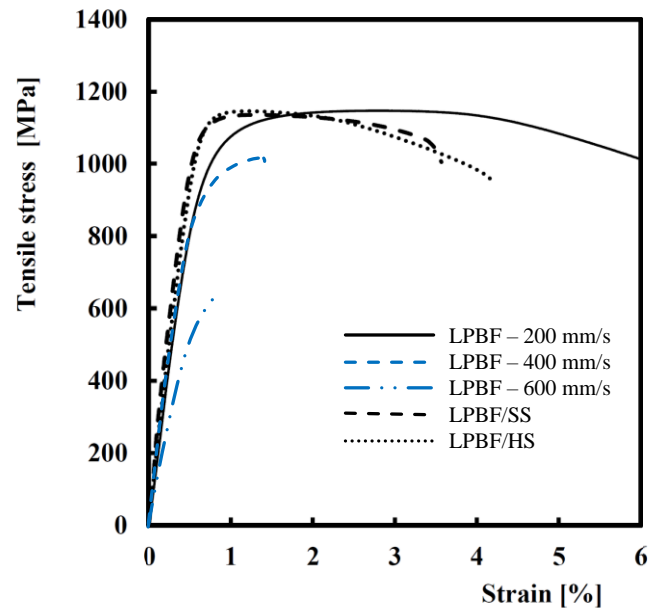


Figure 3.10: Monotonic tensile load-strain curves of the different specimen formulations.

Regarding the mechanical properties of the hybrid formulations, three valid samples and tests were used to achieve each curve. These have a global stiffness higher than the fully SLMed specimens, because the recorded strain is an average value assessed with an extensometer roughly in the middle of the interface region. This interface region is characterized by having a steel base made from different alloys with higher stiffness/Young's modulus than the SLMed material and the bases materials have similar stiffness (AISI 420 and the AISI H13). On the other hand, the strain at failure is lower for the hybrid specimens but, the ultimate tensile stress is similar for all the formulations, hybrid and fully SLMed, because the rupture always happened in the SLM material. Check Table 3, Appendix II.

Young's modulus was calculated by linear regression of the stress-strain curves of the linear region, having a correlation coefficient higher than 99.5%. The ultimate tensile strength corresponds to the maximum stress achieved on the stress-strain curves.

3.4. Fatigue Assessment

All the following fatigue tests were performed for the SLMed material with the lowest porosity, built at 200 mm/s, including the hybrid formulations. The fatigue endurance tests were performed under two different conditions, at constant amplitude under sinusoidal load and under sinusoidal displacement. Both tests were carried out with a frequency varying from 15 to 20 Hz. Fatigue tests were performed for all 3 different specimen formulations under pulsating tensile loading ($R = 0$) and depicted as the initial nominal stress range versus the number of cycles to failure. The respective $S-N$ curves can be seen at Figure 3.11 for the full SLMed specimens.

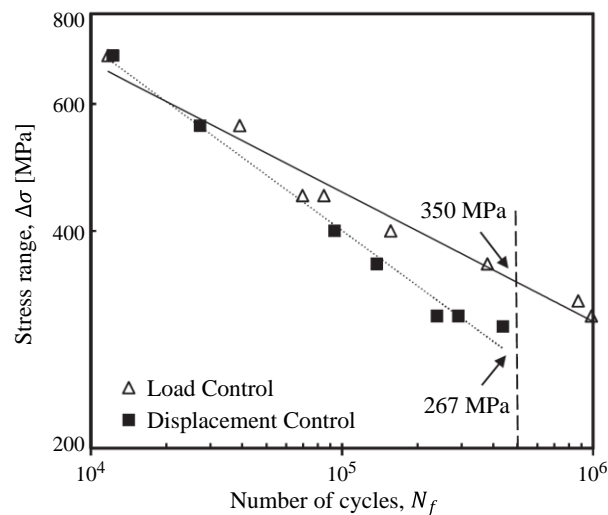


Figure 3.11: Comparison between $S-N$ curves under Load and Displacement control for the fully SLMed 18Ni300 specimen.

For the fully SLMed specimen and for short lives, the values are similar for the two conditions (under load and displacement control) but, for longer lives, the fatigue strength is 31% higher for $N = 5 \times 10^5$ cycles under load control than under displacement control.

The hybrid's specimen $S-N$ curves at Figure 3.12 obtained under load control and displacement control were respectively overlapped with the fully SLMed specimen curves for an easier comparison. In Figure 3.12 a), the life of the hybrid specimens is progressively lower than the one fully built by SLM. On the other hand, the displacement curves for the hybrid and for the fully built specimens have almost the same behaviour and fatigue life, see Figure 3.12 b).

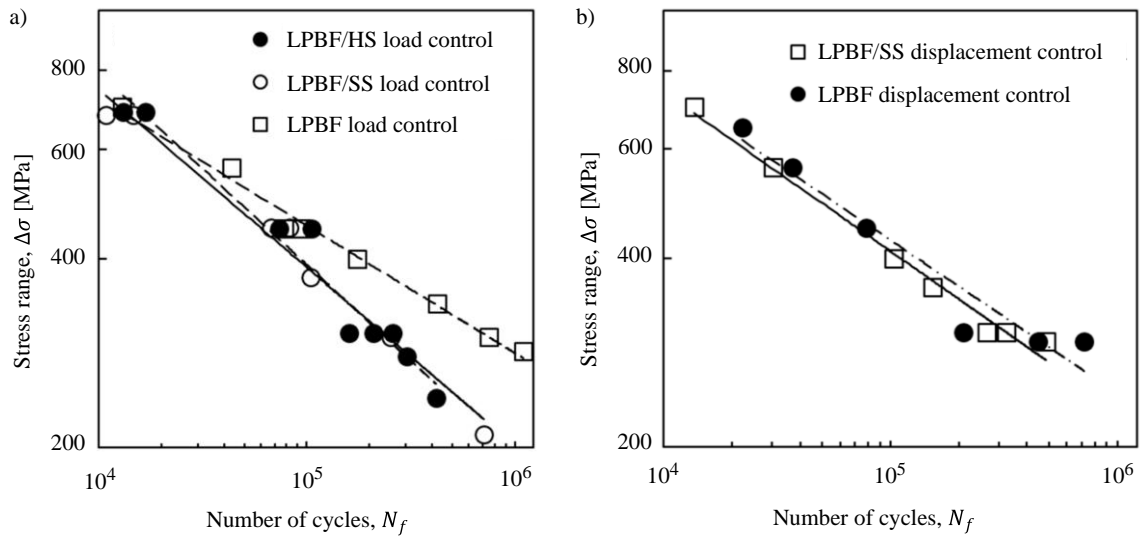


Figure 3.12: Plot of $S-N$ curves under load control (a) and displacement control (b) for fully SLMed and hybrid specimen formulations.

Like this, the fatigue life for all the SLMed material and for all the specimens' formulations is controlled by strain range. Even in the case of the hybrid formulations, their fatigue strength is not significantly affected by the fact of having a steel substrate (AISI 420 and AISI H13). The different substrates have a good adhesion on the interface, and the weakest region in terms of fatigue strength is located on the LPBF region. However, it is important to state that there was a slightly tendency to decrease the fatigue life of the specimens under displacement control, when compared with the load controlled ones. This could be explained due to the material cyclic softening, as observed on the research of Appendix III and Appendix V.

Variable fatigue tests were performed according to the previously mentioned conditions, with the exception of being just performed under variable sinusoidal loading control and with stress ranges applied in three blocks of 1000 cycles, running in a loop until the final rupture, according to the pattern in Figure 3.13.

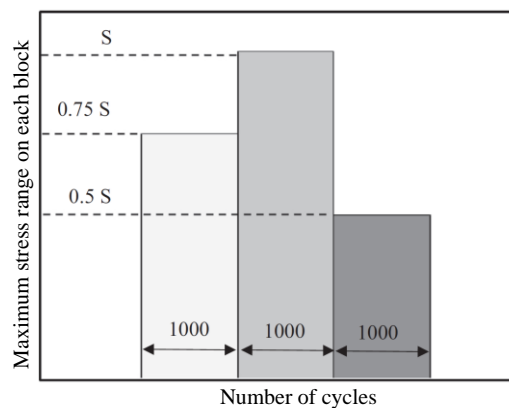


Figure 3.13: Scheme of the stress pattern loop load during the variable amplitude fatigue tests.

Miner's law was used to define an equivalent stress [Miner, 1945], enabling it to be compared with the experimental fatigue results under variable amplitude loading control but, neglecting the existence of a fatigue limit. The tests were performed and the results compare the predicted lives (N_p) from Miner's law and the experimental results under variable amplitude fatigue (N_f) for the fully SLMed and the hybrid specimens (SLM/HS and SLM/SS), Figures 3.14 a) and b) and c), respectively. The predicted lives limits were calculated and a domain was plotted according to the $N_p = 2N_f$ and $N_p = 0.5N_f$, and assumed as a criterion of prediction exactness.

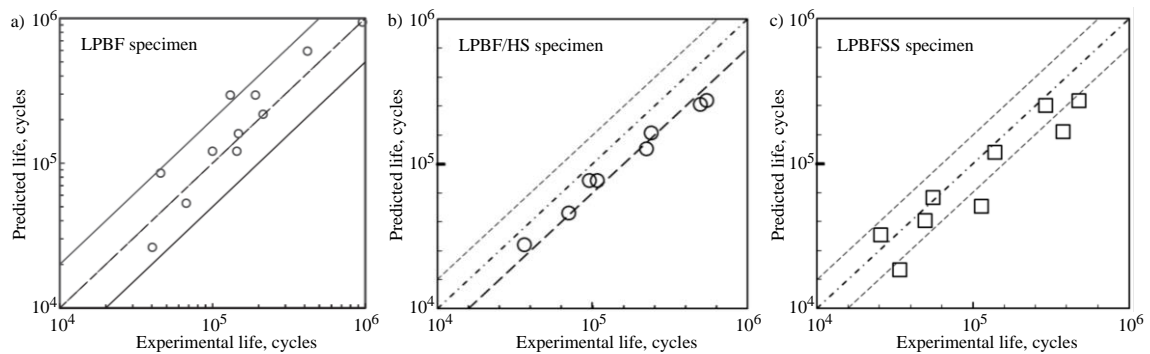


Figure 3.14: Comparison between experimental and predicted lives using Miner's law for fully SLMed specimens (a), and hybrid formulations with substrate materials in AISI H13 (b), and in AISI 420 (c).

This domain, limited by the stripes, contains the majority of the experimental points, indicating a very good agreement between the predicted and the experimental fatigue lives. Like this, it is possible to conclude that the Miner's law is suitable to predict the fatigue lives of the fully SLMed and hybrid specimens, even knowing that there is a tendency to be conservative for the LPBF/HS specimens.

3.5. Low Cycle Fatigue Assessment

Low cycle fatigue tests were performed in accordance with the ASTM E606 and run at fully-reversed strain-controlled conditions ($R = -1$), with sinusoidal waveforms, and strain amplitudes between 0.3 to 1.0%, at a constant strain rate ($d\varepsilon/dt$) of 8×10^{-3} Hz, until final rupture.

The cyclic deformation behaviour of the material is depicted at Figure 3.5, and relates the peak, mean and valley stresses with the different strain amplitudes and the life ratio.

Relative to the stress peak, it was observed that for all strain amplitudes the peak stress increases for the first 2 or 3 cycles, followed by a region of about 90% of the life ratio where the stress peak is continuously decreasing for higher strain amplitudes but which has a very stable response for low strain rates; for the last 10% of the life ratio, there is a fall in the peak stress values independently from the strain amplitudes. The mean stress is slightly decreasing throughout its life for all the strain amplitudes, but it has lower mean stresses for higher strain amplitudes. For the valley stresses, at lower strain amplitudes they are quite constant throughout the life, and at higher strain amplitudes the valley stress increases with the life ratio increases.

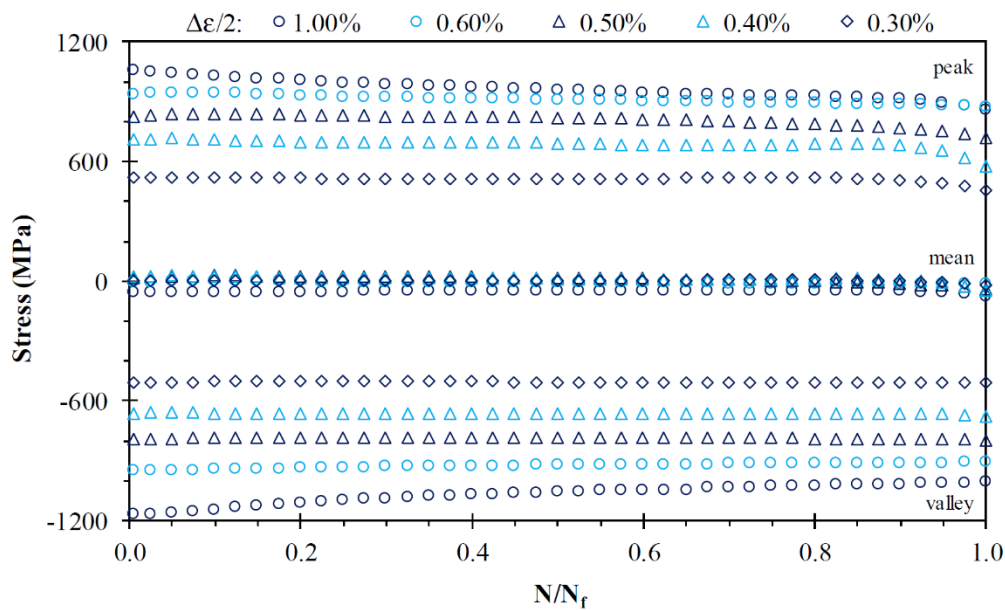


Figure 3.15: Peak, mean and valley stress variation throughout its normalized life.

The plastic strain energy density and the total strain energy density per cycle (plastic + elastic strain energy) are very stable during its life, having a softening region for the first 10% of its life rate and more expressive for higher strain amplitudes, following a quite stable (saturated) region, up to 90% of its total life rate, and in the remaining life, there are small perturbations that culminate in fatigue rupture (Figure 3.16 and 3.17). According to Smith et al, 1963, the materials that have a ratio between tensile strength and yield lower than 1.2 are cyclically softening, but for the present material we have a ratio higher than 1.26 and still, the material is softening.

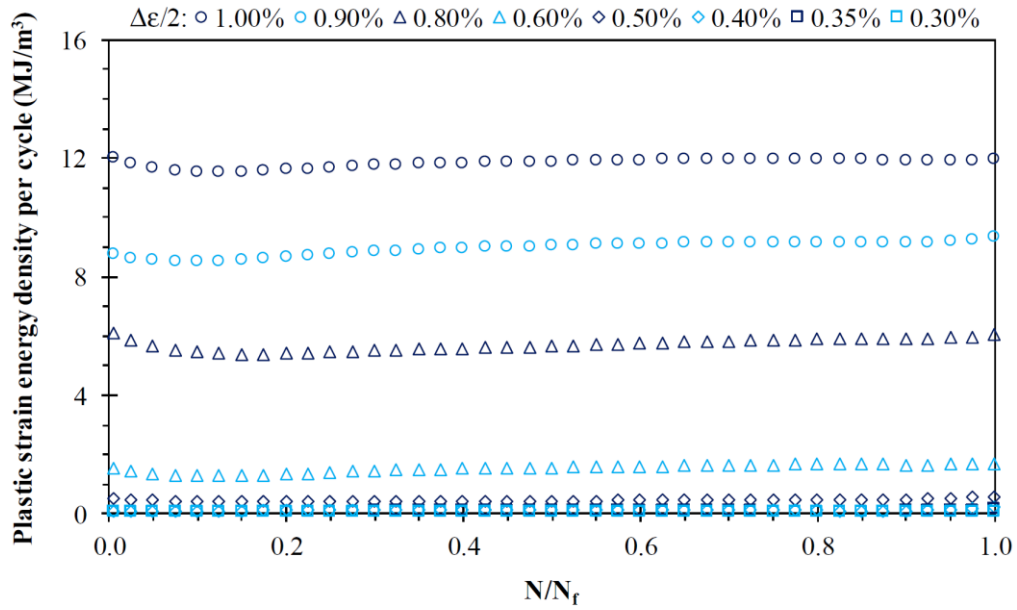


Figure 3.16: Plastic strain energy density per cycle throughout its normalized life, during low-cycle fatigue test at different strain rates.

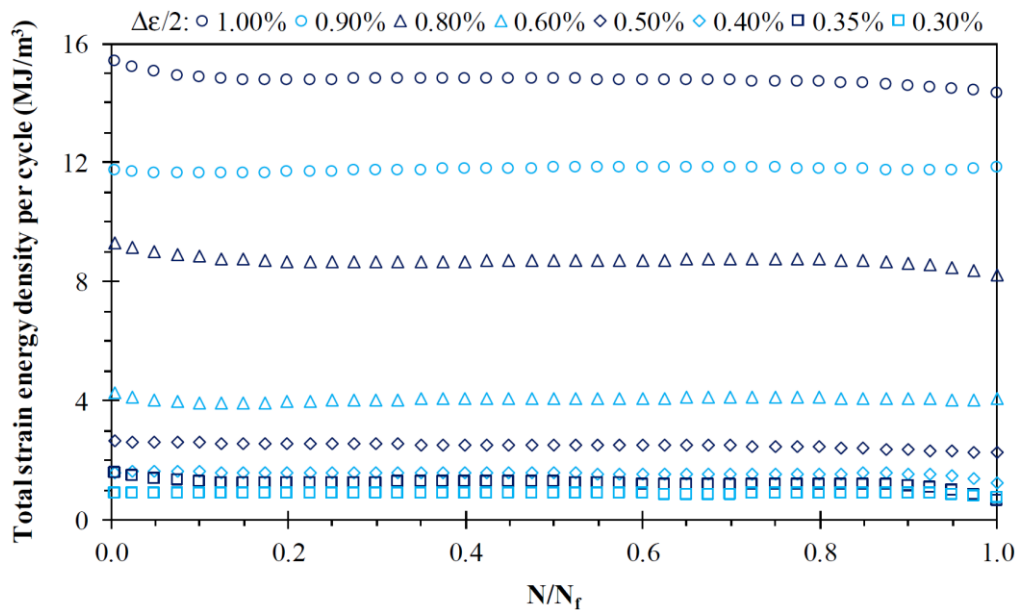


Figure 3.17: Total strain energy density per cycle throughout its normalized life, during low-cycle fatigue test at different strain rates.

Considering the previous fact that the stable hysteresis loop circuits (saturated region) are achieved in an early stage of its life, the mid-life was chosen to study and collect the experimental data from the cyclic stress-strain response of the stable region and the respective plastic and total strain energy densities, see Table 3, Appendix III.

From the data, it was possible to depict the stress-strain loops curves and, in Figure 3.18 a), the saturated cycles at relative coordinates and the lower tips tied together are represented. It can be observed that the upper branches of the hysteresis loops, at different strain amplitudes, do not form a unique curve, suggesting that the material has a non-Masing behaviour, meaning that the linear region is suffering changes. This behaviour is easily observed in Figure 3.18 b) where the upper branches of the loops are tied together, and it is possible to check that the linear region of the loops decreases and is independent of the applied strain amplitudes (loops selected from strain amplitudes higher than 0.5%), an effect normally associated with the dislocation cells' formation [Raouf *et al*, 1977]. These circuits have an area of 40% to 45% of the ideal ones (Masing behaviour).

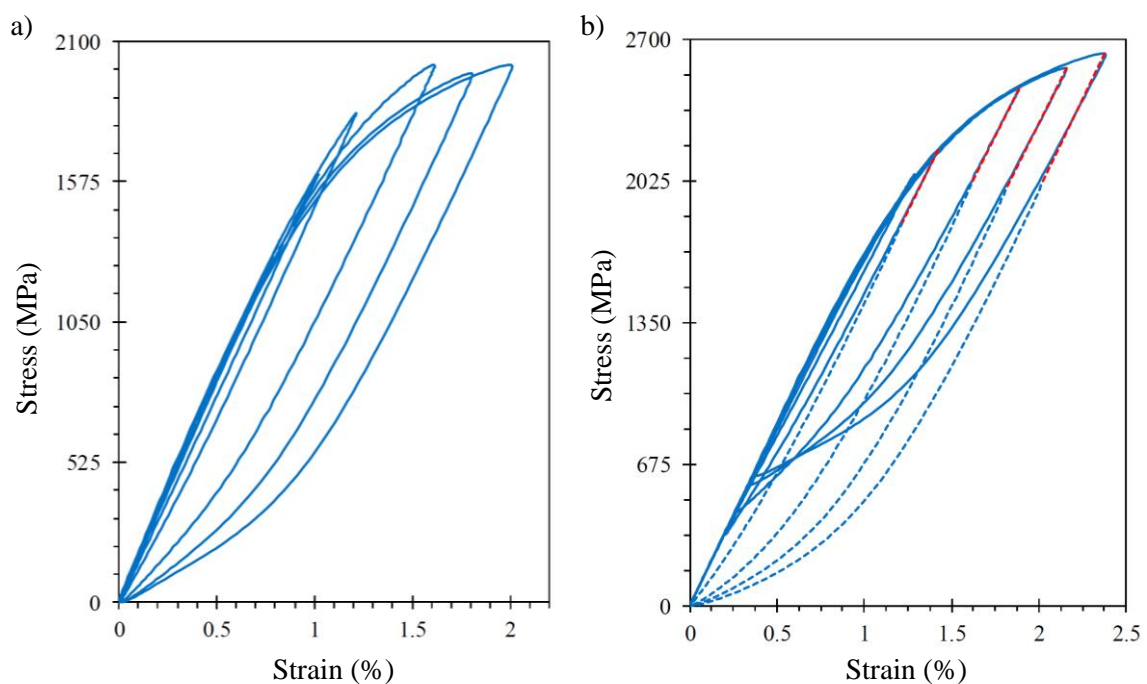


Figure 3.18: Stable mid-life circuits at different strain amplitudes with joined lower tips (a) and with merged upper branches (b).

The cyclic stress and the plastic strain amplitudes are depicted in Figure 3.19, through the relation suggested by Morrow, 1965, in Equation 11, and determining the coefficients' constants by linear regression and the least square method, achieving a correlation coefficient of $r = 0.982$, see Table 4, Appendix III.

For cyclic loading, the slopes of the hysteresis loops curves at the beginning of the loading cycle and at the load reversal could be different, because the effective elastic unloading modulus (E''), immediately after the load reversal, corresponding to the slope of the stable hysteresis loop after strain reversal, is influenced by the cyclic properties of the material (hardening or softening). This effective elastic unloading modulus, measured during the tests is represented in Figure 3.19, by the dash-dotted curve. According to the literature [Branco, 2016; Ellyin, 1997; Kujawski, 1987],

it is possible to define a relationship between the cyclic stress amplitude against the elastic strain amplitude through a power law, Equation 11. The corresponding “effective” coefficients were calculated by a best fit technique with a correlation factor of $r = 0.998$. For clarity and comparison, the linear relationship was calculated using the Elastic Modulus (E), showing a variation of the unloading modulus with the strain amplitude, revealing the nonlinear behaviour on the plastic regime but also in the elastic regime, see Figure 3.19.

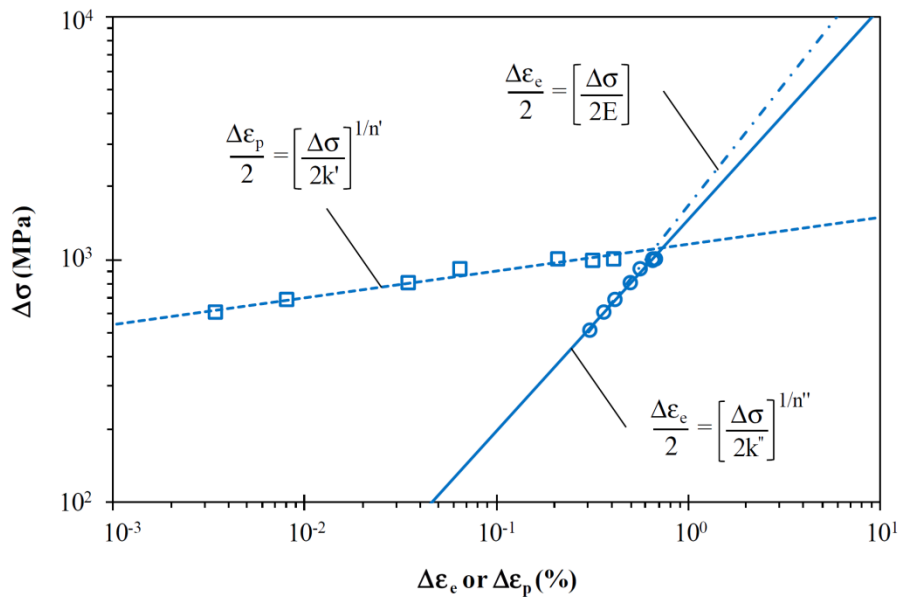


Figure 3.19: Relation between the cyclic stress amplitude and the plastic and elastic strain amplitude, using the unloading modulus resulting from the tests and depicted by the dashed line, the Young’s Modulus (E) resulted from the monotonic tensile tests, depicted by the dashed-dot line.

Through the Equation 12, as suggested by Ramberg-Osgood, it is possible to depict the cyclic stress-strain curve, Figure 3.20, showing that the cyclic behaviour of the material is always below the monotonic curve, an effect caused by the material softening. Despite the softening behaviour, the degree of softening is always different, but with a relatively small degree of softening. The region where the softening degree was higher is located between strain rates of 0.5 and 1.2%, a value at which the softening degree is already decreasing.

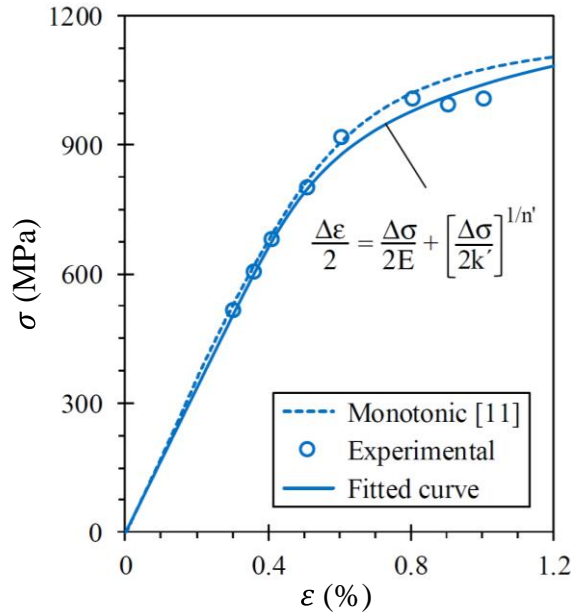


Figure 3.20: Comparison between the monotonic tensile stress-strain curve and the cyclic stress-strain curve, enlightening the softening of the AISI 18Ni300 SLMed material.

The strain-life relation of the elastic, plastic and total strain amplitudes are depicted in Figure 3.21 and were calculated based on the Basquin-Coffin-Manson relation, according to Equation 15. The missing values were calculated by linear regression. The transition life is relatively short, 35 reversals, when compared with the transition life of conventional materials with similar monotonic properties ($2N_T = 3038$ reversals), a difference of about 2 orders of magnitude [Branco *et al.*, 2012].

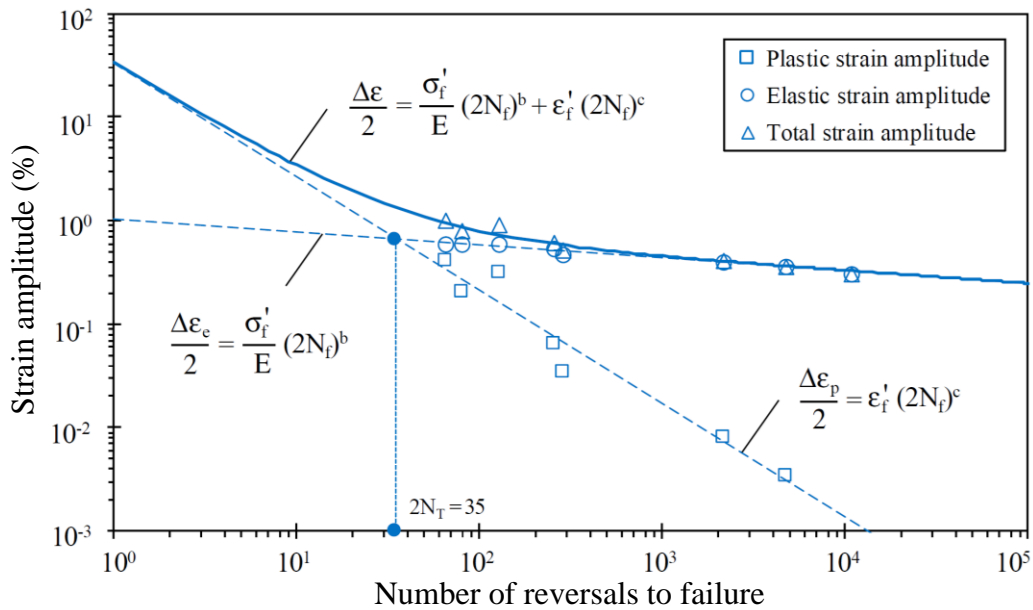


Figure 3.21: Plastic, elastic and total strain amplitude against number of reversals to failure.

The energy-life relation method states that the dissipated strain energy density per cycle contributes to the fatigue damage. Due to the properties of the material, which has a plastic strain and total relatively constant strain energy densities (see Figure 3.9 and 3.10), making it possible to directly estimate the cumulative fatigue damage by the means of the energy dissipation, see Equation 26.

$$\Delta W_p = kp(2N_f)^{\alpha p} \quad (26)$$

where,

- kp and αp – fitting constants

The relation between the plastic strain energy density and the number of cycles to failure in the mid-life cycle, can be described by a power law, and was demonstrated by [Lefebvre *et al*, 1984] for non-Masing materials. This should be used for high strain levels, because it could mislead the fatigue life assessment of materials close to the fatigue limit. On the other hand, the total strain energy density, depicted in Figure 3.15, according to Equation 27, which results from the sum of the plastic and the elastic strain energies densities of the mid-life hysteresis loops, have a good fit with experimental data, and can be used to assess the fatigue life in low and high-cycle fatigue regimes, even being sensitive to the mean-stress. This method was successfully applied in U-notched round bars tested under bending-torsion loading by Branco *et al*, 2017.

$$\Delta W_T = kt(2N_f)^{\alpha t} + \Delta W_0^{e+} \quad (27)$$

where,

- kt and αt – constants
- ΔW_0^{e+} – tensile elastic energy at the material fatigue limit estimated here at $2N_f = 10^7$

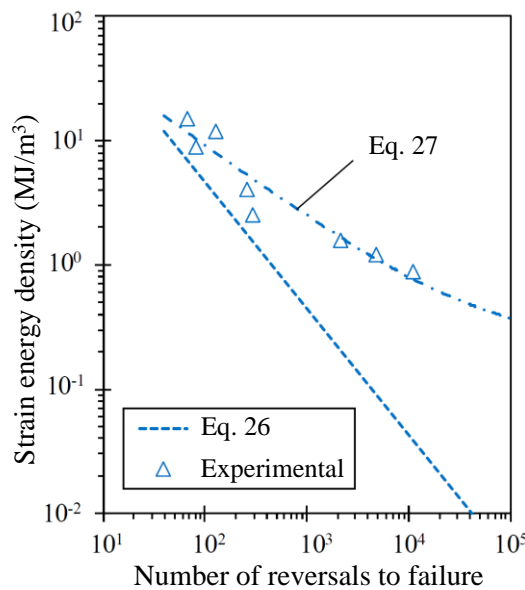


Figure 3.22: Plastic strain energy (Equation 26) and total strain energy (Equation 27) versus number of reversals to failure in the mid-life hysteresis loop.

3.6. Fatigue Fracture Analysis

Fatigue rupture always happened in the SLMed specimens. In this way, the fracture surfaces analyses are always performed on the SLMed material for the specimens built with a scan speed at 200 mm/s. Fatigue fracture surfaces were analysed with the help of SEM, and it was possible to observe that the crack growth initiated from defects on the external surface, and internally near to the surface, propagating through the cross section. Another factor that helps to raise the cracks around the surface is the residual tensile stress near the surface, inherent to the AISI 18Ni300 powder alloy when processed by SLM under these conditions, as assessed on Appendix V.

The rupture surfaces resulted from fatigue tests under load control at constant amplitude (Figure 3.23), and the ones resulting from the low-cycle fatigue under fully-reversed strain-control at 0.60% strain amplitudes (Figure 3.24), showed multi-nucleation in the grand majority of the cases (Figure 3.23 a) and 3.24 a)) and propagation through different layers, revealing a morphology/texture produced by the shape and orientation of the particles due to the laser scan cross hatch pattern created during the melting process. All the cracks propagated by mixed mode (intragranular and intergranular) and the fatigue crack initiation process are predominantly growing by brittle mode (Figure 3.23 b)) with associated cleavage (transgranular mode) and some ductile dimples.

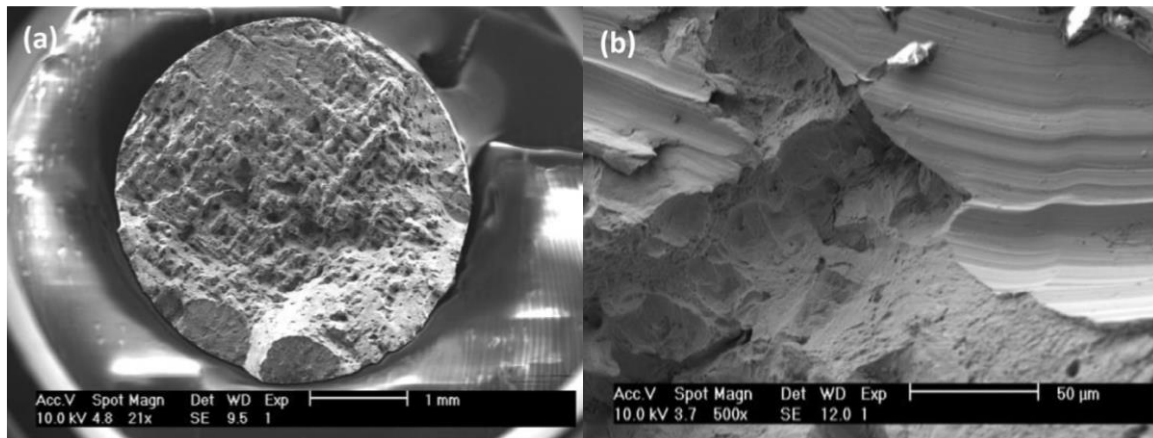


Figure 3.23: Fracture surfaces resulting from fatigue tests; in a) the fracture surface is revealing the cross-hatch texture done by the laser scanning strategy and in b) it is possible to observe the brittle crack propagation facets.

However, the inner cross section reveals mainly a ductile fracture mode formed by ductile dimples and microvoids. Overall, the crack initiates due to material defects in the subsurface from the SLM process, like voids and unmolten particles acting as crack initiation points, and growing across the section, mainly by ductile mode, and at the same time between the deposited layers by cleavage, driven by the presence of defects that acts as a stress intensity factor riser.

The main observed defects arise due to process limitations (parameters, process stability, spatters, gas flow, powder, and so on), which leads to process instabilities and could result in the lack of penetration of the laser beam (3.24 b)), missing the conditions to create a perfect melt pool of metal, originating micro-voids and unmolten material (3.24 d)), see Figure 3.24.

From the observation, there seems that there is no influence from the kind of fatigue test that was performed, even with different specimens' geometries. The only thing that could have some differences is relative to the central cross section, which corresponds to the predominant ductile mode region, which is smaller in Figure 3.23 a) when compared to Figure 3.24 a). Of course, we must take into account that the cross section of specimen in Figure 3.24 a) has more than twice the area of the one from 3.23 a).

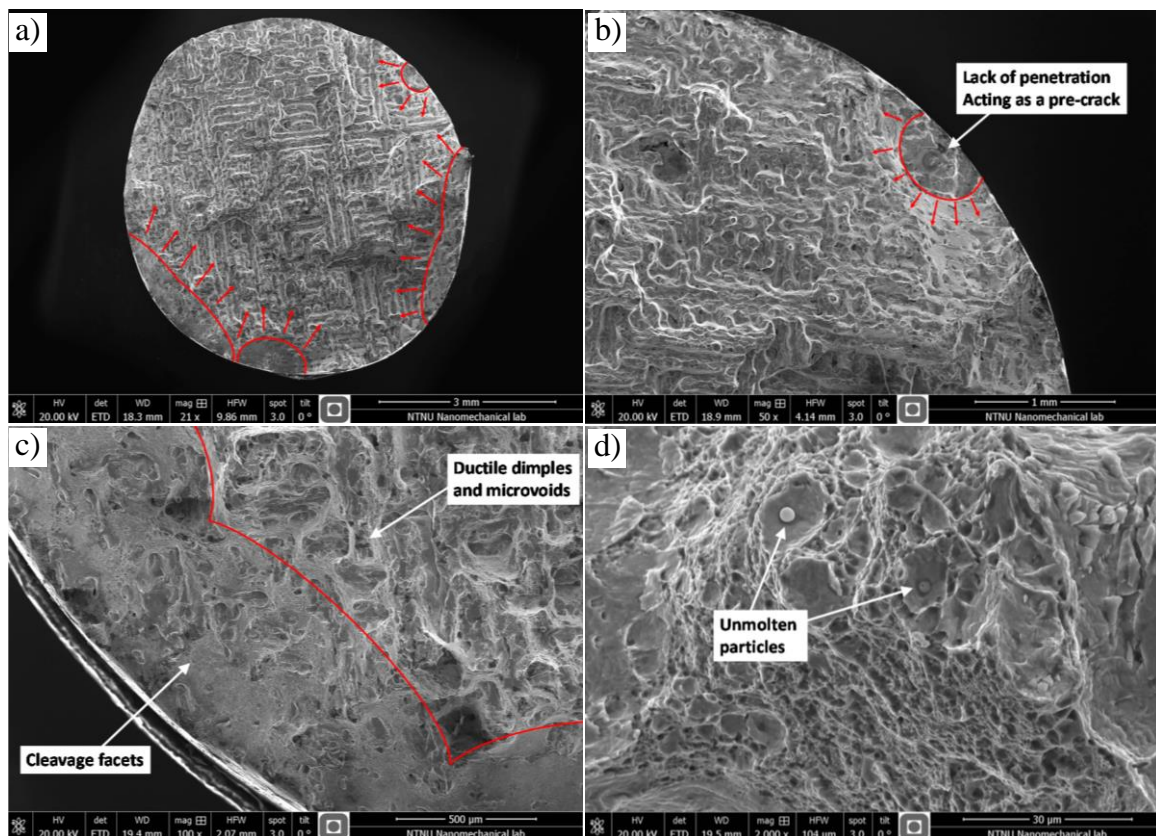


Figure 3.24: Fracture surfaces resulting from the low-cycle fatigue tests; a) multi-nucleation cracks; b) crack nucleation on lack of penetration defect; c) crack propagation by mixed mode, starting with brittle fracture and passing to ductile fracture when growing in the direction of the specimen's center; d) unmolten particles defect.



Contents lists available at ScienceDirect

Theoretical and Applied Fracture Mechanics

journal homepage: www.elsevier.com/locate/tafmec



Fatigue behaviour of selective laser melting steel components



L.M.S. Santos^a, J.A.M. Ferreira^{a,*}, J.S. Jesus^a, J.M. Costa^a, C. Capela^{a,b}

^aCEMUC, Mechanical Engineering Department, University of Coimbra, Rua Luís Reis Santos, 3030-788 Coimbra, Portugal

^bMechanical Engineering Department, ESTG, Polytechnic Institute of Leiria, Portugal

ARTICLE INFO

Article history:

Received 14 May 2016
Revised 27 July 2016
Accepted 19 August 2016
Available online 24 August 2016

Keywords:

Laser sintering metal
Fatigue
Functional materials
Mechanical properties
Structural Integrity

ABSTRACT

Selective laser melting (SLM) is a laser based rapid manufacturing technology that builds metal parts layer-by-layer using metal powders and a computer controlled laser. Various important aspects strongly affect the mechanical properties of sintered metal components, such as: porosity, surface roughness, scan speed, layer thickness, and residual stresses. Therefore, properties of SLM manufactured parts must be carefully analysed, particularly under fatigue conditions.

The purpose of this work was to study the effect of scan speed, porosity and microstructure on the mechanical properties and fatigue strength of sintered laser samples. Sintered laser parts were manufactured in maraging steel AISI 18Ni300. Fatigue behaviour is related to process parameters, such as: surface residual stresses, microstructure and porosity.

The results showed that a very high scan speed (400 or 600 mm/s) causes the appearance of high percentages of porosity and a consequent drastic reduction of tensile strength and stiffness. Fatigue behaviour was assessed in terms of the traditional S-N curves and of the $da/dN-\Delta K$ crack propagation curves. Fatigue life predictions based on Hartman and Schijve's equation underestimated significantly fatigue lives, particularly for low stress levels. The results of the tests performed at variable amplitude loading were well fitted by Miner's law.

© 2016 Elsevier Ltd. All rights reserved.

1. Introduction

Selective laser melting (SLM) is a laser based rapid manufacturing technology that builds metal parts layer-by-layer using metal powders and a computer controlled laser [1,2]. A high power laser is used to fuse metallic powder particles, doing a scan of the transversal cross sections of the final component generated from a CAD model. After the consolidation of one powder layer, a fresh layer of powder is deposited and the laser melting process is repeated until a 3D part is completed. This technique is increasingly used in automotive, aerospace, medical and of injection moulds industries, to obtain components with complex shapes. Abundant literature has been previously reported on the scope of SLM using different metal powders, for instance, the fabricating of titanium [3,4], iron-base alloys [5–8], nickel-base alloys [9,10], copper-base alloys [11], titanium-base alloys [12] and metal matrix composites [13].

SML products could show characteristic cast structure, with high superficial roughness, presence of porosity, heterogeneous microstructure and thermal residual stresses, resulting in mechan-

ical properties which can be improved by additional post-processing treatments. Since SLM can be used to manufacture functional components, a good characterization of the sintered parts is essential to control structural integrity, and to guarantee that the components fulfil the final functional requirements. Some scientific and technical aspects of SML sintered microstructure on the mechanical properties have not been well studied and need be yet understood. Sintered materials are usually anisotropic and heterogeneous [14,15], which affects their performance. Earlier studies mainly focused on the influence of sintering parameters and the selection of metal powder on the microstructure of the sintered parts. Scarce information has been published on fatigue properties of laser sintered materials [16,17], particularly thermal fatigue [18]. Thermal fatigue cracking (or heat checking) is one of the most important failure mechanisms in hot working applications. The main reason for heat checking is rapid alternation of surface temperature, which induces stresses high enough to impose an increment of plastic strain [19].

It has been reported that both powder characteristics (e.g., particle shape, size and its distribution, and component ratio) and processing parameters (e.g., laser power, scan speed, scan line spacing, and powder layer thickness) influence the sintered microstructures [20]. Mechanical properties are mainly affected by parameters

* Corresponding author.

E-mail address: martins.ferreira@dem.uc.pt (J.A.M. Ferreira).

such as: porosity, surface roughness, scan speed, layer thickness, and residual stresses. Internal stresses resulting from steep temperature gradients and the high cooling rates during the processing need also to be taken into account when evaluating the performance of parts manufactured from any metallic powder using selective laser melting process [21]. A major drawback is the occurrence of pores originating from initial powder contaminations, evaporation or local voids after powder-layer deposition [21–24], which act as stress concentrators leading to failure, especially under fatigue loading [25].

The focus of this work is to produce and investigate the fatigue performance of maraging steel specimens obtained by laser sintering. Fatigue tests under constant amplitude and block loadings were carried out. Failure mechanisms and microstructures were analysed in detail. Fatigue life predictions will be performed based on a fracture mechanics approach, and validated by comparison with the experimental results.

2. Materials and testing

The samples were synthesized by Lasercusing®, using the equipment of the brand “Concept Laser” and model “M3 Linear”, shown in Fig. 1(a). This apparatus comprises a laser type Nd:YAG with a maximum power of 100 W in continuous wave mode and a wavelength of 1064 nm. The samples were manufactured with layers growing towards the direction corresponding to the application of load for the mechanical tests, as it is shown in Fig. 1(b) using the sintering scan speeds: 200, 400 and 600 mm/s. The test series are identified by the sample code ST followed by the scan speed. Fig. 1(c) shows some round samples after they have been sintered and their surface mechanically polished.

The sintered laser parts were manufactured in maraging steel AISI 18Ni300, with the chemical composition, according to the manufacturers, indicated in Table 1.

Two types of samples were used: round specimens for tensile and fatigue life tests and compact tension specimens (CTS) for fatigue crack propagation tests, with the geometry and dimensions indicated in Fig. 2(a) and (b), respectively.

The tensile and fatigue endurance tests were carried out at room temperature using a 10 kN capacity Instron Electropuls E10000 machine. Tensile tests were performed with the same machine at room temperature using a testing speed of 2 mm/min. Two types of fatigue endurance tests were performed: at constant amplitude sinusoidal load and constant amplitude sinusoidal displacement; both with a frequency within the range of 15–20 Hz and fatigue ratio of $R = 0$. Variable amplitude loading tests were carried out using the looping loading schematically shown in Fig. 3, composed by three blocks with a stress ratio of $R = 0$, applied during 1000 cycles each one. Fig. 3 also shows the sequence of the

stress range applied during each block, which was repeated until final failure.

Fatigue crack growth tests were conducted, in agreement with ASTM E647 standard, using compact tension specimens (CTS) shown in Fig. 2(b). Experiments were performed in a servo-hydraulic INSTRON, a closed-loop mechanical test machine with a 100 kN capacity, interfaced to a computer for machine control and data acquisition. All tests were conducted in air, at room temperature and with a load frequency of 15–20 Hz. The crack length was measured using a travelling microscope ($45\times$) with an accuracy of 10 μm . The tests were performed in load control mode at $R = 0.05$. Crack growth rates under constant amplitude loading were determined by the incremental polynomial method using five consecutive points.

3. Results and discussion

3.1. Metallography and porosity

Cross and long sectioning of the samples, were observed in microscope in order to identify the microstructure, as well as the presence of porosity. The samples were prepared according to the standard metallographic practice ASTM E407-99; a chemical attack Picral (picric acid solution 4% in ethyl alcohol) was performed for two minutes. After preparation, the samples were observed using a Leica DM4000 M LED optical microscope.

Fig. 4(a) and (b) shows metallography in longitudinal sections of single sintered samples, for a 200 and 400 mm/s scan speed, respectively, in which it is not noticeable a significant difference in the size and shape of the grains for different scan speeds. However, it is all too evident a significant increase of porosity with the scan rate. A more amplified image of microstructure obtained for a 400 mm/s scan speed is shown in Fig. 4(c) suggesting the existence of a significant number of small porosities and the formation of martensitic needles.

The quantification of the level of porosity was done by analysing the images contrast between the pores and the base material in the photographs by optical microscopy using image processing software Image J. The program creates a border with a blank line and calculates the area of each of these zones. Fig. 4(d) shows an example of an image created by the software. The sum of these areas gives the total porosity of the image. Table 2 shows the values of the porosity in percentage obtained for each batch. A second way to analyse the porosity was performed based on the samples density. The corresponding densities for each scan speed were calculated according to the Archimedes principle (and are also summarised in Table 2). Based on these densities, the porosity can be quantified in comparison with the reference formulations. The reference formulation here considered was the sintered

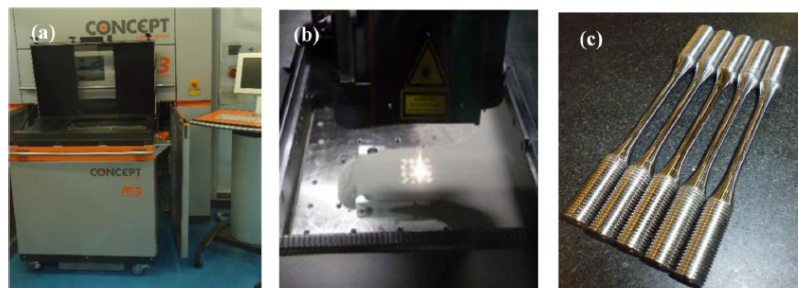


Fig. 1. SLM manufacture process: (a) Machine; (b) Melting process; (c) Sintered and polished samples.

Table 1
Chemical composition of the materials.

Steel	C	Ni	Co	V	Mo	Ti	Al	Cr	P	Si	Mn	Fe
18Ni300	0.01	18.2	9.0	–	5.0	0.6	0.05	0.3	0.01	0.1	0.04	Balance

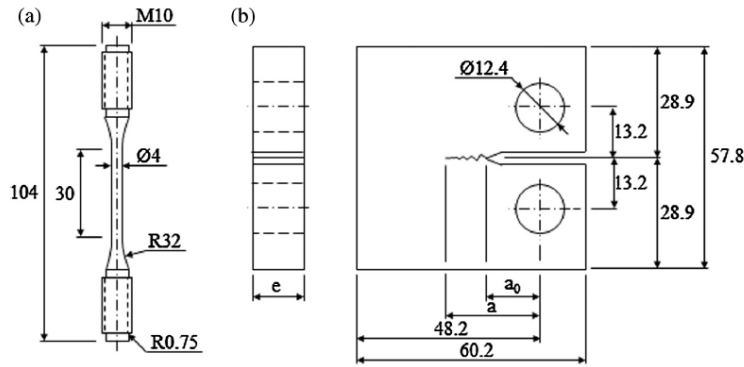


Fig. 2. Geometry and dimensions of the specimens for: (a) Fatigue life; (b) Fatigue crack propagation.

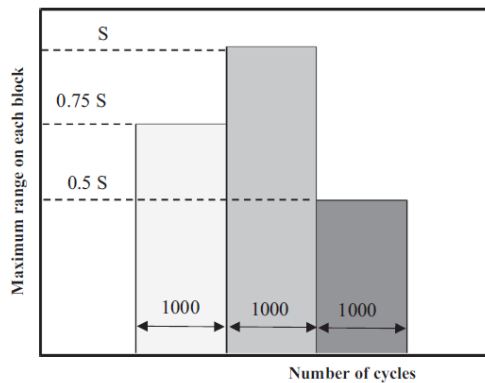


Fig. 3. Variable amplitude looping load.

material produced with the scan speed of 200 mm/s assuming its low porosity values. This method allows to obtain values based on a volumetric analysis (3D), i.e. with a greater accuracy (and in this case significantly lower in consequence of the porous shape) than the former method that uses an analysis in a plane (2D).

Vickers hardness testing was performed according to ASTM E384-11e1 using a Struers Duramin 1 microhardness tester with a 0.5 kg load and 0.5 mm between indentations. The measurements were performed at random locations, and the values of average and standard deviations are also indicated in Table 2. Increasing the scan speed produces only a slight reduction in hardness and an increase in dispersion.

3.2. Mechanical properties

Fig. 5 shows representative load–displacement curves obtained for single sintered specimens for different scan speeds. The typical metallic behaviour showing an initial linear region followed by a

non-linear behaviour was observed. The increase of the sintering scan speed was associated to an increase of the porosity level (particularly the porous size), causing a drastic reduction of the ultimate stress and of the Young's modulus, in consequence of the decrease of the transverse area and the increase of stress concentration.

Ultimate strength was calculated as the maximum stress obtained using peak load of the load versus displacement curves. The Young's modulus was obtained by linear regression of the stress–strain curves considering the larger range corresponding to a correlation coefficient higher than 0.995%.

Table 2 also summarizes the mechanical properties obtained for the three specimens configurations.

3.3. Fatigue results

The fatigue results obtained under pulsating tensile loading, analysed in terms of the stress range against the number of cycles to failure, are depicted in Fig. 6 for single sintered material, manufactured with 200 mm/s scan speed. Two batches of results are shown: control loading tests, and control displacement tests. The analysis of the figure indicates that for short lives the fatigue strength of the two types of tests is similar. However, for longer life, the fatigue strength of control load tests is higher than that of displacement control samples achieving an increment in the order of 31% for $N = 5 \times 10^5$ cycles.

The results of the fatigue crack growth for $R = 0.05$ are presented in Fig. 7(a), which shows crack growth rate da/dN against the range of the stress intensity factor ΔK . The analysis of these results shows two crack propagation regimes: near the threshold with high influence of ΔK value and afterwards a log-linear region quantified by Paris law. Both, the threshold value, ΔK_{th} , and the Paris law are superimposed in Fig. 7(a). The crack propagation results were also analysed, considering the two regions, using the Hartman and Schijve Eq. (1) [26]. Lateral face was subjected to a chemical attack Picral for two minutes and afterwards observed in the microscope Leica DM4000 M LED to highlight the microstructure and analyse the crack path. Fig. 7(b) shows one of these macrographs, indicating that the propagation of the crack

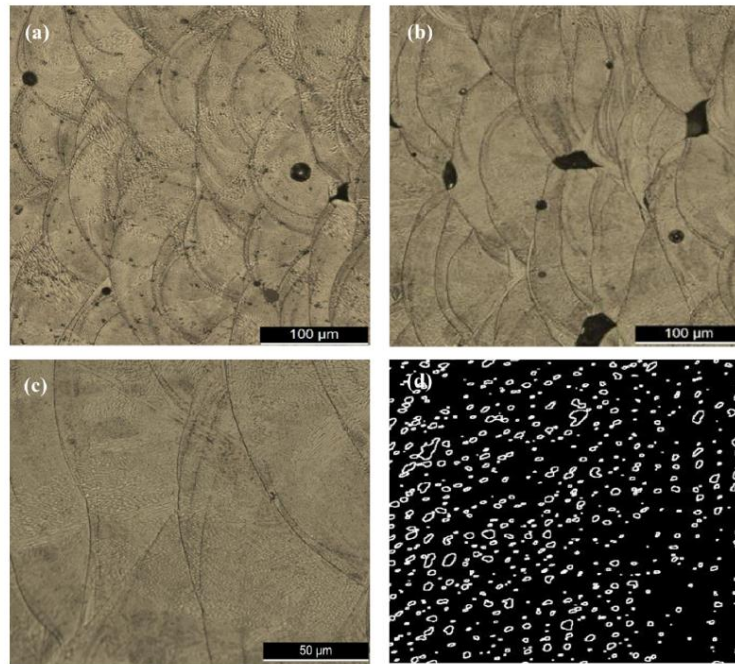


Fig. 4. Microstructure and porosity: (a) Laser scan speed 200 mm/s; (b) Laser scan speed 400 mm/s; (c) Amplified image; (d) Image J pattern.

Table 2
Mechanical properties.

Scan speed, mm/s	Porosity, %	Density, g/cm ³	Hardness HV1	Young's modulus, GPa	Tensile strength, MPa	Strain at failure, %
200	0.74 ± 0.09	7.42	354 ± 5	168 ± 29	1147 ± 13	5.12 ± 0.001
400	7.37 ± 0.99	7.29	348 ± 6	155 ± 30	1032 ± 27	1.45 ± 0.01
600	10.38 ± 2.88	7.14	341 ± 8	104 ± 38	612 ± 22	0.71 ± 0.002

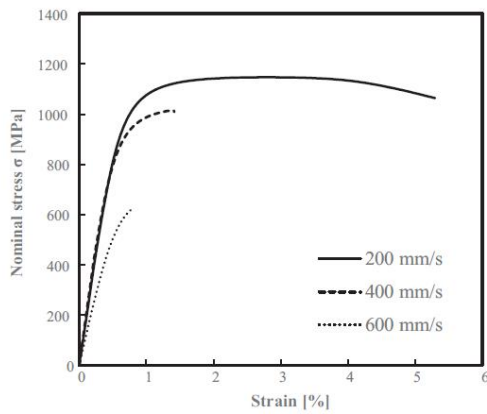


Fig. 5. Example of tensile curves.

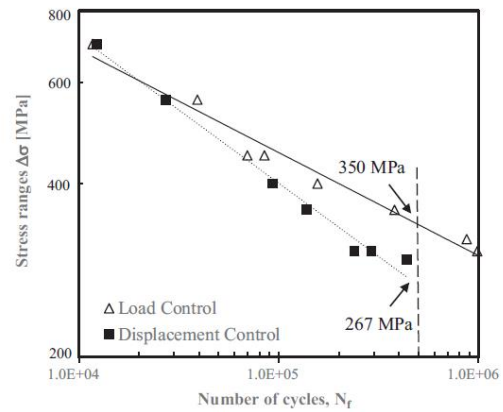


Fig. 6. S-N curves for constant amplitude tests.

is primarily transgranular, being the path constrained by the presence of the pores.

$$\frac{da}{dN} = C(\Delta K - \Delta K_{th})^m \quad (1)$$

The coefficients obtained for Eq. (1), were: $C = 1 \times 10^{-6}$; $m = 1.73$, using da/dN in mm/cycle and ΔK in $\text{MPa}\sqrt{\text{m}}$. Based on Eq. (1) fatigue life was predicted by integration between the initial crack

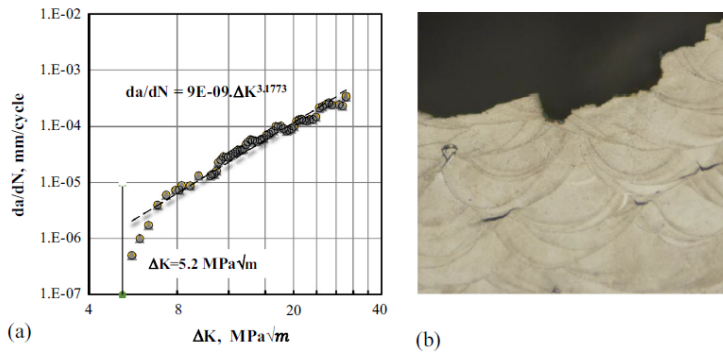


Fig. 7. (a) Fatigue crack propagation curve; (b) Crack path.

(the porous size) and a final crack size at failure, assumed half diameter. Previous porous size analysis, based on Image J software, allowed to obtain the individual porous area. Assuming a circular porous shape; for the samples with sintering scan speeds of 200 mm/s it was obtained a $20.5 \pm 6.7 \mu\text{m}$ porous diameter.

The influence of the crack size on the propagation threshold of short fatigue cracks under pulsating loads ΔK_{th} ($a, R = 0$) can be satisfactorily modelled using the El Haddad-Topper-Smith (ETS) modified stress intensity factor, to describe the fatigue propagation of any, short or long crack, which is estimated from Eq. (2) [27].

$$\Delta K^* = \Delta \sigma \sqrt{\pi(a + a_0)} \quad (2)$$

where,

$$a_0 = \frac{1}{\pi} (\Delta K_0 / \Delta S_0)^2 \quad (3)$$

where $\Delta \sigma$ is the nominal axial stress range, a is the crack size, a_0 is the crack size correction, ΔK_0 is the threshold for long cracks and ΔS_0 is the fatigue limit for short cracks ($a \rightarrow 0$).

The predictions based on Hartman and Schijve's equation were compared with experimental results in Fig. 8, for an initial crack size of 20 μm . In order to analyse the prediction accuracy, two straight lines were used: prediction lives equal to the experimental lives, and experimental lives equals to 10 times the expected life, were also superimposed in the figure. The analysis of this figure

indicates that predictions underestimated significantly fatigue lives, particularly for low stress levels, which is associated with increased fatigue life initiation.

The results of variable amplitude loading tests were summarized in Table 3, where the stress range of each block and the number of cycles to failure are indicated. These results were analysed in terms of the experimental values, N_f , and of the predictions based on Miner's law, N_p . Fig. 9 shows the predicted fatigue life against experimental values. In order to have a criterion of prediction

Table 3
Variable amplitude tests.

Test number	Stress level 1 (MPa)	Stress level 2 (MPa)	Stress level 3 (MPa)	Fatigue life (cycles)
St 01	525	700	350	40,329
St 02	450	600	300	67,247
St 03	405	540	270	45,726
St 04	375	500	250	99,958
St 05	375	500	250	144,162
St 06	353	470	235	147,731
St 07	315	445	210	214,227
St 08	310	410	210	190,840
St 09	310	410	210	130,836
St 10	260	350	210	418,673
St 11	250	300	210	996,490

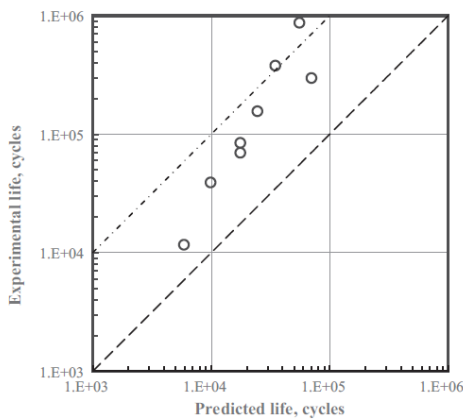


Fig. 8. Comparison of the predicted and experimental fatigue lives.

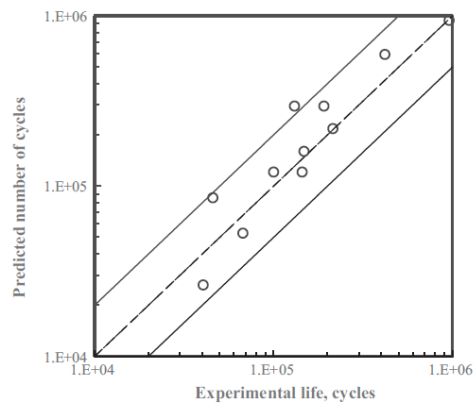


Fig. 9. Miner's law predictions versus experimental variable amplitude lives.

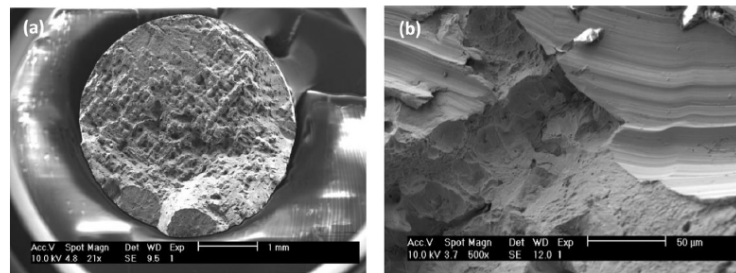


Fig. 10. SEM observations: (a) Multicracking; (b) Failure modes.

exactness, two straight lines $N_p = 2N_f$ and $N_p = 0.5N_f$ were also plotted and used as limits. The predictions agree very well to the experimental results since the points are mainly between the two straight lines, which is usually considered as a correspondent for a very good agreement.

Finally, a fracture surface analysis was performed with a scanning electron microscope (Philips XL30). Fig. 10 shows two examples of SEM images, obtained from one sample tested in load control at constant amplitude for an equivalent stress range 511 MPa. The fracture surface analysis showed that, in all specimens, the crack initiated around the specimen's surface, and propagated through the cross section. In many cases a multi-nucleation was observed, as shown in Fig. 10(a). Brittle crack propagation was the main mechanism observed in all cases. Fig. 10(b) is a representative image, showing the brittle crack propagation. Fig. 10(a) is a low magnification image which reveals the texture of the cross section of the sintered test pieces, i.e. the shape and orientation of the grains deposited in each layer. The morphology shown in Fig. 10(a) shows a fracture surface with high roughness.

4. Conclusions

The present work studied the static and fatigue response of single laser sintered specimens. The main conclusions are:

- Very high scan speed (400 or 600 mm/s) causes high percentage of porosity and consequent drastic reduction of the tensile strength, stiffness and strain at failure;
- Fatigue strength for load control and strain control is similar for high stress level. However, for long lives the fatigue strength for load control tends to be quite higher than that obtained on strain control tests;
- Predominant transgranular fatigue crack propagation was observed;
- Fatigue life predictions based on Hartman and Schijve's equation, for initial crack size of 20 µm underestimated significantly fatigue lives, particularly for a low stress levels, which is associated with increased fatigue life initiation;
- The use of Miner's law for variable amplitude loadings gives very good accuracy predictions for engineering applications.

Acknowledgements

The authors would like to acknowledge the sponsoring under the project number 016713 (PTDC/EMS-PRO/1356/2014) financed by Project 3599 *Promover a Produção Científica e Desenvolvimento Tecnológico e a Constituição de Redes Temáticas* (3599-PPCDT) and FEDER funds and also EROFIO S.A. industry for the supply of the testing samples.






References

- [1] F. Abe, K. Osakada, M. Shiomi, K. Uematsu, M. Matsumoto, The manufacturing of hard tools from metallic powders by selective laser melting, *J. Mater. Process. Technol.* 111 (1–3) (2001) 210–213.
- [2] E.C. Santos, M. Shiomi, K. Osakada, T. Laoui, Rapid manufacturing of metal components by laser forming, *Int. J. Mach. Tools Manuf* 46 (12–13) (2006) 1459–1468.
- [3] X. Wu, J. Mei, Near net shape manufacturing of components using direct laser fabrication technology, *J. Mater. Process. Technol.* 135 (2–3) (2003) 266–270.
- [4] P. Fischer, V. Romano, H.P. Weber, N.P. Karapatis, E. Boillat, R. Gardon, Sintering of commercially pure titanium powder with a Nd:YAG laser source, *Acta Mater.* 51 (6) (2003) 1651–1662.
- [5] A. Simchi, H. Pohl, Direct laser sintering of iron–graphite powder mixture, *Mater. Sci. Eng. A Struct. Mater. Prop. Microstruct. Process.* 383 (2) (2004) 191–200.
- [6] A. Simchi, Direct laser sintering of metal powders: mechanism, kinetics and microstructural features, *Mater. Sci. Eng. A Struct. Mater. Prop. Microstruct. Process.* 428 (1–2) (2006) 148–158.
- [7] J.P. Kruth, L. Froyen, J. Van Vaerenbergh, P. Mercelis, M. Rombouts, B. Lauwers, Selective laser melting of iron-based powder, *J. Mater. Process. Technol.* 149 (1–3) (2004) 616–622.
- [8] Y. Wang, J. Bergstrom, C. Burman, Characterization of an iron-based laser sintered material, *J. Mater. Process. Technol.* 172 (1) (2006) 77–87.
- [9] K.A. Mumtaz, P. Erasenthiran, N. Hopkinson, High density selective laser melting of Waspaloy®, *J. Mater. Process. Technol.* 195 (1–3) (2008) 77–87.
- [10] K. Mumtaz, N. Hopkinson, Top surface and side roughness of Inconel 625 Parts processed using selective laser melting, *Rapid Prototyping J.* 15 (2) (2009) 96–103.
- [11] D.D. Gu, Y.F. Shen, Development and characterisation of direct laser sintering multicomponent Cu based metal powder, *Powder Metall.* 49 (3) (2006) 258–264.
- [12] K. Osakada, M. Shiomi, Flexible manufacturing of metallic products by selective laser melting of powder, *Int. J. Mach. Tools Manuf* 46 (11) (2006) 1188–1193.
- [13] D.D. Gu, Z.Y. Wang, Y.F. Shen, Q. Li, Y.F. Li, In situ TiC particle reinforced Ti–Al matrix composites: powder preparation by mechanical alloying and selective laser melting behavior, *Appl. Surf. Sci.* 255 (22) (2009) 9230–9240.
- [14] M.W. Khaing, J.Y.H. Fuh, L. Lu, Direct metal laser sintering for rapid tooling: processing and characterization of EOS parts, *J. Mater. Process. Technol.* 113 (2001) 269–272.
- [15] A. Simchi, Direct laser sintering of metal powders: mechanism, kinetics and microstructural features, *Mater. Sci. Eng., A* 428 (1–2) (2006) 148–158.
- [16] Y. Wang, J. Bergstrom, C. Burman, Four-point bending fatigue behaviour of an iron-based laser sintered material, *Int. J. Fatigue* 28 (2006) 1705–1715.
- [17] S. Leuders, M. Thöne, A. Riemer, T. Niendorf, T. Tröster, H.A. Richard, H.J. Maier, On the mechanical behaviour of titanium alloy TiAl6V4 manufactured by selective laser melting: fatigue resistance and crack growth performance, *Int. J. Fatigue* 48 (2013) 300–307.
- [18] Y. Wang, J. Bergstrom, C. Burman, Thermal fatigue behavior of an iron-based laser sintered material, *Mater. Sci. Eng., A* 513–514 (2009) 64–71.
- [19] A. Persson, S. Hogmark, J. Bergström, Simulation and evaluation of thermal fatigue cracking of hot work tool steels, *Int. J. Fatigue* 26 (2004) 1095–1107.
- [20] A. Simchi, F. Petzoldt, H. Pohl, Direct metal laser sintering: material considerations and mechanisms of particle: rapid tooling of powdered metal parts, *Int. J. Powder Metall.* 37 (2001) 49–61.
- [21] M. Shiomi, K. Osakada, K. Nakamura, T. Yamashita, F. Abe, Residual stress within metallic model made by selective laser melting process, *CIRP Ann. – Manuf. Technol.* 53 (1) (2004) 195–198.
- [22] L.E. Murr, S.M. Gaytan, A. Ceylan, E. Martinez, J.L. Martinez, D.H. Hernandez, et al., Characterization of titanium aluminate alloy components fabricated by additive manufacturing using electron beam melting, *Acta Mater.* 58 (5) (2010) 1887–1894.
- [23] B. Gorny, T. Niendorf, J. Lackmann, M. Thöne, T. Tröster, H.J. Maier, In situ characterization of the deformation and failure behaviour of non-stochastic

- porous structures processed by selective laser melting, *Mater. Sci. Eng. A* 528 (27) (2011) 962–967.
- [24] T. Vilaro, C. Colin, J.D. Bartout, As-fabricated and heat-treated microstructures of the Ti–6Al–4V alloy processed by selective laser melting, *Metall. Mater. Trans. A* 42A (10) (2011) 3190–3199.
- [25] E. Brandl, U. Heckenberger, V. Holzinger, D. Buchbinder, Additive manufactured AlSi10Mg samples using selective laser melting (SLM): microstructure, high cycle fatigue, and fracture behaviour, *Mater. Des.* 34 (2012) 159–169.
- [26] A. Hartman, J. Schijve, The effects of environment and load frequency on the crack propagation law for macro fatigue crack growth in aluminum alloys, *Eng. Fract. Mech.* 1 (4) (1970) 615–631.
- [27] M.H. El Haddad, T.H. Topper, K.N. Smith, Prediction of non-propagating cracks, *Eng. Fract. Mech.* 11 (1979) 573–584.

Article

Fatigue Behavior of Hybrid Components Containing Maraging Steel Parts Produced by Laser Powder Bed Fusion

Luís Santos ¹, Joel de Jesus ^{1,*} , Luís Borrego ^{1,2} , José A. M. Ferreira ¹ , Rui F. Fernandes ¹ ,
José D. M. da Costa ¹  and Carlos Capela ^{1,3}

¹ Department of Mechanical Engineering, Centre for Mechanical Engineering, Materials and Processes (CEMMPRE), University Coimbra, P-3004 516 Coimbra, Portugal; luis_lms@sapo.pt (L.S.); borrego@isec.pt (L.B.); martins.ferreira@dem.uc.pt (J.A.M.F.); uc2020158278@student.uc.pt (R.F.F.); jose.domingos@dem.uc.pt (J.D.M.d.C.); ccapela@ipleiria.pt (C.C.)

² Department of Mechanical Engineering, Coimbra Polytechnic–ISEC, Rua Pedro Nunes, 3030-199 Coimbra, Portugal

³ Department of Mechanical Engineering, School Tech and Management, Polytechnic Institute of Leiria, 2411-901 Leiria, Portugal

* Correspondence: joel.jesus@uc.pt

Abstract: This investigation concerns about of fatigue behavior under controlled loading and under strain control for hybrid specimens with parts produced with conventional processes in steel AISI H13 and the stainless steel AISI 420 and the rest part produced by laser powder bed fusion in AISI 18Ni300 steel. The controlled loading tests were performed in constant and variable amplitude. Fatigue failure of hybrid samples occurs mostly in laser-melted parts, initiated around the surface, in many cases with multi-nucleation and propagated predominantly between the deposited layers. Fatigue strength of hybrid parts, tested under displacement control is similar, but for specimens tested under load control the fatigue strength the fatigue strength of hybrid specimens is progressively lesser than laser powder bed fusion samples. Despite a tendency to obtain conservative predictions, Miner’s law predicts reasonably the fatigue lives under block loadings. The interface between materials presented an excellent joining and fatigue strength because the fatigue failure of hybrid samples occurred mostly in laser melted parts out of the interface.

Keywords: laser powder bed fusion; fatigue; functional materials; structural integrity



Citation: Santos, L.; de Jesus, J.; Borrego, L.; Ferreira, J.A.M.; Fernandes, R.F.; da Costa, J.D.M.; Capela, C. Fatigue Behavior of Hybrid Components Containing Maraging Steel Parts Produced by Laser Powder Bed Fusion. *Metals* **2021**, *11*, 835. <https://doi.org/10.3390/met11050835>

Academic Editors: Yongho Sohn and Sergey N. Grigoriev

Received: 8 April 2021

Accepted: 17 May 2021

Published: 19 May 2021

Publisher’s Note: MDPI stays neutral with regard to jurisdictional claims in published maps and institutional affiliations.



Copyright: © 2021 by the authors. Licensee MDPI, Basel, Switzerland. This article is an open access article distributed under the terms and conditions of the Creative Commons Attribution (CC BY) license (<https://creativecommons.org/licenses/by/4.0/>).

1. Introduction

Laser powder bed fusion (LPBF) is a technology of rapid manufacturing that builds metal parts layer by-layer using metal powders [1] fused by a high-power laser. This technique is increasingly used to obtain components with complex shapes namely in automotive, aerospace, medical and of injection molds industries. Several studies have been previous published on the area of LPBF technology using different metal powders, for example, the fabricating of iron-base alloys [2–5], nickel-base alloys [6,7], copper-base alloys [8] and titanium-base alloys [9].

LPBF components could present characteristic cast structure, with presence of porosity, high superficial roughness, non-homogeneous microstructure and thermal residual stresses due to the processing with extreme temperature gradients and the high cooling rates, inducing medium mechanical properties. However, additional post-processing treatments can improve these properties [10]. The mechanical properties of components produced by LPBF are mainly affected by above referred parameters, like the scan speed and layer thickness. The different parameters can be grouped in powder characteristics and processing parameters [11]. The occurrence of pores originated from initial powder contaminations, evaporation or local voids after powder-layer deposition is the major drawback in mechanical properties [12–14]. Especially under fatigue, pores can act as stress concentrators leading to easier failure [15].

Since LPBF is an additive manufacturing process with a layer-by-layer deposition, the phenomenon lack of fusion is an inhibitor to the uniform deposition of a fresh powder on the previously sintered layer. Therefore, this behavior tends to cause porosity and even delamination induced by reduced bonding between layers in combination with thermal stress [11,16–19]. This effect is a complex metallurgical process that is controlled by both laser processing conditions and powder material properties [20–23].

Mooney et al. [24] compiled the factors affecting the mechanical properties of maraging Steel 300 fabricated via LPBF, being that: the quality and the powder morphology can play an important role in the LPBF process in order to achieved higher relative density and optimizing mechanical properties; parameters of LPBF process affect directly the material microstructure and therefore they impact on the mechanical properties and anisotropie of the material; the build orientation influences the mechanical performance of the material and can be improved with heat treatments. Anisotropy can be drastically reduced via an appropriate choice of such plans, which are generally easy to implement for this material.

The influence of melting parameters and selection of metal powder on microstructure of the parts have been the main focus of a high number of studies on LPBF materials. These studies, state that for some materials, LPBF components are capable to achieve static mechanical properties comparable to the ones of conventionally produced parts from bulk materials [25]. Zitelli et al. [26] in their review showed that stainless steel alloys have been satisfactorily processed by LPBF process. The reached mechanical properties make stainless steels fit the requirements of numerous applications. High mechanical properties are achieved, since the porosity level achieved by LPBF is quite low and is comparable to conventionally produced materials.

In spite of, significant results recently published about fatigue behavior of steel LPBF parts [27,28], more research is needed, particularly for structural applications. Spierings et al. [29] investigated the S-N curves of two stainless steel types (316L and 15-5PH), focusing the objectives on the comparison of the results obtained from LPBF and conventionally processed materials, concluding that LPBF specimens exhibits comparable dynamic properties than conventionally processed parts. However, they obtained an important influence of the LPBF surface roughness on the fatigue strength, particularly for long fatigue lives. Branco et al. [30] studied the low cycle fatigue behavior of AISI 18Ni300 maraging steel produced LPBF concluding that the fatigue crack nucleated from the surface defects as: unmolten particles and zones with lack of fusion.

On the other hand, Bhaduri et al. [31] evaluated tensile mechanical properties and microstructure of hybrid specimens made from AISi10Mg parts built by LPBF on AA6082 machined parts. The hybrid components failed under tension at their interface. These conditions enable building LPBF structures with <1% porosity. Recent work was produced by the authors about the mechanical properties of parts manufactured in AISI 18Ni300 steel produced by LPBF, including the fatigue behavior of LPBF specimens [32], hybrid components [33], fatigue crack propagation [34] and fracture toughness [35]. The results indicate that the fatigue strength is strongly affected by defects inherent to the LPBF process. Moreover, the failure sites of hybrid components occurred always in the parts produced by LPBF process.

The mold production or reparation by LPBF is a growing practice in the mold industry. In mold reparation by LPBF is often found hybrid parts because not all materials can be used in the LPBF process, therefore it becomes useful to study the mechanical properties in hybrid parts. The objective of this work was to investigate the fatigue performance of hybrid specimens obtained by LPBF maraging steel implants into hot working tools and stainless steels substrates. Since functional components can be manufactured by LPBF, it is necessary to warrant that final functional requirements are fulfilled by the components. For this purpose, were performed tensile tests, fatigue tests under constant amplitude and block loadings and fractography analysis. A detailed analysis was performed about the failure mechanisms and interfaces microstructures.

2. Materials and Methods

Experimental program, involving static and fatigue tests, was performed using round specimens. Two material batches of hybrid samples, in which one part was produced by LPBF and other part is a substrate steel, produced by conventional processes. Fatigue results were compared with previous work with LPFB specimens, produced only by LPBF technique. Figure 1 shows the geometry and dimensions of the hybrid specimens.

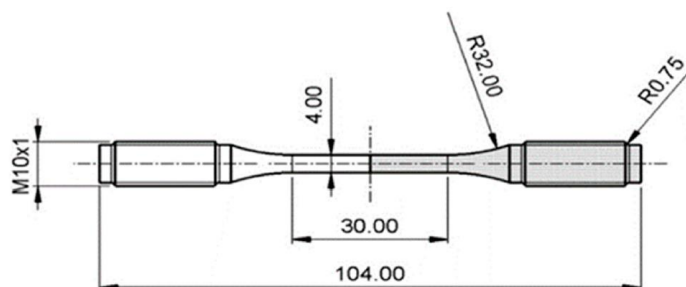


Figure 1. Geometry and dimensions of hybrid specimens.

Laser powder bed fusion (LPBF) was processed using a high-power laser to fuse steel powder particles layer by layer by Lasercusing®. The sample layers are deposited in planes perpendicular to the axial direction of the specimens. The equipment was of the mark "Renishaw" and model "AM 400". This machine is composed by a laser type Nd: YAG with a maximum power of 400 W in continuous wave mode and a wavelength of 1064 nm. Figure 2 shows a SEM image of transversal section being possible to visualize the route of the power melting.

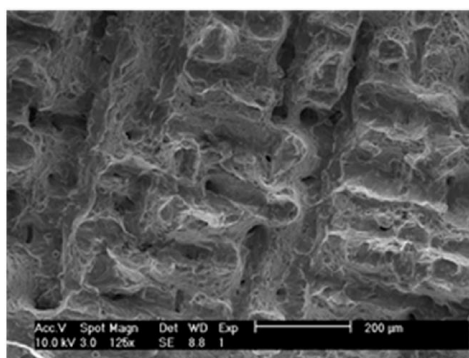


Figure 2. SEM image of melting route.

The scan speed of 200 mm/s was used for processing laser melting, resulting a deposited layer about 30 μm thickness [32]. The material of the powder particles was the maraging steel AISI 18Ni300. The choice of this steel was due to its high utilization in the molds production and reparation given that this steel conserves the mechanical properties in higher temperatures due to the high amount of nickel in its structure. The hybrid specimens were produced alternatively in two materials: the steel for hot work tools AISI H13 (HS) and the stainless steel AISI 420 (SS). Before testing all specimens were polished in order to reduced surface roughness. The average surface roughness in all specimens was about, $R_z = 0.47 \mu\text{m}$.

The scan speed of 200 mm/s was chosen after a detailed analysis by authors in previous work [32], where was studied the effect of the scan speed (the authors used 200,

400 and 600 mm/s) on the microstructure, defect level, density and mechanical properties. The defect level was based on microscopy analysis and by comparing density values. The better results were obtained with 200 mm/s scan speed, for which was obtained: a porosity of 0.74%, density of 7.42 g/cm³, hardness of HV1 354, Young's Modulus of 168 GPa and a tensile strength of 1147 MPa.

The chemical composition, according with the manufacturers, is shown in Table 1. The sample code identifies the test series, corresponding to abbreviations of the materials used for each part. Table 2 show the material design composition of the two batches used in present study.

Table 1. Chemical composition of the materials.

Steel	C	Ni	Co	V	Mo	Ti	Al	Cr	P	Si	Mn	Fe
18Ni300	0.01	18.2	9.0	-	5.0	0.6	0.05	0.3	0.01	0.1	0.04	Balance
1.2344	0.40	-	-	0.94	1.30	-	-	5.29	0.017	1.05	0.36	Balance
1.2083	0.37	-	-	0.17	-	-	-	14.22	0.021	0.64	0.37	Balance

Table 2. Samples materials design.

Sample Code	Substrate Material	Implant Material
LPBF/HS	18Ni300 powder (LPBF)	1.2344 Hot working steel (HS)
LPBF/SS	18Ni300 powder (LPBF)	1.2083 Stainless steel (SS)

A 10 kN capacity Instron EletroPuls E10000 machine (Instron, Norwood, MA, USA) was used to perform both, tensile and fatigue tests. Tensile tests were carried out using a testing speed of 2 mm/min at room temperature. The fatigue tests were performed with a frequency of 15 Hz in tension, also at room temperature. Fatigue tests were carried out:

- Under constant amplitude loading two series of tests were performed: One in load control at constant amplitude sinusoidal load wave with stress ratio $R = 0$ and another in displacement control with zero minimum strain.
- Under variable amplitude tests using a reference block loading, composed by three blocks with stress ratio of $R = 0$, applied during 1000 of cycles for each block. The stress range applied during each block is schematically depicted in Figure 3.

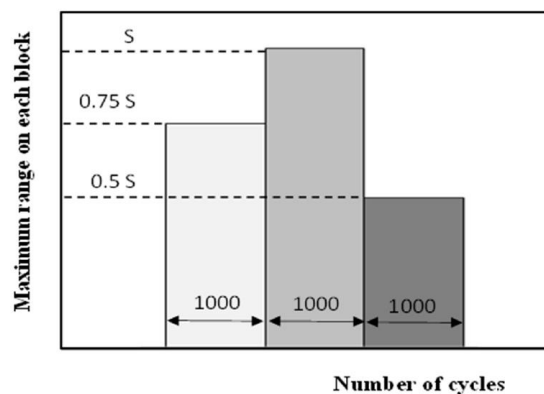


Figure 3. Schematic presentation of the block loadings.

An average of eight specimens were used for each series in order to create the curves of stress vs number of cycles at failure. It is important to notice that this study was conducted with limited number of specimens for each analyzed condition and therefore the obtained

results cannot be addressed as project data. However, the objective is to understand the fatigue behavior of the material hybrid samples, as well as to perform a detailed analysis about the failure mechanisms and interfaces micro-structures. Moreover, the test procedure agrees with the best practice in fatigue studies.

Microstructures were analyzed in LPBF material and interface regions. Therefore, hybrid specimens were cut in planes containing the axial axis of the specimens, polished and attacked Picral solution for two minutes (ethyl alcohol with 4% of picric acid solution), followed by a second attack for 20 s in a solution that results from Picral mixture with addition of 1% hydrochloric acid. After samples preparation, the microscope Leica DM4000 M LED (Leica Microsystems, Wetzlar, Alemanha) was used to make their observation. The fracture surfaces of some fatigue specimens were observed and analyzed by SEM using a scanning electron microscope Philips XL 30 (Philips, Eindhoven, The Netherlands). Figure 4a shows the microstructure into the LPBF material, presenting a good coherency between the elongated deposited layer with about 150 μm wide and about 30–35 μm width, the formation of cellular solidification structure and possible martensitic needles (red dashed line) [36] and a significant number of impurities result of the etching process. Hybrid samples interface region was analyzed in order to better understand the variations in microstructure and quality of adhesion. Figure 4b,c present the metallography in the longitudinal section interface region for a LPBF/HS and a LPBF/SS hybrid specimen, respectively. Both figures show corrugated regions in the substrate material, caused by melting in the first laser pass. In both cases there is an interface region on the substrate with a width of approximately 30–50 μm . In this region there is a significant microstructural change resulting from the high temperature and sudden cooling that occurred in the manufacturing process. Figure 4b presents a darker zone indicating a higher carbon concentration due to decarburization has occurred in the zone near the interface, which is indicated by the white colour of this region. On the other hand, Figure 4c shows that did not occurred decarburization in the interface zone. The presence of porosities was observed (marked by red arrows) in the LPBF material but were not observed at the specimens' interface. In both cases was verified an excellent cohesion between steels.

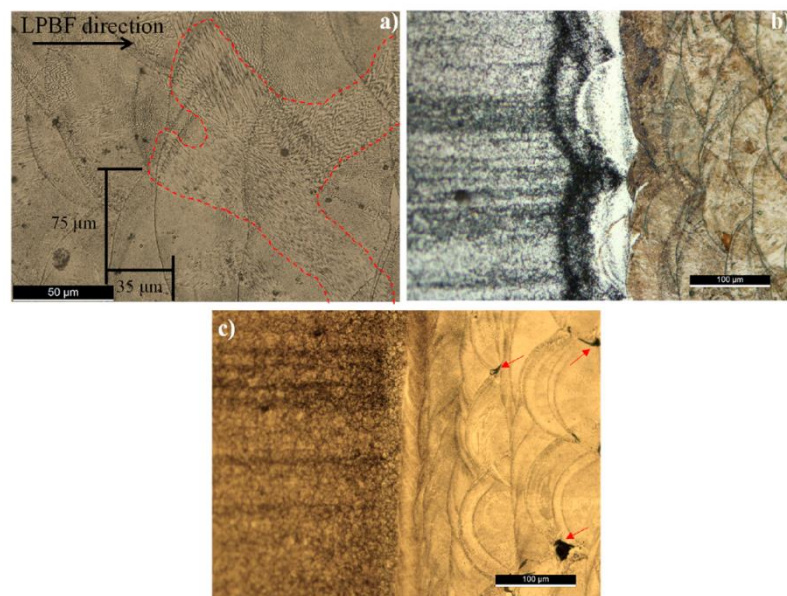


Figure 4. (a) Microstructure of LPBF material; (b) interface LPBF/HS specimen; (c) interface LPBF/SS specimen.

A Struers Duramin 1 microhardness tester was used to perform Vickers hardness testing according to ASTM E384-11e1 [37] at 0.5 mm between indentations with 1 kg load. Distance between indentations in interface region was only 0.25 mm. The following values were obtained for the three materials: 533.1 ± 6.17 , 505.8 ± 2.75 , 339.5 ± 8.60 HV1, for the AISI 420, AISI H13 steels and LPBF material, respectively. In the hybrid specimens, the transition between the typical hardness of the two materials occurs rapidly and progressively in a narrow band less than 2 mm wide.

3. Results and Discussion

Figure 5 shows representative load–displacement curves obtained for the different samples (were tested three samples for each series). It can be observed an initial linear region followed by a non-linear behavior typical of metallic materials. The hybrid samples have higher global stiffness than the LPBF only specimens, as a consequence of the recorded strain to be an average value in the region of the interface between the ends of the extensometer (12.5-gauge length). For hybrid specimens, this region includes two materials with different stiffness, LPBF material with lower Young’s modulus, AISI 420 and AISI H13 steels with similar and higher Young’s modulus. In opposite, strain at failure is lower for hybrid specimens. Failure stress is similar for the three batches of materials, because failure occurs in all cases in LPBF material sections. Ultimate strength was calculated from peak load of the load versus displacement curves. The Young’s modulus was obtained by linear regression of the stress-strain curves considering the larger range corresponding to a correlation coefficient higher than 0.995. The values of the ultimate strength and the Young’s modulus are summarized in Table 3.

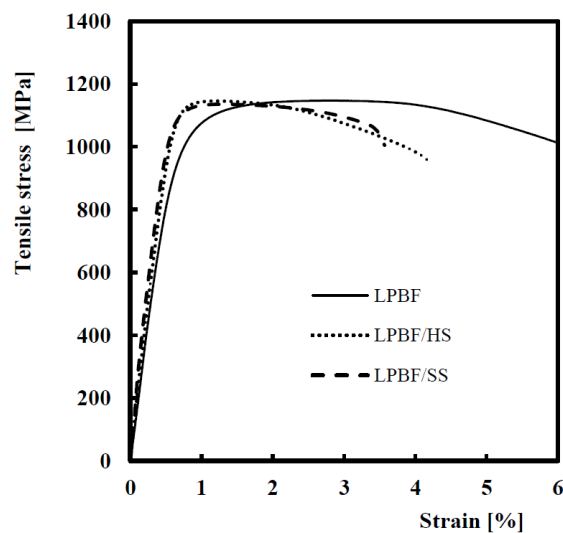


Figure 5. Exemplary tensile curves.

Table 3. Mechanical properties.

Sample Code	Young’s Modulus, GPa	Tensile Strength, MPa	Strain at Failure, %
LPBF	168 ± 9	1147 ± 13	6.12 ± 0.001
LPBF/HS	181 ± 6	1139 ± 12	4.2 ± 0.03
LPBF/SS	173 ± 7	1144 ± 10	3.8 ± 0.08

Five batches of fatigue tests were performed: tests under load control for all the three types of samples and tests under displacement control for LPBF and LPBF/HS samples.

The pulsating tensile loading fatigue results were analyzed using the initial nominal stress range against the number of cycles to failure. Figure 6a,b compare the results obtained for the different specimen configurations, for the tests under load control and displacement control, respectively. The analysis of Figure 6a indicates that for longer lives, the fatigue strength of hybrid specimens is progressively less than that of the fully LPBF only samples, while Figure 6b shows that fatigue strength of LPBF only samples and hybrid LPBF/HS samples, tested under displacement control is similar. These results indicate that fatigue life of laser melting samples is controlled by strain range and the use of hybrid parts manufactured with AISI H13 and AISI 420 steels substrates do not affect significantly the fatigue strength. The effect of the substrate is a result: good adhesion in the interface above mentioned (as observed in Figure 4b,c, and the fact that the LPBF region is constitute itself as the weakest area in terms of fatigue resistance. On the other side, the results indicate that a small tendency to increasing fatigue life under displacement control in comparison with load control tests, which can be caused by the material softening observed by authors [34].

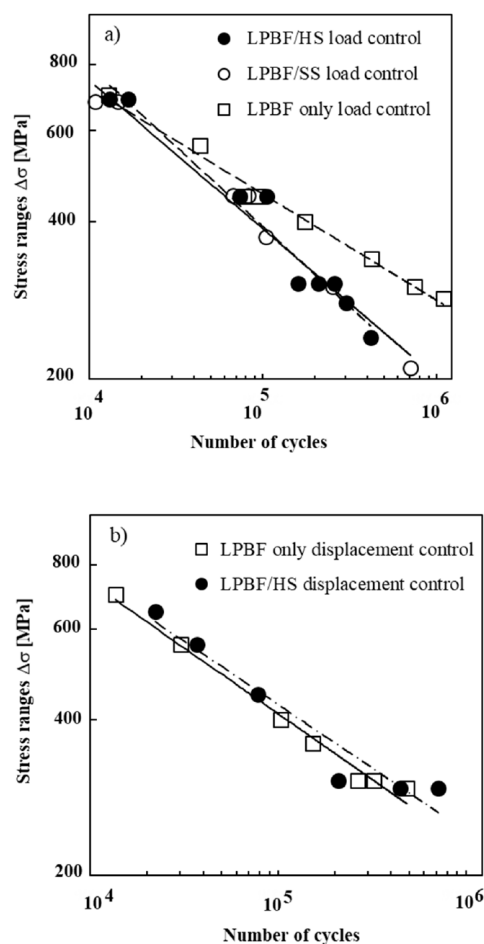


Figure 6. Curves of stress range vs number of cycles at failure; (a) load control; (b) displacement control.

The failure sites were observed and measured from the interface. Figure 7 shows a photo of a longitudinal section, positioning failure section in respect to interface on a

LPBF/HS sample. This figure is representative of failure positions, showing bulk HS steel, interface and failure section, which occurs always in LPBF material. Figure 8 depicts a histogram of the distance of the failure sections from the interface, providing evidence that most of the fractures occur at the LPBF regions. The reasons why these sintered parts are less resistant to nucleation and growth of fatigue cracks will be possible due the type of microstructure, lower microhardness, the presence of a significant number of small micro pores and positive residual stresses around surface in LPBF region. This event confirms good adhesion and metallurgic compatibility between materials of hybrid parts.



Figure 7. View of failure section in a LPBF/HS sample.

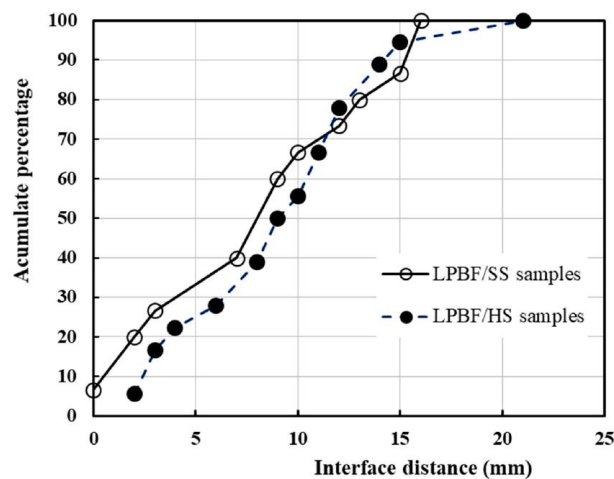


Figure 8. Histogram of failure section position.

Fracture surfaces were analyzed by scanning electron microscope, presenting Figure 9 some exemplary SEM images of the failure in only LPBF material. In spite of the presence of internal micro pores, and also the presence of positive residual stresses [34], fatigue crack initiated around the surface, in laser melted material and propagated through the cross section. As observed by the authors in previous work [32], in many cases, occurred surface multi-nucleation as shown in Figure 9a. Fatigue crack propagation occurs under mixed mode: predominantly between the deposited layers revealing the scan pattern (as shown in Figure 9b), and a transgranular failure through the deposited layer drive by the presence of microporosities and of impurities due to the etching process, as reveals a higher magnification observation, Figure 9c. The observation of the failure surface using 3D microscopy confirms the crack path, contouring the deposited layers and growing through the microporosities and impurities defects, as shown in Figure 9d.

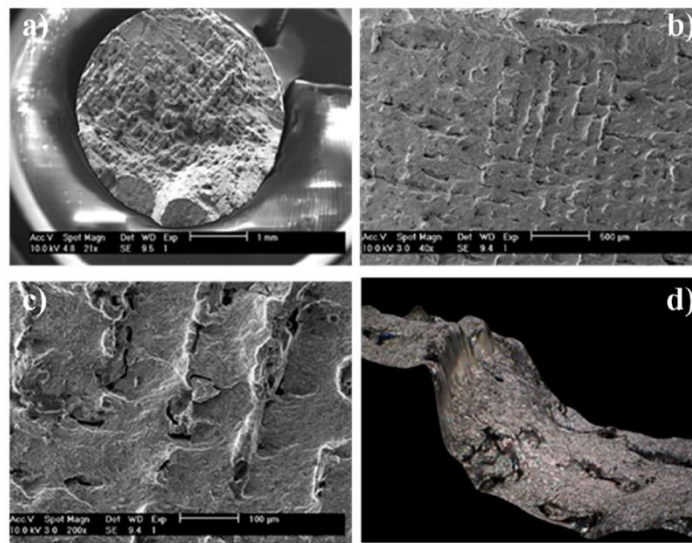


Figure 9. Images of surface fracture. (a) SEM image of fracture surface; (b) magnification of Figure 9a; (c) magnification of Figure 9b; (d) image of failure surface using 3D microscopy.

The fatigue results under variable amplitude loading were analyzed using the known Miner's law. Neglecting the existence of a fatigue limit, in Miner's rule enables the definition of an equivalent stress [38].

Figures 10 and 11 compare the predicted lives, N_p , obtained by the Miner's law and the experimental results of the fatigue tests on variable amplitude of hybrid parts, N_f , for the samples LPBF/HS and LPBF/SS, respectively. In these figures the limits $N_p = 2N_f$ and $N_p = 0.5N_f$ were also plotted and used as a criterion of prediction exactness.

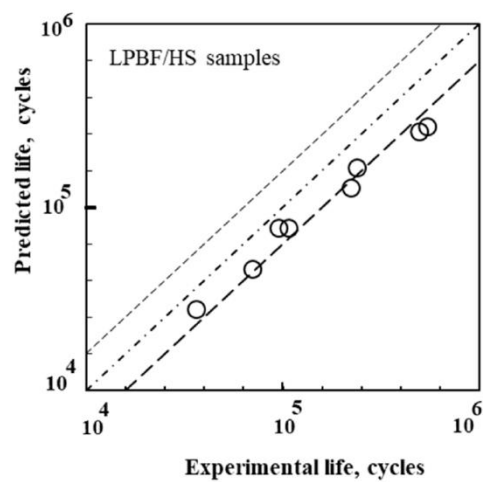


Figure 10. Predicted fatigue for variable amplitude loading. LPBF/HS samples.

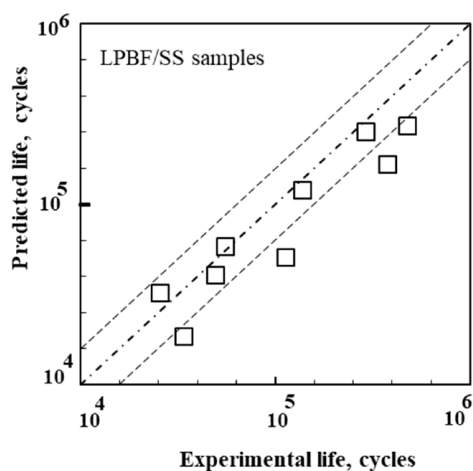


Figure 11. Predicted fatigue for variable amplitude loading. LPBF/SS samples.

A good agreement was obtained between the predicted lives and the experimental results, which is indicated by the presence of the results mainly between the two limits, which is usually considered as a correspondent for a very good agreement. From the analysis of this figure it can be concluded that Miner's law is adequate to predict fatigue life in hybrid components with sintered implants. However, particularly for the LPBF/SS specimens a tendency to be conservative was observed.

4. Conclusions

The main conclusions are:

- Tensile properties of only LPBF and hybrid specimens are quite similar. However, for the materials combinations studied hybrid parts have higher stiffness (+7%) and lower strain at failure (−61%).
- Fatigue failure of hybrid samples occurs in laser melted parts, once LPBF material exhibits lower crack initiation resistance as consequence of lower micro hardness, about of −70%, and the presence of a significant number of small micro pores. Fatigue cracks initiated around the surface, in many cases with multi-nucleation and propagated predominantly between the deposited layers or through the internal microporosities and impurities defects. The interface between materials showed an excellent connection and fatigue strength due to the fatigue failure of hybrid samples occurred frequently in laser melted parts out of the interface.
- For short lives, fatigue strength of LPBF and hybrid parts, tested under load control was quite similar. However, for long lives, the fatigue strength of hybrid specimens is progressively lesser than that of LPBF samples, for 500,000 cycles a loss of 52%. Fatigue strength of LPBF and hybrid parts, tested under displacement control is similar, suggesting that fatigue failure is controlled by the strain range.
- Miner's law provides good predictions of the fatigue lives under block loadings due to the ratio between the experimental and predicted fatigue life showed an error below to 10%, despite a tendency to obtain conservative predictions, particularly for the LPBF/SS specimens.

Author Contributions: Conceptualization, J.A.M.F. and L.B.; methodology, J.D.M.d.C.; software, J.d.J.; formal analysis, L.S. and J.d.J.; investigation, L.S., R.F.F. and J.d.J.; resources, C.C.; data curation, L.S. and J.d.J.; writing—original draft preparation, J.d.J.; writing—review and editing, L.B.; supervision, J.A.M.F. and J.D.M.d.C.; project administration, J.A.M.F.; funding acquisition, J.A.M.F. and L.B. All authors have read and agreed to the published version of the manuscript.

Funding: The authors would like to acknowledge the sponsoring under the project POCI-01-0247-FEDER-042536, financed by European Funds, through program COMPETE2020, under the Eu-reka smart label S0129-AddDies. This research is also sponsored by national funds through FCT—Fundação para a Ciência e a Tecnologia, under the project UIDB/00285/2020.

Data Availability Statement: The data presented in this study are available on request from the corresponding author. The data are not publicly available due to privacy.

Conflicts of Interest: The authors declare no conflict of interest.


References

- Santos, E.C.; Shiomi, M.; Osakada, K.; Laoui, T. Rapid manufacturing of metal components by laser forming. *Int. J. Mach. Tools Manuf.* **2006**, *46*, 1459–1468. [\[CrossRef\]](#)
- Simchi, A.; Pohl, H. Direct laser sintering of iron–graphite powder mixture. *Mater. Sci. Eng. A* **2004**, *383*, 191–200. [\[CrossRef\]](#)
- Simchi, A. Direct laser sintering of metal powders: Mechanism, kinetics and microstructural features. *Mater. Sci. Eng. A* **2006**, *428*, 148–158. [\[CrossRef\]](#)
- Kruth, J.P.; Froyen, L.; Van Vaerenbergh, J.; Mercelis, P.; Rombouts, M.; Lauwers, B. Selective Laser Melting of Iron-Based Powder. *J. Mater. Process. Technol.* **2004**, *149*, 616–622. [\[CrossRef\]](#)
- Wang, Y.; Bergström, J.; Burman, C. Characterization of an iron-based laser sintered material. *J. Mater. Process. Technol.* **2006**, *172*, 77–87. [\[CrossRef\]](#)
- Mumtaz, K.A.; Erasenthiran, P.; Hopkinson, N. High Density Selective Laser Melting of Waspaloy®. *J. Mater. Process. Technol.* **2008**, *195*, 77–87. [\[CrossRef\]](#)
- Mumtaz, K.; Hopkinson, N. Top surface and side roughness of Inconel 625 parts processed using selective laser melting. *Rapid Prototyp. J.* **2009**, *15*, 96–103. [\[CrossRef\]](#)
- Gu, D.; Shen, Y. Development and characterisation of direct laser sintering multicomponent Cu based metal powder. *Powder Met.* **2006**, *49*, 258–264. [\[CrossRef\]](#)
- Osakada, K.; Shiomi, M. Flexible manufacturing of metallic products by selective laser melting of powder. *Int. J. Mach. Tools Manuf.* **2006**, *46*, 1188–1193. [\[CrossRef\]](#)
- Maleki, E.; Bagherifard, S.; Bandini, M.; Guagliano, M. Surface post-treatments for metal additive manufacturing: Progress, challenges, and opportunities. *Addit. Manuf.* **2021**, *37*, 101619. [\[CrossRef\]](#)
- Simchi, A.; Petzoldt, F.; Pohl, H. Direct metal laser sintering: Material considerations and mechanisms of particle: Rand tooling of powdered metal parts. *Int. J. Powder Metall.* **2001**, *37*, 49–61.
- Murr, L.E.; Gaytan, S.M.; Ceylan, A.; Martinez, E.; Martinez, J.L.; Hernandez, D.H.; Machiado, B.I.; Ramirez, D.A.; Medina, F.; Collins, S.; et al. Characterization of titanium aluminate alloy components fabricated by additive manufacturing using electron beam melting. *Acta Mater.* **2010**, *58*, 1887–1894. [\[CrossRef\]](#)
- Gorny, B.; Niendorf, T.; Lackmann, J.; Thoene, M.; Troester, T.; Maier, H.J. In situ characterization of the deformation and failure behaviour of non-stochastic porous structures processed by selective laser melting. *Mater. Sci. Eng. A* **2011**, *528*, 7962–7967. [\[CrossRef\]](#)
- Vilaro, T.; Colin, C.; Bartout, J.-D. As-Fabricated and Heat-Treated Microstructures of the Ti-6Al-4V Alloy Processed by Selective Laser Melting. *Met. Mater. Trans. A* **2011**, *42*, 3190–3199. [\[CrossRef\]](#)
- Brandl, E.; Heckenberger, U.; Holzinger, V.; Buchbinder, D. Additive manufactured AlSi10Mg samples using Selective Laser Melting (SLM): Microstructure, high cycle fatigue, and fracture behavior. *Mater. Des.* **2012**, *34*, 159–169. [\[CrossRef\]](#)
- Zhu, H.H.; Lu, L.; Fuh, J.Y.H. Study on Shrinkage Behaviour of Direct Laser Sintering Metallic Powder. *Proc. Inst. Mech. Eng. Part B J. Eng. Manuf.* **2006**, *220*, 183–190. [\[CrossRef\]](#)
- Chatterjee, A.N.; Kumar, S.; Saha, P.; Mishra, P.K.; Choudhury, A.R. An experimental design approach to selective laser sintering of low carbon steel. *J. Mater. Process. Technol.* **2003**, *136*, 151–157. [\[CrossRef\]](#)
- Murali, K.; Chatterjee, A.N.; Saha, P.; Palai, R.; Kumar, S.; Roy, S.K.; Mishra, P.K.; Choudhury, A.R. Direct selective laser sintering of iron–graphite powder mixture. *J. Mater. Process. Technol.* **2003**, *136*, 179–185. [\[CrossRef\]](#)
- Dingal, S.; Pradhan, T.R.; Sarin Sundar, J.K.; Choudhury, A.R.; Roy, S.K. The application of Taguchi’s method in the experimental investigation of the laser sintering process. *Int. J. Adv. Manuf. Technol.* **2008**, *38*, 904–914. [\[CrossRef\]](#)
- Gu, D.; Shen, Y. Balling phenomena in direct laser sintering of stainless steel powder: Metallurgical mechanisms and control methods. *Mater. Des.* **2009**, *30*, 2903–2910. [\[CrossRef\]](#)
- Niu, H.J.; Chang, I.T.H. Instability of scan tracks of selective laser sintering of high speed steel powder. *Scripta Mater.* **1999**, *41*, 1229–1234. [\[CrossRef\]](#)
- Tolochko, N.K.; Mozzharov, S.E.; Yadroitsev, I.A.; Laoui, T.; Froyen, L.; Titov, V.I.; Ignatiev, M.B. Balling processes during selective laser treatment of powders. *Rapid Prototyp. J.* **2004**, *10*, 78–87. [\[CrossRef\]](#)
- Das, S. Physical Aspects of Process Control in Selective Laser Sintering of Metals. *Adv. Eng. Mater.* **2003**, *5*, 701–711. [\[CrossRef\]](#)
- Mooney, B.; Kourousis, K. A Review of Factors Affecting the Mechanical Properties of Maraging Steel 300 Fabricated via Laser Powder Bed Fusion. *Metals* **2020**, *10*, 1273. [\[CrossRef\]](#)

25. Abe, F.; Osakada, K.; Shiomi, M.; Uematsu, K.; Matsumoto, M. The manufacturing of hard tools from metallic powders by selective laser melting. *J. Mater. Process. Technol.* **2001**, *111*, 210–213. [[CrossRef](#)]
26. Zitelli, C.; Folgarait, P.; Di Schino, A. Laser Powder Bed Fusion of Stainless Steel Grades: A Review. *Metals* **2019**, *9*, 731. [[CrossRef](#)]
27. Wang, Y.; Bergström, J.; Burman, C. Four-point bending fatigue behaviour of an iron-based laser sintered material. *Int. J. Fatigue* **2006**, *28*, 1705–1715. [[CrossRef](#)]
28. Leuders, S.; Thöne, M.; Riemer, A.; Niendorf, T.; Tröster, T.; Richard, H.A.; Maier, H.J. On the mechanical behaviour of titanium alloy TiAl6V4 manufactured by selective laser melting: Fatigue resistance and crack growth performance. *Int. J. Fatigue* **2013**, *48*, 300–307. [[CrossRef](#)]
29. Spierings, A.; Starr, T.; Wegener, K. Fatigue performance of additive manufactured metallic parts. *Rapid Prototyp. J.* **2013**, *19*, 88–94. [[CrossRef](#)]
30. Branco, R.; Costa, J.D.M.; Berto, F.; Razavi, S.M.J.; Ferreira, J.A.M.; Capela, C.; Santos, L.; Antunes, F. Low-Cycle Fatigue Behaviour of AISI 18Ni300 Maraging Steel Produced by Selective Laser Melting. *Metals* **2018**, *8*, 32. [[CrossRef](#)]
31. Bhaduri, D.; Penchev, P.; Essa, K.; Dimov, S.; Carter, L.N.; Pruncu, C.I.; Pullini, D. Evaluation of surface/interface quality, microstructure and mechanical properties of hybrid additive-subtractive aluminium parts. *CIRP Ann.* **2019**, *68*, 237–240. [[CrossRef](#)]
32. Santos, L.; Ferreira, J.; Jesus, J.; Costa, J.; Capela, C. Fatigue behaviour of selective laser melting steel components. *Theor. Appl. Fract. Mech.* **2016**, *85*, 9–15. [[CrossRef](#)]
33. Santos, L.; Ferreira, J.; Costa, J.; Capela, C. Fatigue Performance of Hybrid Steel Samples with Laser Sintered Implants. *Procedia Eng.* **2016**, *160*, 143–150. [[CrossRef](#)]
34. Santos, L.; Borrego, L.; Ferreira, J.; De Jesus, J.; Costa, J.; Capela, C. Effect of heat treatment on the fatigue crack growth behaviour in additive manufactured AISI 18Ni300 steel. *Theor. Appl. Fract. Mech.* **2019**, *102*, 10–15. [[CrossRef](#)]
35. Santos, L.M.S.; De Jesus, J.; Ferreira, J.M.; Costa, J.D.; Capela, C. Fracture Toughness of Hybrid Components with Selective Laser Melting 18Ni300 Steel Parts. *Appl. Sci.* **2018**, *8*, 1879. [[CrossRef](#)]
36. Yao, Y.; Huang, Y.; Chen, B.; Tan, C.; Su, Y.; Feng, J. Influence of processing parameters and heat treatment on the mechanical properties of 18Ni300 manufactured by laser based directed energy deposition. *Opt. Laser Technol.* **2018**, *105*, 171–179. [[CrossRef](#)]
37. ASTM E384-11e1. *Standard Test Method for Knoop and Vickers Hardness of Materials*; ASTM International: West Conshohocken, PA, USA, 2011. [[CrossRef](#)]
38. Miner, M.A. Cumulative Damage in Fatigue. *J. Appl. Mech.* **1945**, *12*, A159–A164. [[CrossRef](#)]

Article

Low-Cycle Fatigue Behaviour of AISI 18Ni300 Maraging Steel Produced by Selective Laser Melting

Ricardo Branco ^{1,*} , José D. M. Costa ¹, Filippo Berto ², Seyed Mohammad Javad Razavi ², José A. Martins Ferreira ¹, Carlos Capela ^{1,3}, Luís Santos ³ and Fernando Antunes ¹

¹ CEMMPRE, Department of Mechanical Engineering, University of Coimbra, Rua Luis Reis Santos, 3030-788 Coimbra, Portugal; jose.domingos@dem.uc.pt (J.D.M.C.); martins.ferreira@dem.uc.pt (J.A.M.F.); carlos.capela@ipleiria.pt (C.C.); uc5161@dem.uc.pt (F.A.)

² Department of Mechanical and Industrial Engineering, Norwegian University of Science and Technology (NTNU), Richard Birkelands vei 2b, 7491 Trondheim, Norway; filippo.berto@ntnu.no (F.B.); javad.razavi@ntnu.no (S.M.J.R.)

³ Department of Mechanical Engineering, ESTG, Polytechnic Institute of Leiria, 2411-901 Leiria, Portugal; luis_lms@sapo.pt

* Correspondence: ricardo.branco@dem.uc.pt; Tel.: +351-239-790-700

Received: 1 December 2017; Accepted: 1 January 2018; Published: 5 January 2018

Abstract: Selective laser melting has received a great deal of attention in recent years. Nevertheless, research has been mainly focused on the technical issues and their relationship with the final microstructure and monotonic properties. Fatigue behaviour has rarely been addressed, and the emphasis has been placed on high-cycle regimes. The aim of this paper is, therefore, to study, in a systematic manner, the cyclic plastic behaviour of AISI 18Ni300 maraging steel manufactured by selective laser melting. For this purpose, low-cycle fatigue tests, under fully-reversed strain-controlled conditions, with strain amplitudes ranging from 0.3% to 1.0%, were performed. After testing, fracture surfaces were examined by scanning electron microscopy to identify the main fatigue damage mechanisms. The analysis of results showed a non-Masing material, with a slight strain-softening behaviour, and non-linear response in both the elastic and plastic regimes. In addition, this steel exhibited a very low transition life of about 35 reversals, far below the values of conventional materials with equivalent monotonic mechanical properties, which can be attributed to the combination of high strength and low ductility. The total strain energy density, irrespective of strain amplitude, revealed itself to be a quite stable parameter throughout the lifetime. Finally, the SEM analysis showed for almost all the tested samples cracks initiated from the surface and inner defects which propagated through the rest of the cross section. A ductile/brittle fracture, with a predominance of brittle fracture, was observed in the samples, owing to the presence of defects which make it easier to spread the microcracks.

Keywords: AISI 18Ni300 steel; low-cycle fatigue; cyclic deformation behaviour; laser sintering metals; functional materials

1. Introduction

Competitiveness at a global scale forces industry to develop efficient manufacturing processes and to reduce the product development cycles. Selective laser melting (SLM) is one promising technology able to meet these goals, allowing the production of complex geometries directly from three-dimensional CAD (computer aided design) models in short time frames and at low cost [1].

Selective laser melting, like other additive manufacturing processes, quickly produces physical objects layer-by-layer, transforming a three-dimensional problem into a bi-dimensional one. The technique is being increasingly used in different strategic sectors, namely automotive, aerospace, biomedical,

and mould industries, among others. Its principle of operation consists of dividing the CAD model into several slices, which are successively formed via a high-power laser beam that scans over the surface of a thin powder layer previously deposited on a substrate [2]. In general, SLM products have a cast structure, high superficial roughness, microstructural heterogeneities, presence of pores, and thermal stresses, which are consequences of pronounced temperature gradients and significant cooling rates. Despite these drawbacks, several studies have suggested that their monotonic properties can be similar to those of the components manufactured using conventional processes [3].

However, a major concern regarding sintered products is the fatigue behaviour. Due to the combination of cyclic loading histories, stress concentration phenomena associated with the complex shapes, and defects and microstructural heterogeneities formed during the fabrication, they have high susceptibility to fatigue failure. Although there is extensive literature on SLM either devoted to the production of sintered objects using different metallic powders or to the influence of sintering parameters on microstructure and mechanical properties, very few studies have addressed the fatigue phenomenon [4–15]. The first studies, conducted in 2006, were focused on the fatigue behaviour of four-point bending specimens made of a laser sintered FeNiCu alloy [4]. A few years later, Leuders et al. [5] evaluated the fatigue resistance and crack growth rates in Ti-6Al-4V titanium alloys manufactured by SLM; Sehr et al. [6] investigated the fatigue strength of 17-4PH stainless steel samples, manufactured in horizontal and upright orientations, subjected to rotating bending; Stoffregen et al. [7] compared the fatigue resistance of SLM 17-4PH as-built and machined specimens; Crococolo et al. [8] addressed the effect of building orientation on fatigue strength in EOS maraging steel MS1 (Electro Optical Systems, Krailling/Munich, Germany) produced by direct metal laser sintering; and Spierings et al. [9] evaluated the fatigue resistance of 316L and 15-5PH stainless steel samples produced by SLM, and by conventional techniques. More recently, Kasperovich and Hausmann [10] optimised the process parameters in order to obtain improved fatigue resistance properties in Ti-6Al-4V samples produced by SLM; Santos et al. [11] examined the effect of scan speed, porosity, and microstructure on static mechanical properties, and fatigue strength of sintered AISI 18Ni300 alloy samples; Yadollahi et al. [12] tackled the influence of building orientation and heat treatment on fatigue behaviour in SLM 17-4PH stainless steel samples; Walker et al. [13] analysed the effect of building orientation and layer thickness on fatigue crack propagation in Ti-6Al-4V titanium alloys manufactured using SLM; Razavi et al. [14,15] assessed the fatigue strength of circular and blunt V-notched samples made of Ti-6Al-4V titanium produced by SLM.

The above-mentioned research has mainly been conducted under stress-controlled conditions, with focus on high-cycle fatigue regimes; systematic studies devoted to strain-controlled low-cycle fatigue are not available in the open literature. Therefore, existing information is clearly insufficient, and more work is needed to develop safe and durable sintered products, as well as adequate design criteria. Design criteria for the prevention of fatigue failure are usually established on the basis of stress-, strain-, or energy-based methods [16]. The first are traditionally used in high-cycle fatigue regimes, and relate the nominal stresses with the local fatigue strength; the other two, on the contrary, account for the localised plastic deformation and, consequently, rely on the knowledge of the cyclic properties, which are usually determined via strain-controlled fatigue tests.

This paper aims at studying the cyclic deformation behaviour of AISI 18Ni300 maraging steel manufactured by selective laser melting, as well as evaluating its cyclic mechanical properties. For this purpose, low-cycle fatigue tests are performed under fully-reversed strain-controlled conditions, with strain amplitudes lying between 0.3–1.0% in air at room temperature, using a constant strain rate. After the tests, fracture surfaces are evaluated by scanning electron microscopy (SEM) to identify the main fatigue damage micro-mechanisms. The paper is organized as follows. Section 2 gathers the main information on the experimental procedure. Section 3 starts with the analysis of microstructure and level of porosity, then addresses the cyclic deformation behaviour, the cyclic stress–strain response, and strain-life and energy-life relationships, and ends with the SEM examination of fracture surfaces. The last section presents the concluding remarks.

2. Experimental Procedure

The material used in this study was an AISI 18Ni300 maraging steel. Its nominal chemical composition in weight percentage, and its main mechanical properties are summarised in Tables 1 and 2, respectively.

Table 1. Chemical composition of AISI 18Ni300 manufactured with a scan speed of 200 mm/s [11].

C	Ni	Mn	Co	Mo	Ti	Al	Cr	P	Si	Mn	Fe
0.01	18.2	0.65	9.0	5.0	0.6	0.05	0.3	0.01	0.1	0.04	balance

Table 2. Mechanical properties of AISI 18Ni300 manufactured with a scan speed of 200 mm/s [11].

Porosity (%)	Density (g/m ³)	Hardness (HV1)	Young's Modulus (GPa)	Tensile Strength (MPa)	Yield Strength (MPa)	Strain at Failure (%)
0.74 ± 0.09	7.42	354 ± 5	168 ± 29	1147 ± 13	910 ± 11	5.12 ± 0.001

The specimens, schematised in Figure 1, were synthesised by Laser CUSING (Concept Laser GmbH, Lichtenfels, Germany) from a Concept Laser M3 linear printing system at a sintering scan speed of 200 mm/s. The layers were deposited vertically on a base plate in the direction of load application. After production, and before fatigue testing, surfaces were mechanically polished to a scratch-free condition.

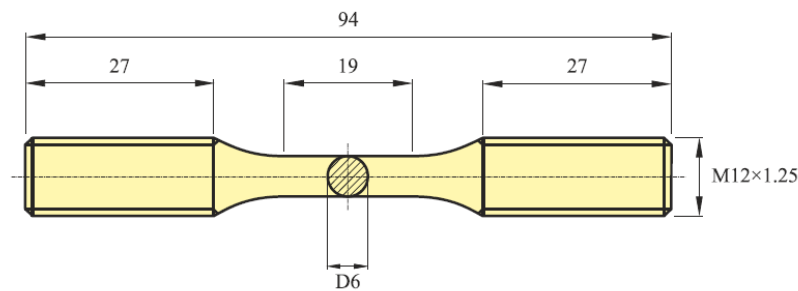


Figure 1. Specimen geometry of the low-cycle fatigue tests (dimensions in mm).

Low-cycle fatigue tests were performed according to the recommendations of ASTM E606 in a 100 kN closed-loop servo-hydraulic testing machine (Zwick, Hereford, UK), under fully-reversed strain-controlled conditions ($R_\epsilon = -1$), with sinusoidal waveforms, and a constant strain rate ($d\epsilon/dt$) of $8 \times 10^{-3} \text{ s}^{-1}$. The strain amplitudes, as indicated in Table 3, lied in the range 0.3–1.0%.

The stress–strain response was acquired from a 12.5 mm-long gauge extensometer (model Instron 2620-601, Instron, Norwood, MA, USA), clamped directly to the gauge section of the specimen via two separated knife-edges, and connected to a digital data acquisition system. Each specimen was subjected to a constant strain amplitude until failure occurs. Tests were interrupted when specimens separated into two pieces.

Fracture surfaces were observed by scanning electron microscopy (Quanta FEG 450, Trondheim, Norway) to identify the main fatigue damage mechanisms. Samples were sectioned perpendicularly to the longitudinal axis of the specimen, and ultrasonically cleaned in trichloroethylene solution for ten minutes.

The material, in the as-received condition, following the recommendations outlined in ASTM E407-99, was examined by optical microscopy (Zeiss Axiotech 100HD microscope, Zeiss, Jena, Germany) to characterise the microstructure, and the level of porosity. Samples were etched with Picral, i.e., picric acid solution (4%) in ethyl alcohol, for 2 min.

Table 3. Summary of low-cycle fatigue program.

Specimen Reference	Total Strain Amplitude, $\Delta\epsilon/2$ (%)	Elastic Strain Amplitude, $\Delta\epsilon_e/2$ (%)	Plastic Strain Amplitude, $\Delta\epsilon_p/2$ (%)	Stress Amplitude, $\Delta\sigma/2$ (MPa)	Plastic Strain Energy Density, ΔW_p (MJ/m ³)	Total Strain Energy Density, ΔW_T (MJ/m ³)	Number of Cycles to Failure, N_f
D100	1.005	0.5975	0.4077	1005.0	11.920	14.803	33
D090	0.905	0.5891	0.3163	990.8	8.992	11.743	64
D080	0.807	0.5984	0.2087	1006.5	5.663	8.703	40
D060	0.609	0.5442	0.0644	915.3	1.478	3.988	129
D050	0.511	0.4764	0.0349	801.3	0.420	2.501	145
D040	0.411	0.4035	0.0080	678.7	0.115	1.561	1087
D035	0.362	0.3584	0.0034	602.8	0.094	1.205	2399
D030	0.304	0.3050	0.0012	512.9	0.078	0.863	5441

3. Results and Discussion

3.1. Microstructure and Porosity

The metallography in the longitudinal section of the sample, for different degrees of magnification, is exhibited in Figure 2. The microstructure is rather coherent and is essentially formed by elongated grains with about 150 μm long and 30–35 μm width. It is also possible to observe a considerable level of small porosities, as well as the formation of martensitic needles identified by the red circles in Figure 2b,c. The percentage of porosity, quantified via the Image J software (version 1.6.0, National Institutes of Health, Bethesda, MD, USA), was about $0.74 \pm 0.09\%$. The *modus operandi* consisted of analysing contrast images (see Figure 2d) between the pores and the base material, obtained from the optical micrographs, and calculating the areas of each of those regions [9].

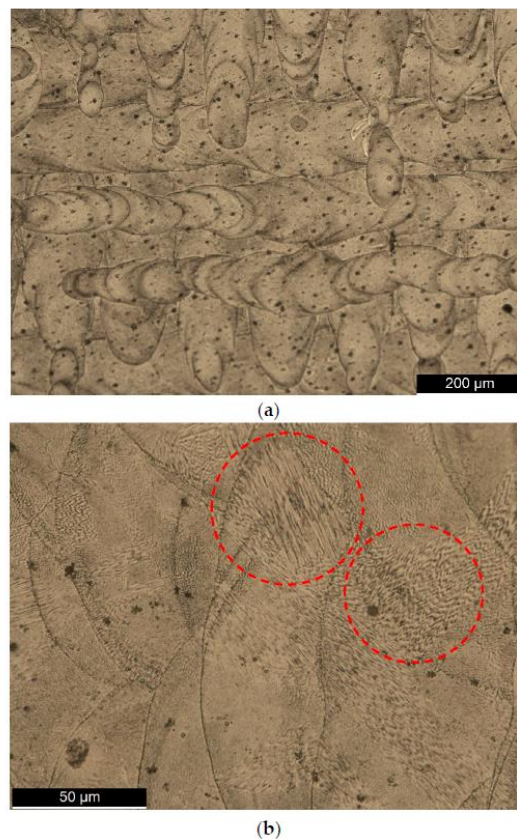


Figure 2. Cont.

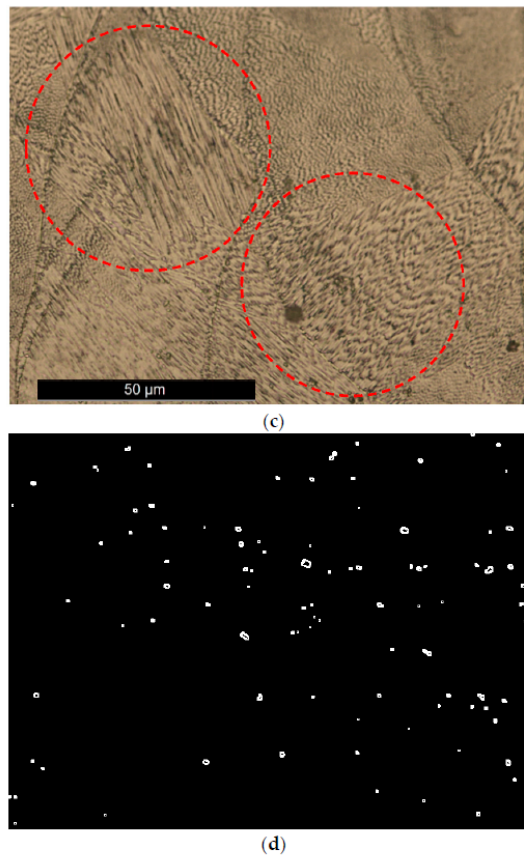


Figure 2. Optical micrographs of the AISI 18Ni300 maraging steel from a sample etched with Picral at magnifications of: (a) 100 \times ; (b) 500 \times ; (c) martensitic needles; (d) contrast image.

3.2. Cyclic Deformation Behaviour

Figure 3 presents the variations of peak, valley, and mean stresses with the life ratio at various strain amplitude levels, during the low-cycle fatigue tests. The peak stresses increase in a very short initial stage, only observable in the first 2–3 cycles; in a second stage, up to about 90% of life ratio, there is a continuous reduction of peak stresses at higher strain amplitudes, and a well-defined stable response at lower strain amplitudes; the third stage, for life ratios higher than 90%, shows an evident drop in peak stresses, irrespective of the applied strain amplitudes. The evolution of the valley stresses, as a function of the strain amplitudes, is also distinct: i.e., at higher strain amplitudes, the valley stresses progressively increase with the life ratio, while at lower strain amplitudes the valley stresses remained essentially constant. Regarding the mean stress, it slightly decreases with the number cycles throughout the entire test, regardless of the strain amplitude. In addition, higher strain amplitudes result in lower mean stresses.

The plastic strain energy density per cycle, accounted for as the area of the hysteresis loop, at various strain amplitudes is presented in Figure 4a. Figure 4b shows the total strain energy density per cycle, defined as the sum of the plastic and the tensile elastic strain energy density components. Overall, as can be seen from the figures, these parameters are quite stable over the course of its life. Initially, there is a slight softening region, more expressive at higher strain amplitudes, of about 10% of the total number of cycles followed by a saturated stage up to 90% of fatigue life, and a third region with small perturbations culminating in fatigue failure. The behaviour observed agrees with the

empirical rule proposed by Smith et al. [17] which states that metals with the tensile strength to yield strength ratios lower than 1.2 cyclically soften.

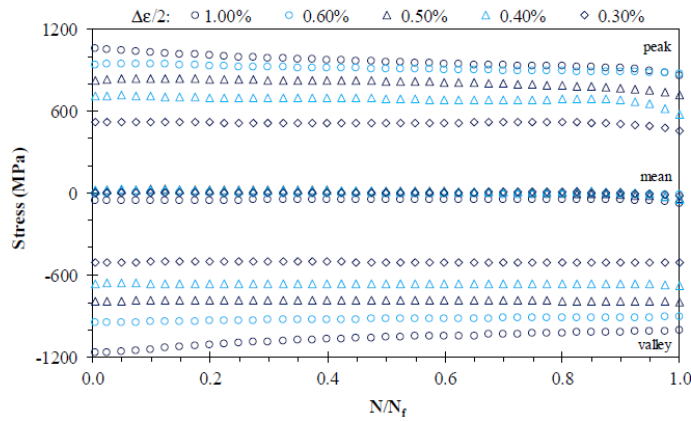


Figure 3. Variation of peak, valley, and mean stresses with the normalised fatigue life during the low-cycle fatigue tests at various strain amplitudes.

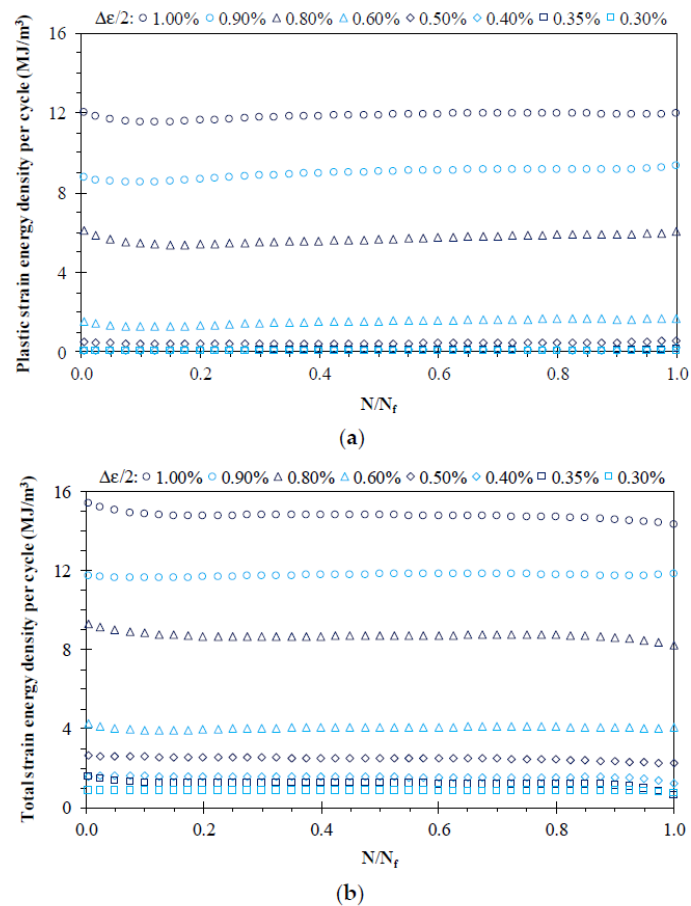


Figure 4. Variation of: (a) plastic strain energy density per cycle; (b) total strain energy density per cycle with the normalised fatigue life during the low-cycle fatigue tests at various strain amplitudes.

3.3. Cyclic Stress–Strain Response

The cyclic stress–strain response of the AISI 18Ni300 steel, relying on the fact that the saturated regime is achieved in the early stage of the tests, was studied via the data collected from the hysteresis loops at the half-life. Table 3 summarises the stress and strain amplitudes, as well as the plastic and the total strain energy densities experimentally measured from the selected circuits. Figure 5a displays the saturated cycles, in relative coordinates, with the lower tips tied together. Since the upper branches at different strain amplitudes do not follow a unique curve, the material does not exhibit Masing-type behaviour, being therefore a non-Masing material. The non-Masing effect is associated with the changes in the linear region of the stable circuits. This is clearly visible in Figure 5b, which shows the stable circuits, in relative coordinates, with the upper branches overlapped. In fact, regardless of the strain amplitude, there is a significant reduction of the linear region. This is usually associated with the formation of dislocation cells [18]. The dashed lines, plotted only for the four higher strain amplitudes, allow inferring the closeness of the stable circuits in relation to perfect Masing-type loops. As can be seen, the differences in the areas is appreciable, and the conversion of such circuits into Masing-type ones would require the increments of linear response represented by the dashed red lines. For the cases represented, i.e., strain amplitudes higher than 0.50%, the areas of the stable circuits area about 40–45% of the ideal ones.

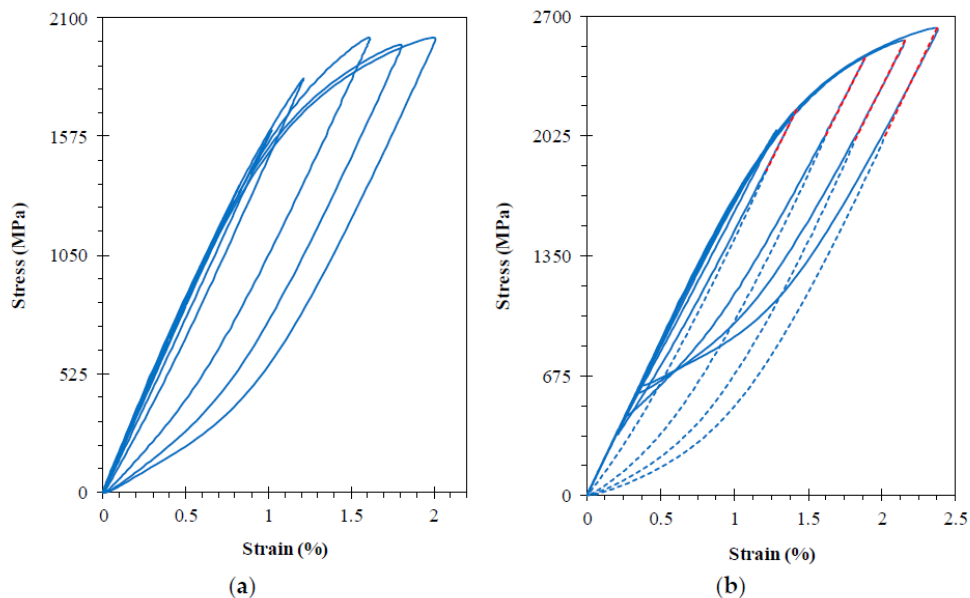


Figure 5. Mid-life circuits at different strain amplitudes with (a) lower tips tied together; (b) upper branches overlapped.

Figure 6 exhibits the relationship between the cyclic stress amplitude and the plastic strain amplitude. As first suggested by Morrow [19], this relationship can be described by a power-law:

$$\frac{\Delta\sigma}{2} = k' \left(\frac{\Delta\varepsilon_p}{2} \right)^{n'} \quad (1)$$

where k' is the cyclic hardening coefficient, and n' is the cyclic hardening exponent. Both constants were determined by linear regression, using the least square method, with a correlation coefficient equal to 0.982, and are given in Table 4.

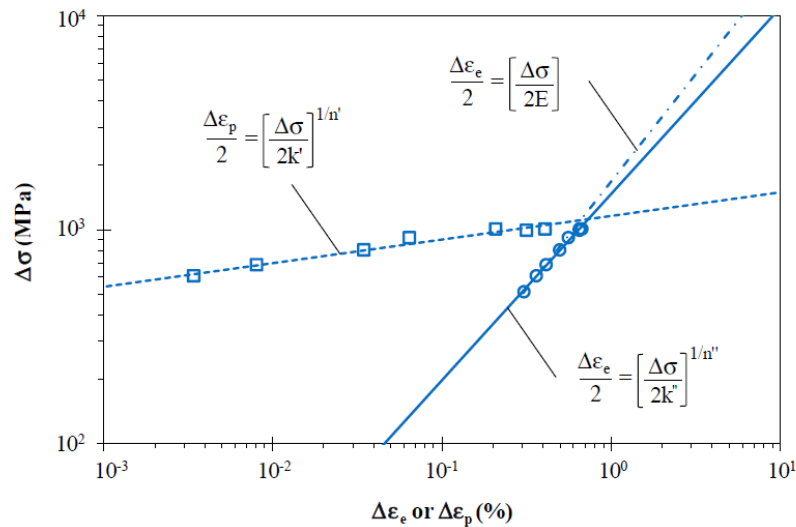


Figure 6. Relation between the cyclic stress amplitude and the elastic and plastic strain amplitude obtained using both the unloading moduli measured in the tests (dashed line) and the value of E determined from the monotonic tensile test (dash-dotted line).

Table 4. Cyclic mechanical properties of AISI 18Ni300 steel manufactured with a scan speed of 200 mm/s.

k' (MPa)	n'	k'' (MPa)	n''
1921.21	0.1100	80,146	0.8706

The slopes of the curves of the hysteresis loops at the start of the loading cycle and immediately after the load reversal are assumed to be equal. Nevertheless, for cyclic loading, this is not entirely true. The effective elastic unloading modulus (E''), defined as the slope of the linear portion of the stable hysteresis loop after strain reversal, is affected by the cyclic properties of the material. Figure 6 plots the cyclic stress amplitude against the elastic strain amplitude using the unloading moduli measured in the tests (dash-dotted line). The relation between these two variables, as already demonstrated in the literature [20–22], can be defined from a power law relationship similar to that of Equation (1). The coefficients, obtained using a best fitting technique with a correlation factor of 0.998, are listed in Table 4. For comparison purposes, a linear relationship determined with the value of E is also displayed. Therefore, not surprisingly, there is a clear variation of the unloading modulus with the strain amplitude, which denotes nonlinear behaviour not only in the plastic regime, but also in the elastic regime.

Figure 7a presents the cyclic stress–strain curve, written in the form:

$$\frac{\Delta\epsilon}{2} = \frac{\Delta\sigma}{2E} + \left(\frac{\Delta\sigma}{2k'}\right)^{1/n'} \quad (2)$$

where k' and n' are, respectively, the cyclic hardening coefficient and exponent (see Table 4). In most of the cases investigated, this alloy exhibits a softening behaviour once the experimental points are below the monotonic curve. The degree of softening (S) is relatively small in the entire range and was estimated by the difference between the stress amplitudes of the first and the mid-life cycles. The outcome of this analysis is shown in Figure 7b. The values of S are relatively small in the entire range. Initially, the amount of softening decreases progressively for strain amplitudes in the interval 0.3–0.4%, except for $\Delta\epsilon/2 = 0.5\%$, and then it increases rapidly to the maximum value, followed by a

new reduction. The same calculations performed on the basis of the stress amplitudes of the cyclic stress–strain curve, instead of the stable circuits, are represented by the dashed line. On average, the results are similar, and the variations with the strain amplitude in a qualitative analysis are identical.

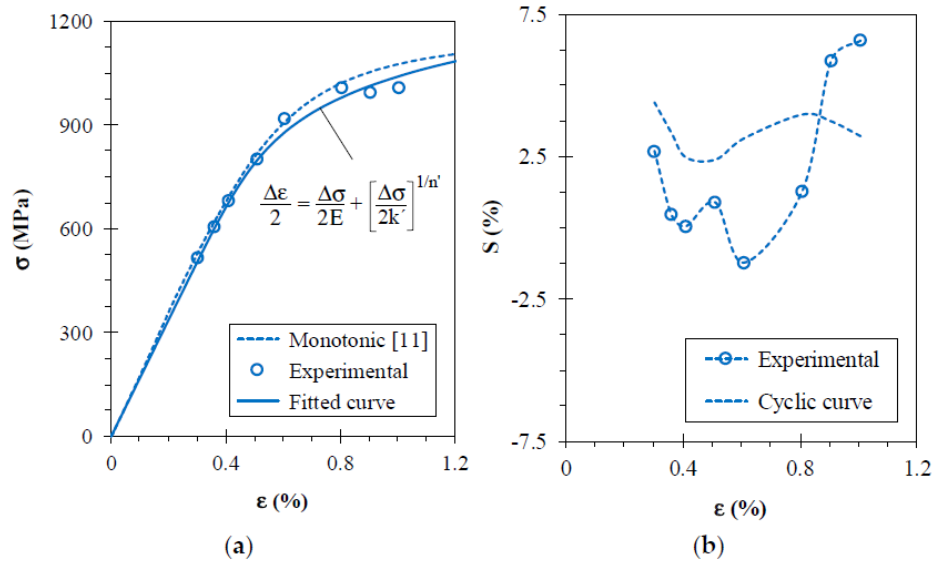


Figure 7. (a) Cyclic stress–strain curve of the AISI 18Ni300 steel; (b) degree of softening versus strain amplitude.

3.4. Strain–Life Relationship

The variation of elastic, plastic, and total strain amplitudes with the number of reversals to failure is shown in Figure 8. Based on the well-known Basquin and Coffin–Manson formulations, the fatigue mid-life and the total strain can be related as follow:

$$\frac{\Delta\varepsilon}{2} = \frac{\Delta\varepsilon_e}{2} + \frac{\Delta\varepsilon_p}{2} \Leftrightarrow \frac{\Delta\varepsilon}{2} = \frac{\sigma'_f}{E} (2N_f)^b + \varepsilon'_f (2N_f)^c \quad (3)$$

where σ'_f is the fatigue strength coefficient, b is the fatigue strength exponent, ε'_f is the fatigue ductility coefficient, and c is the fatigue ductility coefficient. The unknowns, evaluated by linear regression using the least square method, are listed in Table 5. Very satisfactory correlation factors were found for the Basquin ($r = 0.975$) and the Coffin–Manson ($r = 0.981$) relationships. The low transition life, only 35 reversals, is far below the typical values of conventional materials with equivalent monotonic mechanical properties. This results from the combination of high strength and low ductility. For example, this value is two orders of magnitude below the transition life of the DIN 34CrNiMo6 [23] high strength steel ($2N_T = 3038$) which has a tensile strength slightly slower ($\sigma_{UTS} = 1035$ MPa) than the AISI 18Ni300 ($\sigma_{UTS} = 1147$ MPa).

Table 5. Fatigue strength and fatigue ductility parameters of AISI 18Ni300 steel manufactured with a scan speed of 200 mm/s.

σ'_f (MPa)	b	ε'_f	c
1798.73	−0.1311	0.32784	−1.0941

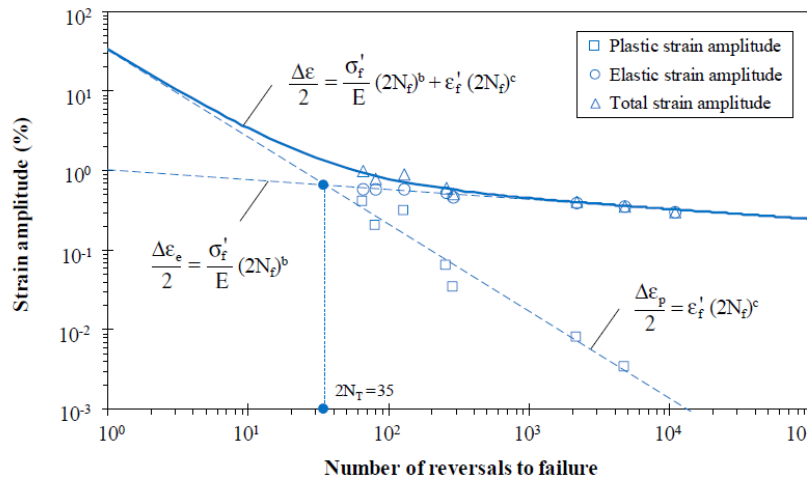


Figure 8. Total, plastic, and elastic strain amplitudes versus number of reversals to failure.

3.5. Energy-Life Relationship

Energy-based approaches assume that the dissipated strain energy density per cycle is a main contribution to the fatigue damage process. Both the plastic strain and the total strain energy densities, as demonstrated in Figure 4, are almost constant throughout the lifetime. This property is advantageous, since it can be used to directly estimate the accumulated fatigue damage through the energy dissipation. Figure 9a exhibits, in a log–log scale, the plastic strain energy density at the mid-life cycle against the number of reversals to failure. The relation between the variables mentioned above can be described by a power-law, i.e.,

$$\Delta W_p = \kappa p (2N_f)^{\alpha p} \tag{4}$$

where κp and αp are fitting constants, which were determined using a best fit technique, and are summarised in Table 6. Although there is some scatter, the correlation coefficient ($r = 0.941$) is satisfactory. For non-Masing materials, the value of ΔW_p [24] can be estimated using the formula:

$$\Delta W_p = \frac{1 - n^*}{1 + n^*} \Delta\sigma \Delta\epsilon_p + \frac{2n^*}{1 + n^*} \delta\sigma_0 \Delta\epsilon_p \tag{5}$$

where n^* is the hardening exponent of the master curve and $\delta\sigma_0 = \Delta\sigma - \Delta\sigma^*$. The master curve is a unique curve defined by matching the upper branches of the hysteresis loops at different strain amplitudes (see Figure 5b). As can be seen, the differences relative to the experimental measurements are relative small.

Table 6. Energy-based properties of AISI 18Ni300 manufactured with a scan speed of 200 mm/s.

κp (MJ/m ³)	αp	κt (MJ/m ³)	αt	ΔW_0^{c+} (MJ/m ³)
513.400	−1.0196	140.667	0.5974	0.2287

The plastic strain energy density, as a fatigue damage parameter, is most appropriate under high strain levels, since it is difficult to measure close to the fatigue limit, resulting in higher errors and improper fatigue life assessments. Figure 9b presents the total strain energy density against the number of reversals to failure. The fitted function of ΔW_p is also plotted for the sake of clarity. The total strain

energy density is accounted for by the sum of the plastic and the tensile elastic strain energy densities of the mid-life hysteresis loops. It can be written as follows:

$$\Delta W_T = \kappa t (2N_f)^{\alpha t} + \Delta W_0^{e+} \quad (6)$$

where κt and αt are constants, and ΔW_0^{e+} is the tensile elastic energy at the material fatigue limit estimated here at $2N_f = 10^7$. The values of the coefficients are given in Table 6. Overall, the fitted function agrees well with the experimental observations. This formulation, unlike the former, can be used either in low- or high-cycle fatigue regime, and is sensitive to the mean stress. In a recent study, the fatigue crack initiation life in round bars with U-notches subjected to combined bending-torsion loading was predicted using this approach [25].

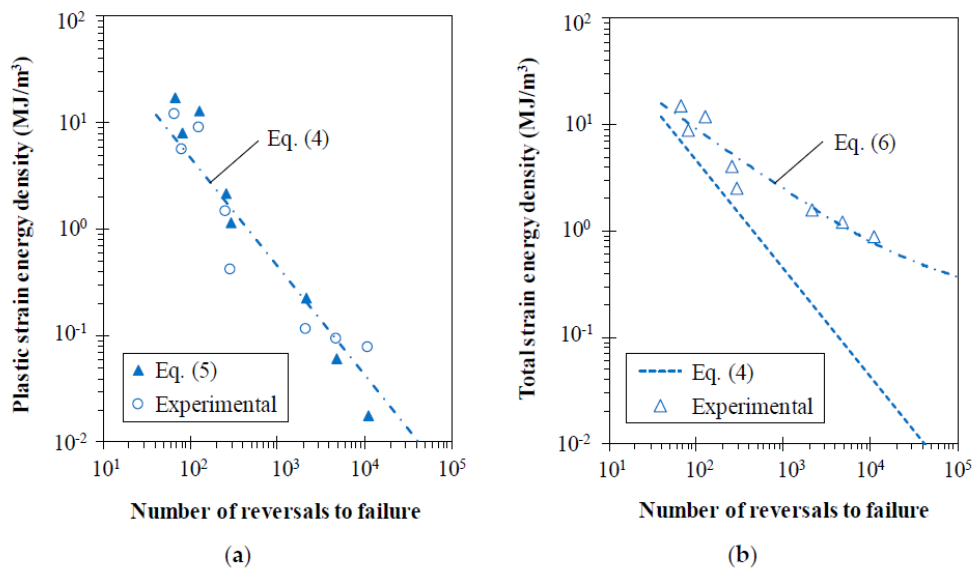


Figure 9. (a) Plastic strain energy density versus number of reversals to failure; (b) Total strain energy density versus number of reversals to failure for the mid-life hysteresis loops.

Regarding components having complex geometries, no specific design criteria have been presented so far to consider stress concentration phenomena arising from geometrical discontinuities [14,15]. Hence, the same methodology can be examined in future for the notched specimens produced by additive manufacturing.

3.6. Analysis of Fracture Surfaces

The fracture surfaces of the samples were investigated by scanning electron microscope (SEM). SEM fractographs of the specimens tested under 0.60% strain amplitudes are shown in Figures 10 and 11. Figure 10 illustrates the texture of the fracture surface of the sintered test samples, i.e., the shape and orientation of the particles deposited in each layer. Severe defects (e.g., voids and unmolten particles) in the material act as crack initiation points (see Figure 11). Hence, for almost all of samples, the fatigue crack initiated from the surface or inner defects and propagated through the cross section. According to Figure 10b,c, the fatigue crack initiation was characterized by considerable percentage of cleavage with a few number of dimples. While the inner cross section of the tested samples was mainly dominated by the ductile mode of fracture and characterized with ductile dimples and microvoids. A ductile/brittle fracture with a predominance of brittle fracture can be observed in the samples owing to the presence of the defects, which make it easier to spread the microcracks.

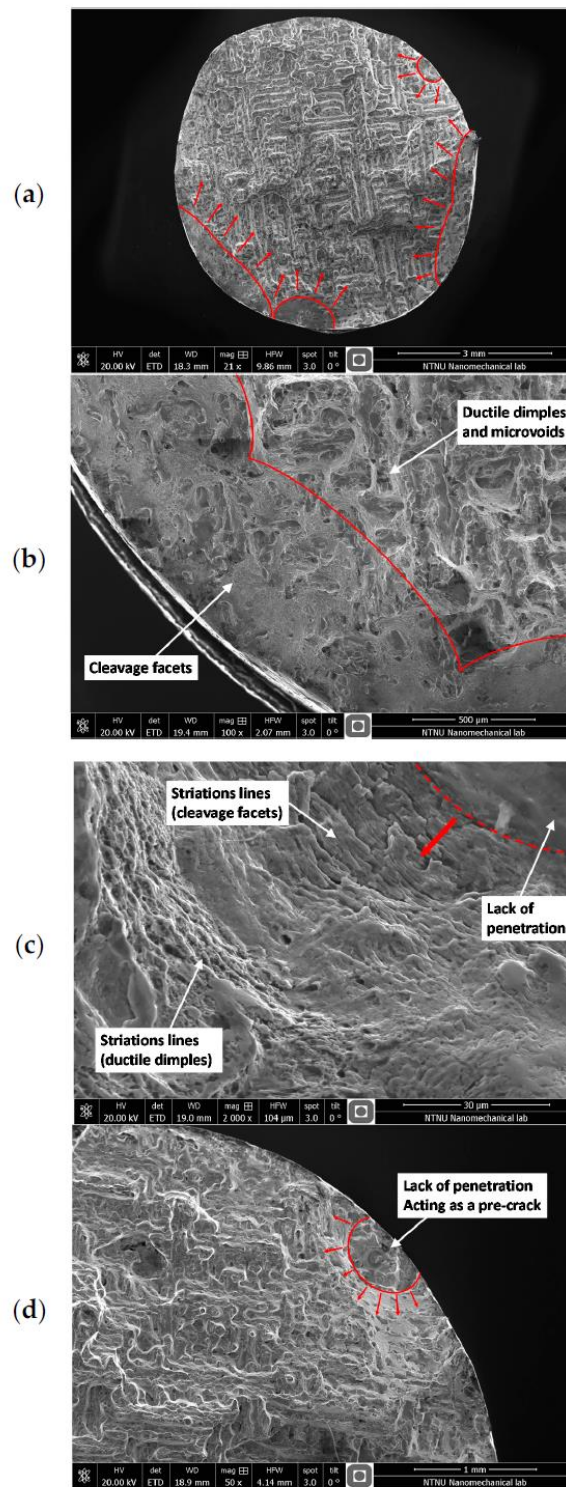


Figure 10. SEM photographs of the tested samples showing multi-nucleation of fatigue cracks from surface (a–c) and crack initiation from a defect (d). The red arrows illustrate the direction of fatigue crack propagation.

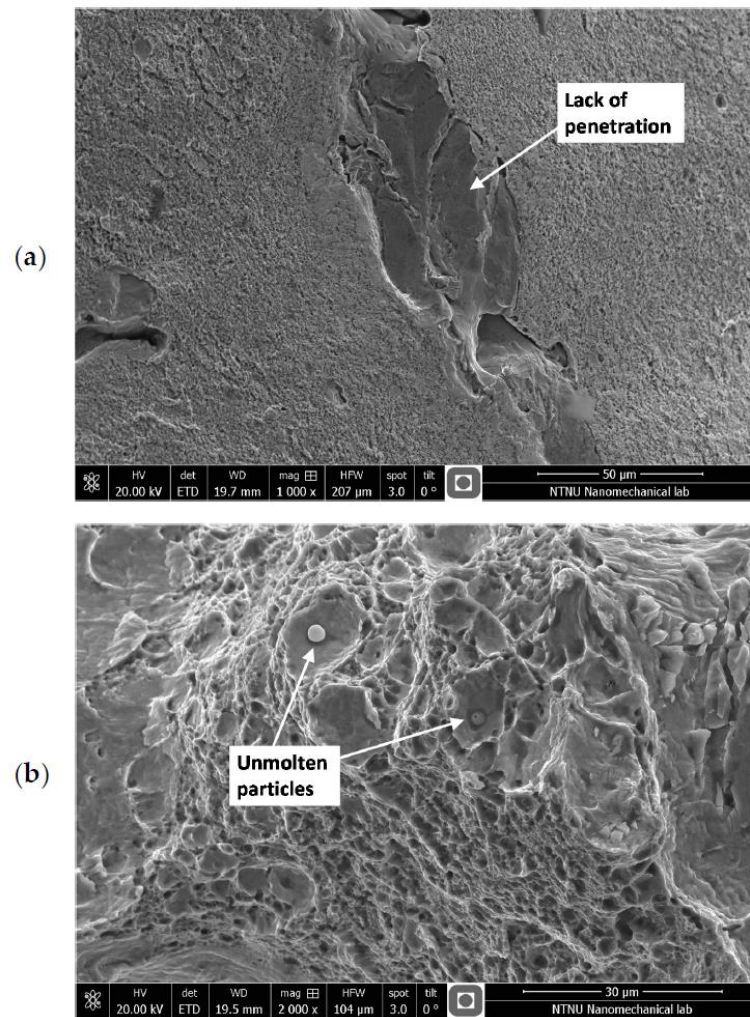


Figure 11. Common defects observed on fracture surface: (a) lack of penetration, and (b) unmolten particles.

4. Conclusions

The paper addressed the low-cycle fatigue behaviour of AISI 18Ni300 steel manufactured by selective laser melting with a scan speed of 200 mm/s. A series of fully-reversed, strain-controlled tests at room temperature were conducted at strain amplitudes ranging from 0.3% to 1.0% in circular cross-section specimens. Before testing, the microstructure in the as-received form was analysed by optical microscopy. After testing, fracture surfaces were examined by scanning electron microscopy. The following conclusions can be drawn:

1. The microstructure was rather coherent and formed by elongated grains. High level of small porosities, as well as the existence of martensitic needles, was also observed.
2. The cyclic stresses response increased in a very short initial stage of about 2–3 cycles; then, it decreased continuously at higher strain amplitudes and remained almost constant at lower strain amplitudes; in a third stage, for life ratios higher than 90%, there was a rapid drop in cyclic stresses.

3. The plastic strain energy density per cycle was quite stable over the entire life. Initially, there was a slight softening region of about 10% of the total number of cycles; followed by a saturated region up to 90% of fatigue life; and a third region with small perturbations culminating in fatigue failure.
4. The mid-life hysteresis loops, bearing in mind that the saturated regimes are achieved in the early stage of the tests, can be selected as representative of the stable behaviour.
5. The degree of softening, evaluated from the maximum stress of the first and the mid-life circuits, was relatively small in the entire strain range studied. In a first stage, at smaller strain amplitudes, the degree of softening decreased; and, in a second stage, for strain amplitudes higher than 0.5%, it increased progressively to the maximum value of about 7%.
6. The material exhibited a non-Masing behaviour which was associated with the changes in the linear region of the stable circuits, possibly caused by the formation of dislocation cells. The areas of the stable loops, for strain amplitudes higher than 0.5%, were about 40–45% of the perfect Masing-type circuits.
7. The increase in strain amplitude decreased the unloading modulus. This is evidence of non-linear behaviour in both the elastic and the plastic regimes.
8. The very low transition life of about 35 reversals was far below the values of conventional materials with equivalent monotonic mechanical properties, which can be attributed to the combination of high strength and low ductility.
9. The plastic strain energy density at mid-life cycle can be satisfactorily related with the number of cycles to failure from a power-law. The total strain energy density, accounted for by the sum of the plastic and the tensile elastic strain energy densities of the mid-life hysteresis loops, is an adequate parameter for both high- and low-cycle fatigue regimes.
10. SEM analysis revealed that the fatigue crack nucleated from the surface and defects within the material. The presence of an unmolten area in the material led to a predominant brittle fracture mechanism in all the tested samples. Crack initiation was dominated by cleavage facets which was followed by ductile dimples and microvoids due to crack extension to the inner part of cross section.

Acknowledgments: The authors would like to acknowledge the sponsoring under the project No. 016713 (PTDC/EMS-PRO/1356/2014) financed by Project 3599: Promover a Produção Científica e Desenvolvimento Tecnológico e a Constituição de Redes Temáticas (3599-PPCDT) and FEDER funds.

Author Contributions: José D. M. Costa performed the low-cycle fatigue tests; José A. Martins Ferreira, Carlos Capela and Luís Santo analysed the microstructure; Filippo Berto and Seyed Mohammad Javad Razavi examined the fracture surfaces; Ricardo Branco and Fernando Antunes analysed the results; Ricardo Branco, Filippo Berto and Seyed Mohammad Javad Razavi wrote the paper.

Conflicts of Interest: The authors declare no conflict of interest.

References

1. Santos, E.C.; Shiomi, M.; Osakada, K.; Laoui, T. Rapid manufacturing of metal components by laser forming. *Int. J. Mach. Tools Manuf.* **2006**, *46*, 1459–1468. [[CrossRef](#)]
2. Yadroitsev, I.; Bertrand, P.; Smurov, I. Parametric analysis of the selective laser melting process. *Appl. Surf. Sci.* **2007**, *253*, 8064–8069. [[CrossRef](#)]
3. Abe, F.; Osakada, K.; Shiomi, M.; Uematsu, K.; Matsumoto, M. The manufacturing of hard tools from metallic powders by selective laser melting. *J. Mater. Process. Technol.* **2001**, *111*, 210–213. [[CrossRef](#)]
4. Wang, Y.; Bergstrom, J.; Burman, C. Four-point bending fatigue behaviour of an iron-based laser sintered material. *Int. J. Fatigue* **2006**, *28*, 1705–1715. [[CrossRef](#)]
5. Leuders, S.; Thöne, M.; Riemer, A.; Niendorf, T.; Tröster, T.; Richard, H.; Maier, H. On the mechanical behaviour of titanium alloy TiAl6V4 manufactured by selective laser melting: Fatigue resistance and crack growth performance. *Int. J. Fatigue* **2013**, *48*, 300–307. [[CrossRef](#)]

6. Sehrt, J.; Witt, G. Dynamic strength and fracture toughness analysis of beam melted parts. In Proceedings of the 36th International MATADOR Conference, Manchester, UK, 5–7 July 2010; pp. 385–388.
7. Crococolo, D.; de Agostinis, M.; Fini, S.; Olmi, G.; Vranic, A.; Ciric-Kostic, S. Influence of the build orientation on the fatigue strength of EOS maraging steel produced by additive metal machine. *Fatigue Fract. Eng. Mater. Struct.* **2016**, *39*, 637–647. [[CrossRef](#)]
8. Stoffregen, H.; Butterweck, K.; Abele, E. Fatigue analysis in selective laser melting: Review and investigation of thin-walled actuator housings. In Proceedings of the 25th Solid Freeform Fabrication Symposium, Austin, TX, USA, 4–6 August 2014.
9. Spierings, A.B.; Starr, T.L.; Wegener, K. Fatigue performance of additive manufactured metallic parts. *Rapid Prototyp. J.* **2013**, *19*, 88–94. [[CrossRef](#)]
10. Kasperovich, G.; Hausmann, J. Improvement of fatigue resistance and ductility of TiAl6V4 processed by selective laser melting. *J. Mater. Process. Technol.* **2015**, *220*, 202–214. [[CrossRef](#)]
11. Santos, L.M.S.; Ferreira, J.A.M.; Jesus, J.S.; Costa, J.M.; Capela, C. Fatigue behaviour of selective laser melting steel components. *Theor. Appl. Fract. Mech.* **2016**, *85*, 9–15. [[CrossRef](#)]
12. Yadollahi, A.; Shamsaei, N.; Thompson, S.; Elwany, A.; Bian, L. Effects of building orientation and heat treatment on fatigue behavior of selective laser melted 17-4 PH stainless steel. *Int. J. Fatigue* **2017**, *94*, 218–235. [[CrossRef](#)]
13. Walker, K.F.; Liu, Q.; Brandt, M. Evaluation of fatigue crack propagation behaviour in Ti-6Al-4V manufactured by selective laser melting. *Int. J. Fatigue* **2017**, *104*, 302–308. [[CrossRef](#)]
14. Razavi, S.M.J.; Ferro, P.; Berto, F. Fatigue assessment of Ti-6Al-4V circular notched specimens produced by selective laser melting. *Metals* **2017**, *7*, 291. [[CrossRef](#)]
15. Razavi, S.M.J.; Ferro, P.; Berto, F.; Torgersen, J. Fatigue strength of blunt V-notched specimens produced by selective laser melting of Ti-6Al-4V. *Theor. Appl. Fract. Mech.* **2017**, in press. [[CrossRef](#)]
16. Socie, D.; Marquis, G. *Multiaxial Fatigue*; Society of Automotive Engineers: Warrendale, PA, USA, 2000.
17. Smith, R.; Hirschberg, M.; Manson, S. *Fatigue Behaviour of Materials under Strain Cycling in Low and Intermediate Life Range*; NACA TN D-1574; National Advisory Committee for Aeronautics: Kitty Hawk, NC, USA, 1963.
18. Raouf, H.A.; Topper, T.H.; Plumtree, A. Cyclically plasticity and mising behaviour in metals and alloys. In Proceedings of the 4th International Conference of Fracture (ICF4), Waterloo, ON, Canada, 19–24 June 1977.
19. Morrow, J. Cyclic plastic strain energy and fatigue of metals. In *International Friction, Damping and Cyclic Plasticity*; ASTM STP 378; American Society for Testing and Materials: Philadelphia, PA, USA, 1965; pp. 45–87.
20. Ellyin, F. *Fatigue Damage, Crack Growth and Life Prediction*, 1st ed.; Chapman & Hall: London, UK, 1997; ISBN 0-412-59600-8.
21. Kujawski, D.; Ellyin, F. The effect of cyclic loading on the slope of the stress-strain immediately upon load reversal. *Res. Mech.* **1987**, *22*, 295–299.
22. Branco, R.; Costa, J.D.; Antunes, F.V.; Perdigão, S. Monotonic and cyclic behaviour of DIN 34CrNiMo6 martensitic steel. *Metals* **2016**, *6*, 98. [[CrossRef](#)]
23. Branco, R.; Costa, J.D.; Antunes, F.V. Low-cycle fatigue behaviour of 34CrNiMo6 high strength steel. *Theor. Appl. Fract. Mech.* **2012**, *58*, 28–34. [[CrossRef](#)]
24. Lefebvre, D.; Ellyin, F. Cyclic response and inelastic strain energy in low cycle fatigue. *Int. J. Fatigue* **1984**, *6*, 9–15. [[CrossRef](#)]
25. Branco, R.; Costa, J.D.; Berto, F.; Antunes, F.V. Fatigue life assessment of notched round bars under multiaxial loading based on the total strain energy density approach. *Theor. Appl. Fract. Mech.* **2017**, in press. [[CrossRef](#)]



© 2018 by the authors. Licensee MDPI, Basel, Switzerland. This article is an open access article distributed under the terms and conditions of the Creative Commons Attribution (CC BY) license (<http://creativecommons.org/licenses/by/4.0/>).

4. Main Results and Discussion of Fatigue Crack Growth in 18Ni300 Maraging Steel Alloy and Hybrid Formulations Built by Selective Laser Melting

4.1. Experimental Overview and Materials

In the following chapter, a new substrate material was introduced due to its lower mechanical properties, when compared with the previously used ones, to verify if there is any change in the fatigue behaviour of the hybrid specimens. See Table 4.1 for its chemical composition and Table 4.2 for mechanical properties.

Table 4.1: Chemical composition of the new substrate material in weight %, according to the supplier.

Alloy [AISI]	C	Ni	Co	V	Mo	Ti	Al	Cr	P	Si	Mn	Fe
CK45E	0.42	-	-	-	-	-	-	-	0.035	0.15	0.5	Balance

Table 4.2: Materials' monotonic tensile properties according to supplier.

Alloy [DIN]	Yield Stress [MPa]	UTS [MPa]	Strain at Break [%]
CK45E	420	670	16

Fatigue crack growth propagation was assessed using experimental tests on CT specimens and using the Finite Element Method.

The numerical approach was used to predict the Crack Tip Opening Displacement (CTOD) for CT specimens and the SLMed material hardening properties were assessed by low-cycle fatigue tests, using specimens according to Figure 4.1.

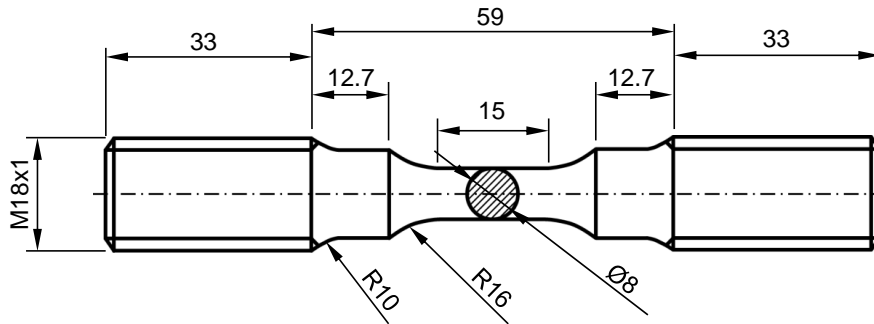


Figure 4.1: Low-cycle fatigue specimen's dimensions for the SLMed material.

The experimental fatigue crack growth propagation tests used CT specimens, like the ones depicted in Figure 4.1, and with dimensions previously indicated in Figure 3.5, with $a_0 = 7$, $e = 6$ and 3 mm, with an apparatus similar to the one from Figure 3.6. Fatigue Crack Growth Rates (FCGR) plotted as $da/dN-\Delta K$ curves, can be found below for the fully SLMed specimens subjected to post heat treatment and for the hybrid formulations too, in as printed condition.

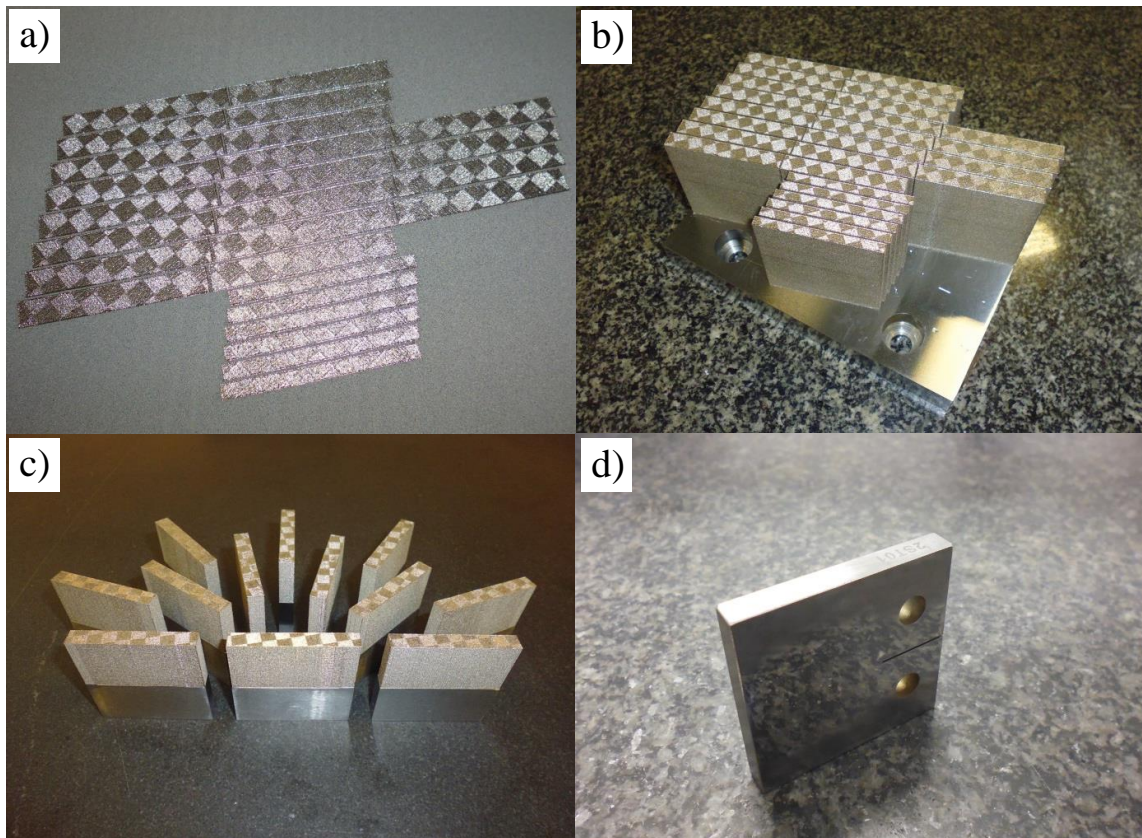


Figure 4.2: Example of CT specimens used in the different tests. In a) it is possible to observe one layer finished during the SLM process, it being possible to observe the CT specimens with a thickness of 3 and 6 mm, and in b) the respective build job after the SLM process, powder removal and still "welded" to the build plate, contrasting with the hybrid ones in c), that were produced individually "attached" to the substrate material. Finally, in d), it is a manufactured specimen ready to test, after grinding, after wired electro discharging process and polishing.

The crack closure phenomenon was assessed by experimental FCGR tests with different stress ratios and transient regimes were analysed after applying single and block overloads. They were performed for all specimens' formulations, using a micro gauge very close to the crack tip, see Figure 4.3.

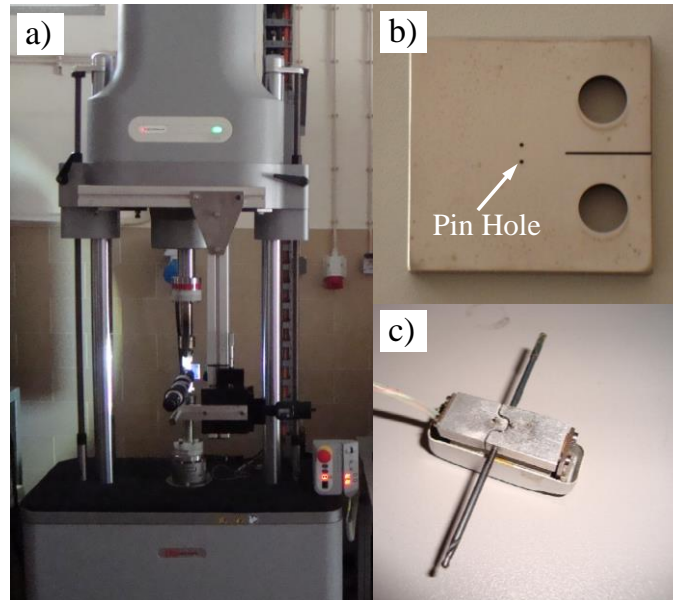


Figure 4.3: Instron EletroPuls E10000 testing machine (a) with an assembled traveling measuring device used for crack tip measurement and details of specimen assembling holes (b) for the micro gauge (c) used to measure the crack tip opening.

4.2. Microstructure Analysis of Hybrid Specimens and the Effect of the Age Hardening Heat Treatment of SLMed 18Ni300 Steel Alloy

The samples were prepared from CT specimens according to the best practices and standards such as those indicated in the different Appendices. For the “as printed” 18Ni300 material condition, the CT’s microstructure was similar to the one found in the round specimens, as previously mentioned in Chapter 3.1. This is valid for all the CT’s hybrid formulations interfaces, regarding the high strength steels AISI H13 and AISI 420, and regarding the new substrate made of CK45E mild steel.

Age hardening heat treatment, also known as precipitation hardening heat treatment, was performed to a batch of totally SLMed CT specimens, causing significant changes in the microstructure. The heat treatment has increased the microhardness by more than 25%, with HV1 = 495, and homogenised the microstructure and the layer interfaces, see Figure 4.4.

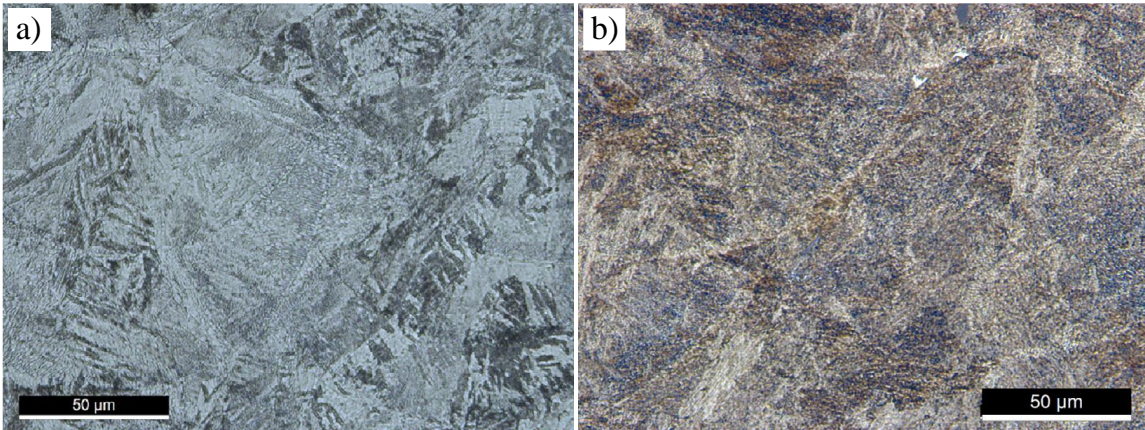


Figure 4.4: SLMed 18Ni300 microstructure in as printed (a) and heat-treated condition (b).

Another advantage of the heat treatment is related to the decrease in the residual stress inherent [Rafi *et al*, 2014] to the SLM process that could lead to stress cracks and to layer delamination [Merzelis *et al*, 2006]. From the assessment of the residual stress by the X-ray Diffraction technique, was possible to calculate a 30% decrease in the residual tensile stress (from 290 to 185 MPa), the maximum being next to the specimens' surface, becoming lower along its thickness, see Figure 4.5.

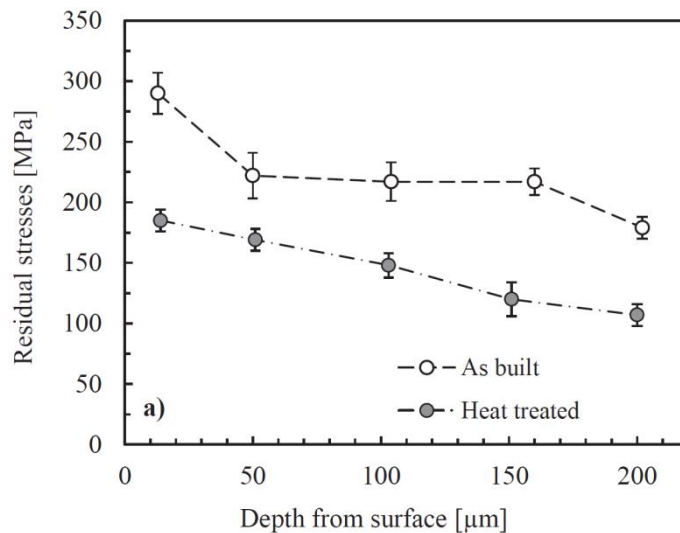


Figure 4.5: Comparison of residual tensile stress in as printed condition and after heat treatment for the SLMed 18Ni300.

4.3. Assessment of the FCG on a 18Ni300 Alloy in as Printed Condition and in Heat Treated Condition

CT specimens, built by SLM in AISI 18Ni300 maraging steel were used to assess the fatigue crack growth according to the ASTM E647 [ASTM, 2000] standard in order to plot da/dN - ΔK curves. Load control mode was used to run the tests at a loading rate of 25 Hz, using specimens with a thickness of 3 and 6 mm and with different stress ratios ($R = 0.05, 0.3$ and 0.6), see Table 2, Appendix IV. The crack displacement was recorded for a crack length (a) longer than 7 mm and the FCGRs were calculated through the five-point incremental polynomial method and plotted curves on a log-log scale, see Figure 4.6.

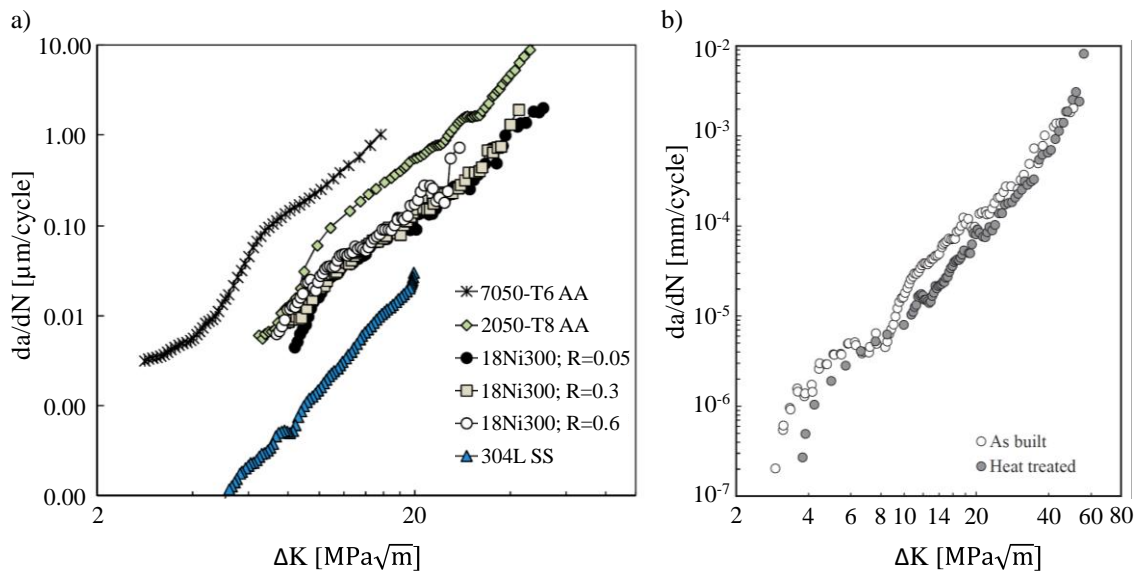


Figure 4.6: Experimental results comparison of SLMed 18Ni300 material da/dN - ΔK curves with different materials (a) and under different conditions (b) at $R=0.05$.

As expected, and as can be observed in Figure 4.6 b), it is possible to verify the existence of the Regime I, II and III. Near the threshold and for relatively small values of ΔK there is a quick reduction of da/dN values, followed by a linear region correspondent to the Regime II where the Paris Law is valid and following a region that resembles Regime III, where a small increase in the ΔK leads to a greater increase in the da/dN and to final rupture. The tests run with increasing stress ratios are indicating a slight increase of the FCGR, and the ones performed in different specimens' thicknesses have curves that are practically coincident, both results indicating a reduced level of "crack closure".

The FCG described by the Laird model [Laird *et al*, 1963; Laird, 1967], was the one adopted and widely accepted to define the phenomenon of fatigue crack propagation mechanism in Regime II of da/dN curves. This model indicates that a new fracture surface appears in the highly stressed concentration 45° region, due to the blunting induced by the plastic deformation in the crack tip. The slippage is partially reversed due to the compression stress at the crack tip, approaching fracture surfaces to each other, but without reconnecting the atomic bonds of the new fracture surface. The resulting linearity and slope of the curves in the Paris regime are quite similar if compared with others from different materials (Figure 4.6 a)), suggesting that the FCG mechanism is controlled by cyclic plastic deformation at the crack tip.

The respective $da/dN-\Delta K$ curves, with $R = 0.05$, and for as built and heat-treated specimen were assessed and reveal a decrease in the FCG rate of the heat-treated specimens near the threshold and in the Paris regime, see Figure 4.6 b). As stated before, this normal behaviour happens due to the microstructure's homogenization and to the lower residual stress, sees Figure 4.5, decreasing the effective loading stress ratio.

FCG tests were performed for the hybrid formulations too, built with substrates of AISI H13, AISI 420 and CK45E materials, under the same conditions with a $R = 0.05$, and the resulting $da/dN-\Delta K$ curves were superimposed with the ones for the SLMed 18Ni300 material. From their comparison, it is possible to say that the effect of the steel base in the fatigue crack growth for the entire ΔK is negligible for all the hybrid formulations. The reason for having similar FCG behaviour is because the crack always initiates in the root of the notch and always propagates next to the interface, but in the SMLed material. Because the SLMed material has always had a similar microstructure, chemical composition and being the less resistant, the crack is always growing towards this material. The AISI 420 steel base is mainly influencing the mean stress effect. This was evaluated comparing the $da/dN-\Delta K$ curves for different $R = 0.05, 0.3$ and 0.6 . Against the expectations, when comparing with other metal alloys, there was a negligible effect of the mean stress on the Paris stable regime, being only observable in Regime III when approaching the fracture toughness (K_{1c}) of the material, with a significant increase in the FCGR, see Figure 4.7.

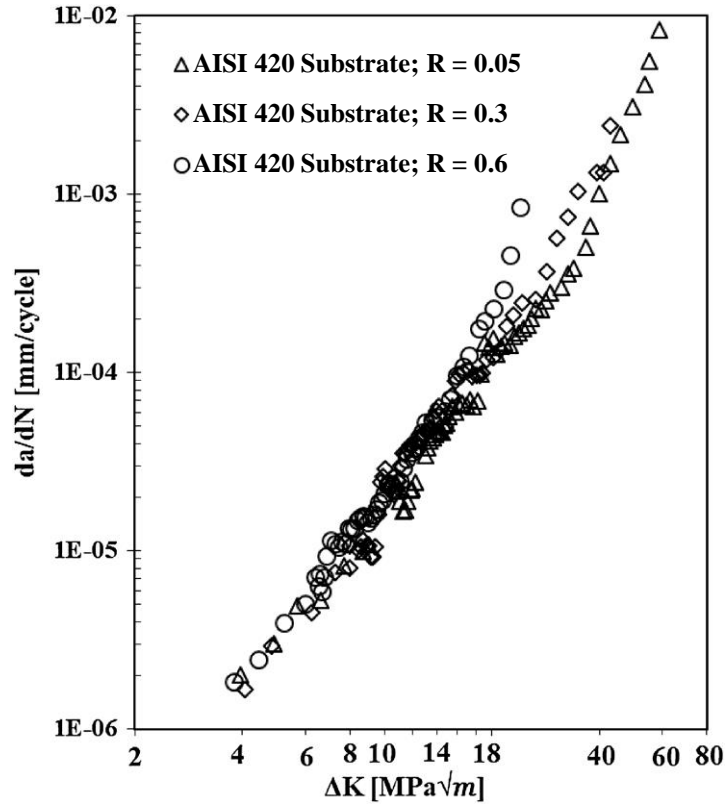


Figure 4.7: Mean stress influence in the da/dN - ΔK curves of the hybrid specimen built on top of an AISI 420 stainless steel substrate.

More tests were performed under the same conditions but only the data from da/dN - ΔK in the Paris regime were used for comparison and with superimposed overloads at 12 and 18 $\text{MPa}\sqrt{\text{m}}$ and overload ratio, $OLR = 2$, with decreased frequency of 0.5 Hz in the transient regimes for better accuracy and data acquisition, using a microgauge [Borrego *et al*, 2004; 2010] placed closer to the crack tip and registering load-displacement behaviour at specific crack lengths.

The OLR is defined by the following Equation 28:

$$OLR = \frac{\Delta K_{OL}}{\Delta K_{BL}} \quad (28)$$

where, ΔK_{OL} is the maximum peak stress intensity factor range and ΔK_{BL} is the baseline stress intensity factor range before the overload is applied.

The overloads were single applied and at blocks of 10 and 100 cycles, under load control and at constant R and ΔK for the SLM'ed specimens with and without heat treatment (single applied and

100 cycles), and for the hybrid formulations with steel bases of AISI H13, AISI 420 and CK45E (see materials properties on Table 3.1 and Table 4.1) and without heat treatment in terms of the SLMed and CK45E materials.

Using the maximization of the correlation coefficient technique [Allison *et al*, 1988; Borrego *et al*, 2003], enables the opening load (P_{op}) to be determined, corresponding to the point where the correlation coefficient reaches a maximum. Contrary to the behaviour usually seen in other alloys [Borrego *et al*, 2003; Borrego *et al*, 2005; Shin *et al*, 1993], from the plot of the correlation coefficient and the opening load during the loading fatigue cycle phase in Figure 4.8 [Luecke *et al*, 2014], it is possible to see that there is no defined maximum, meaning that it was not possible to observe any crack closure phenomenon, which usually justifies the retardation effect [Borrego *et al*, 2001; 2003; 2005; 2008; 2012] and justifying the little effect of the mean stress on the stable crack propagation regime.

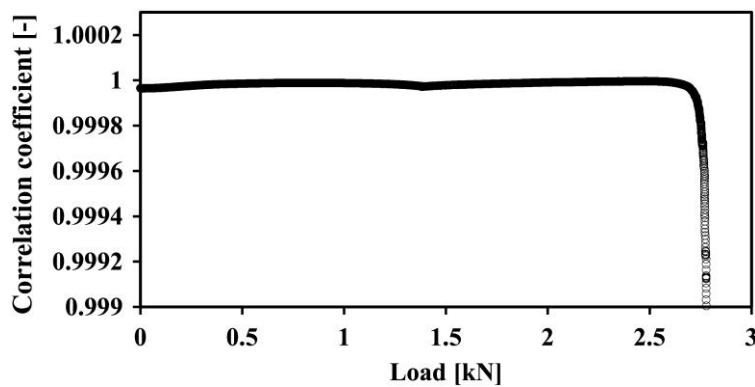


Figure 4.8: Opening load determination using the maximization of the correlation coefficient technique.

However, there is still crack growth retardation in the transient regimes. This retardation effect was more evident in the fully SLM'ed specimens in the as built condition for single applied overloads (Figure 4.9 a), but not for the heat-treated ones. The heat-treated specimens only showed relevant crack retardation when subjected to block overloads of 100 cycles (Figure 4.9 b).

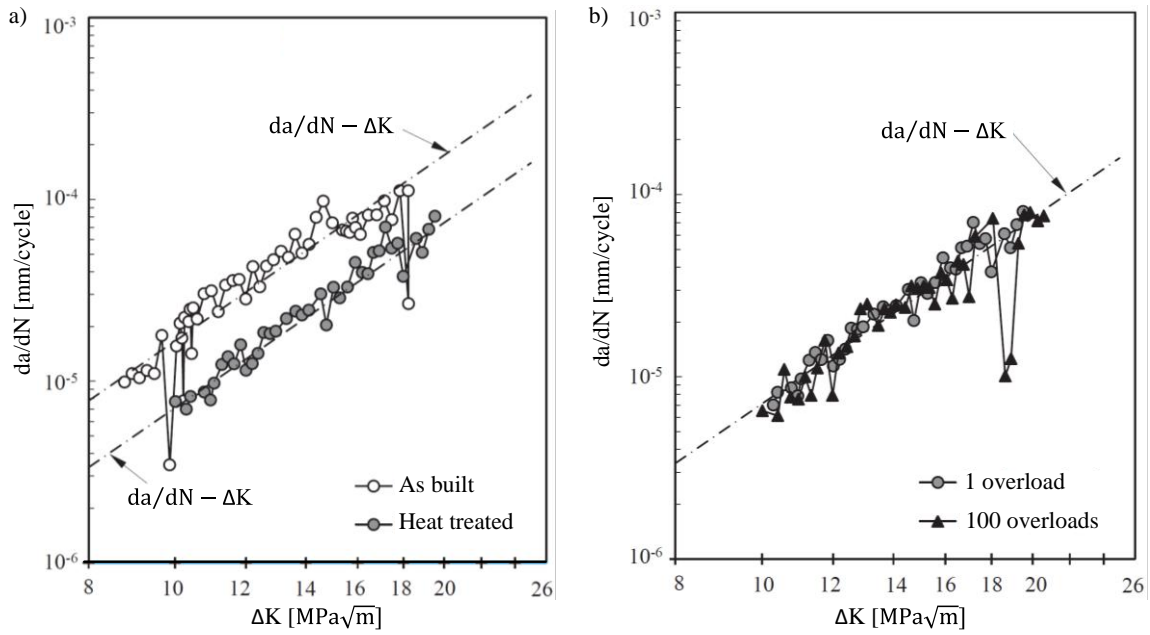


Figure 4.9: Transient regime after single overload with and without heat treatment (a) and the influence of block overloads in heat-treated specimens (b).

The retardation effect in the transient regime was also observed for the studied hybrid formulations. The retardation effect was very similar for the CK45E and AISI 420 hybrid formulations, independently from the steel base, due to the fact that the propagation is always happening in the same as built material. As it happened for the heat-treated specimens, the retardation effect increased for the AISI 420 hybrid formulation with applied overload blocks of 100 cycles for the studied ΔK baseline values (Figure 4.10 a).

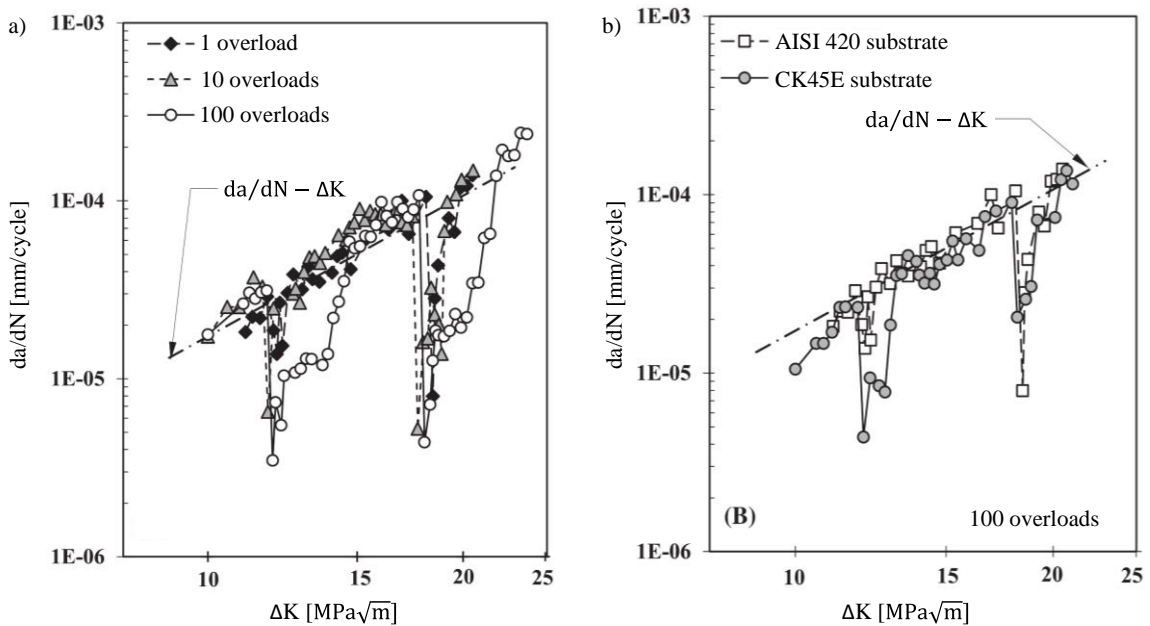


Figure 4.10: Transient regime after single and block overloads for specimens with an AISI 420 substrate (a) and the influence of the substrate when applying blocks of 100 overloads (b).

The retardation effect in the transient regimes could be explained by the crack branching/bifurcation [Suresh, 1983] contouring the deposited layers, rejoining later after the transient regime and continuing to grow in a “stable mode” (as prior to the overload) for both states of the SLMed material, with and without heat treatment, see Figure 4.11 a) and b) respectively. It is important to mention that the heat treatment reduces the crack propagation retardation effect in the transient regime after the overload, especially for lower ΔK values.

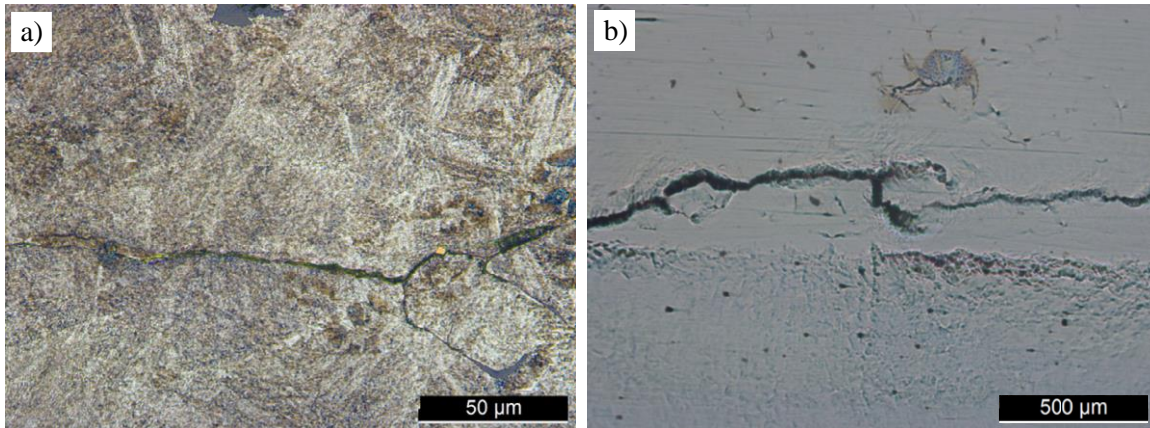


Figure 4.11: Crack path and bifurcation resulting from a single overload for heat-treated SLMed material (a) and for the hybrid formulation with a CK45E substrate.

4.4. FCG Numerical Analysis Based on Plastic CTOD (δ_p) for 18Ni300 Material in as Printed Condition

Low cycle fatigue tests were performed in order to have experimental stress-strain curves (check test details on Appendix IV), which are needed for an accurate modelling of elastic-plastic behaviour. This is critical to obtain feasible predictions of plastic CTOD in the FE numerical simulations. The elastic-plastic material model was based on Hooke’s law, Von Mises yield criterion (Equation 29), Cauchy stress tensor, Voce isotropic hardening law [Voce, 1948], Armstrong-Frederick non-linear kinematic hardening [Chaboche, 2008]. The fitting of material parameters was made by a minimization function based on least-squares method and using SOLVER tool from Microsoft Excel [Lasdon *et al*, 1975]. This fitting technique was already demonstrated with success in a research work from Antunes *et al*, 2017.

$$(\Sigma_{22} - \Sigma_{33})^2 + (\Sigma_{33} - \Sigma_{11})^2 + (\Sigma_{11} - \Sigma_{22})^2 + 3\Sigma_{23}^2 + 3\Sigma_{13}^2 + 3\Sigma_{12}^2 = 2Y^2 \quad (29)$$

where,

- Σ – effective stress tensor (see Equation 1, Appendix IV)
- Y – yield stress and its evolution during plastic deformation

The constants that were calculated throughout the process for the fitting stress-strain curve can be found in Table 3, Appendix IV.

The assessed experimental low-cycle fatigue stress-strain curve and the fitted one from the numerical iteration are depicted in Figure 4.12, showing a good agreement of the modelling procedure with the SLMed material properties.

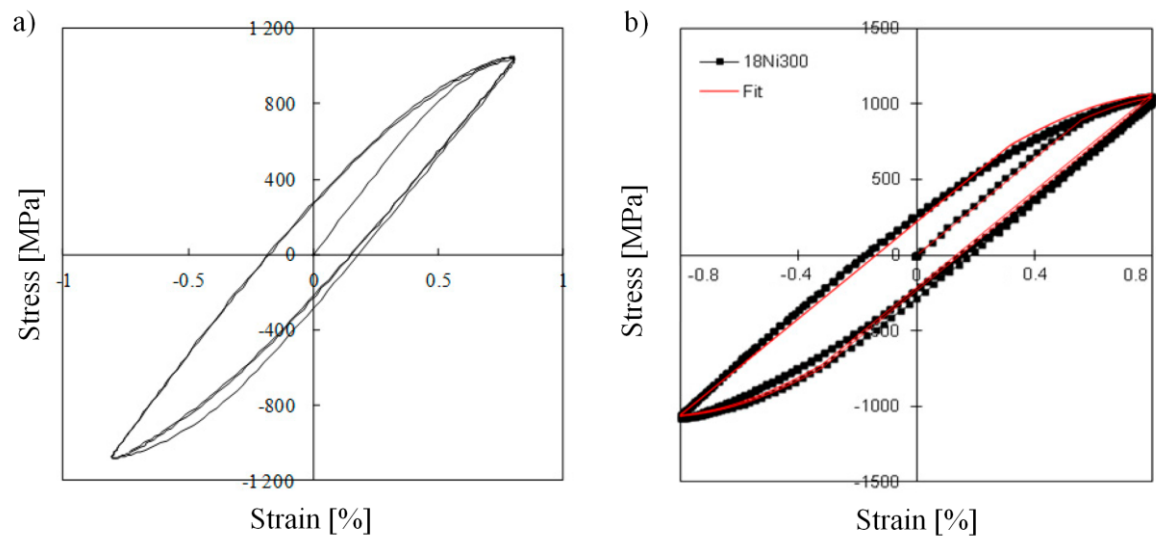


Figure 4.12: Experimental curve resulting from cyclic tests to acquire stress-strain relationship (a) and the superimposed numerical fitted curve (b).

For the FE numerical determination of plastic CTOD (δ_p), a model with $\frac{1}{4}$ of the size of the CT specimen was used, with a thickness of 0.1 mm. The boundary conditions are indicated in Figure 4.13. The simulation was done considering pure plane stress state, due to the relatively low thickness, and knowing from previous experimental tests that FCGR is practically unaffected by the specimen thickness. As with the experimental tests previously done for the CT specimen, the simulation was performed under load control conditions for different initial crack lengths (a_0), with remote loads according to the experimental tests and listed in Table 2, Appendix IV. The finite element mesh is also represented in Figure 4.13. Elements with $8 \times 8 \mu\text{m}^2$ were considered around crack path and only one layer of elements was considered along the thickness.

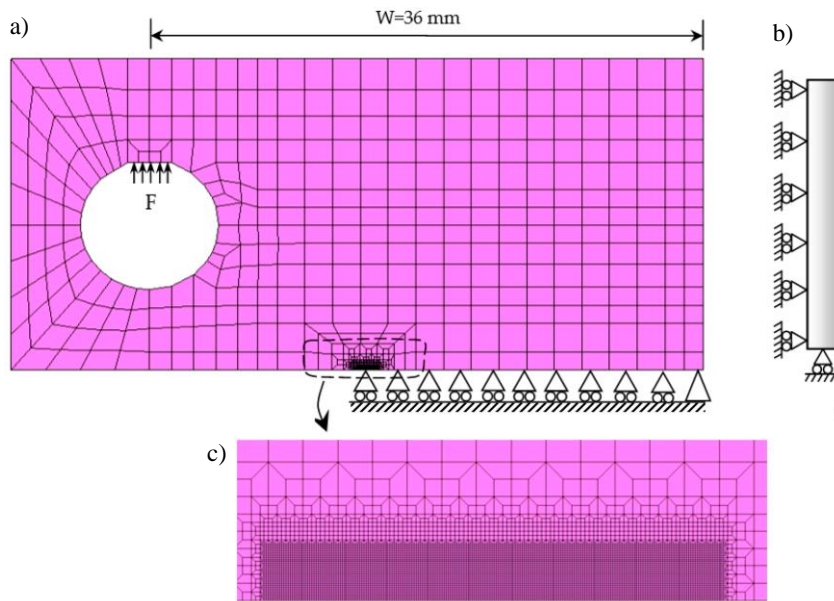


Figure 4.13: Representation of the FE model used to determine CTOD with loading conditions (a), boundary conditions for plane stress state (b) and detail of the refined finite element mesh (c).

Figure 4.14 shows CTOD predictions obtained for an initial crack length of $a_0 = 24 \text{ mm}$, subjected to 20 crack propagations, corresponding to a crack growth of $160 \text{ }\mu\text{m}$. To have a good representation of crack tip mechanisms, the CTOD was first measured at a distance of $8 \text{ }\mu\text{m}$ behind the crack tip. Several points were placed in Figure 4.14, from “A” to “D”, to define different regions of the CTOD simulation. “A” corresponds to the minimum load, where the crack is closed. Despite the increase in the load, the crack remains closed, i.e., with a $\text{CTOD} = 0$, until point “B”. From “B” to “C”, the crack starts to open linearly with the increase of the load. This load range is not effective, meaning that we are only opening the crack but not making it grow, since it corresponds to the linear elastic regime of the material. In “C”, plastic deformations start increasing with the load until it reaches “D”. “D”, which corresponds to the maximum load and to the maximum CTOD, is an inflection point, where the applied load starts decreasing. With the decrease of the load, it is possible to observe a region of reversed elastic deformation with a slope similar to the loading phase, and followed by a reversed plastic deformation. It is important to state that, supposedly, the elastic deformation does not affect the FCG, which is linked to the plastic CTOD.

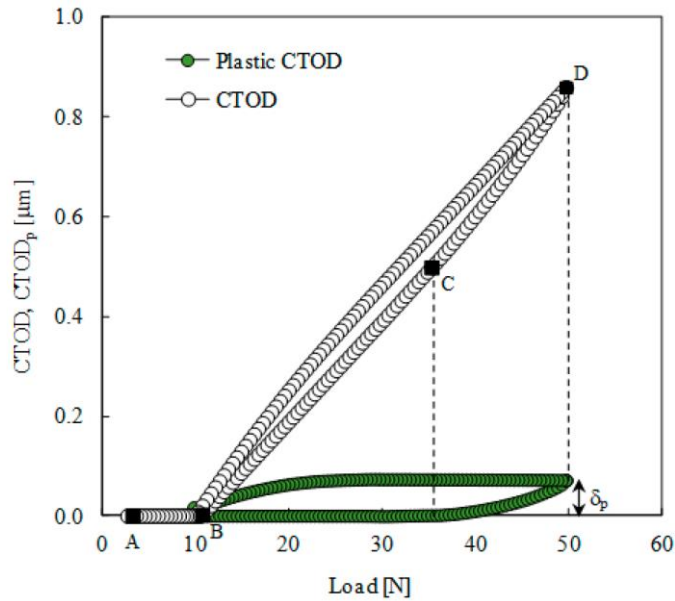


Figure 4.14: Representation of CTOD evolution under a remote single load at stress plane and with an initial crack length of $a_0 = 24$ mm.

From numerical simulations for different crack lengths, the evolution of plastic CTOD (δ_p) with the applied load range was depicted, see Figure 4.15. Relatively small levels of plastic deformation were detected, when compared with other simulated materials with constants indicated in Table 3 Appendix IV. This could be justified by the relatively high yield stress, which explains the low level of plastic deformation and crack closure too (no crack closure found for the plane strain case).

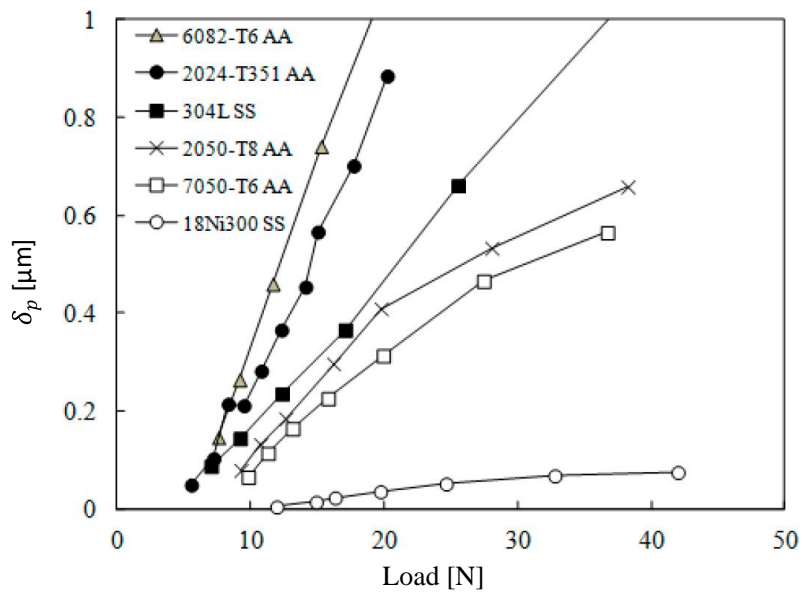


Figure 4.15: Plastic CTOD range (δ_p) evolution with the effective load range ($R = 0.01$).

From the curves of the 18Ni300 material in Figure 4.16, it is possible to observe, as expected, that the FCGR increases with the δ_p , but the curves are moving up with the increase of the stress ratio (R). This small occurrence happens due to errors when modelling δ_p and da/dN . It should not happen, because it was already proved that the da/dN - δ_p curves are independent from the stress ratio [Antunes *et al*, 2016; Vasco-Olmo *et al*, 2018]. For a better comparison, different da/dN - δ_p curves were also plotted for different materials, showing that the FCGR of 18Ni300 SLMed material is higher than for the other listed materials, for the same δ_p , see Figure 4.16.

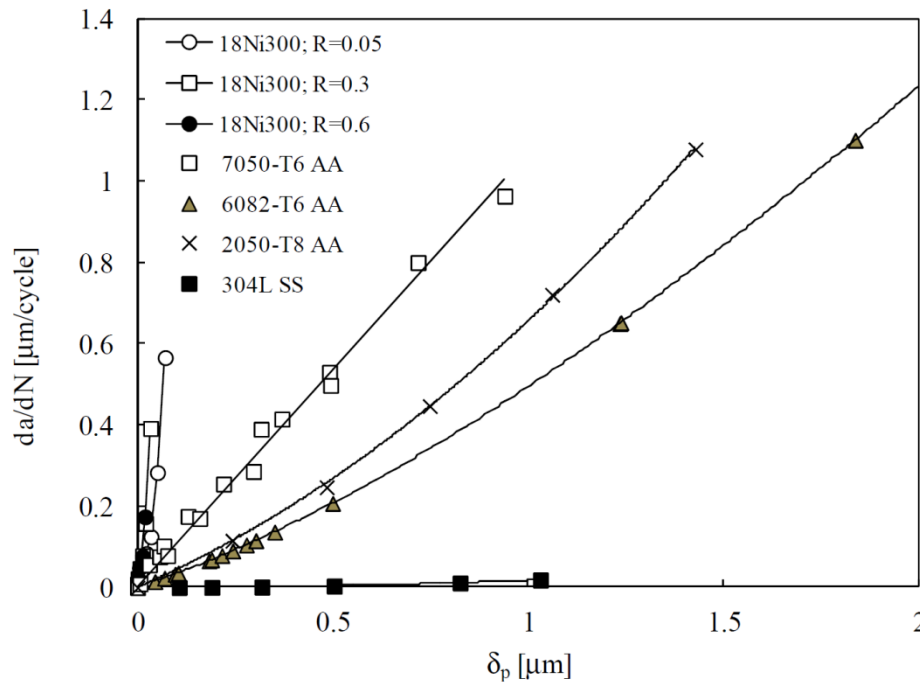


Figure 4.16: Comparison of FCGR behaviour with the plastic CTOD range, δ_p , for different materials.

There are two different procedures proposed by the ASTM E647 standard to determine experimentally the fatigue crack growth threshold (ΔK_{th}), but they are quite laborious and time consuming. Due to these, two numerical solutions for ΔK_{th} for two different load cases are presented here, based on numerical simulated values of plastic CTOD. The respective numerical curves of FCGR versus plastic CTOD are depicted in Figure 4.17, achieving the ΔK_{th} around $11.2 \text{ MPa}\sqrt{\text{m}}$, corresponding to the case when the ΔK is progressively decreasing until the plastic CTOD equals zero ($\delta_p = 0$). It is possible to observe that the numerical model is robust because the ΔK_{th} value is practically the same for both simulated load cases. For better clarity it was plotted the experimental fatigue crack growth threshold curve from the research of Appendix I. When comparing both threshold values, experimental ($5.2 \text{ MPa}\sqrt{\text{m}}$) and the simulated ($11.2 \text{ MPa}\sqrt{\text{m}}$) one, there is more than twice the difference, that could be justified due to the effect of the environment.

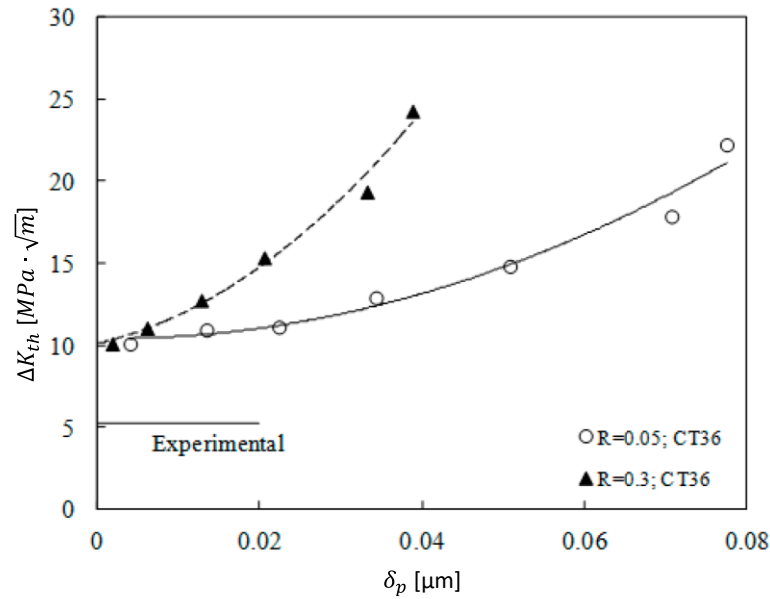


Figure 4.17: Numerical determination of $\Delta K_{th} = 11.2 \text{ MPa}\sqrt{\text{m}}$, for 2 different cases, based on numerical prediction of plastic CTOD versus load plots, and comparison with the experimental value of $5.2 \text{ MPa}\sqrt{\text{m}}$.

4.5. Fracture Surface Analysis

The fracture surfaces, which are a consequence of the tests run under load control mode to achieve da/dN - ΔK curves in as printed 18Ni300 alloy, were analysed by SEM. It was possible to observe on the as built specimens that the fatigue fracture occurred mainly between the deposited layers, layer boundaries, and sometimes creating steps with the thickness of 1 or 2 grains. Where the bonds between layers are stronger, the crack goes through the grains, called by transgranular mode. The tests run with an applied load normal to the layer growth, the weakest material resistance [Luecke *et al*, 2014], originating an irregular crack path, zigzag crack (see Figure 4.18 a), with a higher surface roughness and failure by cleavage without significant plastic deformation.

Regarding the heat-treated 18Ni300 specimen, the crack path propagates in a very distinct way. It is mainly growing on a relative planar and straight path, growing predominantly through the layer on a transgranular mode, as expected from the better homogenization and coherence of the microstructure, see Figure 4.18 b).

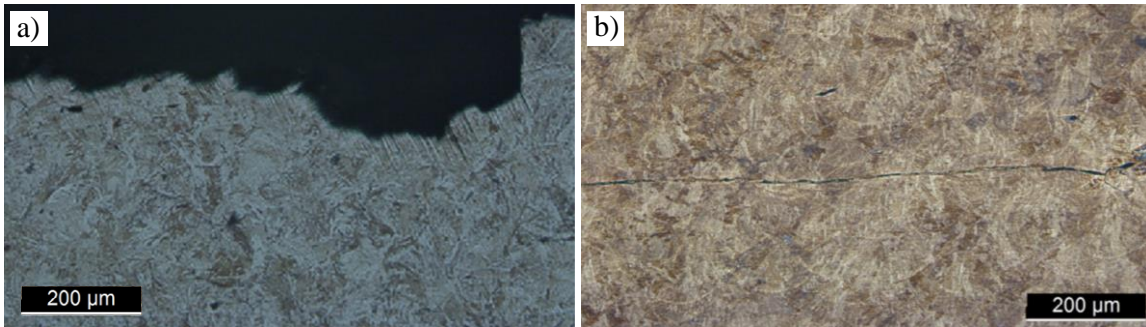


Figure 4.18: Microscopy of fracture crack path of 18Ni300 SLMed material in as printed condition (a) and after precipitation hardening heat treatment (b).

The fracture surface changed the direction/plane resulting from an applied overload at the ΔK baseline value of $18 \text{ MPa}\sqrt{\text{m}}$ and with an $\text{OLR} = 2$, as can be observed in Figure 4.19 for as built and for heat-treated specimens. The observed smoother region corresponds to the stable crack propagation and the peel off of the layer corresponds to the moment when the overload is applied.

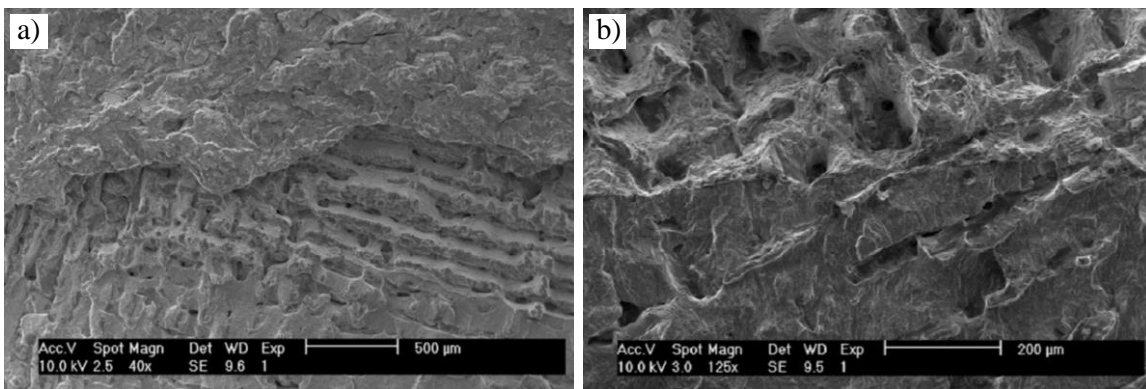




Figure 4.19: SEM of fracture surfaces in the transient regime, resulted from an applied single overload in the 18Ni300 SLMed material in as printed condition (a) and after precipitation hardening heat treatment (b).

Article

Fatigue Crack Growth in Maraging Steel Obtained by Selective Laser Melting

Fernando Antunes ^{1,*}, Luís Santos ², Carlos Capela ², José Ferreira ¹ , José Costa ¹ , Joel Jesus ¹ and Pedro Prates ¹

¹ CEMMPRE, Department of Mechanical Engineering, University of Coimbra, 3030-788 Coimbra, Portugal; martins.ferreira@dem.uc.pt (J.F.); jose.domingos@dem.uc.pt (J.C.); joel.jesus@dem.uc.pt (J.J.); pedro.prates@dem.uc.pt (P.P.)

² Department of Mechanical Engineering, Instituto Politécnico de Leiria, ESTG, 2411-901 Leiria, Portugal; luis_lms@sapo.pt (L.S.); ccapela@ipleiria.pt (C.C.)

* Correspondence: fernando.ventura@dem.uc.pt; Tel.: +351-239-790-722

Received: 10 September 2019; Accepted: 15 October 2019; Published: 18 October 2019



Abstract: Selective Laser Melting (SLM) is an additive manufacturing technology, ideal for the production of complex-shaped components. Design against fatigue is fundamental in the presence of cyclic loads, particularly for these materials which typically have significant porosity, high surface roughness and residual stresses. The main objective here is to study fatigue crack growth (FCG) in the 18Ni300 steel obtained by SLM. Typical da/dN- ΔK curves were obtained in C(T) specimens, indicating that cyclic plastic deformation may be the controlling mechanism. A complementary analysis, based on plastic CTOD range, showed a relatively low level of crack tip plastic deformation, and consequently a reduced level of plasticity induced crack closure. The curve da/dN versus plastic CTOD range is clearly above the curves for other materials.

Keywords: fatigue crack growth; Selective Laser Melting (SLM); Crack tip Opening Displacement (CTOD); crack tip plastic deformation; ΔK

1. Introduction

Selective Laser Melting (SLM) is a technology for additive manufacturing consisting of the fusion of a fine metal powder layer by layer. It is an iterative procedure consisting of (1) deposition of a thin layer of powder; (2) selective melting with a laser; and (3) descent of the manufacturing platform. The laser moves in the build area with controlled speed and scan pattern. The unmelted powder is collected and therefore there is no waste of material. The geometry is defined in a CAD model which is read by the SLM equipment. This procedure is very interesting to generate components with complex geometry and eventually composed of different materials. Therefore, SLM is becoming prominent in the automotive, aerospace, medical and injection molds industries. Various materials, such as titanium alloys [1], nickel-based alloys, iron, aluminum, bronze, copper, stainless steels [2] and high-speed steels of metal matrix, can be considered in this process.

Several studies, primarily focused on the influence of the selection of metal powder and sintering parameters on the microstructure of the sintered components, state that SLM components can provide static mechanical properties competitive with those of conventional bulk materials. Nevertheless, in service the components are typically dynamically loaded; therefore, the design must include the analyses of fatigue performance. Studies focused on the fatigue behavior of sintered materials are relatively scarce. Most previous studies developed tested smooth specimens under stress control [1,3,4] or strain control [2]. Notched specimens have also been tested under stress control in order to obtain S-N curves [5]. The presence of porosity, high surface roughness and thermal residual stresses,

typical of these materials, reduce the fatigue initiation life, increasing the importance of the crack propagation regime. Pores result from powder contaminations, evaporation or local voids after powder-layer deposition. However, few studies on fatigue crack growth can be seen in the literature. Greitemeier et al. [6] obtained $da/dN-\Delta K$ curves in compact tension (CT) specimens made of TiAl6V4 (width, $W = 40$ mm and thickness, $t = 10$ mm). Wang et al. [7] presented $da/dN-\Delta K$ curves obtained in four-point bending specimens and using replica technique to measure the crack length.

The main objective of this work is to study the fatigue crack propagation in AISI 18Ni300 maraging steel obtained by SLM. The mechanisms behind the phenomenon were analyzed using two different approaches. First, the fatigue crack growth rate, da/dN , was obtained using compact tension specimens, in agreement with ASTM E647 standard, and $da/dN-\Delta K$ curves are plotted. Second, the crack tip plastic deformation was analyzed, and da/dN is presented versus plastic Crack Tip Opening Displacement (CTOD), predicted numerically for the C(T) specimen. The material plastic behavior was studied using results obtained from low-cycle fatigue tests on smooth specimens under constant amplitude strain range. The stress-strain hysteresis loops were used for fitting the hardening models.

2. Fatigue Crack Growth Analysis Based on ΔK

2.1. Material

Table 1 presents the chemical composition of the AISI 18Ni300 maraging steel. This steel contains nickel as the primary strengthening source rather than carbon, promoting superior strength and toughness. In addition to its high strength, the 18Ni300 steel can be easily machined or formed; afterwards it can undergo an aging heat treatment step, which forms intermetallic precipitates involving cobalt, molybdenum and titanium that aid in increasing the tensile strength. Samples were manufactured using Lasercusing[®] technology, with layers growing in the same direction as the load application in the mechanical tests. The equipment for selective laser melting is of the mark "Concept Laser" and model "M3 Linear". This apparatus comprises a laser type Nd:YAG with a maximum power of 100 W in continuous wave mode and a wavelength of 1064 nm. The scan speed was 200 mm/s. The material layers were found to have about 40 μm of thickness. The analysis by scanning electron microscope (SEM) showed the presence of a significant amount of small porosities and the formation of martensitic needles [8]. Additionally, the increase of laser speed was found to increase the level of porosity.

Table 1. Chemical composition of the 18Ni300 steel (weight percentage).

Element	Percentage
C	0.01
Ni	18.2
Co	9.0
Mo	5.0
Ti	0.6
Al	0.05
Cr	0.3
P	0.01
Si	0.1
Mn	0.04
Fe	Balance

2.2. $da/dN-\Delta K$ Curves

Fatigue crack growth tests were carried out according to the recommendations outlined in the ASTM E647 standard. Figure 1 shows the geometry of the C(T) specimens, obtained with thicknesses of 3 or 6 mm. The surface finishing of the C(T) specimens was achieved by high-speed mechanical polishing. All fatigue crack growth (FCG) experiments were carried out using a DARTEC servo-hydraulic testing

machine, equipped with a 100 kN load cell. The tests were performed at room temperature in ambient air, under load control mode, at a frequency of 25 Hz, using a PC-based data acquisition system. The load cases studied are presented in Table 2. Three stress ratios were considered: $R = 0.05, 0.3$ and 0.6 . The crack length was measured with a travelling microscope, with magnification of $45\times$ and an accuracy of $10\ \mu\text{m}$. The data was collected and recorded for crack lengths, a , greater than $7\ \text{mm}$, as indicated in Table 2. The fatigue crack growth rates (FCGR) were obtained from the five-point incremental polynomial method.

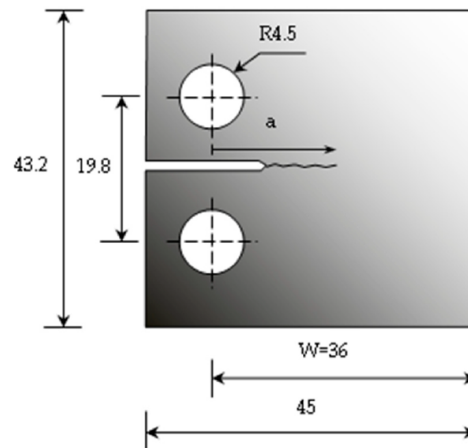


Figure 1. Geometry of C(T) specimen.

Table 2. Load parameters.

R	Thickness, t [mm]	F_{\min} [N]	F_{\max} [N]	A [mm]	ΔK [$\text{MPa}\cdot\text{m}^{0.5}$]
0.05	3	74.4	1488	7.1–27.3	8.1–58.1
0.05	6	114	2284.2	7.2–26.6	7.6–47.8
0.3	6	870	2900	7.1–24.0	7.1–27.6
0.6	6	2850	4750	47.5	79.17

Figure 2a shows da/dN - ΔK plots for the 18Ni300 steel, in log-log scales. The increase of ΔK increases the FCG rate significantly, as is well known. Paris law regime is evident, and for relatively low values of da/dN , there is a significant reduction of da/dN , typical of regime I of FCGR. There is also a trend for the increase of da/dN with stress ratio, as could be expected. Anyway, the influence of stress ratio is relatively small, which indicates a reduced level of crack closure. The results for thicknesses of 3 and 6 mm are nearly coincident, which also indicates a small level of crack closure. Figure 2b compares FCGR for the 18Ni300 steel with results for other materials. The 7050-T6 aluminum alloy (AA) has the highest crack growth rate, followed by the AA2050-T8. The 304L stainless steel has the lowest values. Finally, the 18Ni300 is between the SS304L and the AA2050-T8. The slopes of da/dN - ΔK curves in the Paris law regime are similar. Please note that only the 18Ni300 steel was obtained by SLM.

2.3. Discussion

In this Paris law regime, cyclic plastic deformation is the mechanism usually used to explain FCG. The model of striation formation by crack tip plastic blunting of Laird [9,10] is widely accepted to generally describe the propagation mechanism of fatigue cracks in regime II of da/dN - ΔK curves. According to this model, plastic deformation at the crack tip is highly concentrated along the 45° direction, producing blunting and creation of a new fracture surface. Compression stresses at the crack tip reverse slipping, the fracture surfaces approach, but the new surface cannot be removed by re-connection of the atomic bonds, which is in accordance with the entropy law of thermodynamics.

The results for the SLM steel are very typical in terms of linearity and slope of the Paris law regime; therefore, it can be expected that FCG is controlled by cyclic plastic deformation at the crack tip. The analysis of fracture surface by Scanning Electronic Microscopy (SEM) showed that fatigue crack growth occurs mainly at the interfaces between layers of the SLM material. In some cases where the adhesion between the deposited layers is higher, the failure can occur through the grain itself, in transgranular mode. On the contrary, in many other cases, the failure occurs at the layer boundaries producing steps corresponding to the thickness of one or two grains. Please note that the layer plane is normal to the loading direction, which is expected to have a negative effect. In fact, Edwards and Ramulu [11] showed that a layer plane parallel to the loading direction gives higher fatigue life. The weakness of the interfaces is responsible for a relatively tortuous crack path, and therefore for a relatively high fracture surface roughness.

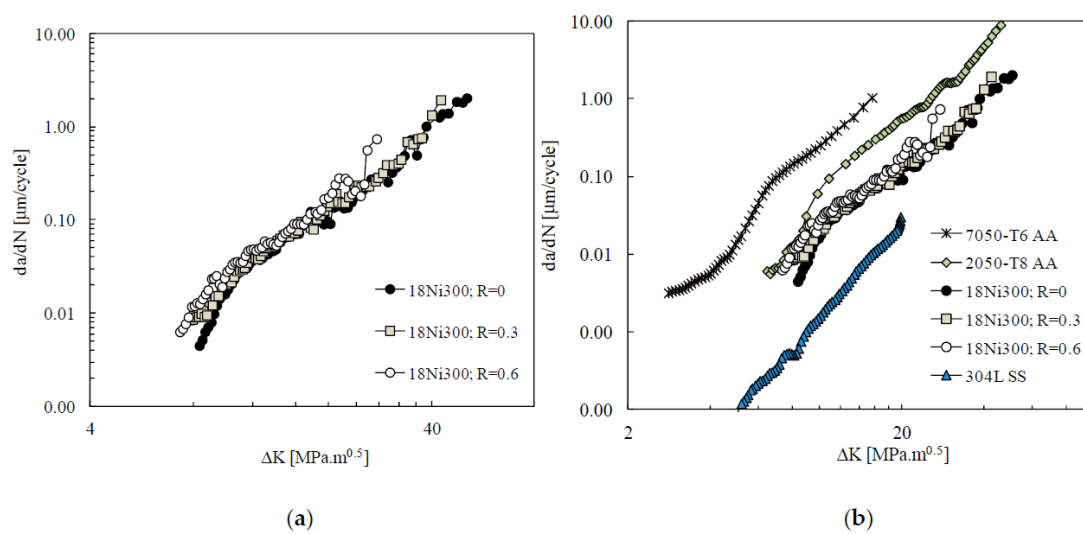


Figure 2. (a) da/dN - ΔK curves (18Ni300 steel; $t = 6$ mm). (b) Effect of material on da/dN - ΔK plots ($R = 0.1$; $R = 0.05$ for the 18Ni300).

It is, therefore, questionable whether da/dN is linked to a brittle mechanism or to crack tip plastic deformation. Llanes et al. [12] studied FCG in WC-Co cemented carbides, which are brittle materials. They observed that da/dN strongly depends on the variation of K_{max} . A law was proposed for FCGR which was a function of K_{max} and ΔK ($da/dN = C(\Delta K)^m(K_{\text{max}})^n$). The values of n were in the range 5–18, while the values of m were in the range 3–5. Intergranular crack growth is also observed in nickel base superalloys [13]. However, in this case the brittle crack growth is associated with oxidation of grain boundaries, which work as highways for the diffusion of oxygen. Tong et al. [14] resorted to the progressive accumulation of tensile strains occurring near the crack tip to predict fatigue crack growth rate in RR1000 nickel base superalloy. They used vacuum in order to remove oxidation, so that viscoplastic deformation controls fatigue crack growth. Figure 3 presents da/dN versus K_{max} for the SLM steel. The comparison with Figure 2a indicates that ΔK is the driving force for FCG, instead of K_{max} . Therefore, cyclic plastic deformation is expected to be the controlling mechanism instead of a brittle mechanism as observed in cemented carbides and nickel base superalloys. For a better understanding of FCG mechanisms, an analysis based on crack tip plastic deformation was developed, as is described in the next section.

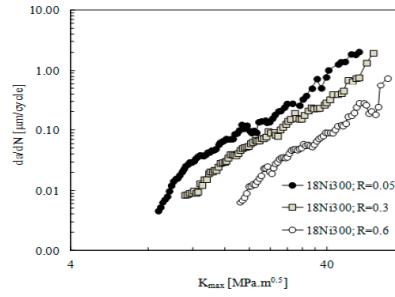


Figure 3. da/dN - K_{max} curves (18Ni300 steel; $t = 6$ mm).

3. FCG Analysis Based on Plastic CTOD Range

A complementary approach was followed to study FCG, making use of the plastic CTOD range, δ_p , instead of ΔK . This approach follows two assumptions: (i) fatigue crack growth is closely connected with plastic deformation at the crack tip; and (ii) the plastic deformation at the crack tip can be quantified by the plastic CTOD. δ_p was numerically determined using the finite element method. The quality of numerical predictions is dictated by the adequate modeling of the material behavior. Therefore, cyclic loading was applied to smooth specimens in order to obtain stress-strain response, which was subsequently used to fit the material constants. The capability of analyzing crack closure and fatigue crack growth using CTOD was fully demonstrated in an earlier work by the authors [15].

3.1. Low Cycle Fatigue Test

Experimental tests were performed at room temperature and in laboratory air environment, on a DARTEC servo-hydraulic testing machine equipped with a 100 kN load cell. The tests were conducted under axial total strain-controlled mode, with sinusoidal waves, using a constant strain rate (da/dt) equal to 0.008 s⁻¹, and total strain ratios (R_ϵ) of zero and total strain amplitude ($\Delta\epsilon/2$) equal to 0.8%. Specimens were produced according to the specifications outlined in ASTM E606 [16], with a gage section measuring 15 mm in length and 8 mm in diameter (Figure 4a).

The final surface finishing was obtained by high-speed mechanical polishing using a sequence of silicon carbide paper grades, P600-grit, P1200-grit, and P2500-grit, followed by 3 μ m diamond paste. A 12.5-mm strain-gage extensometer was attached directly to the specimen gage section, using rubber bands, to assess the stress-strain relationship during the test. A total of 41 loading cycles were obtained to failure. 200 samples were collected for each loading cycle, using a PC-based acquisition system. Figure 4b shows the stress-strain curve obtained. The material exhibits a mild cyclic softening behaviour from the beginning of loading until about 80% of total life.

3.2. Identification of Material Parameters

The high precision in the FE simulation results of the plastic CTOD depends on the accurate modeling of the material behavior. In this work, an elastic-plastic model was used: the isotropic elastic behavior is modeled by the generalized Hooke’s law; the plastic behavior is described by the von Mises yield criterion coupled with a mixed isotropic-kinematic hardening law under an associated flow rule. The von Mises yield surface is described as follows:

$$(\Sigma_{22} - \Sigma_{33})^2 + (\Sigma_{33} - \Sigma_{11})^2 + (\Sigma_{11} - \Sigma_{22})^2 + 3\Sigma_{23}^2 + 3\Sigma_{13}^2 + 3\Sigma_{12}^2 = 2Y^2 \tag{1}$$

where Σ represents the effective stress tensor ($\Sigma = \sigma' - X'$, where σ' and X' are the deviatoric components of the Cauchy stress tensor and back-stress tensor, respectively); Y is the yield stress, and its evolution during plastic deformation is modeled by the Voce isotropic hardening law [17]:

$$Y = Y_0 + (Y_{Sat} - Y_0)[1 - \exp(-C_Y \bar{\epsilon}^P)] \tag{2}$$

where Y_0 , Y_{Sat} and C_Y are material parameters and $\bar{\epsilon}^P$ is the equivalent plastic strain. The non-linear kinematic hardening is modeled by the Armstrong-Frederick law [18], as follows:

$$\dot{\mathbf{X}} = C_X \left[X_{Sat} \frac{\Sigma}{\sigma} - \mathbf{X}' \right] \dot{\epsilon}^P \tag{3}$$

where C_X and X_{Sat} are material parameters and $\dot{\epsilon}^P$ is the equivalent plastic strain rate. An optimization procedure was carried out to obtain the set of material parameters that best model the cyclic plastic behavior of 18Ni300, by minimization of the following least-squares function:

$$F(\mathbf{A}) = \sum_{i=1}^N \left(\frac{\sigma^{Fit}(\mathbf{A}) - \sigma^{Exp}}{\sigma^{Exp}} \right)_i^2 \tag{4}$$

where $\sigma^{Fit}(\mathbf{A})$ and σ^{Exp} are, respectively, the analytically fitted and experimentally measured values of true stress at data point i (that corresponds to an equivalent plastic strain value); N is the number of experimental data points and \mathbf{A} is the set of Voce and Armstrong-Frederick parameters to be identified. The fitting procedure was carried out for 33 loading cycles ($N = 6600$), representing about 80% of total life, using a non-linear gradient-based optimization algorithm available in the Microsoft Excel SOLVER tool [19]. Table 3 shows the fitted material parameters that describe the elastic-plastic behavior of 18Ni300. In this table, the Voce isotropic hardening parameters follow $Y_0 = Y_{Sat}$, and therefore the hardening is purely kinematic, which leads to a cyclically stable stress-strain fitting. This is acceptable in case of 18Ni300, where mild cyclic softening occurs during the first 33 loading cycles. Accordingly, the fitted material parameters describe adequately the experimental results, as can be seen in Figure 4c. Table 3 also shows material parameters for other five metal alloys, which were characterized by the authors in previous works.

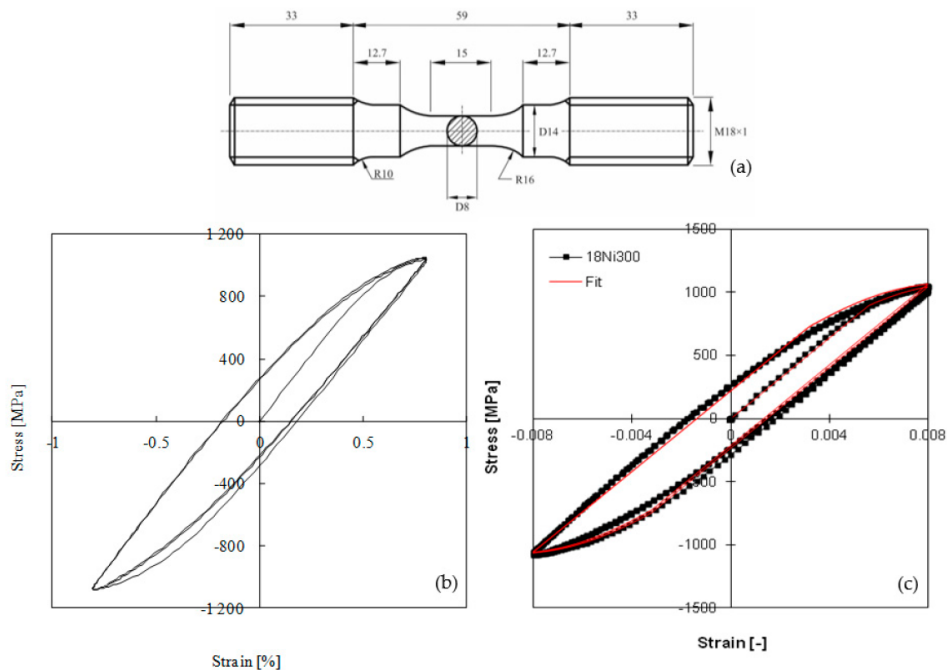


Figure 4. (a) Low cycle fatigue specimens. (b) Stress-strain plot ($\Delta\epsilon = \pm 0.8\%$). (c) Experimental versus fitted curve (18Ni300 steel).

Table 3. Elastic-plastic parameters (AA—Aluminum Alloy; SS—Stainless Steel).

Material	Hooke's Law Parameters		Isotropic Hardening (Voce)			Kinematic Hardening (Armstrong-Frederick)	
	E [GPa]	N [-]	Y_0 [MPa]	Y_{Sat} [MPa]	C_Y [-]	C_X [-]	X_{Sat} [MPa]
18Ni300	160	0.30	683.62	683.62	0	728.34	402.06
AA7050-T6 [15]	71.7	0.33	420.50	420.50	0	228.91	198.35
AA2050-T8 [20]	77.4	0.30	383.85	383.85	0	97.38	265.41
AA6082-T6 [21]	70	0.29	238.15	487.52	0.01	244.44	83.18
AA6016-T4 [22]	70	0.29	124.00	415.00	9.5	146.50	34.90
304L SS [23]	196	0.3	117	87	9	300	176

3.3. Numerical Determination of δ_p

The C(T) specimen (Figure 1) presents geometric, material and loading symmetries; therefore, 1/4 of the specimen was modeled numerically considering adequate boundary conditions, as indicated in Figure 5a,b. A pure plane stress state was simulated by assuming a small thickness equal to 0.1 mm. Several initial crack lengths a_0 were considered, equal to 7 mm, 10 mm, 13 mm, 16 mm, 19 mm, 22 mm and 24 mm, to replicate a wide range of experimental crack lengths. The simulations were done under load control, similar to the experimental tests. The maximum and minimum values of the remote load were defined considering the experimental loads listed in Table 2.

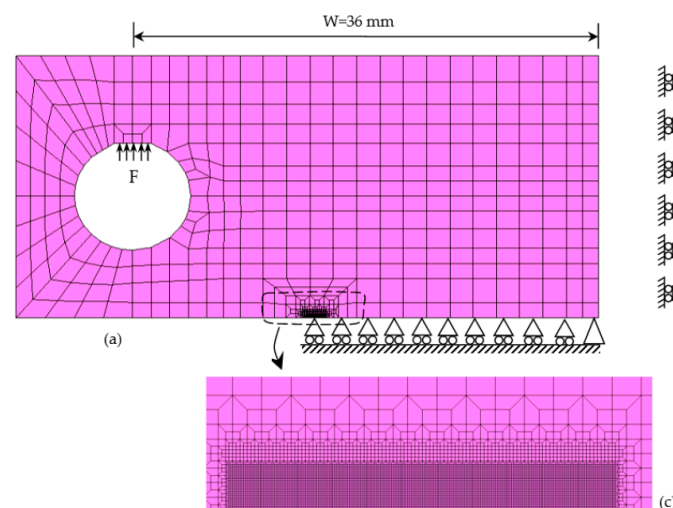


Figure 5. Model of the C(T) specimen. (a) Load and boundary conditions. (b) Boundary conditions for plane stress state. (c) Detail of finite element mesh.

The finite element mesh (Figure 5a,c) comprised 7142 linear isoparametric elements and 14,606 nodes, with two main regions: (i) An ultra-refined mesh near the crack tip, composed of elements with $8 \times 8 \mu\text{m}$ side; and (ii) a coarser mesh in the remaining specimen, to reduce the computational overhead. Only one layer of elements' through-thickness was used. The crack propagation occurs at the minimum load, by successive debonding of both crack front nodes over the thickness. A total of 159 crack propagations were modeled, each propagation corresponding to the size of one finite element ($= 8 \mu\text{m}$), with a total crack advance (Δa) of $1272 \mu\text{m}$ (i.e., $\Delta a = (160 - 1) \times 8 \mu\text{m}$). Five load cycles were applied between each crack increment.

The numerical simulations were performed using the DD3IMP (Deep-Drawing 3D IMPLICIT) in-house code, originally developed to model deep-drawing processes [24]. The evolution of the deformation is modeled by an updated Lagrangian scheme, assuming a hypoelastic-plastic material model. The material plastic behavior was modeled considering the set of elastic-plastic parameters

shown in Table 3. The contact between crack flanks is modeled considering a rigid plane surface aligned with the crack symmetry plane. A master–slave algorithm is used; an augmented Lagrangian approach is used for the contact problem treatment.

3.4. Numerical Results

Figure 6 presents a typical numerical result of CTOD as a function of the remote stress, obtained for an initial crack length $a_0 = 24$ mm, followed by 20 crack propagations ($\Delta a = 160$ μm); the CTOD was assessed at the first node located behind the crack tip, at a distance of 8 μm from the tip, as is schematically indicated, which presents the most sensitivity to crack tip phenomena. The crack is closed between A and B, for relatively low loads, i.e., the CTOD equals zero. The load increase opens the crack at point B. After point B, the crack opening evolves linearly with load increase up to point C, which is the boundary of the linear elastic regime. The range of loads between the opening load and the onset of plastic deformation was used to predict the fatigue threshold, as will be described later. A progressive increase of plastic deformation is found between points C and D, achieving its maximum value for the maximum load. The load decrease generates reversed elastic deformation with the same rate observed during loading. The subsequent load decrease produces reversed plastic deformation. Figure 6 also plots the variation of plastic CTOD. Plastic deformation initiates at point C, achieving its maximum value at maximum load. The plastic CTOD range, δ_p , which is correlated with fatigue crack propagation rate, is shown in Figure 6. It should be noted that crack closure is implicit in the value of δ_p . Increasing the crack closure phenomenon reduces the effective range of stress, also reducing the total CTOD and the plastic CTOD. In the absence of crack closure, the entire load cycle is felt by the crack tip. The plastic CTOD range also excludes the elastic deformation, which is not supposed to affect FCG.

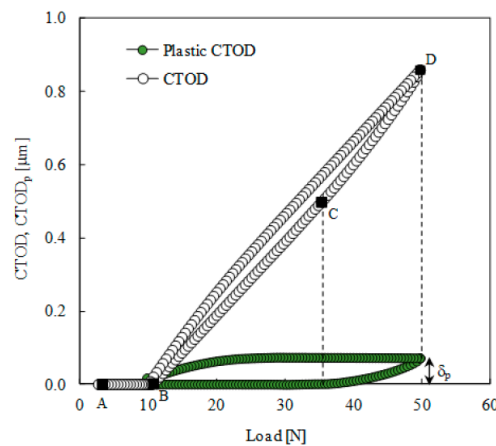


Figure 6. Evolution of Crack Tip Opening Displacement (CTOD) with load ($a_0 = 24$ mm; plane stress).

Figure 7 presents the evolution of plastic CTOD range, δ_p , with load range quantified by ΔK_{eff} ($= K_{\text{max}} - K_{\text{open}}$), i.e., the effective range of stress intensity factor. The remote loads applied were those used in the experimental FCG tests of the SLM material. The numerical tests were repeated for different materials keeping constant the specimen geometry, the crack lengths and loading. The increase in the load level increases δ_p , as might be expected. However, for the SLM material, the plastic deformation level is relatively low, being about one order of magnitude lower than the values obtained for the other materials. In fact, the values of plastic CTOD range, δ_p , are lower than 0.1 μm . As can be seen in Table 3, this material has a relatively high yield stress, which explains the low level of plastic deformation. This smallness makes the results very sensitive to errors of material modeling or geometry. Anyway, there is a well-defined variation of δ_p with load range.

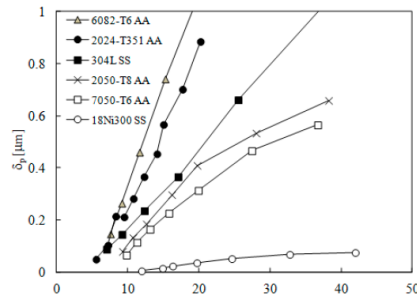


Figure 7. Evolution of plastic CTOD range, δ_p , with effective load range ($R = 0.01$).

The experimental results showed a relatively low influence of specimen thickness and stress on FCGR, which indicates that the crack closure phenomenon may have a low relevance. Figure 8 presents the evolution of crack closure with the crack length. The crack closure level was quantified by two parameters:

$$U_{\text{clos}} = \frac{F_{\text{open}} - F_{\text{min}}}{F_{\text{max}} - F_{\text{min}}} \times 100 \tag{5}$$

where F_{open} is the crack opening load, and

$$R_{\text{eff}} = \frac{F_{\text{open}}}{F_{\text{max}}} \tag{6}$$

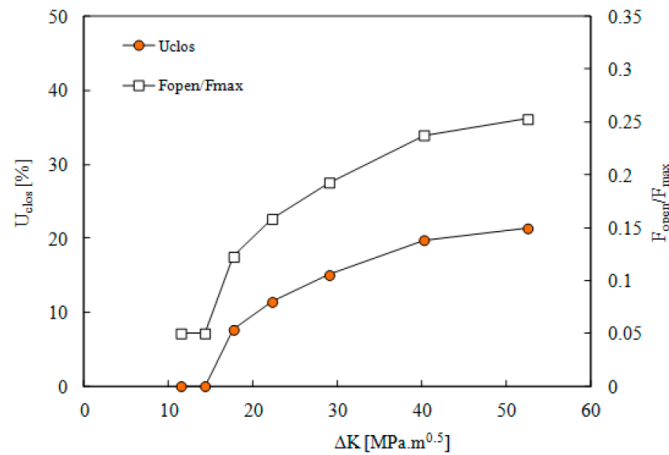


Figure 8. Crack closure level versus ΔK (18Ni300; $R = 0.05$).

The first parameter quantifies the percentage of load range during which the crack is closed, while the second one is the fraction of crack opening load divided by the maximum load. The crack closure level increases with crack length up to 21% (or 25% for $F_{\text{open}}/F_{\text{max}}$). In literature the crack closure level is usually quantified by R_{eff} , and values of 0.25, the maximum value obtained here for the highest crack length studied, are relatively low. This is explained by the relatively low plastic deformation obtained for this material. Values in the range of 0.2 to 0.3 are typical of plane strain state [25–29]. However, no crack closure was found for the SLM steel in the case of plane strain state.

Figure 9 shows the plastic CTOD range, δ_p , versus da/dN for different crack lengths and stress ratios. According to this figure, there is a progressive increase of FCGR with δ_p , as could be expected. The increase of stress ratio, R , moves the curve up. This variation, which should not exist, is relatively small and can be explained by errors of δ_p and da/dN . In fact, in a previous work of the authors [21] it

was shown that the da/dN - δ_p curves are invariant to the stress ratio. In other words, the approach based on plastic CTOD range is able to remove the effect of R observed when ΔK is being used. This indicates that δ_p dictates fatigue crack growth. Vasco et al. [30] also observed independence relatively to stress ratio. In that study, δ_p was measured experimentally using Digital Image Correlation. A 2nd-order polynomial was fitted to the results obtained for $R = 0.05$:

$$\frac{da}{dN} = 95.987 \times \delta_p^2 + 1.052 \times \delta_p \quad (7)$$

where the units of da/dN and δ_p are $\mu\text{m}/\text{cycle}$ and μm , respectively. The correlation coefficient is $R^2 = 0.9842$ and its validity is limited to δ_p in the range 0–0.8 μm . Figure 9 also presents results for other materials. The material models for the 304L stainless steel and the 18Ni300 steel were obtained using C(T) specimens, while the aluminum alloys were studied with M(T) specimens. For the same δ_p , the fatigue crack growth rate is significantly higher for the laser sintered material (18Ni300) than for the remaining materials.

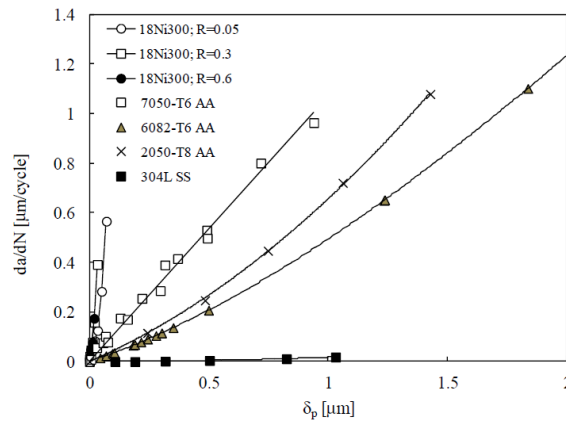


Figure 9. FCGR versus plastic CTOD, δ_p , for different materials.

ASTM E647 standard defines the experimental procedure to obtain fatigue threshold, ΔK_{th} . The load range is gradually reduced until there is no crack propagation. In each loading step, some crack propagation is required to eliminate the influence of crack closure from previous load. The load range reduction can be done setting the stress ratio, R , or the maximum load. In the constant R load reduction method, the maximum and minimum loads are successively reduced such that the stress ratio ($R = K_{min}/K_{max}$) remains constant. However, the measured values of ΔK_{th} are affected by stress ratio, being this effect linked to crack closure phenomenon. To overcome the effect of stress ratio, the constant K_{max} test procedure is proposed in the ASTM E647 standard. In this case, K_{min} is progressively increased in order to eliminate the effect of crack closure. The resulting effective threshold stress intensity, $\Delta K_{th,eff}$ is often referred to as an intrinsic measurement of fatigue crack growth resistance. The experimental approach is however laborious and time consuming. Two alternatives to predict ΔK_{th} were proposed here, based on the numerical analysis of plastic CTOD. In the first numerical approach, K_{max} was kept constant ($= 23.4 \text{ MPa}\cdot\text{m}^{0.5}$), while K_{min} increased. Figure 10a presents the plastic CTOD range versus ΔK . The decrease of ΔK decreased δ_p , as expected, and the extrapolation to the horizontal axis gave a threshold value $\Delta K_{th} = 11.2 \text{ MPa}\cdot\text{m}^{0.5}$. It is assumed that fatigue threshold corresponds to the onset of zero plastic deformation. The second numerical approach uses the range of elastic regime to define the fatigue threshold. In Figure 6, the load range between points B and C defines the elastic regime of CTOD. The corresponding ΔK_{th} is obtained from this load range using the K solution for the C(T) specimen. Please note that this is also an effective load range, free of crack closure. Figure 10b presents the results obtained for two different load cases. The reduction of δ_p to

zero defines the fatigue threshold. There is a convergence to a nearly constant value, which is a good indication of the robustness of the approach. The value obtained with the constant K_{max} approach is also presented, being slightly higher than the values obtained using the COTD-load curve. However, the experimental value is $5.2 \text{ MPa}\cdot\text{m}^{0.5}$ [31] being significantly lower than the numerical predictions. This great difference can be explained by the effect of environment. In fact, the near-threshold FCGR is quite small, giving time for the action of environment.

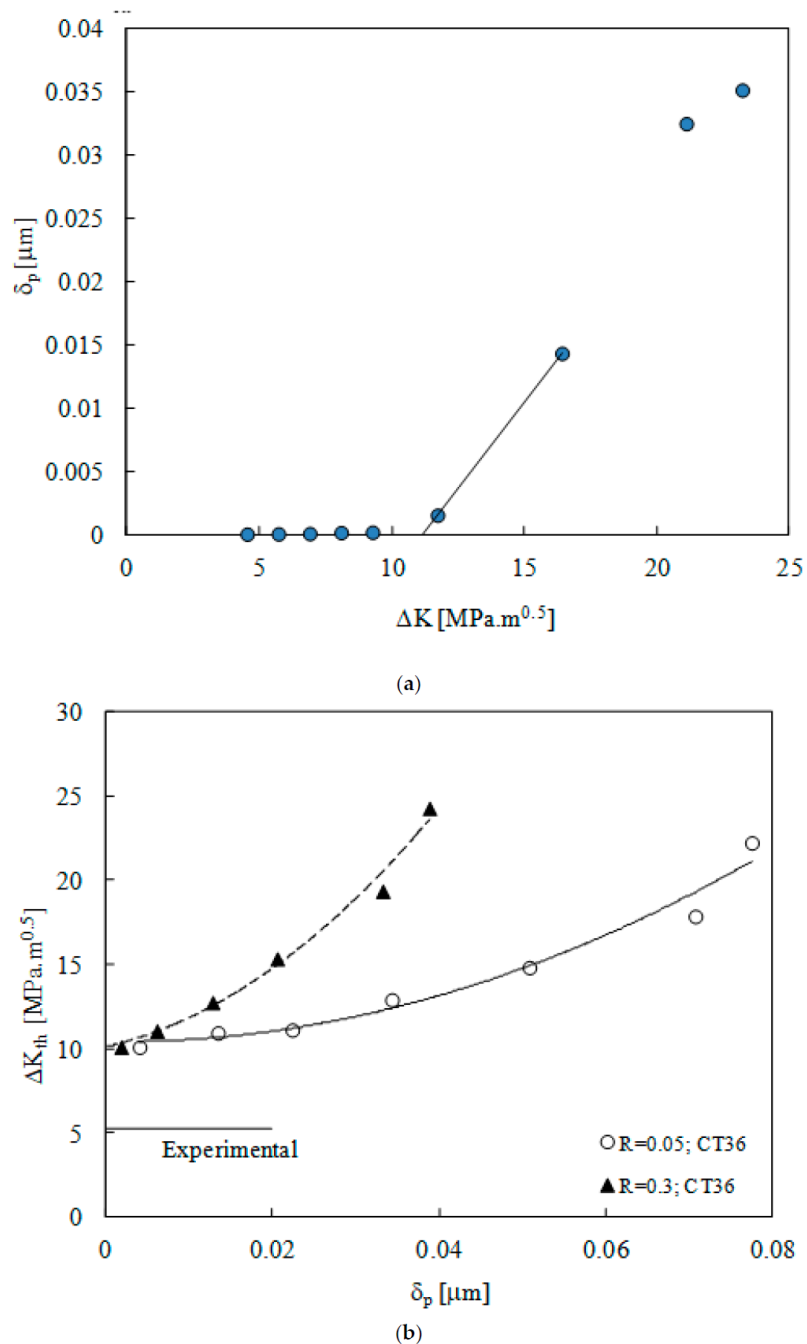


Figure 10. Numerical prediction of fatigue threshold. (a) Constant K_{max} approach ($a = 17.272 \text{ mm}$; $K_{max} = 23.4 \text{ MPa}\cdot\text{m}^{0.5}$). (b) Analysis based on the CTOD versus load plots.

4. Conclusions

The fatigue crack growth of the AISI 18Ni300 maraging steel made by Selective Laser Melting was studied numerically and experimentally. The experimental study considered ΔK as the crack driving force while the numerical work used the plastic CTOD. The main conclusions are:

The FCG rate, da/dN , plotted versus ΔK showed a classical Paris law regime with a typical value of the slope. This indicates that cyclic plastic deformation is probably the mechanism controlling fatigue crack growth. The influence of stress ratio and specimen thickness was found to be relatively small, indicating a reduced level of crack closure. The analysis of fracture surfaces by SEM showed propagation between deposition layers.

A complementary analysis was developed, based on plastic CTOD range, to better understand crack growth mechanisms. The level of plastic deformation at the crack tip was found to be relatively low, which also explains the relatively low level of crack closure. Consequently, the curve da/dN versus plastic CTOD range is clearly above the curves for other materials.

Author Contributions: Conceptualization, F.A., J.F. and C.C.; formal analysis, F.A. and P.P.; investigation, J.J., J.C. and L.S.; writing—original draft preparation, F.A.; writing—review and editing, F.A.; funding acquisition, J.F.

Funding: The authors acknowledge sponsorship under the project Hibsilaser, funded by the European Regional Development Fund (FEDER), through the Portugal-2020 program (PT2020), under the Regional Operational Program of the Center (CENTRO-01-0145-FEDER-028789) and the Foundation for Science and Technology IP/MCTES through national funds (PIDDAC).

Conflicts of Interest: The authors declare no conflict of interest. The funders had no role in the design of the study; in the collection, analyses, or interpretation of data; in the writing of the manuscript, or in the decision to publish the results.

References

- Walker, K.F.; Liu, Q.; Brandt, M. Evaluation of fatigue crack propagation behaviour in Ti-6Al-4V manufactured by selective laser melting. *Int. J. Fatigue* **2017**, *104*, 302–308. [[CrossRef](#)]
- Yadollahi, A.; Shamsaei, N.; Thompson, S.M.; Elwany, A.; Bian, L. Effects of building orientation and heat treatment on fatigue behavior of selective laser melted 17-4 PH stainless steel. *Int. J. Fatigue* **2017**, *94*, 218–235. [[CrossRef](#)]
- Crocco, D.; De Agostinis, M.; Fini, S.; Olmi, G.; Bogojevic, N.; Ciric-Kostic, S. Effects of build orientation and thickness of allowance on the fatigue behaviour of 15–5 PH stainless steel. *Fatigue Fract. Eng. Mater. Struct.* **2017**, *41*, 1–17. [[CrossRef](#)]
- Spierings, A.B.; Starr, T.L.; Wegener, K. Fatigue performance of additive manufactured metallic parts. *Rapid Prototyp. J.* **2013**, *19*, 88–94. [[CrossRef](#)]
- Mohammad, S.; Razavi, J.; Ferro, P.; Berto, F. Fatigue Assessment of Ti-6Al-4V Circular Notched Specimens Produced by Selective Laser Melting. *Metals* **2017**, *7*, 291.
- Greitemeier, D.; Palm, F.; Syassen, F.; Melz, T. Fatigue performance of additive manufactured TiAl6V4 using electron and laser beam melting. *Int. J. Fatigue* **2017**, *94*, 211–217. [[CrossRef](#)]
- Wang, Y.; Bergstrom, J.; Burman, C. Four-point bending fatigue behaviour of an iron-based laser sintered material. *Int. J. Fatigue* **2006**, *28*, 1705–1715. [[CrossRef](#)]
- Ferreira, J.A.M.; Santos, L.M.S.; da Silva, J.; Costa, J.M.; Capela, C. Assessment of the fatigue life on functional hybrid laser sintering steel components. *Procedia Struct. Integr.* **2016**, *1*, 126–133. [[CrossRef](#)]
- Laird, C.; Smith, G.L. Initial Stages of Damage in High Stress Fatigue in Some Pure Metals. *Phil. Mag.* **1963**, *95*, 1945–1963. [[CrossRef](#)]
- Laird, C. The Influence of Metallurgical Structure on the Mechanisms of Fatigue Crack Propagation. *Fatigue Crack Propag.* **1967**, 131–180.
- Edwards, P.; Ramulu, M. Fatigue performance evaluation of selective laser melted Ti-6Al-4V. *Mat. Sci. Eng. A-Struct.* **2014**, *598*, 327–337. [[CrossRef](#)]
- Lanes, L.; Torres, Y.; Anglada, M. On the fatigue crack growth behaviour of WC-Co cemented carbides: Kinetics description, microstructural effects and fatigue sensitivity. *Acta Mater.* **2002**, *50*, 2381–2393. [[CrossRef](#)]

13. Antunes, F.V.; Ferreira, J.A.M.; Branco, C.M.; Byrne, J. Influence of stress state on high temperature fatigue crack growth in Inconel 718. *Fatigue Fract. Eng. Mat. Struct.* **2001**, *24*, 127–135. [[CrossRef](#)]
14. Tong, J.; Zhao, L.G.; Lin, B. Ratchetting strain as a driving force for fatigue crack growth. *Int. J. Fatigue* **2013**, *46*, 49–57. [[CrossRef](#)]
15. Antunes, F.V.; Branco, R.; Prates, P.A.; Borrego, L. Fatigue crack growth modelling based on CTOD for the 7050-T6 alloy. *Fatigue Fract. Eng. Mater. Struct.* **2017**, *40*, 1309–1320. [[CrossRef](#)]
16. ASTM E606. *Standard Test Method for Strain-Controlled Fatigue Testing*; American Society for Testing of Materials: West Conshohocken, PA, USA, 2012.
17. Voce, E. The relationship between stress and strain for homogeneous deformation. *J. Inst. Met.* **1948**, *74*, 537–562.
18. Chaboche, J.L. A review of some plasticity and viscoplasticity constitutive theories. *Int. J. Plast.* **2008**, *24*, 1642–1693. [[CrossRef](#)]
19. Lasdon, L.S.; Waren, A.D.; Jain, A.; Ratner, M.W. *Design and Testing of a Generalized Reduced Gradient Code for Non-Linear Optimization*; NTIS National Technical Information Service U. S. Department of Commerce: Cleveland, OH, USA, 1975.
20. Antunes, F.V.; Serrano, S.; Branco, R.; Prates, P.; Lorenzino, P. Fatigue crack growth in the 2050-T8 aluminium alloy. *Int. J. Fatigue* **2018**, *115*, 79–88. [[CrossRef](#)]
21. Antunes, F.V.; Rodrigues, S.M.; Branco, R.; Camas, D. A numerical analysis of CTOD in constant amplitude fatigue crack growth. *Theor. Appl. Fract. Mech.* **2016**, *85*, 45–55. [[CrossRef](#)]
22. Antunes, F.V.; Rodrigues, D.M. Numerical simulation of plasticity induced crack closure: Identification and discussion of parameters. *Eng. Fract. Mech.* **2008**, *75*, 3101–3120. [[CrossRef](#)]
23. Antunes, F.V.; Ferreira, M.S.C.; Branco, R.; Prates, P.; Gardin, C.; Sarrazin-Baudoux, C. Fatigue crack growth in the 304L stainless steel. *Eng. Fract. Mech.* **2019**, *214*, 487–503. [[CrossRef](#)]
24. Oliveira, M.C.; Alves, J.L.; Menezes, L.F. Algorithms and Strategies for Treatment of Large Deformation Frictional Contact in the Numerical Simulation of Deep Drawing Process. *Arch. Comput. Methods Eng.* **2008**, *15*, 113–162. [[CrossRef](#)]
25. McClung, R.C.; Thacker, B.H.; Roy, S. Finite element visualization of fatigue crack closure in plane stress and plane strain. *Int. J. Fracture* **1991**, *50*, 27–49.
26. Sehitoglu, H.; Sun, W. Modelling of plane strain fatigue crack closure. *ASME J. Eng. Mat. Technol.* **1991**, *113*, 31–40. [[CrossRef](#)]
27. LLorca, J.; Gálvez, V.S. Modelling plasticity-induced fatigue crack closure. *Eng. Fracture Mech.* **1990**, *37*, 185–196. [[CrossRef](#)]
28. Solanki, K.; Daniewicz, S.R.; Newman, J.C., Jr. Finite element modelling of plasticity-induced crack closure with emphasis on geometry and mesh refinement effects. *Eng. Fract. Mech.* **2003**, *70*, 1475–1489. [[CrossRef](#)]
29. Pokluda, J. Dislocation-based model of plasticity and roughness-induced crack closure. *Int. J. Fatigue* **2013**, *46*, 35–40. [[CrossRef](#)]
30. Vasco-Olmo, J.M.; Díaz, F.; Antunes, F.V.; James, M.N. Evaluación Experimental Del CTOD En El Crecimiento De Grieta A Fatiga A Partir De Los Campos De Desplazamientos. In Proceedings of the XXXV Encuentro del Grupo Español de Fractura, Málaga, Spain, 14–16 March 2018.
31. Santos, L.M.S.; Ferreira, J.A.M.; Jesus, J.S.; Costa, J.M.; Capela, C. Fatigue behaviour of selective laser melting steel components. *Appl. Fract. Mech.* **2016**, *85*, 9–15. [[CrossRef](#)]



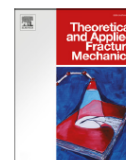
© 2019 by the authors. Licensee MDPI, Basel, Switzerland. This article is an open access article distributed under the terms and conditions of the Creative Commons Attribution (CC BY) license (<http://creativecommons.org/licenses/by/4.0/>).



Contents lists available at ScienceDirect

Theoretical and Applied Fracture Mechanics

journal homepage: www.elsevier.com/locate/tafmec



Effect of heat treatment on the fatigue crack growth behaviour in additive manufactured AISI 18Ni300 steel



L.M.S. Santos^a, L.P. Borrego^{a,b,*}, J.A.M. Ferreira^a, J. de Jesus^a, J.D. Costa^a, C. Capela^{a,c}

^a CEMMPRE, Department of Mechanical Engineering, University of Coimbra, Coimbra, Portugal

^b Department of Mechanical Engineering, Coimbra Polytechnic – ISEC, Coimbra, Portugal

^c Department of Mechanical Engineering, Instituto Politécnico de Leiria, Leiria, Portugal

ARTICLE INFO

Keywords:

Fatigue crack propagation
Additive manufacturing
Overloads
Maraging steels

ABSTRACT

Additive manufacturing (AM) technologies have a strong appeal to the industry targeting low-volume production for specific applications, as they currently provide mechanical properties under static loading comparable to those of conventionally fabricated parts. The current study presents results of fatigue crack propagation obtained using standard 6 mm thick Compact Tension specimens (CT) laser sintered and tested at $R = 0$. The main parameter studied was the effect of post-manufacturing heat treatment on the stable crack propagation and the transient behaviour after overloads. It was found that the thermal treatment caused important changes on both microstructure and crack path and promoted the increase of the fatigue crack propagation resistance. Both material microstructures exhibit significant transient crack propagation retardation after overloads probably by crack bifurcation effect, as the crack closure phenomena was not observed.

1. Introduction

Additive manufacturing (AM) technologies are increasingly used due to its potential advantages in comparison with traditional subtractive manufacturing. Processes such as selective laser melting (SLM) in which the components are produced layer by layer using selectively full melting and under a protective atmosphere, offers a wide range of advantages in comparison with the traditional manufacturing methods, such as: low material consumption and facility of manufacturing complex-shape parts, with almost no need for further post-processing [1,2]. SLM technology has been widely used for metal parts manufacturing, including titanium alloys [3], aluminium alloys [1,2,4,5], steels [6] and super alloys [7]. AM technologies have a strong appeal to industry targeting low-volume production for specific applications, like medical devices, aeronautical parts and even mould industry components [8]. However, the use of AM parts in structural applications remains limited and subject to constraints by the uncertainty in their mechanical properties, as consequence of the formation of porosities, internal defects, residual stresses and microstructural heterogeneities during fabrication [9].

The main parameters of the additive manufacturing of parts by SLM are the laser power and the scan speed. Porosities and building orientation also have a major influence in the mechanical behaviour of SLM-produced components. The building orientation of the components

during AM leads to anisotropic mechanical properties [9]. Abundant works are reported in the literature about the mechanical behaviour of titanium and stainless steel parts produced by AM process. One of them is the 17-4 PH stainless steel, for which the microstructural and mechanical properties are reported and discussed in the literature [10–13]. Murr et al. [10] studied the effect of raw powders, concluding that powder preparation and fabrication atmosphere can affect microstructure, precipitates, phase volume fractions and hardness of the manufactured alloy.

Due to high heating/cooling rate in laser processing, high residual stresses occur frequently in SLM-produced components. Residual stresses may produce stress cracking and/or interlayer debonding. According to Mercelis and Kruth [14], residual stresses usually reach high tensile stress at both top and bottom of the SLM-processed sample and intermediate compression stress at large intermediate zone. Stress level is largely dependent of laser processing parameters and can be controlled by preheating the build substrate leading to the decrease in temperature gradient [15]. In addition, post-fabrication heat treatments (PFHT) can eliminate or reduce the residual stress level. Rafi et al. [11] investigated the effect of post-fabrication heat treatments on the mechanical properties of AM 17-4 PH SS.

Recently, Stoffregen et al. [13] studied the effect of surface condition on high cycle fatigue behaviour and Mower and Long [16] and Aref Yadollahi [17] investigated the effect of building orientation on the

* Corresponding author at: Department of Mechanical Engineering, Coimbra Polytechnic – ISEC, Coimbra, Portugal.
E-mail address: borrego@isec.pt (L.P. Borrego).

<https://doi.org/10.1016/j.tafmec.2019.04.005>

Received 31 October 2018; Received in revised form 31 March 2019; Accepted 3 April 2019

Available online 04 April 2019

0167-8442/ © 2019 Elsevier Ltd. All rights reserved.

fatigue behaviour. The mechanical properties of AM TiAl6V4 alloy under static loading were recently investigated and tensile properties have been well characterized for different heat treatments and surface conditions [18,19]. Significant work has been also reported on the literature about the fatigue performance of AM TiAl6V4 alloy and the influence of surface roughness [20–22]. In general, fatigue results show high scatter resulting from surface roughness and porosity. However, fatigue performance can be improved, reducing porosity by optimizing SLM parameters or by hot isostatic pressing (HIP) post-processing [19].

Unlike titanium alloys, few studies have been performed on the mechanical properties of AM parts in maraging steels, currently widely used in the mould industry and other applications. Mainly, fatigue behaviour, needs more in-depth research for a safe design, since this is the most common means for mechanical failure in many engineering components and structures.

Recent work of the authors [23,24] studied the effect of laser speed melting, and porosity on the fatigue strength of sintered laser melting steel components and hybrid implanted parts. In addition to porosity, residual stresses play an important role on the fatigue behaviour of the selective laser melting materials. The main objective of this work was to evaluate the effect of post-manufacturing heat treatment on the stable fatigue crack propagation rate and on the crack growth transient behaviour after overloads.

2. Materials and testing

Experimental tests were performed using Compact Tension specimens (CT) additively manufactured by Lasercusing® technology. The SLM equipment was the “Concept Laser”, model “M3 Linear”. This apparatus comprises a laser type Nd:YAG with a maximum power of 100 W in continuous wave mode and a wavelength of 1064 nm and 0.2 mm of spot laser diameter. Material of powder particles to produce SLM parts was the maraging steel AISI 18Ni300 with the chemical composition indicated in Table 1. The specimens were manufactured using a scan speed of 200 mm/s, adding layers of 40 µm thickness with hatch spacing of 100 µm and 25% overlapping, growing towards the direction corresponding to the application of the load in the mechanical tests. After manufacturing the specimens were mechanically polished. The specimens’ geometry and respective dimensions are indicated in Fig. 1.

Two different batches of tests were performed: as-built SLM specimens and also SLM specimens subjected to a post-manufacturing heat treatment. The purpose of the heat treatment was to increase the hardness and reduce the residual stress level. A slow and controlled heating was performed during 2 h up to 635 °C, followed by maintenance at 635 °C for 6 h. Then, the specimens were submitted to a controlled cooling in the oven for 3 h up to 360 °C. The final cooling to room temperature was carried out in the air. This heat treatment was selected because it is the one generally performed in the mould industry for components of maraging steel AISI 18Ni300.

Some samples were sectioned in a plane parallel to the specimen face and observed in an optical microscope, in order to identify the microstructure and morphology of the grains. The samples were prepared according to the standard metallographic practice ASTM E407-99; a chemical attack Picral (picric acid solution 4% in ethyl alcohol) was performed during two minutes. After preparation, the samples were observed using a Leica DM4000 M LED optical microscope.

Fig. 2a) and b) show metallography images of an as-built SLM specimen and a SLM post-manufacturing heat treatment specimen,

Table 1
Chemical composition of the powder 18Ni300 steel in wt.%

C	Ni	Co	Mo	Ti	Al	Cr	Si	Mn	Fe
0.01	18.2	9.0	5.0	0.6	0.05	0.3	0.1	0.04	Balance

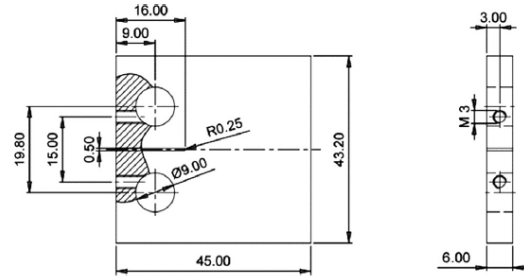


Fig. 1. CT specimen geometry and dimensions (mm).

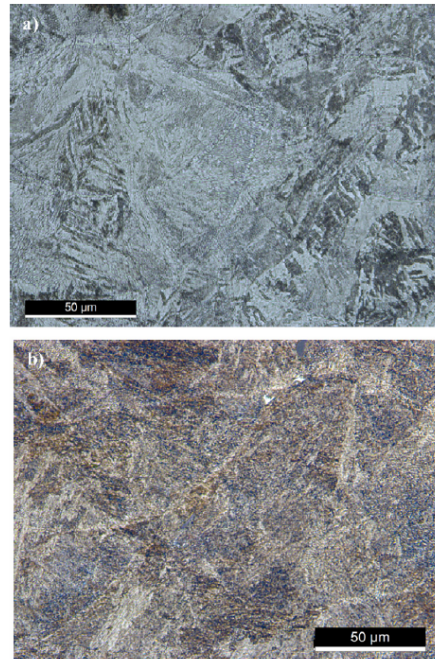


Fig. 2. Microstructures: (a) as-built SLM sample; (b) SLM and heat treated sample.

respectively. The analysis of these figures shows that the presence of porosities is negligible and that the heat treatment promotes important microstructural changes, homogenizing the structure and the transitions between layers. For the as built specimens it is noticed the formation of large elongated grains with average length of 100 µm and average thickness of about 40 µm.

Vickers hardness was measured according to ASTM E384-11e1 using a Struers Duramin 1 microhardness tester with a 0.5 kg load and a distance of 0.5 mm between indentations. The measurements were randomly done at the surface of the specimens. The values of average and standard deviations are $HV1 = 354 \pm 5$ for as-built specimens and $HV1 = 495 \pm 10$ for heat treated SLM samples. Therefore, post-manufacturing heat treatment promotes an important increasing in hardness by more than 25%.

Residual stresses are a major cause of the low fatigue strength of SLM materials. Residual stress analysis was performed by X-ray diffraction using a Proto iXRD equipment. Fig. 3a) presents the effect of the post-manufacturing heat treatment on the average values and

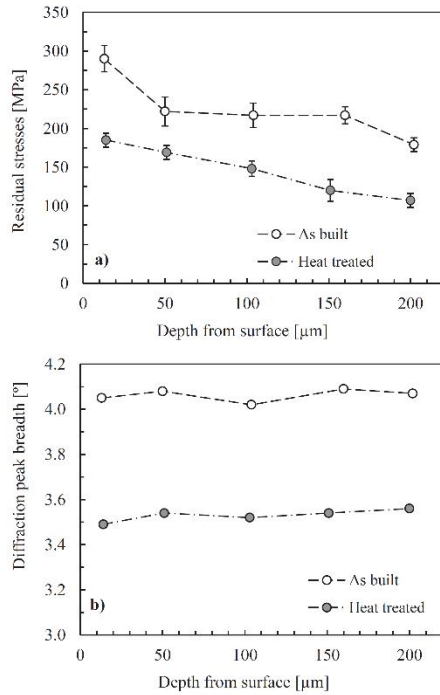


Fig. 3. Effect of the heat treatment: (a) longitudinal residual stresses; (b) diffraction peak breadth.

standard deviation of the longitudinal residual stresses against the distance from the surface while Fig. 3b) shows the diffraction peak breadth in the same points. The analysis of the residual stresses profile (Fig. 3a) shows the presence of high tensile stresses in all measured points. Post built heat treatment reduced significantly, in order of 30%, the residual stress levels. Maximum tensile residual stresses occur, in both specimen batches, in points near the surface, decreasing significantly for inner points. The maximum value near the surface was 290 MPa for the as-built specimen and 185 MPa for the heat-treated SLM specimen. Fig. 3b) shows also a significantly reduction of the average diffraction peak breadth from around 4.05° for as the as-built specimen to 2.55° for the heat-treated specimen.

The fatigue crack growth rate data were generated using the K-increasing procedure for $da/dN < 1 \times 10^{-5}$ mm/cycle and the K-decreasing procedure for $da/dN < 1 \times 10^5$ mm/cycle, in agreement with ASTM E647 standard [25], using 6 mm thick CT specimens. The tests were performed at room temperature using a 10 kN capacity Instron EletroPuls E10000 machine, at constant amplitude load with a frequency within the range 10–15 Hz and a stress ratio of $R = 0.05$. All tests were performed under load control. The crack length was measured using a travelling microscope (45×) with an accuracy of 10 μm. Fig. 4 shows the fatigue-testing machine and the crack measurement system. Crack growth rates under constant amplitude loading were determined by the incremental polynomial method using five consecutive points [25].

The influence of post-manufacturing heat treatment was analysed in terms of the comparison of the da/dN - ΔK curves in the Paris regime at $R = 0.05$ and in the transient regime after single and 100 cycles block tensile overloads. Transient regime crack growth tests were performed also under load control, at a ΔK baseline level of 12 and 18 MPa√m, and an overload ratio of 2. The overload ratio, OLR, is defined as:

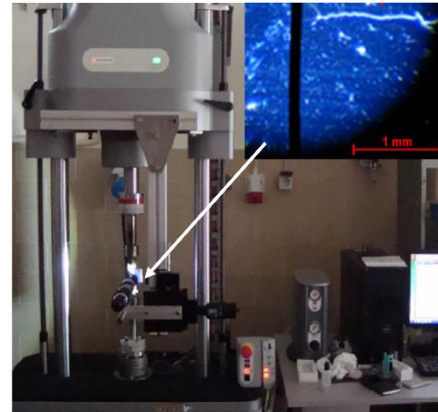


Fig. 4. View of the fatigue testing apparatus.

$$OLR = \Delta K_{OL} / \Delta K_{BL} \quad (1)$$

where ΔK_{OL} and ΔK_{BL} are the peak overload stress intensity factor range and the baseline intensity factor range before the overload application, respectively.

3. Results and discussion

Fig. 5 summarizes the constant amplitude tests, comparing da/dN - ΔK curves in the Paris regime and also in the near threshold regime, for the as built SLM samples and the post-built heat-treated SLM specimens. For each batch two tests were performed, one with constant ΔK (constant load) and another with ΔK successively decreasing, both starting from $\Delta K = 8$ MPa√m. This methodology justifies some irregularity found in the crack propagation rate around $\Delta K = 8$ MPa√m, which is not a feature of the material, but is due to the stabilization of the crack propagation rate.

The results presented in the figure show that the post-manufacturing heat treatment has a significant influence on the fatigue crack propagation rate, decreasing da/dN not only in the stable Paris Law regime, but also near threshold. The main causes for this behaviour are the

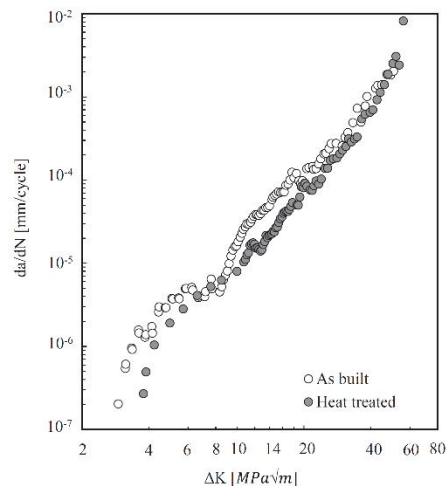


Fig. 5. Comparison of da/dN - ΔK curves for as built SLM material and heat treated SLM specimens.

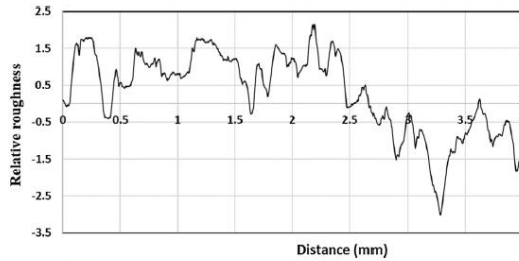


Fig. 6. Normalized roughness in as-built failure surfaces.

microstructure changes and the hardness increase, as stated before. In addition, as the results plotted in Fig. 3a) show, the residual stresses for SLM heat-treated specimens are much lower than for as-built specimens, reducing the effective loading stress ratio. The microstructure modification also causes both different crack path and failure mechanisms for the two types of samples.

Surface roughness and crack profiles complementary analysis were performed in order to understand the fatigue crack path and failure mechanisms. A detailed analysis of the surface roughness was performed, according to DIN EN ISO 4288 standard using the rugosimeter SurfTest SJ-500 Mitutoyo. The roughness profiles were normalized against the thickness of the deposition layer, quantified by the average value measured by the metallographic analysis and very close to the average diameter of the metal powder, 40 μm .

Fig. 6 depicts an example of a roughness profile of the as-built material measured in the stable Paris Law regime on the as-built material. This profile shows that fatigue crack propagation occurs with a zigzag path over a median plane, but often plane changes occur, corresponding approximately to the height of one or two grains, indicating fractures at the boundary of the deposited layer.

Another complementary way to analyse the failure crack path was performed by the optical observation of the lateral face around the crack, etched with Picral. Fig. 7a) shows the microscopy path observation, confirming the zigzag crack growth behaviour stated by the roughness analysis. Both studies point to a fatigue failure in as-built specimens occurring predominantly around the boundaries of deposited powder layers. Failure mechanism was also investigated using scanning electron microscopy (SEM). Fig. 7b) shows a representative example of the appearance of the failure surface in as-built specimens during fatigue crack propagation in the Paris law regime, showing failure by cleavage without significant plastic deformation.

Optical microscope analysis of the crack path for heat-treated specimens indicates significant changes on the propagation path in comparison with as-built material, as shown in Fig. 8. Contrary to the observed in the as-built material, the fatigue crack path for heat-treated specimens (shown in Fig. 8) is almost a straight line, indicating that the crack passes through successive deposit layers pointing to a significant transgranular failure mode. This behaviour is in agreement to the homogenization of the structure and the transition between deposit layers promoted by the performed heat treatment as observed in Fig. 2a).

All the overloads were applied under load control and constant ΔK and R conditions during both one unique cycle and a block of 100 cycles. After overloading, the transient crack growth behaviour was monitored.

Load-displacement behaviour was monitored at specific crack length increments using a pin microgauge elaborated from a high sensitive commercial axial extensometer [26,27]. The gauge pins were placed in two drilled holes of 0.5 mm diameter located at the outside face of the specimen notch. The distance between these holes was 3.5 mm. In order to collect as many load-displacement data as possible during a single cycle, the loading frequency was reduced to 0.5 Hz. The

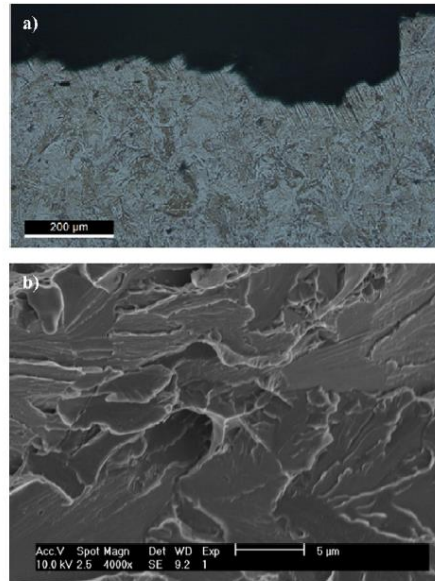


Fig. 7. Failure analysis: (a) microscopy view of the path for as built material; (b) SEM observation.

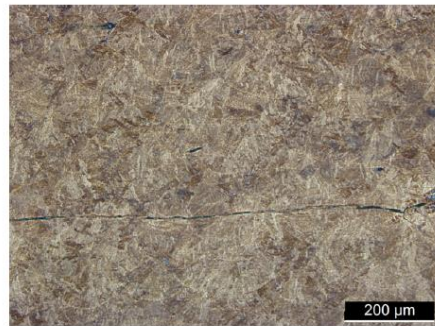


Fig. 8. Crack path for heat-treated specimens.

opening load, Pop , was derived from these records using the technique known as maximization of the correlation coefficient [28]. This technique involves taking the upper 10% of the load-displacement data and calculating the least squares correlation coefficient. The next data pair is then added and the correlation coefficient is again computed. This procedure is repeated for the whole data set. The point at which the correlation coefficient reaches a maximum can then be defined as Pop . However, contrary to the generally observed in other alloys, with data obtained with the same method [29,30], no crack opening loads were observed for the analysed material under the described test conditions.

Fig. 9a) shows the effect of the heat treatment on the transient crack growth behaviour after a single tensile overload under constant amplitude loading tests, plotting the results in terms of $da/dN-\Delta K$ curves. For the stable crack propagation phase, i.e., before overloading, these tests confirm the correspondent crack growth rate levels obtained under constant amplitude loading and therefore the beneficial effect of the heat treatment. After overloading, the results show the typical retardation effect, usually obtained and abundantly reported in literature for cast materials. This retardation is usually attributed to the crack

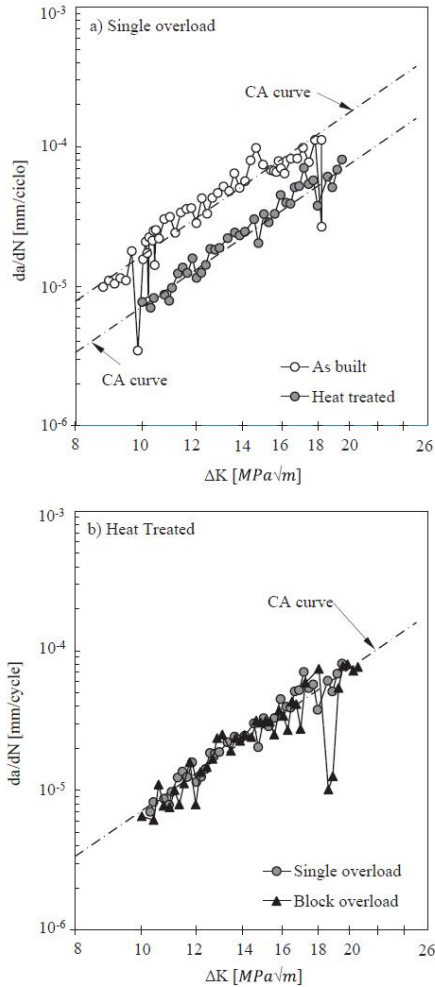


Fig. 9. Transient da/dN - ΔK curves: (a) Effect of the heat treatment; (b) Effect of the number of overload cycles.

closure effect, both in aluminium alloys [29,30] and in steels [31]. However, as already stated, in the current study no crack closure was observed in spite of the significant crack growth retardation effect.

Anyway, Fig. 9a) shows that the retardation effect is significantly lower for the heat treated SLM specimen than for the as-built material, particularly for the lower ΔK baseline value. Fig. 9b) shows the effect of the number of overload cycles on the transient crack growth behaviour for the heat-treated specimens. When a block of 100 overload cycles were applied the retardation effect increases for both ΔK baseline values analysed.

As referred before, the main factors for the transient fatigue crack retardation are the crack tip plasticization and crack closure [29]. Moreover, of the several mechanisms proposed to explain the crack growth transients following overloads, the crack branching mechanism [32] is also able to explain the retardation period that was observed for the material and loading conditions used in this work.

In the current study crack closure induced by plasticity was not detected in any of either microstructures, in spite of the increasing in

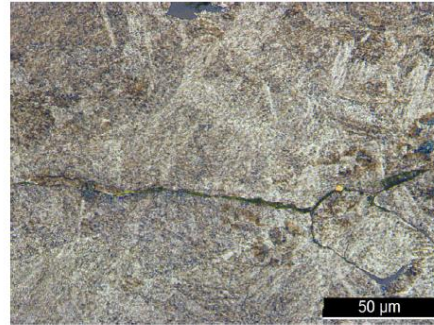


Fig. 10. Optical microscope image of the path for heat-treated specimens.

local plasticity caused by the overload application. However, the crack branching mechanism can explain crack growth retardation because crack branching or crack deflection from its original path implies a reduction of the crack driving force. Therefore, the possible reason for the fatigue crack rate retardation after overload application in the analysed material is the bifurcation of the crack in the contour of the deposited layers.

This occurrence was observed in some cases as shown in Fig. 10, which presents a micrograph of a heat-treated sample, whose focus is the propagation mode after the application of an overload with OLR = 2. This should be the main cause of the transient retardation of crack growth, until, afterwards, it reacquires a scheme of propagation of a single crack.

The sudden changes of the propagation plan were confirmed by SEM analysis. Fig. 11a) and b) show low magnification observations of

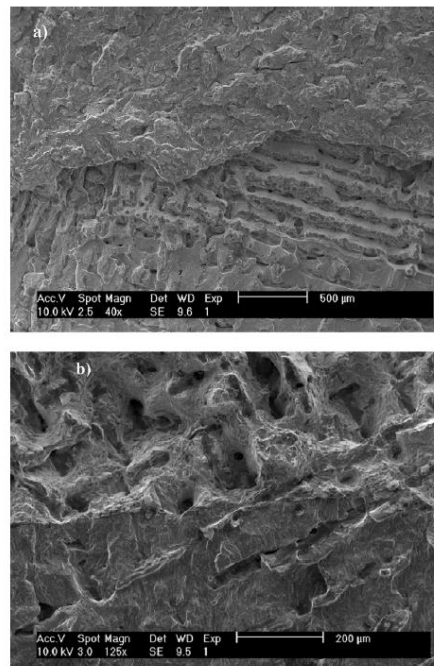


Fig. 11. SEM observations on the transient region: (a) As-built material; (b) Heat-treated sample.

the failure surface at the transient points after the overload application at a ΔK baseline level of 18 MPa \sqrt{m} , and overload ratio of 2, for as-built and heat-treated samples, respectively. Both pictures clearly suggest the existence of a change in propagation plan and even some disorder in fatigue crack growth mechanisms.

4. Conclusions

Fatigue crack propagation on both as-built and post-manufacturing heat treated selective laser melted AISI 18Ni300 maraging steel series were studied using standard 6 mm thick CT specimens under constant amplitude loading and after tensile overloads application. The following conclusions can be drawn:

- The heat treatment promotes important microstructural changes homogenizing the structure and the transitions between selective laser melted layers.
- Heat treatment increases the hardness in about 25% and reduces the crack propagation rate, not only near threshold, but also in the Paris law regime.
- In many cases, crack path in heat-treated SLM specimens is almost linear crossing the crack through the deposited layers, in contrast with the predominant inter-layer propagation mode observed for as built SLM specimens.
- Heat treatment reduces also the crack propagation retardation in the transient regime after overload application, particular for the lower ΔK baseline value analysed.
- The study carried out in the transient crack growth regime did not detect the crack closure phenomenon, being probably the retardation of the propagation rate due to the very significant crack bifurcation observed during the overload.


Acknowledgements

The authors would like to acknowledge the sponsoring under the project number 016713 (PTDC/EMS-PRO/1356/2014) financed by Project 3599 Promover a Produção Científica e Desenvolvimento Tecnológico e a Constituição de Redes Temáticas (3599-PPCDT) and FEDER funds and also EROFIO S.A. industry for the supply of the testing samples.

References

- [1] K.G. Prashanth, H.S. Shahabi, H. Attar, V.C. Srivastava, N. Ellenndt, V. Uhlenwinkel, J. Eckert, S. Scudino, Production of high strength Al 85 Nd 8 Ni 5 Co 2 alloy by selective laser melting, *Addit. Manuf.* 6 (2015) 1–5.
- [2] K.G. Prashanth, S. Scudino, H.J. Klauss, K.B. Surreddi, L. Loeber, Z. Wang, A.K. Chaubey, U. Kuehn, J. Eckert, Microstructure and mechanical properties of Al-12Si produced by selective laser melting: Effect of heat treatment, *Mater. Sci. Eng., A* 590 (2014) 153–160.
- [3] D.D. Gu, Y.C. Hagedorn, W. Meiners, G. Meng, R.J.S. Batista, K. Wissenbach, R. Poprawe, Densification behaviour, microstructure evolution, and wear performance of selective laser melting processed commercially pure titanium, *Acta Mater.* 60 (2012) 3849–3860.
- [4] E. Louvis, P. Fox, C.J. Sutcliffe, Selective laser melting of aluminium components, *J. Mater. Process. Technol.* 211 (2011) 275–284.
- [5] X.J. Wang, L.C. Zhang, M.H. Fang, T.B. Sercombe, The effect of atmosphere on the structure and properties of a selective laser melted Al-12Si alloy, *Mater. Sci. Eng., A* 597 (2014) 370–375.
- [6] R.D. Li, Y.S. Shi, Z.G. Wang, L. Wang, J.H. Liu, W. Jiang, Densification behaviour of gas and water atomized 316L stainless steel powder during selective laser melting, *Appl. Surf. Sci.* 256 (13) (2010) 4350–4356.
- [7] K.N. Amato, S.M. Gaytan, L.E. Murr, E. Martinez, P.W. Shindo, J. Hernandez, S. Collins, F. Medina, Microstructures and mechanical behaviour of Inconel 718 fabricated by selective laser melting, *Acta Mater.* 60 (5) (2012) 2229–2239.
- [8] S.M. Thompson, L. Bian, N. Shamsaei, A. Yadollahi, An overview of direct laser deposition for additive manufacturing; part I: transport phenomena, modelling, and diagnostics, *Addit. Manuf.* 8 (2015) 36–62.
- [9] N. Shamsaei, A. Yadollahi, L. Bian, S.M. Thompson, An overview of direct laser deposition for additive manufacturing; part II: mechanical behaviour, process parameter optimization and control, *Addit. Manuf.* 8 (2015) 12–35.
- [10] L.E. Murr, E. Martinez, J. Hernandez, S. Collins, K.N. Amato, S.M. Gaytan, et al., Microstructures and properties of 17–4 PH stainless steel fabricated by selective laser melting, *J. Mater. Res. Technol.* 1 (2012) 167–177.
- [11] H.K. Rafi, D. Pal, N. Patil, T.L. Starr, B.E. Stucker, Microstructure and mechanical behaviour of 17–4 precipitation hardenable steel processed by selective laser melting, *J. Mater. Eng. Perform.* 23 (2014) 4421–4428.
- [12] L. Facchini, N. Vicente, I. Lonardelli, E. Magalini, P. Robotti, A. Molinari, Metastable austenite in 17–4 precipitation-hardening stainless steel produced by selective laser melting, *Adv. Eng. Mater.* 12 (2010) 184–188.
- [13] H.A. Stoffregen, K. Butterweck, Eberhard Abele, Fatigue analysis in selective laser melting: review and investigation of thin-walled actuator housings, *Solid Free Fabr. Symp.* (2013) 635–650.
- [14] P. Mercelis, J.P. Kruth, Residual stresses in selective laser sintering and selective laser melting, *Rapid Prototype. J.* 12 (5) (2012) 254–265.
- [15] H. Yves-Christian, W. Jan, M. Wilhelm, W. Konrad, P. Reinhart, Net shaped high performance oxide ceramic parts by selective laser melting, *Phys. Procedia* 5 (Part B) (2010) 587–594.
- [16] T.M. Mower, M.J. Long, Mechanical behaviour of additive manufactured, powder-based laser-fused materials, *Mater. Sci. Eng. A* 651 (2015) 198–213.
- [17] A. Yadollahi, N. Shamsaei, M. Scott, A. Thompson, L. Bian Elwany, Effects of building orientation and heat treatment on fatigue behaviour of selective laser melted 17-4 PH stainless steel, *Internat. J. Fat.* 94 (Part 2) (2017) 218–235.
- [18] G. Kasperovich, J. Hausmann, Improvement of fatigue resistance and ductility of TiAl6V4 processed by selective laser melting, *J. Mater. Process. Technol.* 220 (2015) 202–214.
- [19] S. Leuders, M. Thöne, A. Riemer, T. Niendorf, T. Tröster, H.A. Richard, et al., On the mechanical behaviour of titanium alloy TiAl6V4 manufactured by selective laser melting: fatigue resistance and crack growth performance, *Int. J. Fat.* 48 (2013) 300–307.
- [20] E. Wycisk, A. Solbach, S. Siddique, D. Herzog, F. Walther, C. Emmelmann, Effects of defects in laser additive manufactured Ti-6Al-4V on fatigue properties, *Phys. Procedia* 56 (2014) 371–378.
- [21] P. Edwards, M. Ramulu, Fatigue performance evaluation of selective laser melted Ti-6Al-4V, *Mater. Sci. Eng. A* 598 (2014) 327–337.
- [22] D. Greitemeier, F. Palm, F. Syassen, T. Melz, Fatigue performance of additive manufactured TiAl6V4 using electron and laser beam melting, *Int. J. Fat.* 94 (2017) 211–217.
- [23] L.M.S. Santos, J.A.M. Ferreira, J.S. Jesus, J.M. Costa, C. Capela, Fatigue behaviour of selective laser melting steel components, *Theor. Appl. Fract. Mech.* 85 (2016) 9–15.
- [24] L.M.S. Santos, J.A.M. Ferreira, J.M. Costa, C. Capela, Fatigue performance of hybrid steel samples with laser sintered implants, *Proc. Eng.* 160 (2016) 143–150.
- [25] American Society for Testing and Materials. Standard test method for measurement of fatigue crack growth rates. *Annual Book of ASTM Standards Volume 03.01, ASTM E 647*; 2000.
- [26] L.P. Borrego, J.M. Costa, S. Silva, J.M. Ferreira, Microstructure dependent fatigue crack growth in aged hardened aluminium alloys, *Int. J. Fatigue* 26 (2004) 1321–1331.
- [27] L.P. Borrego, J.M. Costa, F.V. Antunes, J.M. Ferreira, Fatigue crack growth in aluminium alloys, *Eng. Fail. Anal.* 17 (2010) 11–18.
- [28] L.E. Allison, R.C. Ku, M.A. Pompetzki, A comparison of measurement methods and numerical procedures for the experimental characterization of fatigue crack closure. In: *Mechanics of Fatigue Crack Closure*. ASTM STP 982. Newman Jr JC, Elber W (eds). Philadelphia PA, ASTM, pp. 171–185.
- [29] L.P. Borrego, J.M. Ferreira, J.M. Costa, Evaluation of overload effects on fatigue crack growth and closure, *Engng. Fract. Mech.* 70 (2003) 1379–1397.
- [30] L.P. Borrego, J.M. Ferreira, J.M. Pinho da Cruz, J.M. Costa, Fatigue crack growth in thin aluminium alloy sheets under loading sequences with periodic overloads, *Thin-Wall. Struct.* 43 (2005) 772–788.
- [31] C.S. Shin, S.H. Hsu, On the mechanisms and behaviour of overload retardation in AISI 304 stainless steel, *Int. J. Fatigue* 15 (3) (1993) 181–192.
- [32] S. Suresh, Micromechanisms of fatigue crack growth retardation following overloads, *Engng. Fracture Mech.* 18 (1983) 577–593.

Fatigue crack propagation along interfaces of selective laser melting steel hybrid parts

Luis M.S. Santos¹ | José A.M. Ferreira¹ | Luis P. Borrego^{1,2}  | Jose D. Costa¹ | Carlos Capela^{1,3} | Joel de Jesus¹

¹CEMMPRE, Department of Mechanical Engineering, University of Coimbra, Coimbra, Portugal

²Mechanical Engineering Department, Coimbra Polytechnic—ISEC, Coimbra, Portugal

³Mechanical Engineering Department, ESTG, Polytechnic Institute of Leiria, Leiria, Portugal

Correspondence

José A.M. Ferreira, CEMMPRE, Department of Mechanical Engineering, University of Coimbra, Coimbra P-3004 516, Portugal.
Email: martins.ferreira@dem.uc.pt

Abstract

Selective laser melting (SLM) is an emerging additive manufacturing technology, capable of producing complex geometry components. The current work studied both the effect of substrate material and mean stress on the fatigue crack growth behaviour along interfaces of bi-material specimens, substrate, and part by SLM. Fatigue tests were carried out in agreement with ASTM E647 standard, using 6-mm-thick compact specimens. The substrate steel has only a negligible effect both on the fatigue crack propagation rate and on the crack path. The failure occurs in the material additively manufactured by SLM, near the interface. The mean stress produced only a reduced influence on the fatigue crack propagation rate in the Paris regime. For larger values of ΔK , where K_{\max} approaches K_{Ic} , a significant influence of the mean stress was observed. In spite of nondetection of crack closure, the application of overloads promoted significant fatigue crack retardation, quite similar for both substrate materials, probably due to the crack bifurcation during the overload.

KEYWORDS

additive manufacturing, compact (tension) specimens, crack paths, crack propagation, fatigue

1 | INTRODUCTION

Additive manufacturing (AM) processes produce components, directly from computer-aided design information, without the need of moulds or forming tools. In comparison with conventional manufacturing processes, AM

allows raw material and manufacturing time savings and offer more freedom in design, which is an enabler for weight savings through topology optimization. Selective laser melting (SLM) produces mechanical components layer by layer, from a 3D model, by melting metal powder using a laser energy source. SLM offers the ability to generate highly customized parts for application in various industries,¹ but the presence of defects and microstructural heterogeneities creates uncertainty in their mechanical properties, making their widespread use difficult.² Moreover, high mechanical properties are required for many structural materials applications. Therefore, a significant research effort is still needed to better understand the mechanical behaviour of AM materials.

Nomenclature: AM, additive manufacturing; CPM, conventional powder metallurgy; da/dN , fatigue crack propagation rate; N , fatigue life; OLR, overload ratio; P_{op} , opening load; R , stress ratio; R^2 , determination factor; SEM, scanning electron microscopy; SLM, selective laser melting; ΔK , stress intensity factor range; ΔK_{BL} , baseline stress intensity factor range before overload application; ΔK_{OL} , peak overload stress intensity factor range.

Material properties of SLM parts are also affected by residual stresses, internal defects, and the inherent roughness of the surface.^{3,4} Recently, several conclusive studies⁵⁻⁷ report the influence of different heat treatments and surface conditions on the tensile strength for SLM powder materials, while its influence on the fatigue behaviour⁸ needs better understanding. The effect of different post-manufacturing heat treatments on the mechanical properties and microstructure was also studied by Rafi et al⁹ and Facchini et al¹⁰ for SLM 17-4 PH SS steel.

The manufacturing growing direction affects thermal history during fabrication and microstructure grain aspect ratio leading to an anisotropic behaviour of SLM materials. The loading direction in relation to the layer deposition plane also plays an important role on the mechanical properties of AM materials.² The influence of building orientation on tensile properties was confirmed by Luecke and Slotwinski¹¹ for the SLM 17-4 PH steel.

The fatigue behaviour of SLM components needs better understanding through more in-depth studies in order to obtain more reliable results and accurate predictions on fatigue design.² Recently, Mower and Long¹² and Yadollahi et al¹³ studied the effect of building orientation on the fatigue behaviour of 17-4 PH steel.

The presence of pores in AM materials highly influences their fatigue behaviour. A significant number of studies were conducted in conventional powder metallurgy (CPM) materials reporting that crack initiation¹⁴⁻¹⁶ and crack propagation^{16,17} are influenced by porosity. In the presence of pore clusters, the interaction between pores usually occurs as a crack propagation mechanism.

According to Phillips et al,¹⁸ the fatigue crack growth for several CPM steels is well predicted by a modified Paris growth law. They also concluded that the exponent of the Paris law during stable crack growth highly depends on the relative density, decreasing sharply to 2.6 to 4.0 when the full density is approximately achieved. In spite of the similarities of CPM and SLM processes in respect to typical porous, pore clusters and heterogeneous microstructure, fatigue crack growth in SLM materials have specific features.

No fatigue crack closure studies were found in SLM materials, contrary to conventional metals where fatigue crack growth is highly affected by plasticity at crack tip and consequently by the crack closure phenomenon.¹⁹ For conventional metals, the crack closure approach generally permits to correlate the majority of the crack growth rate variations, after single overloads,¹⁹⁻²¹ periodically applied overloads,²² and two-level block loading, using experimental crack closure measurements.²³

The present work intends to characterize fatigue crack propagation and failure mechanisms at both constant amplitude loading and transient regimes after overload application, for several stress ratios, in hybrid components with AISI 18Ni300 SLM steel built on three different substrate materials. Crack closure was monitored in all tests in order to investigate the eventual correlation with the stress ratio effect and crack growth rate variations after single overloads.

2 | MATERIALS AND EXPERIMENTAL PROCEDURE

Hybrid specimens were produced using conventional steel substrates over which were deposited the remaining part by selective laser melting (SLM). The SLM parts were manufactured in maraging steel AISI 18Ni300, while three steel substrates were used: the steel for hot work tools AISI H13, the stainless steel AISI 420, and a low-strength CK45E steel. The chemical composition and mechanical properties of these four materials are indicated in Tables 1 and 2, respectively.

Samples were manufactured using LaserCUSING technology, with layers growing in the same direction as the load application in the mechanical tests. The equipment for selective laser melting was the "Concept Laser," model "M3 Linear." This apparatus comprises a laser-type Nd:YAG with a maximum power of 100 W in continuous wave mode and a wavelength of 1064 nm. The samples were manufactured with a scan speed of 200 mm/s, adding layers of 30- μ m thickness with hatch spacing of 100 μ m and 25% overlapping, growing towards the direction corresponding to the application of load in the mechanical tests. After manufacturing, the specimens were ground on all surfaces, without post-heat treatment, and mechanically polished to facilitate optical observation of the crack during fatigue tests. Finally, the notch was performed by wire electrical discharge machining. Figure 1 shows schematically the building orientation where layer deposition plane is perpendicular to the loading direction.

Fatigue tests were carried out under sinusoidal load control, in agreement with ASTM E647²⁴ standard, using 6-mm-thick compact tension specimens (CT). Figure 2 shows the geometry and dimensions of the hybrid CT specimens, in which the direction of growth of the samples is in the test loading direction. All tests were carried out under load control and frequency of 10 Hz at room temperature using an Instron EletroPuls E10000 machine with 10-kN load capacity (Figure 3). The crack length was measured using a travelling microscope (45 \times) with an accuracy of 10 μ m, as also shown in detail in Figure 3.

TABLE 1 Chemical composition of the materials (% wt)

Steel	C	Ni	Co	V	Mo	Ti	Cr	P	Si	Mn	Fe
18Ni300	0.01	18.2	9.0	-	5.0	0.6	0.3	0.01	0.1	0.04	Bal.
AISI 420	0.37	-	-	0.17	-	-	14.22	0.021	0.64	0.037	Bal.
AISI H13	0.4	-	-	0.94	1.30	-	5.29	0.017	1.05	0.036	Bal.
CK45E	0.42	-	-	-	-	-	-	≤0.035	0.15	0.50	Bal.

TABLE 2 Tensile properties of SLM material and substrate steels

Material	Yield Stress, MPa	UTS, MPa	Extension at Break, %
SLM material	1000	1147	6
AISI 420	1360	1600	12
AISI H13	1280	1520	12
CK45E	420	670	16

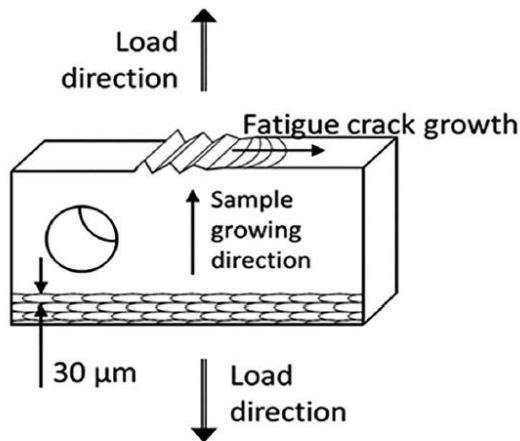


FIGURE 1 Sample building details

Crack growth rate under constant amplitude loading was determined by the incremental polynomial method using five consecutive points.²⁴ Figure 3 shows also a detail of the microgauge pin and its position in order to perform the measurements of crack closure loads.

The microstructure of the SLM material and interface zone of hybrid specimens were analysed according to the standard ASTM E407-99 of metallographic practice, performing a chemical attack with Picral (picric acid solution 4% in ethyl alcohol) during 2 minutes. After preparation, the microstructures of the samples were observed using a Leica DM4000 M LED optical microscope. Figure 4 shows the microstructures of the SLM part in Figure 4A and interface region for hybrid samples with AISI H13 and AISI 420 substrates in Figure 4B,C,

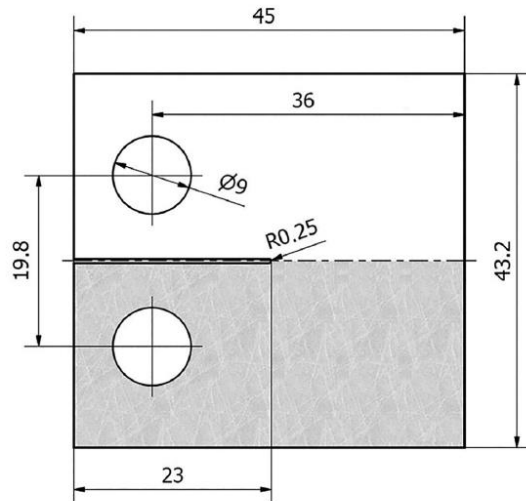


FIGURE 2 CT specimen dimensions (mm)

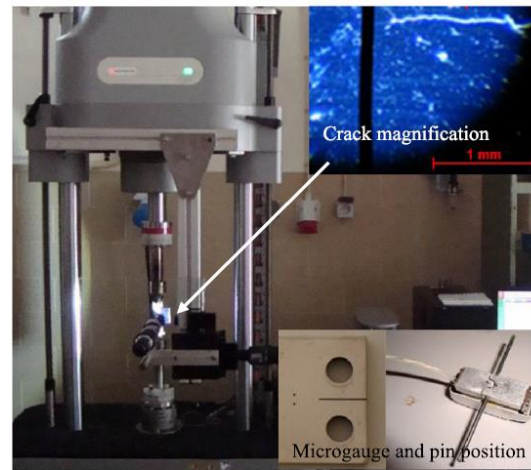


FIGURE 3 Testing machine and details of crack measurement, pin position, and crack closure measurement microgauge [Colour figure can be viewed at wileyonlinelibrary.com]

respectively. Figure 4A shows a typical SLM microstructure with elongated grains and martensitic regions. The substrate material shows a corrugated region created by

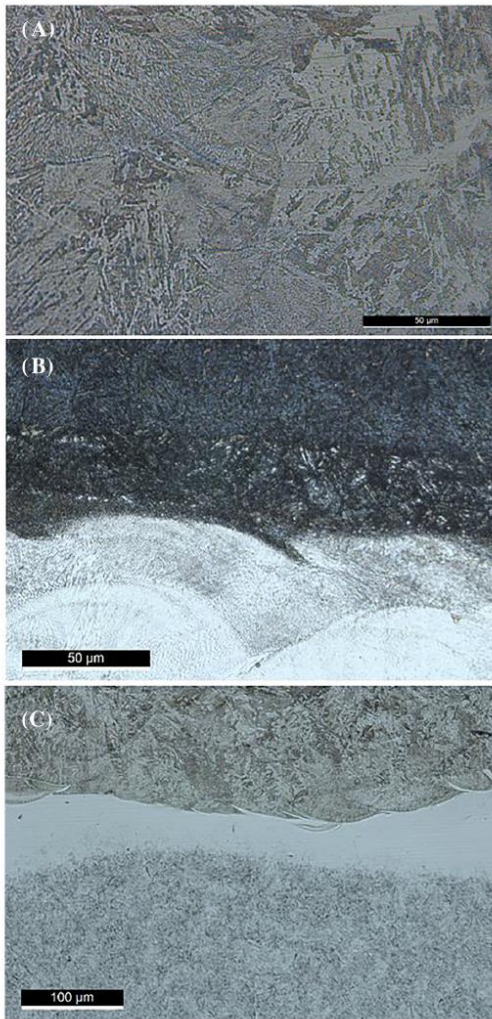


FIGURE 4 Macrostructure and microscopy observations of interface regions: A, SLM microstructure; B, interface for AISI H13 substrate; C, interface for AISI 420 substrate [Colour figure can be viewed at wileyonlinelibrary.com]

the melting in the first laser pass. A reduced formation of micro-pores was observed in the SLM part and also a transition between substrate and AM materials without the presence of lack of fusion zones. All the analysed samples presented the formation of lighter zones at the interface, resulting from the migration of carbon and consequently the occurrence of decarbonisation. In order to confirm these observations, the chemical analysis of the interface was performed on some specimens. Figure 5 compares the chemical composition at the interfaces of the hybrid samples with that of the SLM material, represented with an offset on the X-axis to make the graph

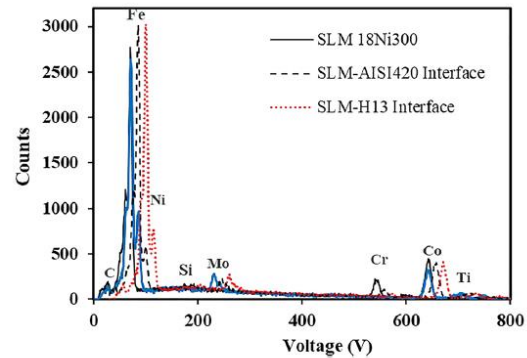


FIGURE 5 Chemical analysis on the interface for hybrid samples [Colour figure can be viewed at wileyonlinelibrary.com]

clearer. With the exception of Ni and Cr, the amounts of the remaining chemical elements are very similar in the three substrate materials, justifying the reduced influence of the substrate material on the results.

Vickers hardness was measured on the surface of the specimens in a line perpendicular to the interface using a Struers Duramin 1 microhardness tester with a 0.5-kg load and following the ASTM E384-11e1 standard. Figure 6 presents the hardness profiles for the three hybrid test samples with different substrate materials. This figure shows an average hardness of 340 HV for the SLM material, while for two of the analysed substrates, a much higher hardness was obtained, 530 HV in the AISI420 and 510 HV in the AISI H13 and a much lower hardness of 180 HV in the CK45 steel. The interface zone presents intermediate values of hardness between the substrate and the SLM materials.

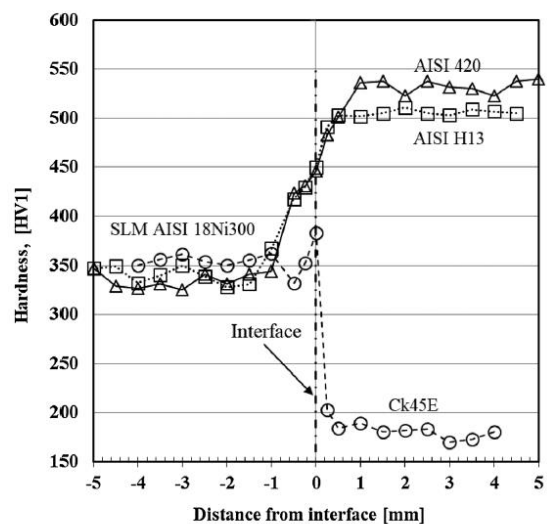


FIGURE 6 Hardness profiles around the interface region

Residual stresses are one of the main factors that affect fatigue performance of selective laser-melted materials. Residual stress analysis was performed by X-ray diffraction using a Proto iXRD equipment. Figure 7 presents the mean values and standard deviation of the longitudinal stress (y-axis in Figure 1) in a region close to the surface of the SLM material at coordinates $x = 5$ and $y = 1.5$ mm. These results show that the residual stresses decrease with the distance to the surface, having a tensile stress with a mean value of 220 MPa in a 200- μ m surface layer and stable values of the diffraction peak breadth around 4.05° . As the residual stresses were measured in only one position of the SLM material and close to the surface, it is impossible to carry out a conclusive discussion on its influence on the crack propagation rate during constant amplitude load tests and during the transient regime after the application of overloads. For this, it would be necessary to obtain a complete characterization of the residual stresses both in the direction of the z-axis, up to half thickness, and in the direction of crack propagation of the crack (x-axis in Figure 1), which was outside the objectives to be achieved with this work.

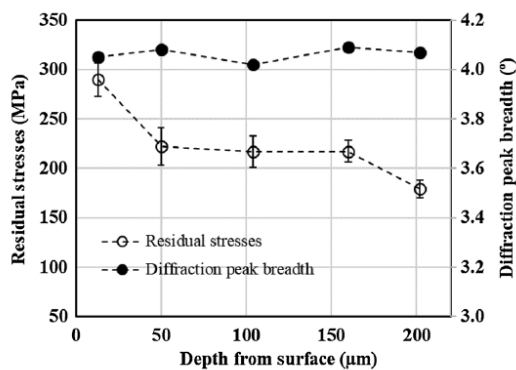


FIGURE 7 Profile of the longitudinal (loading direction) residual stresses

TABLE 3 Fatigue testing program

Test	Material	R	ΔP , kN	ΔK_{BL} , $\text{MPa}\sqrt{\text{m}}$	OLR	No. of Overloads	
Constant amplitude	SLM	0.05	2.63	-	-	-	
	SLM + CK45	0.05	2.63	-	-	-	
	SLM + AISI H13	0.05	2.63	-	-	-	
	SLM + AISI 420	0.05	2.63	-	-	-	
			0.3	2.26	-	-	-
			0.6	1.70	-	-	-
Overloads	SLM + CK45	0.05	2.63	12; 18	2	1	
	SLM + AISI 420	0.05	2.63	12; 18	2	1; 10; 100	

The influence of tensile overloads was investigated in the Paris regime at $R = 0.05$. Single and multiple tensile overloads were also performed under load control, with a ΔK baseline level (ΔK_{BL}) of 12 and 18 $\text{MPa}\sqrt{\text{m}}$. The overload ratio, defined as,

$$\text{OLR} = \frac{\Delta K_{OL}}{\Delta K_{BL}}, \quad (1)$$

was $\text{OLR} = 2$, where ΔK_{OL} and ΔK_{BL} are the peak overload stress intensity factor range and the baseline stress intensity factor range before the overload application, respectively. Therefore, each overload was applied with 100% increase in load, respectively, to the baseline loading range.

Load-displacement curves were monitored at specific crack length increments throughout each of the tests using a pin microgauge elaborated from a high sensitive commercial axial extensometer (± 0.625 mm of maximum displacement). As showed also in Figure 3, the gauge pins were placed at the centre of the specimens in two drilled holes of 0.5-mm diameter with 3.5-mm distance between them. Load-displacement data acquisition was done after the crack advances beyond the pins. Data collection was performed at a reduced frequency of 0.5 Hz. Table 3 summarizes all fatigue tests that were performed indicating the loading parameters used.

The fracture surface analysis was performed with a scanning electron microscope Philips XL30.

3 | RESULTS AND DISCUSSION

3.1 | Crack propagation under constant amplitude loading

Mechanical properties of the SLM AISI 18Ni300 steel were previously obtained by the Santos et al²⁵ in terms of the tensile strength and Young's modulus, hardness, and porosity.

Fatigue crack growth tests were carried out under constant amplitude loading (ΔK increase) in order to study the stable crack growth in the Paris law regime. Figure 8 depicts da/dN - ΔK curves for the three hybrid specimens series with different conventional steels (AISI H13, or AISI 420, or CK45E), showing the influence of the substrate material for the stress ratio $R = 0.05$. The reference da/dN - ΔK curve obtained in this work for fully SLM samples, as well as crack propagation curves for the three substrate materials, taken from the literature,²⁶⁻²⁸ was superimposed for comparison. The analysis of the figure shows a negligible influence of the substrate steel on the fatigue crack propagation over the entire ΔK range analysed. The main causes for these results are the site of crack initiation and the path of propagation. Figure 9 presents an exemplary and representative image of all fatigue tests, showing the crack initiation site and the propagation path in a sample with CK45 substrate. The analysis of this figure shows that crack initiated at the tip of the notch and propagated through the SLM material, within the layer near the interface, where the carbon migration occurred. As this layer has similar microstructure and chemical composition in all sample batches, and being the least resistant, it is the preferred region for crack growth.

The effect of mean stress on the da/dN - ΔK curves was studied for the samples with AISI420 steel substrate. The results for $R = 0.05, 0.3$, and 0.6 are plotted in Figure 10. Contrary to that observed in most conventional metals, a negligible effect of the mean stress was obtained in the

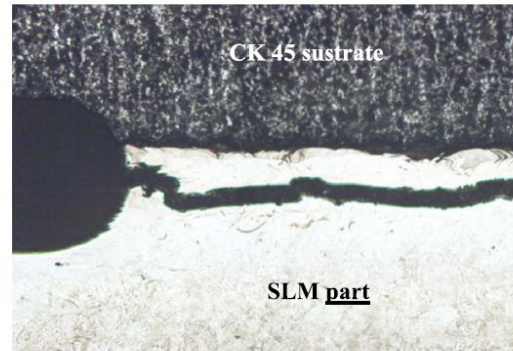


FIGURE 9 Fatigue crack initiation from the specimen notch tip. Hybrid specimen with CK45 substrate [Colour figure can be viewed at wileyonlinelibrary.com]

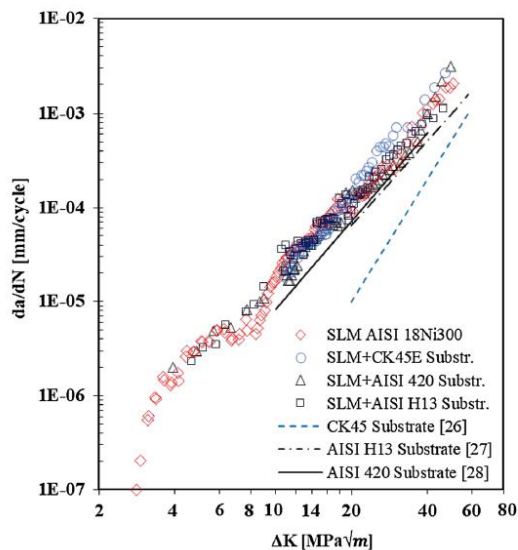


FIGURE 8 Comparison of da/dN - ΔK curves for SLM material, three different hybrid samples, and substrate materials²⁶⁻²⁸; $R = 0.05$ [Colour figure can be viewed at wileyonlinelibrary.com]

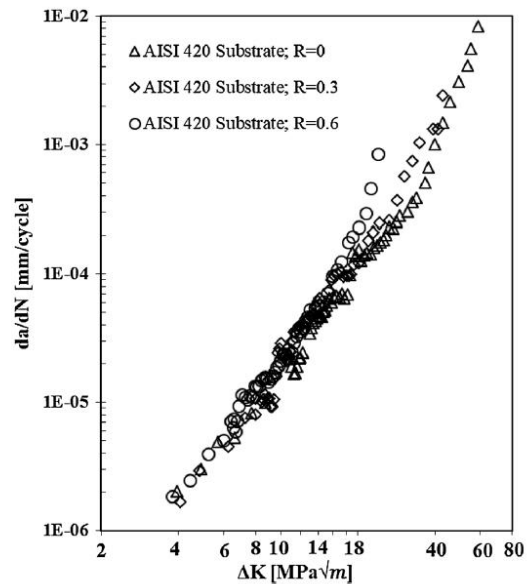


FIGURE 10 Effect of mean stress on the da/dN - ΔK curves of hybrid specimens with AISI420 steel substrate

Paris regime for SLM materials. Only in regime III, for the maximum K value approaching the fracture toughness of the material, a significant increase in crack growth rate with mean stress was observed.

For conventional metal materials, the fatigue crack growth is normally affected by mean stress, being this effect mainly caused by the plasticity at crack tip and consequently by crack closure.^{19,29} Considering the reduced effect of the mean stress observed in Figure 10, the question arises whether this material produced by SLM exhibits crack closure.

To get answer to this question, the crack closure was monitored in all tests. As indicated previously, load-displacement curves were monitored at specific crack length intervals over each of the tests using the pin microgauge shown in Figure 3.

Opening loads, P_{op} , were derived from these records using the technique known as maximization of the correlation coefficient.²⁰ This technique involves taking the upper 10% of the load-displacement data (cycle loading phase) and calculating the least squares correlation coefficient. The next data pair is then added, and the correlation coefficient is again computed. This procedure is repeated for the whole data set. The point at which the correlation coefficient reaches a maximum can then be defined as P_{op} . Figure 11 shows one exemplary curve plotting the correlation coefficient against the load during the loading fatigue cycle phase. The analysis of the figure shows that a maximum on the correlation coefficient curve is not defined, this means no observance of the crack closure phenomena, which justify the reduced effect of the mean stress on the stable crack propagation regime.

As shown in Figure 9, the cracks started on the SLM material for all hybrid specimens and continue to propagate in this material near the interface with the substrate. Figure 12A,B shows the crack path for AISI420 and CK45 steel substrates, respectively, where cracks initially started from the notch in the SLM side. In all fatigue tests, the crack propagates in a zigzag path, showing mixed failure mode: transgranular with crack passing through the layer or interlayer failure, where the crack contours the deposited layers having steps of one, two, or three layers.

Table 4 summarizes the values of the Paris law constants obtained for the different hybrid samples tested under constant amplitude loading, considering da/dN in mm/cycle and ΔK in $\text{MPa}\sqrt{\text{m}}$.

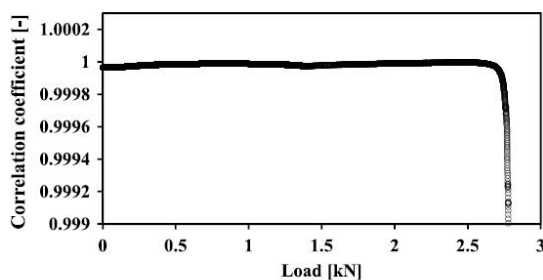


FIGURE 11 Opening load determination by the maximization of the correlation coefficient technique

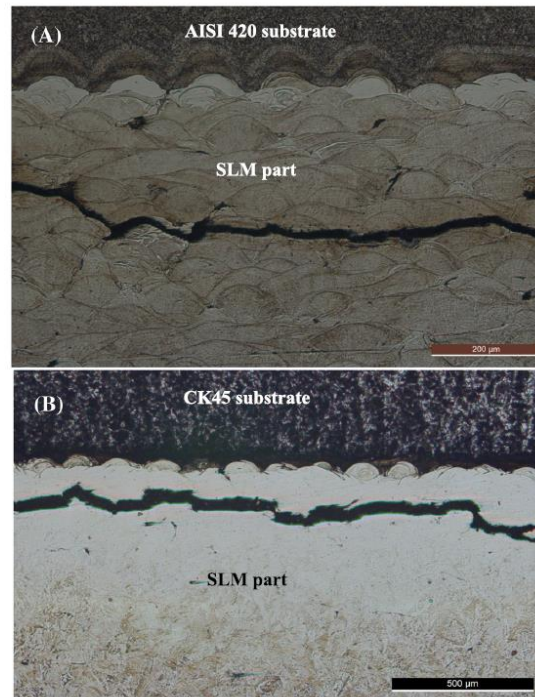


FIGURE 12 Crack path for hybrid samples: A, AISI 420 substrate; B, CK 45 substrate [Colour figure can be viewed at wileyonlinelibrary.com]

TABLE 4 Paris law parameters (da/dN in mm/cycle and ΔK in $\text{MPa}\sqrt{\text{m}}$)

Substrate Material	Stress Ratio R	C	m	Determination coefficient, R^2
Reference SLM material	0.05	4.218×10^{-8}	2.67	0.992
AISI H13	0.05	3.741×10^{-8}	2.71	0.989
CK45E	0.05	1.178×10^{-8}	3.30	0.981
AISI 420	0.05	4.606×10^{-8}	2.59	0.985
AISI 420	0.3	1.953×10^{-8}	2.64	0.979
AISI 420	0.6	2.132×10^{-8}	3.06	0.974

3.2 | Transient crack growth regime after overloading

The transient crack growth behaviour after the application of 1, 10, or 100 of tensile overloads applied at ΔK baseline levels of 12 and 18 $\text{MPa}\sqrt{\text{m}}$ with OLR = 2 was analysed. Figure 13A highlights the effect of the number of overloads on the da/dN - ΔK curves for samples with

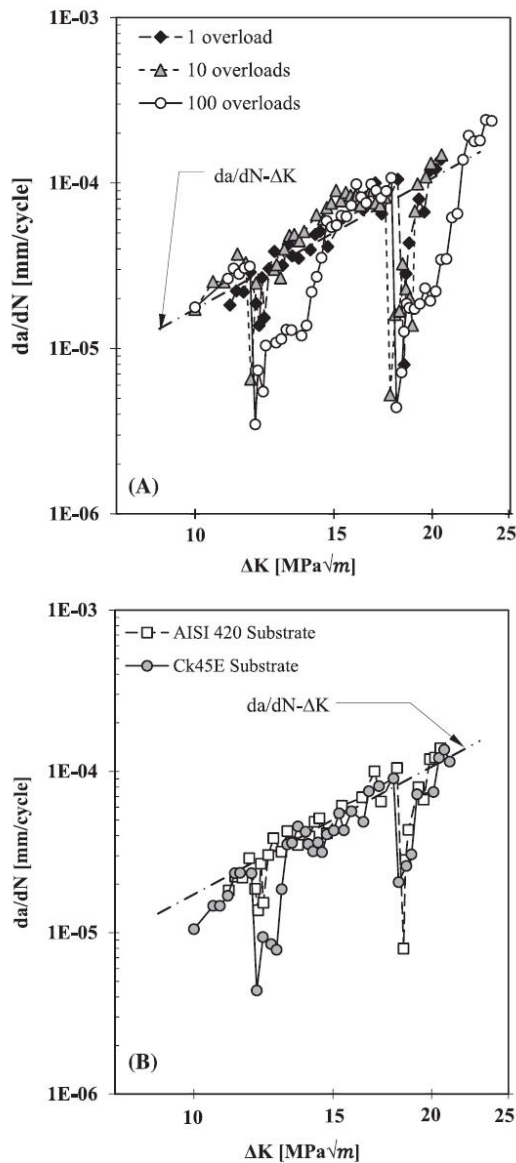


FIGURE 13 Transient regime due to overload application on hybrid samples: A, effect of the number of overloads for AISI 420 substrate; B, effect of the substrate with application of a single peak overload

AISI 420 steel substrate. For better comparison, the curve obtained under constant amplitude loading is superimposed in the figure. The results show the typical delay effect after overloading, which is normally reported in the literature for casting materials. This retardation is usually attributed to the crack closure effect.¹⁹⁻²³ However, despite the significant crack growth retardation induced by the overloads, crack closure was not observed

in the present study, similarly to the depicted in Figure 11. Figure 13A also shows that by increasing the number of overload cycles, the retardation effect increases significantly for both ΔK baseline values.

Figure 13B compares the transient propagation behaviour after application of a single peak overload in samples with CK45 and AISI 420 substrate steels. Both samples exhibit a very similar behaviour, which is once again due to the propagation of the crack occurring, in both cases, through SLM material close to the interface, similar to what was observed in constant load amplitude tests.

Failure surfaces were analysed in scanning electron microscope to identify the mechanisms of crack propagation. Figure 14A presents a representative image, obtained for a sample with CK45 substrate at a ΔK about 15 MPa√m, showing that brittle fracture is predominant. Figure 14B was also obtained for a sample with CK45 substrate after the application of an overload at a ΔK baseline level of 18 MPa√m, showing changes in the crack propagation plane and failure mode. The change of the crack path after the application of overloads is

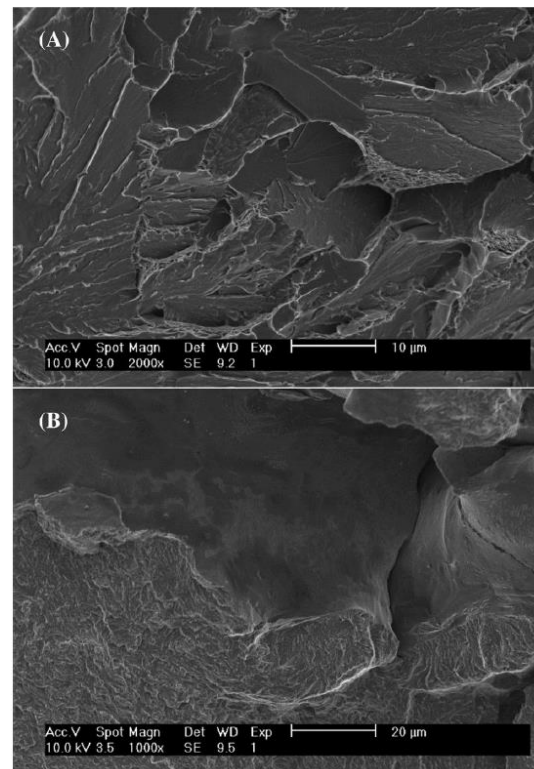


FIGURE 14 SEM observations of the surface failure on samples with CK45 substrate: A, stable crack growth; B, after a single tensile overload application at ΔK baseline of 18 MPa√m

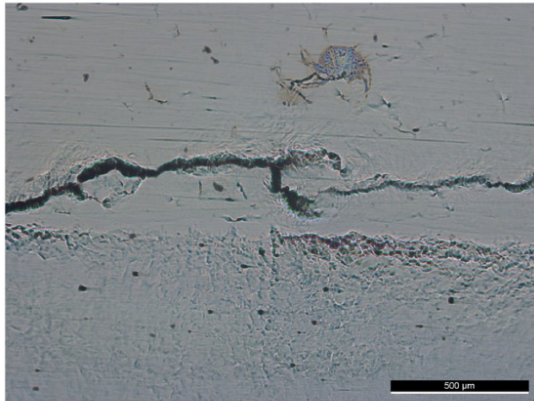


FIGURE 15 Crack bifurcation after overloading [Colour figure can be viewed at wileyonlinelibrary.com]

confirmed in Figure 15, which illustrates the respective crack bifurcation. The same figure also shows that cracks re-join after a transient period, and this behaviour is probably the main reason by the retardation observed in the fatigue crack propagation rate, despite the reduced crack closure phenomena observed in the SLM material.

4 | CONCLUSIONS

SLM and hybrid samples constituted by SLM material AISI 18Ni300 built on substrates in conventional steels were manufactured and tested in order to study the effect of substrate material and stress ratio on the fatigue crack propagation rate when subjected to constant amplitude loadings. The transient crack growth behaviour after overloads application was also investigated. The following conclusions can be drawn:

- Good fusion was achieved at the interface of the hybrid parts in all substrates, presenting a small level of defects and only some decarbonisation.
- The selective laser melting process induced longitudinal tensile residual stresses in near surface regions with an average value of about 220 MPa.
- The hardness and tensile strength of substrate steel has only a negligible effect on the fatigue crack propagation rate and on the crack path. Independent of the hardness of the substrate material, the fatigue failure occurs in the SLM material, near interface, at a distance between 150 and 200 μm .
- Fatigue crack retardation after single overload is very similar for all substrate materials. The study carried out did not detect the crack closure phenomena, being probably the retardation of the crack propagation due


to the crack bifurcation observed after the overloads application.

- In agreement with the fact that crack closure was not observed, the mean stress produced only a reduced influence on the fatigue crack propagation rate under constant amplitude loading.

ACKNOWLEDGEMENTS

The authors would like to acknowledge the sponsoring under the project number 016713 (PTDC/EMS-PRO/1356/2014) financed by Project 3599 *Promover a Produção Científica e Desenvolvimento Tecnológico e a Constituição de Redes Temáticas* (3599-PPCDT) and FEDER funds and also EROFIO S.A. industry for the supply of the testing samples.

ORCID

Luis P. Borrego  <https://orcid.org/0000-0003-0259-8926>

REFERENCES

1. Thompson SM, Bian L, Shamsaei N, Yadollahi A. An overview of direct laser deposition for additive manufacturing; part I: transport phenomena, modeling, and diagnostics. *Addit Manuf.* 2015;8:36-62.
2. Shamsaei N, Yadollahi A, Bian L, Thompson SM. An overview of direct laser deposition for additive manufacturing; part II: mechanical behavior, process parameter optimization and control. *Addit Manuf.* 2015;8:12-35.
3. Chan KS, Koike M, Mason RL, Okabe T. Fatigue life of titanium alloys fabricated by additive layer manufacturing techniques for dental implants. *Metall Mater Trans A.* 2013;44(2):1010-1022.
4. Wycisk E, Emmelmann C, Siddique S, Walther F. High cycle fatigue (HCF) performance of Ti-6Al-4V alloy processed by selective laser melting. *Adv Mat Res.* 2013;816:134-139.
5. Kasperovich G, Hausmann J. Improvement of fatigue resistance and ductility of TiAl6V4 processed by selective laser melting. *J Mater Process Technol.* 2015;220:202-214.
6. Leuders S, Thöne M, Riemer A, et al. On the mechanical behaviour of titanium alloy TiAl6V4 manufactured by selective laser melting: fatigue resistance and crack growth performance. *Int J Fatigue.* 2013;48:300-307.
7. Rafi HK, Starr TL, Stucker BE. A comparison of the tensile, fatigue, and fracture behavior of Ti-6Al-4V and 15-5 PH stainless steel parts made by selective laser melting. *Int J Adv Manuf Technol.* 2013;69(5-8):1299-1309.
8. Li P, Warner DH, Fatemi A, Phan N. Critical assessment of the fatigue performance of additively manufactured Ti-6Al-4V and perspective for future research. *Int J Fatigue.* 2016;85:130-143.
9. Rafi HK, Pal D, Patil N, Starr TL, Stucker BE. Microstructure and mechanical behavior of 17-4 precipitation hardenable steel processed by selective laser melting. *J Mater Eng Perform.* 2014;23(12):4421-4428.

10. Facchini L, Vicente N, Lonardelli I, Magalini E, Robotti P, Molinari A. Metastable austenite in 17-4 precipitation-hardening stainless steel produced by selective laser melting. *Adv Eng Mater.* 2010;12(3):184-188.
11. Luecke WE, Slotwinski JA. Stainless steel made by additive manufacturing. *J Res Natl Inst Stand Technol.* 2014;119:398-418.
12. Mower TM, Long MJ. Mechanical behavior of additive manufactured, powderbed laser-fused materials. *Mater Sci Eng A.* 2015;651:198-213.
13. Yadollahi A, Shamsaei N, Thompson SM, Elwany A, Bian L. Effects of building orientation and heat treatment on fatigue behavior of selective laser melted 17-4 PH stainless steel. *Int J Fatigue.* 2017;94(2):218-235.
14. Chawla N, Murphy TF, Narasimhan KS, Koopman M, Chawla KK. Axial fatigue behaviour of binder-treated versus diffusion alloyed powder metallurgy steels. *Mater Sci Eng A.* 2001;308(1-2):180-188.
15. D'Armas H, Llanes L, Penafiel J, Bas J, Anglada M. Tempering effects on the tensile response and fatigue life behaviour of a sinter-hardened steel. *Mater Sci Eng A.* 2000;277(1-2):291-296.
16. Carabajar S, Verdu C, Fougères R. Damage mechanisms of a nickel alloyed sintered steel during tensile tests. *Mater Sci Eng A.* 1997;232(1-2):80-87.
17. Sudhakar KV. Fatigue behaviour of a high density powder metallurgy steel. *Int J Fatigue.* 2000;22(9):729-734.
18. Phillips RA, King JE, Moon JR. Fatigue crack propagation in some PM steels. *Powder Metall.* 2000;43(2):149-156.
19. Borrego LP, Ferreira JM, Costa JM. Fatigue crack growth and crack closure in an AlMgSi alloy. *Fatigue Fract Eng Mater Struct.* 2001;24(4):255-266.
20. Borrego LP, Ferreira JM, Costa JM. Evaluation of overload effects on fatigue crack growth and closure. *Eng Fract Mech.* 2003;70(11):1379-1397.
21. Borrego LP, Antunes FV, Costa JD, Ferreira JM. Numerical simulations of plasticity induced closure under overload and high-low blocks. *Eng Fract Mech.* 2012;95:57-71.
22. Borrego LP, Ferreira JM, Pinho da Cruz JM, Costa JM. Fatigue crack growth in thin aluminium alloy sheets under loading sequences with periodic overloads. *Thin-Wall Struct.* 2005;43(5):772-788.
23. Borrego LP, Ferreira JM, Costa JM. Partial crack closure under block loading. *Int J Fatigue.* 2008;30:1789-1796.
24. American Society for Testing and Materials. Standard test method for measurement of fatigue crack growth rates. Annual Book of ASTM Standards 2000: Volume 03.01, ASTM E 647.
25. Santos LMS, Ferreira JAM, Jesus JS, Costa JM, Capela C. Fatigue behaviour of selective laser melting steel components. *Theor Appl Fract Mech.* 2016;85:9-15.
26. Costa JDM, Ferreira JAM. Effect of stress ratio and specimen thickness on fatigue crack growth of the CK45 steel. *Theor Appl Fract Mech.* 1998;30(1):65-73.
27. Shah M, Ali M, Sultan A, et al. An investigation into the fatigue crack growth rate of electron beam-welded H13 tool steel: effect of welding and post-weld heat treatment. *Metallog Microstruc Anal.* 2014;3(2):114-125.
28. Plesiutchnig E, Fritzl P, Enzinger N, Sommitsch C. Fracture analysis of a low pressure steam turbine blade. *Case Studies Eng Fail Anal.* 2016;56:39-50.
29. Borrego LP, Costa JM, Antunes FV, Ferreira JM. Fatigue crack growth in aluminium alloys. *Eng Fail Anal.* 2010;17(1):11-18.

How to cite this article: Santos LMS, Ferreira JAM, Borrego LP, Costa JD, Capela C, de Jesus J. Fatigue crack propagation along interfaces of selective laser melting steel hybrid parts. *Fatigue Fract Eng Mater Struct.* 2019;1–10. <https://doi.org/10.1111/ffe.13072>

5. Conclusion and Future Works

The so-called 3D Printing technologies are being proven for industrial applications and with time conquering their space on the workshop's floor. Their applications are increasing according to the availability of the materials and to the confidence in the systems and the technology. The complexity comes when the same 3D printer could be producing components for strongly regulated markets, like the aviation and medic industries, or for small objects with "no" risk associated with ludic applications. Like this, there is still the need to correctly assess the technologies *versus* materials *versus* applications performance and the need for research work that could make the knowledge gap narrower, enabling the possibility for new applications, and more specifically the confidence in the SLM/LPBF technology.

From the present research work and considering that the specimens were assessed in the as built condition, unless a different condition is stated, and processed by the SLM technology from AISI 18Ni300 powder material, the following main conclusions can be drawn;

- The main consequence of the scan speed increase from 200 to 400 and to 600 mm/s during the SLM process was to reduce the energy density input, inducing porosity and affecting the mechanical properties of the SLMed material, reducing tensile strength, stiffness and strain at failure. Given the poor quality of the material obtained at 400 and 600 mm/s, subsequent studies were carried out with a scanning speed of 200 mm/s. Other defects were detected even for the best density at 200 mm/s, like, lack of penetration and unmolten particles, favouring the crack nucleation process.
- The AISI 18Ni300 powder material formed using the SLM process achieved good monotonic mechanical properties similar to the casting material and independent from the post heat-treatment. Regarding hybrid specimens composed of casted standard materials, AISI H13 and AISI 420, as substrate/support to the build/SLM material, the stiffness increased around 7% at the cost of the strain at failure that decreased around 61%.
- The fatigue damage of the SLMed material is controlled by strain range and has a slightly softening behaviour for strain amplitudes higher than 0.5% and reducing after 1.2%.
- The hybrid specimens' formulations, AISI H13 and AISI 420, have slightly worse fatigue behaviour than the fully SLMed material, but no defects were detected on SLMed's material interfaces.

- The SLMed processing of the 18Ni300 powder under the current conditions, induced tensile residual stress (mean value: 220 MPa), being higher in the specimen periphery.
- Crack nucleation is always happening on surface or subsurface defects, like unmolten particles and voids, but it was delayed for the heat-treated specimens, due to its influence on the microstructure refinement and homogeneity.
- Miner's law is suitable for predicting fatigue lives under block loadings for the full SLMed and hybrid specimens with substrates made from (AISI H13 and AISI 420), with an error lower than 10% and even being conservative for the hybrid formulations.
- Under a low-cycle fatigue regime, the SLMed material, presented a slight strain-softening behaviour and a non-linear response for the elastic and plastic regime, being possible to model its life using the total strain energy density, which is irrespective of the strain rate.
- Rupture always happened in the SLMed material independent from the specimen formulation and testing conditions. For the hybrid CT specimens, with substrates of AISI H13, AISI 420 and AISI CK45E alloys, the crack propagated at a distance around 150 to 200 microns from the interface.
- The mean stress has a slightly influence on the FCGR for the SLMed specimens, including the hybrid formulation using the AISI 420 substrate, in the stable Paris regime. The effect of the mean stress was evident when approaching the critical ΔK value, the material's fracture toughness.
- For transient regimes after applying single overloads on CT hybrid specimens (substrate: AISI H13, AISI 420 and AISI CK45E), the crack closure effect was very similar, in reality no crack closure was detected, instead, a retardation phenomenon that could be explained by the detected crack path bifurcation was detected. The crack retardation effect response increased when increasing the number of overloads per block, 10 and 100 respectively.
- Fully SLMed and heat-treated CT specimens have an increased resistance to the fatigue crack nucleation and propagation, when compared with the as printed ones. On the other hand, the heat treated ones have a retardation effect significantly lower than the ones in as printed condition, especially, for low ΔK baseline values.

In summary, the AISI 18Ni300 powder alloy can be successfully processed by the SLM technology and used to manufacture mechanical components or hybrid ones. The post process heat-treatment is recommended to improve the microstructure and reduce the residual stresses, increasing the fatigue performance of the component. On the other hand, it was demonstrated that

it was possible to assess and estimate the fatigue life performance of this specific AISI 18Ni300 alloy processed by the SLM technology under the current parameters and using the traditional methodology.

Due to the new developments in the SLM technology, the availability of new materials, and the option of doping powders that are brought to light every day, it is suggested that the following research lines be addressed:

- Design of fatigue curves of doped maraging stainless tool steel at high temperatures and its interaction with creep for a better understanding of its potential applications and limits.
- Influence of doped maraging stainless tool steel powder on the SLM process and its mechanical, fatigue and tribological properties, with the intention of increasing the wear resistance.
- Design and fatigue assessment of composites with metallic matrix, sandwich like, reinforce with glass, kevlar and carbon fibres.
- Research on the joining of different classes of materials using the SLM technology in order to remove bonding compounds and fasteners, e.g., between metal alloys and ceramics, and metals alloys and polymers. This could lead to improved joints reducing the final component weight, improving its structural integrity or life span.
- Fatigue design curves of metamaterials formed by light weight and functional structures, and how to simplify the problems to enable these highly complex structures to be numerically simulated based on an everyday or industrial practice.

6. References

- 3DMicroPrint, accessed at 6 October 2023. <https://www.3dmicroprint.com/products/machines/dmp70series/>
- 3DPrinting, accessed at 6 October 2023. <https://3dprinting.com/news/aurora-labs-commercialise-multi-layer-concurrent-printing/>
- Abdel-atif M, Abdel-Ghany K, El-Mahallawy N, Mattar T. Effect of Laser Speed on Microstructure and Mechanical Properties of AISI H13 Tool Steel Prepared by Laser Powder Bed Fusion Process. *Journal of Material Engineering and Performance*, 2021, <https://doi.org/10.1007/s11665-021-06321-y>.
- Addcreative, accessed at 6 October 2023. <https://addcreative.tech/ac-addcreator/>
- Akinlabi ET, Okamoto Y, Maina MR, Akinlabi SA, Pityana S, Tlotleng M, Soliu GA, Mahamood RM, Laser Metal Deposition of Titanium Alloy (Ti6Al4V): A Review, 2019 International Conference on Engineering, Science, and Industrial Applications (ICESI), Engineering, Science, and Industrial Applications (ICESI), 2019 International Conference on August 2019:1-5. <https://doi.org/10.1109/ICESI.2019.8863018>
- Alafaghani A, Qattawi A, Castañón MAG, Effect of manufacturing parameters on the microstructure and mechanical properties of metal laser sintering parts of precipitate hardenable metals, *Int J Adv Manuf Technol* 99, 2491–2507 (2018). <https://doi.org/10.1007/s00170-018-2586-5>
- Allison LE, Ku RC, Pompetzki MA. A comparison of measurement methods and numerical procedures for the experimental characterization of fatigue crack closure. *Mechanics of Fatigue Crack Closure*. ASTM STP 982. Newman Jr JC, Elber W (eds). Philadelphia PA, ASTM International, 1988, pp. 171–185.
- Anas S, Khan MY, Rafey M, Faheem K. Concept of 5D printing technology and its applicability in the healthcare industry. *Materials Today: Proceedings*. 2022; 56 (Part 4) : 1726-1732. <https://doi.org/10.1016/j.matpr.2021.10.391>.
- Anderson TL, *Fracture Mechanics – Fundamentals and Applications*, CRC Press, 1991.

- Andrenelli A, López-González J, Porras J. 3D printing and international trade : What is the evidence to date? Organisation for Economic Co-operation and Development : Trade and Agriculture Directorate, TAD/TC/WP(2021)12/FINAL, JT03484187, 2021.
- Antunes FV, Branco R, Prates PA, Borrego L. Fatigue crack growth modelling based on CTOD for the 7050-T6 alloy. *Fatigue & Fracture of Engineering Materials & Structures*, 2017, 40: 1309–1320. <https://doi.org/10.1111/ffe.12582>
- Antunes FV, Rodrigues SM, Branco R, Camas D. A numerical analysis of CTOD in constant amplitude fatigue crack growth. *Theoretical and Applied Fracture Mechanics*, Volume 85, Part A, 2016, Pages 45-55, ISSN 0167-8442. <https://doi.org/10.1016/j.tafmec.2016.08.015>
- ARCAM (1), accessed at 25 September 2019. <http://www.arcam.com/wp-content/uploads/arcamebm-corp-brochure-fnlv3.pdf>
- ARCAM (2), accessed at 29 January 2020. <http://www.arcam.com/solutions/orthopedic-implants/>
- ASM International, *ASM Handbook – Properties and Selection: Irons Steels and High Performance Alloys*, Volume 1, 1993, 1870-1888.
- ASTM, American Society for Testing and Materials. Standard test method for measurement of fatigue crack growth rates. *Annual Book of ASTM Standards Volume 03.01, ASTM E 647*; 2000.
- Balachandramurthi AR, Moverare J, Dixit N, Deng D, Pederson R, Microstructural influence on fatigue crack propagation during high cycle fatigue testing of additively manufactured Alloy 718, *Materials Characterization*, Volume 149, 2019, Pages 82-94, ISSN 1044-5803. <https://doi.org/10.1016/j.matchar.2019.01.018>.
- Balachandramurthi AR, Moverare J, Dixit N, Pederson R, Influence of defects and as-built surface roughness on fatigue properties of additively manufactured Alloy 718, *Materials Science and Engineering: A*, Volume 735, 2018, Pages 463-474, ISSN 0921-5093. <https://doi.org/10.1016/j.msea.2018.08.072>.
- Bandyopadhyay A, Heer B, Additive manufacturing of multi-material structures, *Materials Science and Engineering: R: Reports*, Volume 129, 2018, Pages 1-16, ISSN 0927-796X. <https://doi.org/10.1016/j.mser.2018.04.001>
- Borrego LP, Antunes FV, Costa JD, Ferreira JM. Numerical simulations of plasticity induced closure under overload and high-low blocks. *Eng Fract Mech*. 2012;95:57-71. <https://doi.org/10.1016/j.engfracmech.2012.07.016>

- Borrego LP, Costa JM, Antunes FV, Ferreira JM. Fatigue crack growth in aluminium alloys. *Eng. Fail. Anal.* 17 (2010) 11–18. <https://doi.org/10.1016/j.engfailanal.2008.11.007>
- Borrego LP, Costa JM, Silva S, Ferreira JM. Microstructure dependent fatigue crack growth in aged hardened aluminium alloys. *Int. J. Fatigue* 26 (2004) 1321–1331. <https://doi.org/10.1016/j.ijfatigue.2004.04.004>
- Borrego LP, Ferreira JM, Costa JM. Evaluation of overload effects on fatigue crack growth and closure. *Eng Fract Mech.* 2003;70(11):1379-1397. [https://doi.org/10.1016/S0013-7944\(02\)00119-4](https://doi.org/10.1016/S0013-7944(02)00119-4)
- Borrego LP, Ferreira JM, Costa JM. Fatigue crack growth and crack closure in an AlMgSi alloy. *Fatigue Fract Eng Mater Struct.* 2001;24(4):255-266. <https://doi.org/10.1046/j.1460-2695.2001.00383.x>
- Borrego LP, Ferreira JM, Costa JM. Partial crack closure under block loading. *Int J Fatigue.* 2008;30:1789-1796. <https://doi.org/10.1016/j.ijfatigue.2008.02.004>
- Borrego LP, J.M. Costa, Ferreira JM. Fatigue crack growth in thin aluminium alloy sheets under loading sequences with periodic overloads. *Thin-Wall. Struct.* 43 (2005) 772–788. <https://doi.org/10.1016/j.tws.2004.11.001>
- Branco M, Augusto F, de Castro P; *Fadiga de Estruturas Soldadas; 4ª edição, 2006*
- Branco R, Costa JD, Antunes FV, Perdigão S. Monotonic and cyclic behaviour of DIN 34CrNiMo6 martensitic steel. *Metals* 2016, 6, 98. <https://doi.org/10.3390/met60500981>
- Branco R, Costa JD, Antunes FV. Low-cycle fatigue behaviour of 34CrNiMo6 high strength steel. *Theor. Appl. Fract. Mech.* 2012, 58, 28–34. <https://doi.org/10.1016/j.tafmec.2012.02.004>
- Branco R, Costa JD, Berto F, Antunes FV. Fatigue life assessment of notched round bars under multiaxial loading based on the total strain energy density approach. *Theor. Appl. Fract. Mech.* 2017, in press. <https://doi.org/10.1016/j.tafmec.2017.06.003>
- Chaboche JL. A review of some plasticity and viscoplasticity constitutive theories. *International Journal of Plasticity*, Volume 24, Issue 10, 2008, Pages 1642-1693, ISSN 0749-6419. <https://doi.org/10.1016/j.ijplas.2008.03.009>
- Chartrain NA, Williams CB, Whittington AR, A review on fabricating tissue scaffolds using vat photopolymerization, *Acta Biomaterialia*, 74, 2018, 90-111. <https://doi.org/10.1016/j.actbio.2018.05.010>

- Chen A-N, Wu J-M, Liu K, Chen J-Y, Xiao H, Chen P, Li C-H, Shi Y-S, High-performance ceramic parts with complex shape prepared by selective laser sintering: a review, *Advances in Applied Ceramics*, 117:2, 2018, 100-117. <https://doi.org/10.1080/17436753.2017.1379586>
- Childerhouse T, Jackson M, Near Net Shape Manufacture of Titanium Alloy Components from Powder and Wire: A Review of State-of-the-Art Process Routes, *METALS*, 2019, 9(6). doi:10.3390/met9060689
- Concept Laser, accessed at 9 September 2019. <https://www.concept-laser.de/en/technology.html>
- Cordero ZC, Meyer HM, Nandwana P, Dehoff RR, Powder bed charging during electron-beam additive manufacturing, *Acta Materialia*, Volume 124, 2017, Pages 437-445, ISSN 1359-6454. <https://doi.org/10.1016/j.actamat.2016.11.012>
- DMG Mori (1), accessed at 18 December 2019. <https://en.dmgmori.com/resource/blob/396772/c9877c2ed13d4535124c09aada07dd55/pl1uk-lasertec-125-3d-hybrid-pdf-data.pdf>
- DMG Mori (2), accessed at 18 December 2019. <https://en.dmgmori.com/resource/blob/71066/2851a85ce795b8faf6702eaf8804edbe/pl0uk-additive-manufacturing-pdf-data.pdf>
- Dowling NE, Maher F, Prasad KS, Narayanasamy R, *Mechanical Behaviour of Materials – Engineering Methods for Deformation, Fracture, and Fatigue*, 4th Edition (International), Pearson Education Limited, 2013.
- Ellyin F. *Fatigue Damage, Crack Growth and Life Prediction*. 1st ed.; Chapman & Hall: London, UK, 1997; ISBN 0-412-59600-8.
- EOS, accessed at 11 March 2019. https://www.eos.info/additive_manufacturing/for_technology_interested
- Fabrisonic, accessed at 4 December 2019. <https://fabrisonic.com/gradient-material-solutions/>
- Fatemi A, Yang L, Cumulative fatigue damage and life prediction theories: a survey of the state of the art for homogeneous materials, *International Journal of Fatigue*, Volume 20, Issue 1, 1998, Pages 9-34, ISSN 0142-1123. [https://doi.org/10.1016/S0142-1123\(97\)00081-9](https://doi.org/10.1016/S0142-1123(97)00081-9)
- Fayazfar H, Salarian M, Rogalsky A, Sarker D, Russo P, Paserin V, Toyserkani E, A critical review of powder-based additive manufacturing of ferrous alloys: Process parameters, microstructure and mechanical properties, *Materials & Design*, Volume 144, 2018, Pages 98-128, ISSN 0264-1275. <https://doi.org/10.1016/j.matdes.2018.02.018>

- Froend M, Ventzke V, Kashaev N, Klusemann B, Enz J, Thermal analysis of wire-based direct energy deposition of Al-Mg using different laser irradiances, *Additive Manufacturing*, Volume 29, 2019, 100800, ISSN 2214-8604. <https://doi.org/10.1016/j.addma.2019.100800>
- Garmeh S, Jadidi M, Dolatabadi A, Three-Dimensional Modeling of Cold Spray for Additive Manufacturing, *J Therm Spray Tech* 29, 38–50 (2020). <https://doi.org/10.1007/s11666-019-00928-3>
- Garmulewicz A, Holweg M, Veldhuis H, Yang A. Disruptive Technology as an Enabler of the Circular Economy: What Potential Does 3D Printing Hold? *California Management Review*, 2018;60(3):112-132. <https://doi.org/10.1177/0008125617752695>.
- Gisario A, Kazarian M, Martina F, Mehrpouya M, Metal additive manufacturing in the commercial aviation industry: A review, *Journal of Manufacturing Systems*, Volume 53, 2019, Pages 124-149, ISSN 0278-6125. <https://doi.org/10.1016/j.jmsy.2019.08.005>
- Greiner S, Wudy K, Lanzl L, Drummer D, Selective laser sintering of polymer blends: Bulk properties and process behaviour, *Polymer Testing*, Volume 64, 2017, Pages 136-144, ISSN 0142-9418. <https://doi.org/10.1016/j.polymertesting.2017.09.039>
- Griffiths RJ, Petersen DT, Garcia D, Yu HZ. Additive Friction Stir-Enabled Solid-State Additive Manufacturing for the Repair of 7075 Aluminum Alloy, *Applied Sciences*, 2019; 9(17):3486. <https://doi.org/10.3390/app9173486>
- Hu X, Xue Z, Ren TT, Jiang Y, Dong CL, Liu F, On the fatigue crack growth behaviour of selective laser melting fabricated Inconel 625: Effects of build orientation and stress ratio, *Fatigue Fract Eng Mater Struct*. 2020; 43: 771– 787. <https://doi.org/10.1111/ffe.13181>
- Hubs, 3D Printing Trend Report 2022 : Market Changes and Technological Shifts in the 3D Printing Market. Accessed at 25 Mars 2023. <https://www.hubs.com/get/trends/>.
- Ion A, Frohnhofen J, Wall L, Kovacs R, Alistar M, Lindsay J, Lopes P, Chen H-T, Baudisch P. Metamaterial Mechanisms. In *Proceedings of the 29th Annual Symposium on User Interface Software and Technology (UIST '16)*, Association for Computing Machinery, New York, NY, USA, 529–539, 2016. <https://doi.org/10.1145/2984511.2984540>.
- ISO, accessed at April 2023. <https://www.iso.org/obp/ui/#iso:std:iso-astm:52900:ed-2:v1:en>
- Jiang R, Klier R, Piller FT. Predicting the future of additive manufacturing: A Delphi study on economic and societal implications of 3D printing for 2030, *Technological Forecasting and Social Change*. Volume 117, 2017, Pages 84-97, ISSN 0040-1625. <https://doi.org/10.1016/j.techfore.2017.01.006>.

- Jiménez M, Romero L, Domínguez IA, Espinosa, M, Domínguez M. Additive Manufacturing Technologies: An Overview about 3D Printing Methods and Future Prospects. 2019, SN - 1076-2787. <https://doi.org/10.1155/2019/9656938>.
- Kelly CN, Evans NT, Irvin CW, Chapman SC, Gall K, Safranski DL. The effect of surface topography and porosity on the tensile fatigue of 3D printed Ti-6Al-4V fabricated by selective laser melting, *Materials Science and Engineering: C*, Volume 98, 2019, Pages 726-736, ISSN 0928-4931. <https://doi.org/10.1016/j.msec.2019.01.024>.
- Kouraytem N, Chanut RA, Watring DS, Loveless T, Varga J, Spear AD, Kingstedt OT. Dynamic-loading behaviour and anisotropic deformation of pre- and post-heat-treated IN718 fabricated by laser powder bed fusion, *Additive Manufacturing*, Volume 33, 2020, 101083, ISSN 2214-8604. <https://doi.org/10.1016/j.addma.2020.101083>.
- Kujawski D, Ellyin F. The effect of cyclic loading on the slope of the stress-strain immediately upon load reversal. *Res. Mech.* 1987, 22, 295–299.
- Kurita M, Yamamoto M, Toyama K, Effects of Strengthening Mechanisms on Fatigue Properties of Ferrite-Pearlite Hot Rolled Sheet Steel, *Iron and Steel Institute of Japan (ISIJ) – International*, 1996, 36:4:481-486
- Laird C, Smith GL. Initial Stages of Damage in High Stress Fatigue in Some Pure Metals. *Phil. Mag.* 1963, 95, 1945–1963. <https://doi.org/10.1080/14786436308209084>
- Laird C. The Influence of Metallurgical Structure on the Mechanisms of Fatigue Crack Propagation. *Fatigue Crack Propag.* 1967, 131–180.
- Lamarre J-M, Bernier F, Permanent Magnets Produced by Cold Spray Additive Manufacturing for Electric Engines, *Journal of Thermal Spray Technology*, 2019, 28(7), 1709–1717. <https://doi.org/10.1007/s11666-019-00917-6>
- Lasdon LS, Waren AD, Jain A, Ratner MW. Design and Testing of a Generalized Reduced Gradient Code for Non-Linear Optimization. NTIS National Technical Information Service U. S. Department of Commerce: Cleveland, OH, USA, 1975.
- Lefebvre D, Ellyin F. Cyclic response and inelastic strain energy in low cycle fatigue. *Int. J. Fatigue* 1984, 6, 9–15. [https://doi.org/10.1016/0142-1123\(84\)90003-3](https://doi.org/10.1016/0142-1123(84)90003-3)
- Li W (1), Cao C, Xu Y, Yang X, Wang G, Wang F, “Cold spray +” as a new hybrid additive manufacturing technology: a literature review, *Science and Technology of Welding and Joining*, 2019, 24(5), 420–445. <https://doi.org/10.1080/13621718.2019.1603851>

- Li W (2), Cao C, Yin S. Solid-state cold spraying of Ti and its alloys: A literature review, *Progress in Materials Science*, 2019, 100633, ISSN 0079-6425. <https://doi.org/10.1016/j.pmatsci.2019.100633>
- Llewellyn DT, Hudd RC, *Steels: Metallurgy & Applications*, Third Edition, Butterworth-Heinemann Publisher, 1998, Pages 260-264, ISBN 0 7506 3757 9
- Luecke WE, Slotwinski JA. Mechanical Properties of Austenitic Stainless Steel Made by Additive Manufacturing *Journal of Research of the National Institute of Standards and Technology*, 2014;119:398-418. <http://doi.org/10.6028/jres.119.015>
- Luecke WE, Slotwinski JA. Mechanical Properties of Austenitic Stainless Steel Made by Additive Manufacturing. *Journal of research of the National Institute of Standards and Technology*. 2014;119:398-418. <https://doi.org/10.6028/jres.119.015>
- Markforged (1), accessed at 20 October 2019. <https://markforged.com/materials/>
- Markforged (2), accessed at 20 October 2019. <https://markforged.com/mark-two/>
- Matsuura, accessed at 19 June 2023. <https://www.lumex-matsuura.com/english/about>
- Mcor, accessed at 4 December 2019. <https://www.mcor technologies.com/industries/entertainment/>
- Mercelis P, Kruth JP. Residual stresses in selective laser sintering and selective laser melting, *Rapid Prototype. J.* 12 (5) (2012) 254–265. <https://doi.org/10.1108/13552540610707013>
- Meyers MA and Chawla KK, *Mechanical Behaviour of Materials*, Prentice Hall 2009 and Cambridge University Press 2009 (USA).
- Miner MA. Cumulative Damage in Fatigue. *J. Appl. Mech.* 1945, 12, A159–A164. <https://doi.org/10.1115/1.4009458>
- Mitchell A, Lafont U, Hołyńska M, Semprimoschnig C, Additive manufacturing – A review of 4D printing and future applications, *Additive Manufacturing*, Volume 24, 2018, Pages 606-626, ISSN 2214-8604. <https://doi.org/10.1016/j.addma.2018.10.038>
- Morrow J. Cyclic plastic strain energy and fatigue of metals. In *International Friction, Damping and Cyclic Plasticity*; ASTM STP 378; American Society for Testing and Materials: Philadelphia, PA, USA, 1965; pp. 45–87.

- MPreport, New machine combines 3D printing and machining, Metal Powder Report, Volume 70, Issue 3, 2015, Pages 150-151, ISSN 0026-0657. <https://doi.org/10.1016/j.mprp.2015.03.013>
- Mugwagwa L, Yadroitsev I, Matope S, Effect of Process Parameters on Residual Stresses, Distortions, and Porosity in Selective Laser Melting of Maraging Steel 300, Metals, 2019, 9(10):1042. <https://doi.org/10.3390/met9101042>
- Ngo TD, Kashani A, Imbalzano G, Nguyen KTQ, Hui D, Additive manufacturing (3D printing): A review of materials, methods, applications and challenges, Composites Part B: Engineering, Volume 143, 2018, Pages 172-196, ISSN 1359-8368. <https://doi.org/10.1016/j.compositesb.2018.02.012>
- Nida S, Moses JA, Anandharamakrishnan C. Emerging applications of 5D and 6D printing in the food industry. Journal of Agriculture and Food Research, 2022; 10. <https://doi.org/10.1016/j.jafr.2022.100392>.
- Ning Y, Fuh JYH, Wong YS, Loh HT, An intelligent parameter selection system for the direct metal laser sintering process, International Journal of Production Research, 42:1, 2004, 183-199. <http://dx.doi.org/10.1080/00207540310001595873>
- Oh Y, Bharambe V, Mummareddy B, Martin J, McKnight J, Abraham MA, Walker JM, Rogers K, Conner B, Cortes P, MacDonald E, Adams JJ, Microwave dielectric properties of zirconia fabricated using NanoParticle Jetting™, Additive Manufacturing, Volume 27, 2019, Pages 586-594, ISSN 2214-8604. <https://doi.org/10.1016/j.addma.2019.04.005>
- Padhy GK, Wu CS, Gao S, Friction stir based welding and processing technologies - processes, parameters, microstructures and applications: A review, Journal of Materials Science & Technology, Volume 34, Issue 1, 2018, Pages 1-38, ISSN 1005-0302. <https://doi.org/10.1016/j.jmst.2017.11.029>
- Pearce J, Jun-Yu Qian. Economic Impact of Home Manufacturing of Consumer Products with Low-cost 3D Printing of Free and Open-Source Designs. European Journal of Social Impact & Circular Economy. 2022;3(2):1-24. <https://doi.org/10.13135/2704-9906/6508>.
- Qian G, Jian Z, Qian Y, Pan X, Ma X, Hong Y. Very-high-cycle fatigue behaviour of AlSi10Mg manufactured by selective laser melting: Effect of build orientation and mean stress, International Journal of Fatigue, Volume 138, 2020, 105696, ISSN 0142-1123. <https://doi.org/10.1016/j.ijfatigue.2020.105696>.

- Rafi HK, Pal D, Patil N, Starr TL, Stucker BE. Microstructure and mechanical behaviour of 17-4 precipitation hardenable steel processed by selective laser melting. *J. Mater. Eng. Perform.* 23 (2014) 4421–4428. <https://doi.org/10.1007/s11665-014-1226-y>
- Raouf HA, Topper TH, Plumtree A. Cyclically plasticity and mising behaviour in metals and alloys. In *Proceedings of the 4th International Conference of Fracture (ICF4)*, Waterloo, ON, Canada, 19–24 June 1977.
- Ryan KR, Down MP, Banks CE. Future of additive manufacturing: Overview of 4D and 3D printed smart and advanced materials and their applications. *Chemical Engineering Journal*, Volume 403, 2021, 126162, ISSN 1385-8947. <https://doi.org/10.1016/j.cej.2020.126162>.
- Sarkar S, Kumar CS, Nath AK. Effect of mean stresses on mode of failures and fatigue life of selective laser melted stainless steel, *Materials Science and Engineering: A*, Volume 700, 2017, Pages 92-106, ISSN 0921-5093. <https://doi.org/10.1016/j.msea.2017.05.118>.
- Sha W, Guo Z, *Maraging Steels: Modelling of microstructure, properties and applications*, Woodhead publishing limited, Pages 1-16, 2009, ISBN 978-1-84569-693-1.
- Shahrubudin N, Lee TC, Ramlan R, An Overview on 3D Printing Technology: Technological, Materials, and Applications, *Procedia Manufacturing*, Volume 35, 2019, Pages 1286-1296, ISSN 2351-9789. <https://doi.org/10.1016/j.promfg.2019.06.089>
- Sharma KS. Artificial Intelligence Assisted Fabrication of 3D, 4D and 5D Printed Formulations or Devices for Drug Delivery. *Current drug delivery*, 2023; 20(6):752-769. <https://doi.org/10.2174/1567201820666221207140956>.
- Shen X, Naguib HE, A robust ink deposition system for binder jetting and material jetting, *Additive Manufacturing*, Volume 29, 2019, 100820, ISSN 2214-8604. <https://doi.org/10.1016/j.addma.2019.100820>
- Sheng R, *3D Printing: A Revolutionary Process for Industry Applications*. London, United Kingdom: Academic Press, SN – 9780323994637, 2022.
- Shin CS, Hsu SH. On the mechanisms and behaviour of overload retardation in AISI 304 stainless steel. *Int. J. Fatigue* 15 (3) (1993) 181–192. [https://doi.org/10.1016/0142-1123\(93\)90175-P](https://doi.org/10.1016/0142-1123(93)90175-P)
- Shirazi SFS, Gharekhani S, Mehrali M, Yarmand H, Metselaar HSC, Kadri NA, Osman NAA, A review on powder-based additive manufacturing for tissue engineering: selective laser sintering and inkjet 3D printing, *Science and Technology of Advanced Materials*, 16:3, 2015, 033502. <https://doi.org/10.1088/1468-6996/16/3/033502>

- Simchi A, Direct laser sintering of metal powders: Mechanism, kinetics and microstructural features, *Materials Science and Engineering: A*, Volume 428, Issues 1–2, 2006, Pages 148-158, ISSN 0921-5093. <https://doi.org/10.1016/j.msea.2006.04.117>.
- SLMSolutions, accessed at 6 October 2023. <https://www.slm-pushing-the-limits.com/>
- Smith R, Hirschberg M, Manson S. Fatigue Behaviour of Materials under Strain Cycling in Low and Intermediate Life Range. NACA TN D-1574; National Advisory Committee for Aeronautics: Kitty Hawk, NC, USA, 1963.
- Sodick, accessed at 6 October 2023. <https://sodick.com/machines/metal-3d-printing/>
- Souza AF, Al-Rubaie KS, Marques S, Zluhan B, Santos EC, Effect of laser speed, layer thickness, and part position on the mechanical properties of maraging 300 parts manufactured by selective laser melting, *Materials Science and Engineering: A*, Volume 767, 2019, 138425, ISSN 0921-5093. <https://doi.org/10.1016/j.msea.2019.138425>
- Srivastava M, Rathee S, Maheshwari S, Siddiquee AN; Kundra TK, A Review on Recent Progress in Solid State Friction Based Metal Additive Manufacturing: Friction Stir Additive Techniques, *Critical Reviews in Solid State and Materials Sciences*, 44:5, 2019, 345-377, <https://doi.org/10.1080/10408436.2018.1490250>
- Stephens RI, Fatemi A, Stephens RR, Fuchs HO, *Metal Fatigue in Engineering*, Second Edition, John Wiley & Sons 2001, Chap. 1, ISBN 0-471-51059-9
- Suresh S, *Fatigue of Materials*, Second Edition, Cambridge: Cambridge University Press, 2004. <https://doi.org/10.1017/CBO9780511806575>
- Suresh S. Micromechanisms of fatigue crack growth retardation following overloads. *Eng. Fracture Mech.* 18 (1983) 577–593. [https://doi.org/10.1016/0013-7944\(83\)90051-6](https://doi.org/10.1016/0013-7944(83)90051-6)
- TCT, accessed at 6 October 2023. <https://www.tctmagazine.com/additive-manufacturing-3d-printing-news/aurora-labs-testing-beta-rmp1-3d-printer/>
- Thompson MK, Moroni G, Vaneker T, Fadel G, Campbell RI, Gibson I, Martina F, Design for Additive Manufacturing: Trends, opportunities, considerations, and constraints. *C I R P Annals*, 24, 2016. <https://doi.org/10.1016/j.cirp.2016.05.004>
- Tofail SAM, Koumoulos EP, Bandyopadhyay A, Bose S, O'Donoghue L, Charitidis C, Additive manufacturing: scientific and technological challenges, market uptake and opportunities, *Materials Today*, Volume 21, Issue 1, 2018, Pages 22-37, ISSN 1369-7021. <https://doi.org/10.1016/j.mattod.2017.07.001>

- Van de Velde E (1), Kretz D, European Commission, Executive Agency for Small and Medium-sized Enterprises. Advanced technologies for industry: product watch: 3D printing of hybrid components. Publications Office, 2021, <https://doi.org/10.2826/6144>.
- Van de Velde E (2), Kretz D, European Commission, Executive Agency for Small and Medium-sized Enterprises. Advanced technologies for industry : product watch : 3D printing for the machine tool industry. Publications Office, 2021, <https://doi.org/10.2826/45768>.
- Vasco-Olmo JM, Díaz F, Antunes FV, James MN. Evaluación Experimental Del CTOD En El Crecimiento De Grieta A Fatiga A Partir De Los Campos De Desplazamientos. In Proceedings of the XXXV Encuentro del Grupo Español de Fractura, Málaga, Spain, 14–16 March 2018.
- Velo3D, accessed at 6 October 2023. <https://velo3d.com/product-brief-sapphire-and-sapphire-1mz-printer/>
- Velu R, Fernyhough A, Smith DA, Guen MJL, Singamneni S, Selective Laser Sintering of Biocomposite Materials, *Lasers in Engineering* (Old City Publishing), 2016, 35(1-4):173-186, ISSN: 0898-1507.
- Voce E. The relationship between stress and strain for homogeneous deformation. *J. Inst. Met.* 1948, 74, 537–562.
- Wang D, Liu L, Deng G, Deng C, Bai Y, Yang Y, Wu W, Chen J, Liu Y, Wang Y, Lin X, Han C. Recent progress on additive manufacturing of multi-material structures with laser powder bed fusion. *Virtual and Physical Prototyping*, 2022; 17:2, 329-365. <https://doi.org/10.1080/17452759.2022.2028343>.
- Wang (1), Chou K, EBSD study of beam speed effects on Ti-6Al-4V alloy by powder bed electron beam additive manufacturing, *Journal of Alloys and Compounds*, Volume 748, 2018, Pages 236-244, ISSN 0925-8388. <https://doi.org/10.1016/j.jallcom.2018.03.173>
- Wang (2), Chou K, Effect of support structures on Ti-6Al-4V overhang parts fabricated by powder bed fusion electron beam additive manufacturing, *Journal of Materials Processing Technology*, Volume 257, 2018, Pages 65-78, ISSN 0924-0136. <https://doi.org/10.1016/j.jmatprotec.2018.02.038>
- Wu H, Fahy W, Kim S, Kim H, Zhao N, Pilato L, Kafi A, Bateman S, Koo JH, Recent Developments in Polymers/Polymer Nanocomposites for Additive Manufacturing, *Progress in Materials Science (journal pre-proofs)*, 2020. <https://doi.org/10.1016/j.pmatsci.2020.100638>

- Xiang Z, Yin M, Dong G, Mei X, Yin G, Modeling of the thermal physical process and study on the reliability of linear energy density for selective laser melting, *Results in Physics*, Volume 9, 2018, Pages 939-946, ISSN 2211-3797. <https://doi.org/10.1016/j.rinp.2018.03.047>
- Yao Y, Huang Y, Chen B, Tan C, Su Y, Feng J. Influence of processing parameters and heat treatment on the mechanical properties of 18Ni300 manufactured by laser based directed energy deposition. *Opt. Laser Technol.* 2018, 105, 171–179. <https://doi.org/10.1016/j.optlastec.2018.03.011>
- Yin S, Cavaliere P, Aldwell B, Jenkins R, Liao H, Li W, Lupoi R, Cold spray additive manufacturing and repair: Fundamentals and applications, *Additive Manufacturing*, Volume 21, 2018, Pages 628-650, ISSN 2214-8604. <https://doi.org/10.1016/j.addma.2018.04.017>
- Zeng Z, Deng X, Cui J, Jiang H, Yan S, Peng B, Improvement on Selective Laser Sintering and Post-Processing of Polystyrene, *Polymers*, 2019, 11(6):956. <https://doi.org/10.3390/polym11060956>
- Zhang B, Dembinski L, Coddet C, The study of the laser parameters and environment variables effect on mechanical properties of high compact parts elaborated by selective laser melting 316L powder, *Materials Science and Engineering: A*, Volume 584, 2013, Pages 21-31, ISSN 0921-5093. <https://doi.org/10.1016/j.msea.2013.06.055>
- Zhang J, Lü C, Guo W, Van Der Gert H. A Probability Model of Fatigue Life Assessment Based on Modified Paris Law with Independent Material Coefficients. *Ship Building of China*, 2020; 61(4):95-104-104. <https://doi.org/10.21278/TOF.452015320>.
- Zhang Z, Tan ZJ, Li JY, Zu YF, Liu WW, Sha JJ, Experimental and numerical studies of re-stirring and re-heating effects on mechanical properties in friction stir additive manufacturing, *International Journal of Advanced Manufacturing Technology* (2019) 104:767–784. <https://doi.org/10.1007/s00170-019-03917-6>
- Zhao Z, Yang X, Li S, Li D, Interfacial bonding features of friction stir additive manufactured build for 2195-T8 aluminum-lithium alloy, *Journal of Manufacturing Processes*, Volume 38, 2019, Pages 396-410, ISSN 1526-6125. <https://doi.org/10.1016/j.jmapro.2019.01.042>
- Zhou L, Yuan T, Li R, Tang J, Wang G, Guo K, Yuan J. Densification, microstructure evolution and fatigue behaviour of Ti-13Nb-13Zr alloy processed by selective laser melting. *Powder Technology*. 2019; 342:11-23. <https://doi.org/10.1016/j.powtec.2018.09.073>
- Ziaee M, Crane NB. Binder jetting: A review of process, materials, and methods. *Additive Manufacturing* 28. 2019, 781–801. <https://doi.org/10.1016/j.addma.2019.05.031>